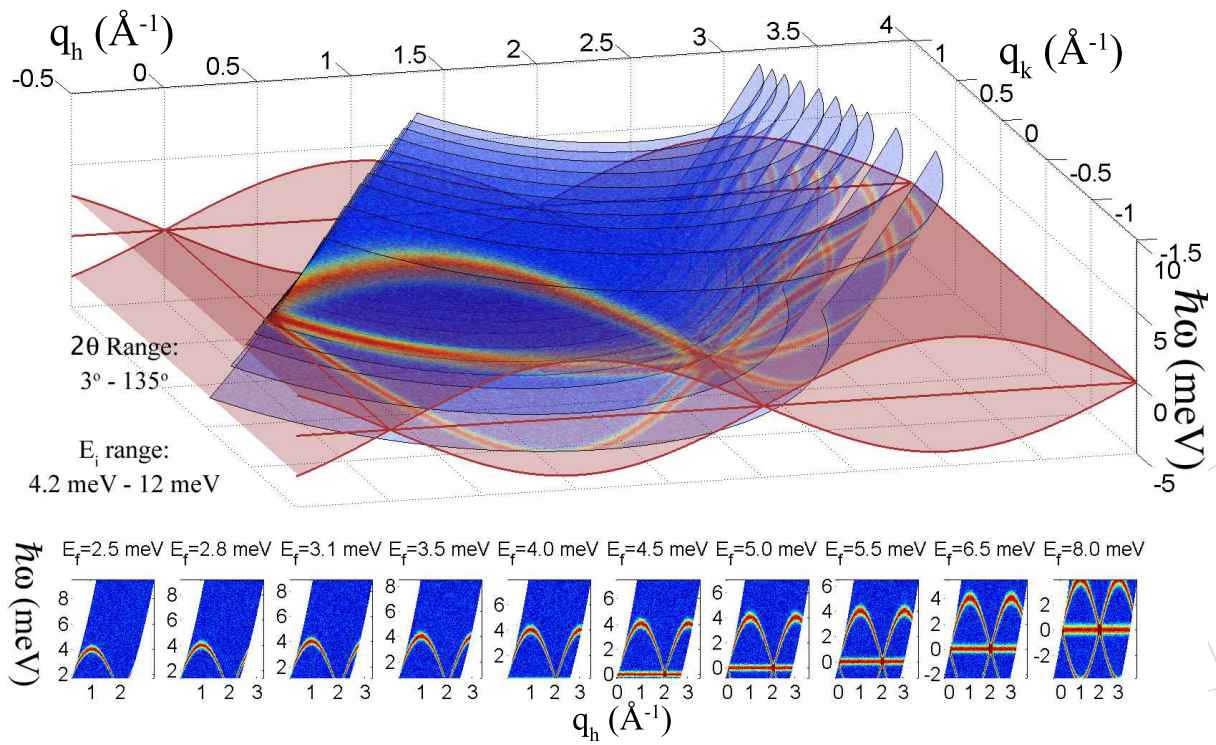




# New Techniques in Neutron Scattering



## PhD Thesis

October 31, 2014

Jonas Okkels Birk

Nano-Science Center  
Niels Bohr Institute  
University of Copenhagen

### Supervisors:

Prof. Dr. Kim Lefmann  
As. Prof. Henrik Ronnow  
Prof. Kurt Clausen



# Contents

<b>Abstract</b>	<b>7</b>
<b>Dansk Resumé</b>	<b>9</b>
<b>Acknowledgements</b>	<b>11</b>
<b>1 Magnetism</b>	<b>13</b>
1.1 Origin of Magnetism . . . . .	13
1.1.1 Paramagnetism . . . . .	14
1.1.2 Exchange Interactions . . . . .	14
1.2 Magnetic Order . . . . .	15
1.2.1 Ferromagnetism . . . . .	15
1.2.2 Antiferromagnetism . . . . .	15
1.2.3 Next nearest Neighbours . . . . .	15
1.2.4 Magnetic Excitations . . . . .	16
1.2.5 Phase Transitions . . . . .	16
1.2.6 Multiferroics . . . . .	16
<b>2 Neutron Scattering</b>	<b>17</b>
2.1 Scattering . . . . .	17
2.1.1 Cross Sections . . . . .	19
2.1.2 Resolutions . . . . .	20
2.1.3 Peak Broadening . . . . .	21
2.2 Neutron Scattering . . . . .	21
2.2.1 Incoherent Scattering . . . . .	22
2.2.2 Inelastic Scattering . . . . .	22
2.2.3 Magnetism . . . . .	23
2.2.4 Sample Environments . . . . .	24
<b>3 Neutron Instrumentation</b>	<b>25</b>
3.1 Neutron Spectroscopy . . . . .	25
3.1.1 Neutron Sources . . . . .	25
3.1.2 Moderators . . . . .	27
3.1.3 Neutron Guides . . . . .	27
3.1.4 Sample Area . . . . .	29
3.1.5 Diffractometers . . . . .	29

---

3.1.6	Triple Axis Spectrometers . . . . .	31
3.1.7	Time-of-Flight Spectrometers . . . . .	32
3.1.8	Background . . . . .	32
3.1.9	Polarization . . . . .	33
3.1.10	Time resolved Scattering . . . . .	33
3.1.11	Other Neutron Techniques . . . . .	35
3.1.12	X-ray Instruments . . . . .	35
3.2	Increasing the Performance of Instruments . . . . .	35
3.2.1	Focusing . . . . .	36
3.2.2	Mapping . . . . .	37
3.3	Examples of Existing Instruments . . . . .	38
3.3.1	RITA II . . . . .	38
3.3.2	ToFToF . . . . .	39
3.4	Monte Carlo Simulations of Instruments . . . . .	39
3.4.1	McStas . . . . .	39
<b>4</b>	<b>CAMEA</b> . . . . .	<b>41</b>
4.1	Instrument Overview . . . . .	42
4.2	The Prototype . . . . .	43
4.2.1	Preliminary Prototyping . . . . .	44
4.2.2	Design of the Prototype . . . . .	45
4.2.3	Installation of the Prototype . . . . .	48
4.3	Simulations . . . . .	55
4.3.1	Detectors . . . . .	55
4.3.2	guide_bot . . . . .	56
4.3.3	Potential errors in the Simulations . . . . .	56
4.3.4	Errors in the guide_bot Results . . . . .	57
4.4	Instrument Design . . . . .	57
4.4.1	Moderator . . . . .	57
4.4.2	Instrument Length . . . . .	58
4.4.3	The Neutron Guide . . . . .	60
4.4.4	The Chopper System . . . . .	65
4.4.5	Diffraction Resolution . . . . .	76
4.4.6	Sample Area . . . . .	76
4.4.7	Polarisation Analysis . . . . .	78
4.4.8	Collimation and Slits . . . . .	78
4.4.9	High Energy Filter . . . . .	80
4.4.10	Analysers . . . . .	80
4.4.11	Detectors . . . . .	94
4.4.12	a4 Coverage . . . . .	98
4.4.13	Dark Angles . . . . .	98
4.4.14	Secondary time Resolution . . . . .	105
4.4.15	Background . . . . .	106
4.5	Optimizing CAMEA . . . . .	113
4.6	Final Design and Performance . . . . .	114
4.6.1	Comparison to a TAS at ESS . . . . .	114

---

4.6.2	Comparison to a Cold Chopper Spectrometer at ESS . . .	116
4.6.3	Comparison to Existing Instruments . . . . .	119
4.7	Demonstration Experiments . . . . .	119
4.8	Uncertainties . . . . .	124
4.9	Comming CAMEA Instruments . . . . .	124
4.9.1	Other CAMEA Implementations . . . . .	124
<b>5</b>	<b>NiMn<sub>2</sub>O<sub>4</sub></b>	<b>127</b>
5.1	Measurements . . . . .	127
5.1.1	Elastic Data Treatment . . . . .	127
5.1.2	Inelastic Data Treatment . . . . .	128
5.1.3	Neutron Spectroscopy Results . . . . .	131
<b>6</b>	<b>LiNiPO<sub>4</sub></b>	<b>133</b>
6.1	Measurement . . . . .	134
6.1.1	Experimental Setup . . . . .	134
6.1.2	Experimental Results . . . . .	135
6.2	Conclusion . . . . .	138
<b>7</b>	<b>Concluding Remarks</b>	<b>139</b>
<b>8</b>	<b>List of Publications</b>	<b>143</b>
	<b>Litterature</b>	<b>145</b>
<b>A</b>	<b>Articles</b>	<b>155</b>



# Abstract

Neutron scattering is a constantly evolving technique. New facilities and more powerful instrumentation enables measurements on smaller samples but also provide the means to perform more parametric studies. This thesis describes the designing of the CAMEA inverse time-of-flight neutron spectrometer for the future European Spallation Source. In parallel with the CAMEA design I participated in a number of small scientific projects, of which 2 is documented in this thesis and 2 in the attached articles. The described work was done as part of my PhD enrolment at the Niels Bohr Institutue, Copenhagen University.

The European Spallation Source has the potential to become the highest performing neutron scattering facility in the world. The source brightness will equal the currently brightest existing facility but will be pulsed, providing possibilities for instruments with greater coverage if the instruments are designed to use this pulse. The new long pulsed concept was used as an opportunity to redesign a number of instrument concepts using the instrumental advances of recent decades with the goal of building unprecedented powerful instruments that take advantage of the source. One of these designs is the CAMEA instrument.

CAMEA combines time-of-flight and crystal analyser technologies to achieve the highest possible count rates in each detector channel. This is combined with a multiplexed backend that will record an unprecedented large fraction of the horizontal scattering plane, and a new prismatic analyser technique that ensures improved energy resolution. The high coverage and count rates will make it ideal for parametric studies in the horizontal scattering plane.

The design of CAMEA involved kinematic calculations, simulations and prototyping to optimize the instrument and ensure that it will deliver the predicted performance when constructed. The design work was compiled into an instrument proposal for the European Spallation Source, and approved for construction.

$\text{LiNiPO}_4$  in a combined electric and magnetic field was investigated as a step towards the long term goal of developing a method for time resolved neutron spectroscopy of quantum phase transitions. The measurements showed considerable difficulties with electric sparks and hysteresis issues around the phase transition. However, some interesting relaxation phenomena was observed.

$\text{NiMn}_2\text{O}_4$  have proven difficult to synthesis in a uniform sample. A new chem-

ical process was expected produce a more uniform material. This sample was investigated with neutron spectroscopy. The data showed agreement with other manufacturing processes and gave new insight in the spin structures and excitations. A possible new phase transition was also identified.

# Dansk Resumé

Neutronspredning er en teknik i konstant udvikling. Nye faciliteter og bedre instrumenter muliggør målinger på stadig mindre prøver, samt giver mulighed for flere parametriske studier. Denne afhandling beskriver designet af det inverse time-of flight spektrometer CAMEA til den kommende Europæiske Spallations Kilde. Jeg deltog parallelt med CAMEA designet i et antal mindre videnskabelige projekter, af hvilke to er dokumenteret i denne afhandling og to i de vedhæftede artikler. Det beskrevne arbejde var en del af min Ph.d. ansættelse ved Niels Bohr Institutet, Københavns Universitet.

Den Europæiske Spallations Kilde har potentialet, til at blive verdens ledende neutronspretnings facilitet. Kildens styrke bliver på linje med den kraftigste eksisterende kilde, men den vil grundet sin pulsede karakter give mulighed for instrumenter med meget store dækningsområde, hvis instrumenterne er designet til at udnytte pulserne. Kildens nye langpulsede koncept var en anledning til at gendesigne en række eksisterende instrumentkoncepter, og inddrage de sidste årtiers landvindinger indenfor neutroninstrumentering til at designe nye bedre ydende instrumenter, der kan udnytte den nye kilde. CAMEA er et sådan nydesignet instrument.

CAMEA kombinerer time-of-flight teknikken med analysator krystaller for at opnå den højest mulige intensitet i hver målekanal. Dette bliver kombineret med en multi-analysator, der kommer til at dække en uset stor del af det horisontale spredningsplan, og en ny prismatisk analysator teknik, der giver en forbedret energiopløsning samt øger den samlede tællestatistik. Den høje dækningsgrad og tællestatistik vil gøre CAMEA ideel til parametriske studier i det horisontale spredningsplan.

For at optimere CAMEA og sikre, at instrumentet vil levere den forventede ydeevne involverede designet kinematiske beregninger, simuleringer og prototype målinger. Resultatet blev sammenfattet i en instrument konstruktions ansøgning til den Europæiske Spallationskilde, og instrumentet er blevet udvalgt til konstruktion.

$\text{LiNiPO}_4$  i et kombineret elektrisk og magnetisk felt blev undersøgt som et skridt på vejen mod at udføre tidsopløst neutronspredning på kvantefaseovergange. Målingerne afslørede alvorlige problemer med elektriske gnister samt hystereseproblemer omkring faseovergangen. Nogle interessante relaxationsfænomener blev dog observeret.

$\text{NiMn}_2\text{O}_4$  har vist sig vanskeligt at syntetisere til en ensartet prøve. En ny kemisk fremstillingsproces forventedes dog at producere et mere ensartet resultat. En sådan prøve blev undersøgt med neutronspektroskopi. Data var i overensstemmelse med resultater fra andre fremstillingsmetoder og gav ny viden om spinstrukturen i materialet samt de magnetiske eksitationer. En hidtil uobserveret faseovergang blev også fundet.

# Acknowledgements

All projects described in this thesis were collaborations between a number of scientists. None of the results could have been achieved without dedicated work by the many contributors and I would like to thank everyone for their participation. Below I will describe my involvement in the different projects.

The CAMEA instrument design was made as a collaboration between a number of people: Henrik Rønnow was leader of the group and my co-supervisor. Kim Lefmann was coordinator of the contribution from Copenhagen University and my direct supervisor. Christof Niedermeyer coordinated the PSI work on the instrument. Fanni Jurányi was responsible for the MARS instrument, where the prototype was installed. Niels Bech Cristensen coordinated the DTU effort and did most of the costing work. Paul Freeman did most of the science case and the quarterly reportings to ESS. Márton Markó worked on the prototype installation and experiments and produced an analytical model of the instrument that I will quote for resolutions. Mads Bertelsen did much of the guide simulation. Johan Jacobsen produced the first McStas file of the first analyser setup for his master thesis. Ove Rasmussen and Finn Saxild were the technicians behind the prototype. A number of technicians worked on the prototype on PSI, including Dieter Graf, Greuter Urs, and Roman Bürge. I was daily leader of the first part of the work, did all kinematic calculations, provided input for the guide simulations and finished them when Mads had other obligations, and did all other simulations mentioned here, designed the prototype and the final proposed instrument together with the technicians, worked together with Marton on installation of the prototype and experiments, gave input to the science case and did resolution calculations for time resolutions.

I will mainly focus on parts where I contributed substantially to the work and quote my collaborators for result and figures where it is necessary to explain the choices taken in the instrument design.

The  $\text{LiNiPO}_4$  project was undertaken in collaboration between Henrik Rønnow, Kim Lefmann, Michel Kenzelmann, and me. I aligned and prepared the crystals while Marek Bartkowiak did most of the work on the new sample stick, used for the experiment. Rasmus Toft-Petersen, Kim Lefmann, Henrik Jacobsen and I performed the experiment. Henrik Jacobsen and I performed the data analysis.  $\text{NiMn}_2\text{O}_4$  was a project led by Heloisa Bordallo. When I joined the project the samples was prepared and measured by x-ray diffraction, neutron diffraction,

and magnetisation measurements. I performed a neutron spectroscopy measurement of the sample together with Giovanna Simeoni, Nina Jacobsen and Fabiano Yokaichiya. I also analysed the neutron spectroscopy data. Walter Kalceff, Rafael A. Ferreira, and Julio C.G. Tedesco collected the result and wrote the attached article.

Goethite ( $\text{FeO}(\text{OH})$ ) was a project led by Cathrine Frandsen where a number of different methods was used to investigate the sample. I participated in the neutron spectroscopy measurement together with Giovanna Simeoni, Henrik Jacobsen, Morten Lundgren Olsen, and Giacomo Mariotti and performed a large part of the neutron spectroscopy data analysis. Erik Brok collected the results and wrote most of the article.

The simulated instruments used for the European Spallation Source was simulated by Kaspar H Klenø, Britt R Hansen, Sonja L Holm, Erik Knudsen, Klaus Lieutenant, Lars von Moos, Morten Sales, Kim Lefmann, and Peter K Willendrup with input from Ken Andersen. I collected the results from the different simulators and used this to produce the final performance numbers with input from the remaining group members. Kim Lefmann and Ken Andersen wrote the article.

# Chapter 1

## Magnetism

*I will here present a brief description of magnetic solid state theory. A more thorough presentation can be found in a dedicated textbook [45]. I assume general knowledge of solid state physics, for example the knowledge of lattice structures, reciprocal lattices and phonons. [37, 83]*

Magnetism in solid state physics describes the distribution of magnetic moments inside materials. Although magnetic materials can be observed in everyday life it is pure quantum mechanical in its core, and does lead to many exotic phenomena.

### 1.1 Origin of Magnetism

Magnetic moments can be caused by the electronic and nuclear spins as well as electron orbits. The electron is a fermion with a spin of  $m_s = \pm \frac{1}{2}\hbar$  and a magnetic moment of  $-g\mu_B \mathbf{s}$ , where  $\mathbf{s}$  is the vector describing the spin and  $g$ , called the electronic g-factor, describes the intrinsic magnetic moment of an electronic spin and takes a value of  $\sim 2$ .  $\mu_B$  is the Bohr magneton and takes the value  $\mu_B = -\frac{e\hbar}{2m_e} = 9.274 \times 10^{-24} \text{ Am}^2$ , where  $e$  is the electronic charge and  $m_e$  is the electronic mass. Furthermore, the electron can have an orbital momentum  $m_l$  giving rise to a magnetic moment of  $-\mu_B \mathbf{l}$  where  $\mathbf{l}$  is the vector describing the angular momentum. Since the magnetic moment of a particle is inversely proportional to its mass the magnetic moments of the nuclei are much weaker than the magnetic moment of electrons. The nuclear magnetic moments are still able to influence the electrons, but the main magnetic contribution is from the electrons.

When several electrons are bound to the same atom the moments are added. Since electrons are fermions only a single spin up and a single spin down electron can occupy a given state. This causes the inner shells of an atom to be filled with equal number of spins with spin up and down and the magnetic moments cancel out. However, for shells, that are only partially filled, the electrons generally arrange themselves according to Hund's rules[45] in the ground state, and this can give rise to several uncompensated magnetic moments aligning in parallel. Of special interest are materials where the 3d (transition metals) or 4f (lanthanides) shell is partially filled.

### 1.1.1 Paramagnetism

The actual magnetic forces between the electrons are very weak so with no other interactions present, magnetic order breaks down at very low temperature. The uncompensated spins will in this paramagnetic phase be aligned randomly. If an external magnetic field,  $B$ , is applied the spins will align along the field. However, the strength of the response will be low and inversely proportional to the temperature. If the field is later removed the thermal fluctuation will remove any order from the system again.

### 1.1.2 Exchange Interactions

Rather than from direct dipole coupling, magnetic ordering arises from quantum mechanics and Coulomb repulsion between electrons. If one considers two electrons situated on two different atoms, but with overlapping electronic wave functions, the collective wave function is a product of the two. However, since this new wave function is required to be anti-symmetric under exchange[115] the spacial wave function needs to be symmetric and the spin wave function anti-symmetric or vice versa. Since the product of the two is neither symmetric nor anti-symmetric, it is necessary to change to a basis of wave functions to a collective state. 4 such states exist. An anti-symmetric singlet state  $\frac{1}{\sqrt{2}}(\phi(1)\phi(2) - \phi(2)\phi(1))$ , where  $\phi(i)$  is an electron located on the  $i$ 'th position or with the spin value  $i$  depending on whether the spacial or spin part of the wave function is considered. The 3 symmetric triplet states are:  $\frac{1}{\sqrt{2}}(\phi(1)\phi(2) + \phi(2)\phi(1))$ ,  $\phi(1)\phi(1)$ , and  $\phi(2)\phi(2)$ . Electrostatic repulsion can now ensure that it is advantageous for the electrons to be furthest possible away - i.e. have an anti-symmetric spatial wave function, ensuring a symmetric spin wave function.

However, there is also an energetic advantage of being as delocalized as possible which is often achieved with the symmetric spatial distribution, causing an anti-symmetric spin distribution. A typical example is the so called superexchange, usually mitigated by an oxygen bridge between the two atoms. Such a bridge enables the electrons to jump to the neighbouring atom, increasing their position uncertainty. By Heisenberg's uncertainty principle this allows a lower momentum uncertainty and thus lower average momentum and kinetic energy. This is best achieved with anti-symmetric spins. Which interaction factor is dominating depends on the crystal structure and electronic wave functions in question. The resulting energy landscape can often be expressed in the Heisenberg model by the Hamiltonian:

$$\hat{H}_{spin} = - \sum_{i,j} J_{i,j} \hat{\mathbf{s}}_i \cdot \hat{\mathbf{s}}_j \quad (1.1)$$

where  $J$  is some effective exchange constant originating from the effects above. However, there are other possible exchange interactions and crystal anisotropies can also influence the system. If a crystal anisotropy term that makes it advantageous for the spins to point along a certain direction are considerably stronger

than  $J$  reducing the problem to one spin dimension (the Ising model):

$$\hat{H}_{spin} = - \sum_{i,j} J_{i,j} \tilde{s}_i \cdot \tilde{s}_j \quad (1.2)$$

## 1.2 Magnetic Order

The exchange interactions described above can cause the system to order in many different ways, some of which will be described here.

### 1.2.1 Ferromagnetism

If  $J > 0$ , neighbouring the electrons will find it energetically advantageous to have parallel spins. This means that the system will order macroscopically over large distances with parallel spins. Entropy, dipole interactions, and boundary considerations can break the order and ensure that the system only orders in large domains with spins pointing in the same direction, but even a relatively small magnetic field will provoke a strong response as the domains align along the external field reinforcing the external field. Such systems are called ferromagnetic.

### 1.2.2 Antiferromagnetism

If  $J < 0$  the system is called antiferromagnetic. Antiferromagnetic spins will reach the lowest energy by pointing in opposite directions in some checker board pattern. However, this might not always be possible due to quantum mechanical fluctuations or lattice structures. A Heisenberg antiferromagnet can thus not have the intuitive checker board pattern in the ground state since it is not an eigenstate of the Hamiltonian. Instead, a complicated superposition of different patterns with antiparallel spins is the ground state. Furthermore, if the lattice has a triangular structure (or any other structure where loops of an odd number of magnetic moments dominate) it is not possible to order the spins so that all spins have antiparallel neighbouring spins. This is called frustration and can lead to severely degenerate ground states.

### 1.2.3 Next nearest Neighbours

Exchange interactions are not limited to neighbouring atoms but can include atoms further away in the lattice. Often a next nearest neighbour term is needed in the Hamiltonian but third or fourth nearest neighbour terms can also be present. If the longer ranged exchange interaction are antiferromagnetic and strong enough compared to the nearest neighbour interactions the spin can order in spin spirals where the spins will turn a small angle for each lattice site. Such spin spirals are examples of incommensurate order - i.e. order where the ordering length does not fit the length scale of the crystal structure.

### 1.2.4 Magnetic Excitations

Magnetic excitations are called spin-waves or magnons. Unlike phonons they do not express physical displacements but rather reorientation of spins. The simplest magnetic excitation is a single spin pointing the opposite way of the ground state. For Heisenberg systems such an excitation is, however, not allowed and the excitation takes the form of a superposition of waves in the spins where neighbouring spins are only slightly dislocated with respect to each other. The energy is now a function of the wavelength of this distortion. In the limit of large  $\lambda$  the energy goes to zero (Goldstone modes).

For Ising systems, the single spin flip is the lowest possible excitation causing a gap-energy below which no excitations can exist.

### 1.2.5 Phase Transitions

When heated, systems of magnetic order will at some point break down and become paramagnetic. The transition temperature depends on the strength of the magnetic interaction. For some materials it will be very high. *e.g.*  $\alpha\text{-Fe}_2\text{O}_3$  has a transition temperature of 950 K. However, many of the more complicated magnetic systems have far lower transition temperatures, often in the 1-50 K range.

If an external field or pressure is applied it is also possible to force the system to change its magnetic ground state at low temperatures by a quantum phase transition. In such a transition it is the ground state of the system that changes. The quantum effects are often best investigated at very low temperatures, even though effects of such a transition can be observed far above the ground state

### 1.2.6 Multiferroics

Multiferroic systems are a class of systems where at least two of the following mix: Magnetic order, electric order and atomic displacement. A well-known example is piezoelectric crystals, where the dimension of the crystal is controlled with an electric field, but the other possible interactions involving magnetism have also attracted attention in recent years.

## Chapter 2

# Neutron Scattering

### 2.1 Scattering

Many experimental techniques in solid-state and soft-matter sciences are based on scattering of a known probe particles on a sample. By selecting particles with a well-known set of parameters and recording the same parameters after an interaction with the sample it is possible to determine important properties of the sample. Different particles can be used as probes depending on what properties are investigated, the most common being photons, electrons and neutrons.

As all particles the probe can both be described as particles, which is done during most of the experimental setup, and as waves, which is done in the interaction with the sample and certain other instrument components. In the wave description a probe has a wavelength  $\lambda$  and a corresponding wave vector  $\mathbf{k} = 2\pi/\lambda \cdot \mathbf{v}/v$ . As  $\hbar\mathbf{k}$  is the momentum of the probe the wavevector is often referred to as a momentum. Before interacting with the sample, the probe can be described as function of the position  $\mathbf{r}$  as a planar wave:

$$\psi(\mathbf{r}) = \frac{1}{Y} e^{i\mathbf{k}\cdot\mathbf{r}}$$

where  $Y$  is a normalization factor. A probe that is scattered from a particle at position  $\mathbf{r}_j$  with a cross section  $b_j^2$  can be described by a spherical wave

$$\psi(\mathbf{r}) = \psi_0(\mathbf{r}_j) \frac{-b_j}{|\mathbf{r} - \mathbf{r}_j|} e^{ik_i|\mathbf{r} - \mathbf{r}_j|} \quad (2.1)$$

If several scattering centres exists the result become a sum of spherical waves.

$$\psi(\mathbf{r}) = \sum_j \psi_0(\mathbf{r}_j) \frac{-b_j}{|\mathbf{r} - \mathbf{r}_j|} e^{ik_f|\mathbf{r} - \mathbf{r}_j|} \quad (2.2)$$

$$= \sum_j \frac{1}{Y} e^{i\mathbf{k}_i\cdot\mathbf{r}_j} \frac{-b_j}{|\mathbf{r} - \mathbf{r}_j|} e^{ik_f|\mathbf{r} - \mathbf{r}_j|} \quad (2.3)$$

$$\approx \sum_j \frac{1}{Y} e^{i\mathbf{k}_i\cdot\mathbf{r}_j} \frac{-b_j}{r} e^{i\mathbf{k}_f\cdot(\mathbf{r} - \mathbf{r}_j)} \quad (2.4)$$

$$= \frac{1}{Y} e^{i\mathbf{k}_f\cdot\mathbf{r}} \sum_j \frac{-b_j}{r} e^{i(\mathbf{k}_i - \mathbf{k}_f)\cdot\mathbf{r}_j} \quad (2.5)$$

Where in 2.4 have been assumed that the observation happens sufficiently far away that  $r \gg r_j$  and thus  $\frac{1}{|\mathbf{r}-\mathbf{r}_j|} \approx \frac{1}{r}$  and  $k|\mathbf{r}-\mathbf{r}_j| \approx k|\mathbf{r}-\mathbf{r}_{j,\parallel}| \approx \mathbf{k}_f \cdot (\mathbf{r}-\mathbf{r}_j)$  where  $\mathbf{k}_f$  is the wavevector parallel to  $\mathbf{r}$ . Furthermore we have assumed that the cross section for interaction with a single particle is very small so we can assume that all particles in either the full volume or a sufficiently big subspace only interact with the same planar wave of constant amplitude. So seen from the position  $\mathbf{r}$  the scattered beam becomes a planar wave traveling towards  $\mathbf{r}$  with an amplitude:

$$\frac{1}{Y} \sum_j \frac{-b_j}{r} e^{iq \cdot \mathbf{r}_j} \quad (2.6)$$

with

$$\mathbf{q} = \mathbf{k}_i - \mathbf{k}_f \quad (2.7)$$

called the scattering vector and  $\hbar\mathbf{q}$  the momentum transfer. The term in (2.6) is very central in scattering. In solid state physics it is often split into a sum over each lattice cell and sum of lattice cells:

$$\frac{1}{Y} \sum_j \frac{-b_j}{r} e^{iq \cdot \mathbf{r}_j} = \frac{1}{Y} \sum_i \frac{-b_j}{r} e^{iq \cdot \mathbf{r}_i} \sum e^{iq \cdot \mathbf{r}_j} \quad (2.8)$$

Where the sum of the lattice cell consist of a finite number of scatterers and can be computed exact, while the sum over the cells are very large but reduces to 0 when  $\mathbf{q} \cdot \mathbf{r}_j \neq n2\pi, n \in N$  due to the many different complex phases cancelling out (see figure 2.1).  $\mathbf{q} \cdot \mathbf{r}_j = n2\pi$  if and only if  $\mathbf{r}$  is a reciprocal lattice vector, defined as  $\mathbf{G} = h\mathbf{a}^* + k\mathbf{b}^* + l\mathbf{c}^*$  where  $h, k, l \in N^3$  and  $\mathbf{a}^* = 2\pi\mathbf{b} \cdot \mathbf{c}/V_0$ ,  $\mathbf{b}^* = 2\pi\mathbf{c} \cdot \mathbf{a}/V_0$  and  $\mathbf{c}^* = 2\pi\mathbf{a} \cdot \mathbf{b}/V_0$  with  $\mathbf{a}, \mathbf{b}, \mathbf{c}$  being the lattice vectors, describing the crystal structure[83].  $V_0 = \mathbf{a} \cdot \mathbf{b} \times \mathbf{c}$  is the volume of a unit cell. The condition

$$\mathbf{q} = \mathbf{G} \quad (2.9)$$

is known as the Laue condition and is equivalent with the 1 dimensional formulation, known as Bragg's law:

$$n\lambda = 2d \sin \theta \quad (2.10)$$

where  $d$  is the distance between scattering planes and  $2\theta$  is the scattering angle, or the angle between the incoming and scattered beam. If  $\mathbf{q} = \mathbf{G}$  scattering can occur. However, the sum over a single unit cell needs to be evaluated to see if scattering actually occur and with what strength.

If the probe is able to resolve the structure within the individual atoms (*e.g.* x-rays scatter from the electron cloud around an atom and have a wavelength comparable with the structure of the electronic cloud making it able to see the structure of the atom.) Each individual scattering particle within the atom is grouped together in the sum much like the atoms in a unit cell and the full cross section of the atom called the form factor is used instead of  $b_j$ . This form factor will generally be dependent on  $\mathbf{q}$ [34]. Other factors describing the actual interaction type can also exist. For example the x-ray scattering cross section from a single electron is a function of the scattering angle, and magnetic neutron scattering is a function of the angle between  $\mathbf{q}$  and the scattering spins.

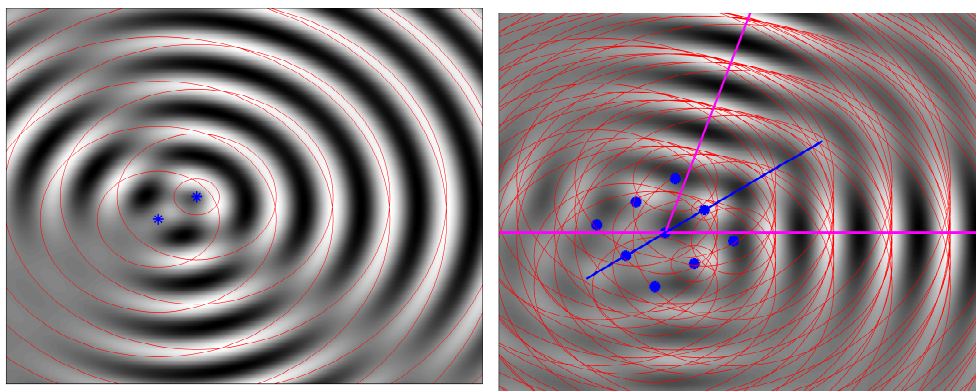


Figure 2.1: **Bragg scattering.** Illustration of Bragg scattering. A planar wave traveling from left to right scatters on a number of scattering centres. The blue are scattering centres, the red wave fronts of the scattered beam, and the grey tones the actual wave after interference. Left: Scattering from two centres. Right: Scattering from 3\*3 cores in a lattice. Already here a Bragg angle can be seen. The blue line shows the direction of the lattice planes and the purple line the incoming and scattered beam.

### 2.1.1 Cross Sections

In actual experiments the cross section is measured rather than the amplitude. In general scattering cross sections are defined as number of particles scattered into a specific volume element in some space divided with the incoming particle flux and the volume of the element. For example, the partial differential scattering cross section is defined as:

$$\frac{d^2\sigma}{d\Omega dE_f} = \frac{1}{\psi} \frac{\# \text{ of particles scattered into } (d\Omega \times [E_f; E_f + dE]) \text{ per second}}{d\Omega dE_f} \quad (2.11)$$

where  $\Omega$  is some solid angle and  $E_f$  is some energy. The differential is defined as:

$$\frac{d\sigma}{d\Omega} = \int \frac{d^2\sigma}{d\Omega dE_f} dE_f \quad (2.12)$$

or, as the number of particles is the norm square of the amplitude of the wave inside the given volume element times the element volume.

$$\frac{d\sigma}{d\Omega} = \left| \sum_i b_j e^{i\mathbf{q}\cdot\mathbf{r}_i} \sum_j e^{i\mathbf{q}\cdot\mathbf{r}_j} \right|^2 \quad (2.13)$$

Since the volume of  $\Omega$  is  $r^2$  and the incoming flux is  $1/Y$ . Unfortunately, all phase information is lost in the measurement of the cross section, which makes reconstruction of the measured sample more complicated.

### 2.1.2 Resolutions

In a scattering experiment, a compromise between how well the incoming and outgoing probes are determined and the count rate have to be made. It is usually not possible to alter the properties of the probe in order to make it more uniform and instead the instruments removes particles that does not fulfil certain criteria, thereby reducing the statistics but increasing the accuracy of the measurement. For example, most scattering experiments will want to know the change in flight direction of the probe during the scattering process and will thus need to determine the incoming and outgoing flight direction. However, the probes will have a distribution of slightly different flight directions, called divergence, so the instrument will need to remove particles that are furthest from the desired flight direction (high divergence particles) if a high precision is required. The accuracy with which a probe parameter or change in probe parameter can be measured is called the resolution of the instrument, and the probability distribution of measured values when the sample signal is a delta function is called the resolution function  $O$ .

Different parts of an experimental setup will have different resolution functions. If the resolutions are uncorrelated the total resolution function is found by convolution:  $O(x) = O_1 \otimes O_2 = \int_{-\infty}^{\infty} O_1(y)O_2(x-y)dy$ . The convolution of two functions with a finite variance gives a new function where the variance is sum of the variances[73].

A particular important function is the Gaussian function since most resolution functions are Gaussians or Gauss like and a series of convolutions of functions converge towards a Gaussian[39]. Convoluting two Gaussians gives a new Gaussian. Another important function is the Lorentzian distribution. Unfortunately, the Lorentzian function does not have a finite variance and the convolution of a Lorentzian and a Gaussian (called a Voigt) cannot be analytically solved, although a numerical solution is implemented in many data analysis programs.

Assuming that the efficiency (understood as the fraction of probes that are not lost or absorbed in a part of the instrument) of the  $i$ 'th part of the instrument can be written as a powerlaw  $E_i = a_i\sigma_i^n$  where  $a_i$  is a constant,  $\sigma_i$  is the resolution of the instrument and  $n$  is some exponent, the combined efficiency of two sections becomes  $E_{1,2} = E_1 \cdot E_2 = a_1a_2\sigma_1^n\sigma_2^n$ . Given a desired resolution of  $\sigma = \sqrt{\sigma_1^2 + \sigma_2^2} = \sqrt{\sigma_1^2 + (\alpha\sigma_1)^2}$  for some  $\alpha$ , the efficiency becomes:  $E_{1,2} = a_1a_2\alpha^n\sigma^{2n} = a_1a_2\sigma^{2n} \left(\frac{\alpha}{1+\alpha^2}\right)^n$ . As  $a_1, a_2, n > 0$  for any physical meaningful setup the maximum is achieved when  $\alpha = 1$  or  $\sigma_1 = \sigma_2 = \frac{\sigma}{\sqrt{2}}$ . It is thus important to design the experiment so that the resolutions of the different independent parts of the instrument match in order to get the highest possible efficiency out of the instrument. This is not necessarily the case if the two contributions are correlated. However, usually the resolutions will be uncorrelated if they are associated with different parts of the instrument.

Adjectives describing resolution tend to cause some confusion. It is common to refer to resolution with a narrow width as high resolution even though the parameters describing the resolution ( $\sigma$  and FWHM) are in this case low. To avoid

this confusion people also speak about good and bad resolution, however, one could argue that the best resolution is when the compromise between resolution and intensity is perfect for the instrument. Indeed modern guide designs and some monochromator/analyser designs spend considerable resources increasing the width of the signal in order to increase the count rates[33, 47, 72, 86]. I will use coarse and fine resolution wherever possible to avoid any confusion however, for resolution changes improved resolution will mean a more narrow distribution since it will only be used in a context where the statistics are not reduced at the same time.

Many instruments are able to measure large volumes that can be resolved into smaller subspaces in a single data acquisition. If a measured volume can be resolved into a set of smaller disjoint subspaces by the instrument I will call the any set with a maximal number of elements the measured channels.

### 2.1.3 Peak Broadening

In the equations for Bragg scattering (2.9) the system was assumed to be infinitely big, so that contributions even close to the Bragg peak will cancel out and the peak become a delta function. However, if the signal comes from a finite sized domain or particle this is no longer true. Instead one gets a broadening of the peak following the Sherrer formula[118], which can be stated as:

$$w = c \frac{2\pi}{d} \quad (2.14)$$

where  $w$  is the FWHM of the peak,  $d$  is the diameter of the domain and  $c$  is a constant with values between 0.8 and 0.95 depending on particle shape and symmetry direction. The shape is usually quoted as Lorentzian though that is only true if the particles follows certain lognormal size distributions.

## 2.2 Neutron Scattering

The neutron is an uncharged particle with a rest mass of  $m_n = 939.6 \text{ MeV}/c^2$  and a magnetic moment of  $\mu = \gamma\mu_N$ , where  $\gamma = -1.913$  and  $\mu_N = 5.051 \cdot 10^{-27} \text{ J/T}$ [90]. Like all particles with a rest mass, it have a wavelength of  $\lambda = 2\pi\hbar/(mv)$ , a wave vector of  $\mathbf{k} = m\mathbf{v}/\hbar$  and an energy of  $E = \hbar^2 k^2/(2m)$ . [93]

Using neutrons as the probe in scattering experiments has a number of advantages:

- **Length and energy scales.** The rest mass of the neutron means that neutrons can simultaneously have an energy and wavelength ideal for solid state experiments.
- **Neutrons can see magnetic structures.** Due to the magnetic moment of the neutron it is sensitive to magnetic moments in the sample. This makes it ideal to study the distributions of magnetic moments in materials.
- **Neutrons interacts weakly with matter.** This means that multiple scattering events can generally be neglected, and that the neutron beam

can often be taken to be almost constant throughout the sample. This makes it possible to compare measured absolute intensities with theory.

- **Neutrons can penetrate many materials easily.** This makes it possible to make experiments with sample environments. Sample environments often demands that the sample is separated from the surroundings for example to control the temperature or the pressure. Since Al is almost invisible to neutron beams it is possible to build separation walls of solid pieces of machined Al and still perform experiments on the sample inside the walls.
- **The cross section for neutron scattering varies with isotopes.** Light elements have much smaller x-ray cross sections than heavy elements and are thus nearly invisible if both are present in the sample. For neutrons the cross sections are comparable, though different and they even vary between different isotopes. The former means that light elements (*e.g.* gas fumes) can be seen inside heavy elements (*e.g.* a motor). The latter enables phase contrast studies by use of for example deuterated water and is especially useful in biology.

Since the neutrons scatter from the nuclei which have a size of the order  $10^{-5}$  Å and thermalized neutrons have wavelengths in the order 1-10 Å, the neutrons will not be able to resolve any structural information about the nuclei.

### 2.2.1 Incoherent Scattering

By default neutrons are scattered in all directions by an assembly of scatterers. However, since the neutron waves interfere we measure the Fourier transform of the symmetries in the sample. This leads to peaks in the signal. In the derivation of Bragg's law these symmetries were assumed to be perfect. However, that is usually not the case. Reduced symmetry will occur due to variations in isotopes or nuclear spin. This causes a general background called incoherent scattering. The scattering cross section is often given as a function of atom number. However, it will change with the exact isotope distribution of a substance. For example Hydrogen has a very high incoherent scattering cross section of  $80.26 \cdot 10^{-28} \text{ m}^2$ , while it only is  $2.05 \cdot 10^{-28} \text{ m}^2$  for deuterium.

### 2.2.2 Inelastic Scattering

All scattering events will fulfil the conservation of energy:

$$E_{f,\text{sample}} - E_{i,\text{sample}} = \hbar\omega \quad (2.15)$$

where  $\hbar\omega = E_i - E_f$  is the change in probe energy also called the energy transfer. In the case of neutrons  $\hbar\omega = E_i - E_f = \frac{\hbar^2(k_i^2 - k_f^2)}{2m_n}$ . If  $\hbar\omega = 0$ , the scattering is called elastic and otherwise inelastic. The cross section for inelastic neutron scattering now becomes:

$$\left. \frac{d^2\sigma}{d\Omega dE_f} \right|_{\lambda_i \rightarrow \lambda_f} = \frac{k_i}{k_f} \left( \frac{m_n}{2\pi\hbar^2} \right)^2 |\langle \lambda_i \psi_i | V | \psi_f \lambda_f \rangle|^2 \delta(E_{\lambda_i} - E_{\lambda_f} + \hbar\omega) \quad (2.16)$$

where  $|\lambda_i, \psi_i\rangle$  and  $|\lambda_f, \psi_f\rangle$  are the incoming and outgoing states of the system respectively,  $E_{\lambda_i}$  and  $E_{\lambda_f}$  are the energy of the states, and  $\mathbf{k}_i, \mathbf{k}_f$  the wavevectors.  $V$  is the interaction potential.[90]. Many experiments will thus not measure in the 3 dimensional reciprocal space spanned by  $\mathbf{q}$  but the 4 dimensional space spanned by  $\mathbf{q}$  and  $\hbar\omega$ , which is called  $(\mathbf{q}, \omega)$ -space. Incoherent scattering will be distributed as quasi elastic scattering. This means that the scattering will be distributed as a Lorentzian as a function of energy transfer with a centre at  $\hbar\omega = 0$  and a width that corresponds to the inverse of some characteristic time of the system[124]. This is for example often used to investigate hydrogen diffusion.

Elastic and quasi elastic scattering is generally more intense than inelastic scattering so many experimental setups assumes that all measured scattering is elastic. If the energy transfer is measured one will see a spike in the signal centred at  $\hbar\omega = 0$ . Inelastic data are often presented in a color map with  $\hbar\omega$  on one axis and  $q$  or a component of  $\mathbf{q}$  on the other. Here the intense elastic signal and the peak in the quasi-elastic signal becomes a line called the elastic line.

Scattering with  $\hbar\omega > 0$  is called down scattering since the neutron loses energy by producing an excitation in the sample whereas scattering with  $\hbar\omega < 0$  is called up scattering. In many experiments it is necessary to cool the sample in order to get into the desired phase or be close to the ground state where quantum effects are more clearly expressed. However, the phonon density and thus the up scattering cross section is proportional to the Bose occupation factor and goes to 0 when the temperature goes to 0. The cross section for down scattering does also become small at low temperatures but it goes to a finite value meaning that inelastic low temperature measurements will normally be down scattering measurements.

### 2.2.3 Magnetism

The neutrons, magnetic moment can interact with the local magnetic field produced by the spin distribution inside a sample. This leads to elastic scattering with cross section of:

$$\left. \frac{d\sigma}{d\Omega} \right|_{\text{magn,el}} = (\gamma r_0)^2 \left( \frac{g}{2} F(\mathbf{q}) \right)^2 e^{-2W(\mathbf{q})} \left| \sum_j \langle e^{-i\mathbf{q}\cdot\mathbf{r}_j} \mathbf{s}_{j,\perp} \rangle \right|^2 \quad (2.17)$$

where  $d$  denotes the position of the electronic spins  $\mathbf{s}$  at the  $j$ th atom, and  $r_0$  is the classical electron radius of 2.818 fm. The  $\perp$  index means that only the spin component perpendicular to  $\mathbf{q}$  can be observed with neutrons.  $F(q)$  is the magnetic form factor  $F(\mathbf{q}) = \int e^{i\mathbf{q}\cdot\mathbf{r}} \mathbf{s}(\mathbf{r}) d\mathbf{r}$ . The displacement of scatterers due to vibrations is the Debye-Waller factor and denoted  $e^{-2W(\mathbf{q})}$ . [90] It turns out that the prefactor in 2.17 is of the same size (5 fm) as typical nuclear scattering lengths so it is possible to see both structural and magnetic signal at the same time in scattering experiments. If the spin orientation is ordered in a pattern with a period different from that of the atoms the spin will give rise to extra peaks at the corresponding reciprocal lattice vectors of the magnetic lattice.

Such peaks are called magnetic peaks while peaks arising from scattering of the nucleus are called structural peaks. The study of magnetic peaks is very powerful method to determine the spin order inside a crystal.

Magnetic excitations can be measured by inelastic magnetic scattering just like nonmagnetic elastic scattering. The cross section describes the number of neutrons scattered inelastically and is given by the space and time Fourier transform of the spin-spin correlation function:

$$\begin{aligned} \left( \frac{d^2\sigma}{d\Omega dE_f} \right)_{magn} &= (\gamma r_0)^2 \frac{k_i}{k_f} \left[ \frac{g}{2} F(\mathbf{q}) \right]^2 e^{-2W(\mathbf{q})} \sum_{\alpha,\beta} (\delta_{\alpha\beta} - \mathbf{q}_\alpha \mathbf{q}_\beta) \\ &\quad \times \frac{1}{2\pi\hbar} \int_{-\infty}^{\infty} dt e^{-i\omega t} \sum_{j,j'} e^{i\mathbf{q}\cdot(\mathbf{r}_j)} \langle \mathbf{s}_j^\alpha(0) \mathbf{s}_{j'}^\beta(t) \rangle \end{aligned} \quad (2.18)$$

where  $\sum_{\beta} \delta_{\alpha\beta} - \mathbf{q}_\alpha \mathbf{q}_\beta$  describes that only spins perpendicular to  $\mathbf{q}$  contributes to the scattering cross section.[90]

#### 2.2.4 Sample Environments

There are many reasons to study samples away from the normal laboratory environments. In some cases, experiments seek to replicate the environments of the investigated materials. For example inside the earth's mantle or a car engine. In other cases, experiments seek to get new knowledge about a sample by applying some external fields or cooling it to temperatures near 0 K. The most common environmental parameters to control in solid state physics are temperature, magnetic field and pressure but in other fields other parameters such as electric field, humidity, stress factor or PH can also be of interest.

To change the sample environments it is usually necessary to separate the sample from the laboratory, for example to keep the temperature different from that of the laboratory and surround it with materials producing the sample environments. Many environments outside neutron scattering include large amounts of materials with a relatively high absorption or scattering cross section that will block or significantly reduce the neutron beam. They can however, also be constructed with some open angles. It is for example possible to build split coil magnet or pressure cell without big chunks of material in a horizontal plane. It is, however, usually necessary to include some strong machinable material in these windows. One reason is to separate the sample environment from the laboratory environment, for example to control the temperature of the sample. In other cases a structural component is necessary, for example to keep the two coils of a split coil magnet apart. Fortunately Aluminium has a very low absorption cross section, is nonmagnetic and decays quickly after irradiation by neutrons. Al will however, produce a scattering Debye Sherrer cone (see section 3.1.5) background - depending on the amount used.

## Chapter 3

# Neutron Instrumentation

Neutrons sources are expensive and have a limited brightness. In the early days of neutron scattering this weakness was overcome by the use of large samples, but this puts a severe limitation on both what samples can be studied, and also reduces the possibilities for sample environments since the possible magnetic fields, electric fields, and pressures that can be achieved depends strongly on the required volume. Thus, there have in many years been a push towards both brighter sources and instruments that use the generated neutrons more efficiently. Below, I will describe some of the techniques used in neutron scattering and how instrumentalists have increased the efficiency of their instruments.

### 3.1 Neutron Spectroscopy

The scattering abilities of the neutron can be used for many different kinds of measurements. I will not try to describe all techniques, but concentrate on triple axis and time-of-flight spectroscopy and only touch some of the other techniques briefly.

#### 3.1.1 Neutron Sources

Free neutrons have a half-life of  $\sim 15$  minutes [98, 119]. This is sufficient to perform neutron scattering experiments without worrying about natural decays, but requires that the neutrons are produced when needed for experiments. As neutrons are electrically neutral and strongly bound to their nucleus it is hard to produce free neutrons, but it can be done using different techniques. The simplest is to use a radioactive source however, the neutron brightness emitted from such sources are too low for all but the simplest neutron scattering experiments. Instead all large scale neutrons scattering facilities relies on either a reactor or a spallation source to produce the needed free neutrons. A list of some the most important facilities can be seen in table 3.1.

Source	Technology	Type	Place
ILL[20]	Reactor	Continuous	Grenoble, France
FRM II[17]	Reactor	Continuous	Munich, Germany
HZB[19]	Reactor	Continuous	Berlin, Germany
HFIR[13]	Reactor	Continuous	Oak Ridge, USA
LLB[15]	Reactor	Continuous	Paris, France
ANSTO[16]	Reactor	Continuous	Sidney, Australia
NIST[27]	Reactor	Continuous	Washington DC, USA
ESS[12]	Spallation	Pulsed	Lund, Sweden, in construction
PSI[28]	Spallation	Continuous	Villigen, Switzerland
ISIS[21]	Spallation	Pulsed	London, UK
SNS[13]	Spallation	Pulsed	Oak Ridge, USA
J-Parc[24]	Spallation	Pulsed	Ibaraki, Japan

Table 3.1: *Neutron sources.* A list of some of the most important neutron sources.

### 3.1.1.1 Reactor Sources

The first large scale neutron scattering facilities used reactor sources and they are still the most common source at large scale facilities. Reactor sources usually produce free neutrons from fission of Uranium. As in nuclear power plants, some of the free neutrons are used to sustain the chain reaction. The chain reaction makes it possible to sustain much higher neutron fluxes than from a normal radioactive source. Apart from the usual security and environmental issues connected to nuclear reactors, the brightness also limits the development in reactor sources. It is limited how bright a stable reactor source can be made because the heat from the fission process needs to be removed in order to keep the reaction running. Even so, the source with the highest time-averaged brightness today is the ILL reactor source[20] in Grenoble. Reactor sources normally produce a continuous flow of neutrons.

### 3.1.1.2 FRM II

The FRM II source in Munich differs from many other reactor sources in that it uses highly enriched Uranium as its fuel. Because of that it reaches a relatively high neutron flux even though the effect is more moderate.

### 3.1.1.3 Spallation Sources

In a spallation source, free protons are accelerated to high energies and directed into a target of heavy elements (for example Lead, Mercury, or Tungsten). The reactions will produce 15 times more free neutrons per MeV of excess heat than in reactors. At the same time it is relatively simple to generate the proton beam in bursts and thereby pulsing the neutron beam. This adds information about the starting time of the neutrons. This information can then be used by the time-of-flight technique to produce more efficient instruments. Spallation

sources have a large energy consumption and have yet to surpass reactor sources in total flux but the pulsing capabilities and smaller environmental and safety issues means that many new sources constructed the last 30 years are spallation sources, like PSI, JPARC, ISIS, SNS and the coming ESS.

#### 3.1.1.4 PSI

The spallation source at the Paul Scherrer Institute in Switzerland is the world's only continuous spallation source. This is done because the proton beam is also used to generate muons for complementary measurements.

#### 3.1.1.5 ESS

ESS will be the first spallation source to rival ILL in total brightness, while being 30 times brighter in the pulses than ILL. This is achieved by generating longer pulses at a lower frequency than any other pulsed facility today. This requires new instrument designs that can utilize the longer pulse. In chapter 4 I will describe further how this impacts instruments and how to get most out of the possibilities of a long pulsed spallation source for an in-plane scattering spectrometer.

### 3.1.2 Moderators

Both reactor and spallation sources produce neutrons with far too short wavelengths (high energy) to be useful for neutron scattering. To slow the neutrons, they are led through a moderator, where they transfer some of their energy by inelastic scattering. Hydrogen, either as  $H_2$ ,  $H_2O$  or some organic material, is often used as moderator because it has a high neutron scattering cross section, relatively low absorption cross section, and a mass comparable to the neutrons. If the moderator has a temperature close to room temperature (300-400 K) it is called "thermal", and if the moderator is  $\sim 25$  K it is called "cold". Neutrons in thermal equilibrium with a thermal moderator are called "thermal" and instruments designed for them "thermal instruments" and likewise for cold.

### 3.1.3 Neutron Guides

The actual neutron instrument needs to be placed some distance from the moderators. This is needed in order to get space for radiation shielding, have space for more instruments and for time-of-flight instruments to separate the neutrons in time. In order to transport the neutrons from the moderator to the instruments, guides are needed. The guides are evacuated tubes with walls of neutron mirrors.

The reference mirror is a polished piece of Ni. Neutrons will travel slightly faster in most materials than in Vacuum, leading to a refractive index above 1. If the neutron hits the material with a small enough angle, total reflection will thus occur. The angle of total reflection will depend on the neutron energy and it is thus more natural to define a momentum transfer  $q_c$  below which total

reflection will occur.  $q_c$  depends on the scattering cross section of the isotope in question. For naturally occurring nickel  $q_c = 0.0219 \text{ \AA}^{-1}$ , corresponding to a critical angle of  $0.4^\circ$  for 5 meV neutrons. In order to increase the reflective angles Neutron mirrors are often produced by depositing many Nickel layers of decreasing thickness separated by another material (typical titanium) on a substrate. These layers act as crystals producing Bragg peaks at different positions, depending on the thickness of the layers. By tuning the thickness of the layers, the many Bragg peaks are combined together to produce a single region of high but decreasing reflectivity above  $q_c$ . Such "super mirror" will have a cut off above which the reflectivity drops to 0 at  $m \cdot q_c$  and are usually described by this m-value. Examples of mirror profiles can be seen in figure 3.1.

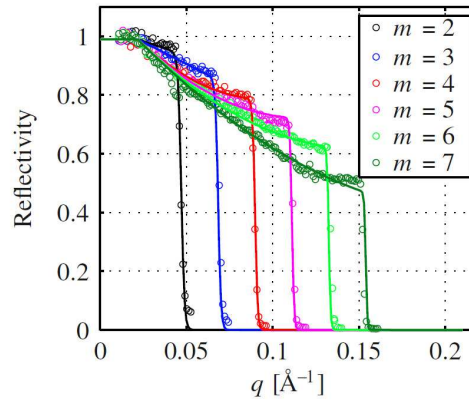


Figure 3.1: *Neutron mirrors.* Reflectivity of supermirrors from Swiss Neutronics[30] with different m-values. From [77].

### 3.1.3.1 Brilliance Transfer

From Liouville's Theorem we know that a phase space density can never be increased passively [87]. This leads to a good measure for guide efficiency in terms of the phase space density within a given phase space in the end of the guide compared to the start of the guide. The relevant phase space density is brilliance, defined as:

$$B = \frac{\text{neutrons}}{\text{time} \cdot \text{area} \cdot \text{solidangle} \cdot \text{wavelengthband}}, \quad \left[ \frac{1}{\text{s} \cdot \text{cm}^2 \cdot \text{sterradian} \cdot \text{\AA}} \right] \quad (3.1)$$

From Liuviles Theorem it is clear that if we define the brilliance transfer as  $B_1/B_2$  where  $B_1$  and  $B_2$  are the brilliance at two different positions then the brilliance transfer cannot exceed 1 for any given phase space volume. This gives a measure between 0 and 1 for a guides performance[84]. Though brilliance transfer is a very important number it does not tell everything about the guide performance. It is considerably easier to transport a small than a large phase space volume, and thermal neutrons are also harder to transport than cold. Furthermore, the shape of the desired phase space is important so giving a Brilliance

transfer without defining the incoming and outgoing phase space is meaningless. Generally, the possible incoming phase space will be given by the moderator dimensions that are considerably larger than the outgoing phase space. So the guide can pick any desired subspace to transfer, leaving the incoming phase space less important. However, in some cases the shape of this phase space will impact the guide performance. Of course there are also parameters such as background suppression, beam shape and cost to consider when designing an actual guide.

### 3.1.3.2 Guide Geometries

Traditionally, neutron guides have been straight or curved rectangular guides with a constant cross section[53, 97, 101, 103], but in the later year there has been a huge development towards more advanced guide geometries[32, 86, 47, 111]. The general idea of these guides are first to expand the beam in a way that reduces the divergence then transport the low divergent beam that towards the sample, and in the end of the guide reduce the beam size while increasing the divergence. The low divergent beam will not only reflect from the sides with a lower angle but also need to reflect fewer times. This has led to an increase of brilliance transfer from a few percent to up to a simulated brilliance transfer of *sim*90% for cold neutrons even for 150 m long guides[86]. The 100 m long elliptic guide at WISH, ISIS[22, 51] proves that long elliptic guides can deliver the expected performances. There are, however, still work to be done concerning *e.g.* background, thermal neutrons, higher divergences and beam profiles.

### 3.1.4 Sample Area

The sample itself will usually be placed on a sample table. This table normally allows motorized translation in 3 dimensions of the sample and any sample surroundings as well as rotation around 3 axes. The possible rotation around the vertical axes will usually be more than 360°. However, the two other rotations will often be limited to for example  $\pm 15^\circ$ . The sample table is durable enough to support heavy sample environments. However, for some experiments the sample table might be removed *e.g.* big magnets. Strong magnets also require that nearby parts of the instrument is constructed from nonmagnetic materials, such as Al. Before and after the sample it is common to place adjustable slits by neutron absorbing materials in order to reduce the background. These slits limit the amount of sample environments that can be seen from the primary and secondary instrument. Everything before the sample is called primary, while everything after the sample is called secondary.

### 3.1.5 Diffractometers

In diffraction experiments, only the elastic scattering is considered. The instruments are designed with a known incoming energy and the outgoing energy is assumed to be identical. Figure 3.2 (left) shows a simple diffractometer. A polychromatic beam (also called a white beam) is guided to the instrument, where a well-known single crystal called a monochromator, of for example Pyrolytic

Graphite (PG), is used to reflect the wanted wavelength towards the sample by the use of Bragg's law. In order to select the right compromise between flux and energy resolution, monochromators are not perfect crystals but will have slightly unparallel lattice planes. The distribution of the lattice planes are called the mosaicity ( $\eta$ ) and will typically be in the order 10 to 60 arch minutes("). Just as for resolutions some confusion exists about what high and good mosaicity means. Here I will also use coarse and fine when possible.

A detector measures scattering from the sample in a specific direction. Neutron

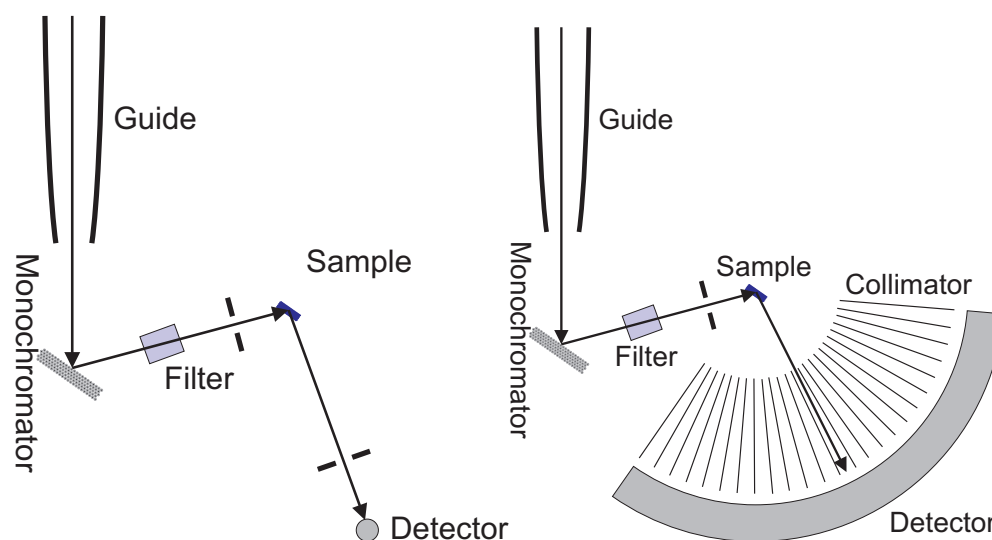


Figure 3.2: **Diffractometer.** Left: Classic diffractometer. Right: Diffractometer with a large detector to improve the data taking rate.

detectors have traditionally been based on  $^3\text{He}$  that have a large absorption cross section. The released energy in the resulting nuclear reaction causes an ionization that can be amplified *e.g.* by high voltage sparks in Ar gas, and detected with electrodes. By moving the detector and rotating the sample it is possible to map out a large subspace of the reciprocal space. It is common to replace the single detector with a collection of detectors or a position sensitive detector (PSD) that covers a large selection of scattering angles at once. In this case a radial collimator is usually inserted before the detector. A collimator is a component consisting of thin neutron absorbing sheets that is used to control the possible neutron flight paths. In the case of radial collimators to limit the area the next component (*i.e.* the detector) can see and thus reduce the background. With a PSD on a diffractometer it is only necessary to rotate the sample in order to do a full measurement (see figure 3.2 right). Diffraction is often done on powders. The powder crystals are assumed to be isotropically oriented. A reflection in the crystals will thus reflect in all directions that obeys Bragg's law, independent of sample rotation. The resulting cone is called a Debye-Scherrer cone. Since the sample rotation can be omitted when investigating powders a full measurement on a diffractometer with a PSD can be done in just one data acquisition.

### 3.1.5.1 Laue Diffraction

In a Laue diffractometer a white beam is guided directly to the single-crystal sample and the reflection is recorded on a PSD. From Brags law it follows that all reflections will be seen if the sample is illuminated with a wavelength such that  $\frac{2d}{n} \sin \theta_{min} < \lambda < \frac{2d}{n} \sin \theta_{max}$ , where  $\theta_{min}$  and  $\theta_{max}$  are given by the instrument layout. Some information is lost with the unknown reflected wavelength. However, Laue diffractometers are excellent at aligning samples since many reflections can be seen simultaneously.

### 3.1.6 Triple Axis Spectrometers

In order to measure energy transfers it is necessary to measure the outgoing energy as well as the incoming. This can be done by inserting a second monochromating crystal, called an analyser between the sample and detector in a diffractometer setup. This will now control which energy is reflected to a detector. Triple axis spectrometers (TAS) are named after their 3 controllable axes: the

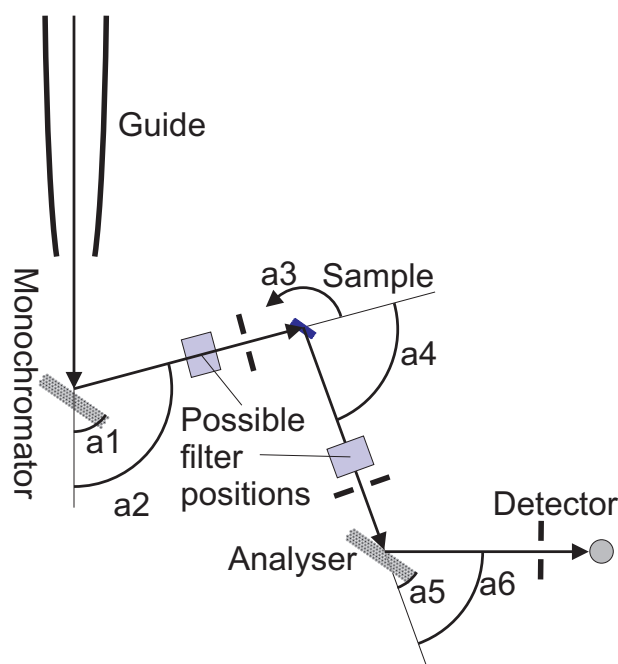


Figure 3.3: *Triple axis spectrometer.*

axis from monochromator to sample, the axis from sample to analyser, and the axis from analyser to detector. Each axis has two relevant angles, labelled a1-a6 associated to it (see figure 3.3):

- **a1** is the angle between the centre of the beam passing through the monochromator and the scattering plane of the monochromator.
- **a2** is the angle between the beam passing through the monochromator and the direction from the monochromator to the sample.

- **a3** is the angle between the centre of the beam passing through the sample and some direction in the sample. This angle is often used somewhat arbitrarily as the direction in the sample is not always specified.
- **a4** is the angle between the beam passing through the sample and the direction from the sample to the analyser of interest.
- **a5** is the angle between the centre of the beam passing through the analyser and the scattering plane of the analyser.
- **a6** is the angle between the beam passing through the analyser and the direction from the analyser towards the detector of interest.

I will use these names for the relevant angles even if the instrument in question is not a standard TAS and all angles are not in the same scattering plane. If the instrument for example does not have a monochromator, I only use the angles a3-a6.

### 3.1.7 Time-of-Flight Spectrometers

Due to the neutron mass, the velocity of cold neutrons is in the 1 km/s range. This makes it possible to separate a polychromatic pulse of neutrons into a spectrum of energies by propagating the neutrons through the instrument. If the start time is known, the energy can now be calculated for each detection time. This makes it possible to do experiments with a wide band of well determined energies within each neutron pulse. In spectroscopy, time-of-flight (ToF) can be used to determine both the incoming and outgoing energies. If both are determined with ToF the technique is called direct ToF, if analysers are used indirect ToF. In order to use the technique, it is necessary to use a pulsed beam. If the source is pulsed it is possible to use the pulse directly, but it is often preferable to be able to adjust pulse by the use of choppers. A disk chopper is a rotating disk of some neutron absorbing material with a window that is transparent to neutrons. By changing the phase and the rotation speed of the chopper it is possible to tailor the neutron pulse to the experiment. Choppers may be used in pairs to enable control of the opening time of the double chopper system. If ToF is also used for the secondary instrument, choppers are needed to pulse the beam just before the sample, and the measured intensity at each channel will be reduced significantly (*e.g.* a factor  $\sim 400$  for a cold chopper spectrometer at ESS with a resolution of  $\frac{\delta E}{E} = 1.1\%$ ). This is countered by the many channels it is possible to measure at the same time.

### 3.1.8 Background

Many neutron signals are rather weak so to make sure that the signals are not hidden in background, large emphasis is placed on background reduction. Neutron detectors can in principle detect any kind of ionizing radiation, although the low kinetic energy of the neutrons and well defined energy of the nuclear reaction it produces means that it is possible to discriminate most other background sources with several orders of magnitude. It is still important to stop

gamma and x-ray radiation from the source, guides and beamstops but within the instrument the main focus is neutron background. In order to minimize this, detectors are shielded by neutron absorbing materials and shielding is also inserted at other strategic positions.

The 3 most common neutron shielding materials are Cadmium, Gadolinium and Boron. Only a few mm's of Cd is enough to stop most neutrons and since Cd is a soft metal it is very useful to wrap around sample sticks and other frequently exchanged parts to reduce the background from these. Gd has the largest absorption cross section and is often used when the thickness of the shielding is an issue, *e.g.* for collimators. Both materials do, however, have cut-off values above which the absorption cross section decreases dramatically[65] so to block high energy neutrons B is used, for example as detector housing. This is often done with Boron-plastic blocks of thicknesses between a few and 30 cm.

Air produces incoherent background scattering due to N<sub>2</sub> so it is not unusual to evacuate parts of an instrument, or to replace the normal air with Argon that has a considerably lower scattering cross section.

Another source of background is higher order neutrons. These are unwanted neutrons that are transported to the sample and even detectors because their energy fits the instrument settings. In TAS (and diffraction), neutrons with wave vectors that are some multiple of the desired wavevector are often reflected by the monochromator and analyser since they also fulfil Bragg's law. In ToF spectroscopy, neutrons with energies that slip through the chopper sequence are also often labelled higher order neutrons though they will usually be of lower energy than the desired neutrons. In TAS (and diffraction) it is common to remove higher orders with a high energy filter. This is normally a powder that reflects all neutrons with a wavelength above a certain threshold out of the main beam path. The reflected neutrons are then absorbed by collimators or slits. The most common filters for cold neutrons are Beryllium with a cut-off of 5.2 meV.

### 3.1.9 Polarization

If the neutron scatters from a structural signal its spin is conserved whereas it may flip its spin if it scatters from a magnetic signal. So by knowing the spin before and after the sample, it is possible to determine whether a signal is magnetic or not. In order to do so, components that remove neutrons with a spin in one direction are inserted before and after the sample. By inserting a spin flipper (*e.g.* a magnetic field of a specific strength and direction) it is possible to choose whether only neutrons that keep the spin orientation or neutrons with a spin that is flipped will make it through to the detector.

Polarization is provided by monochromators and analysers composed of Heussler crystals, polarizing super mirrors, or a polarized <sup>3</sup>Helium gas.

### 3.1.10 Time resolved Scattering

Time resolved scattering have proven extremely fruitful in later years - especially in x-ray scattering[69, 70, 131]. The basic idea is to study a setup with some time

dependence. This could be a non-equilibrium process such as a sample reacting to a changed external influence, a biological process in the sample, or it could be a study of a setup that can only exist in a short time. For example, it is possible to achieve much higher fields with pulsed magnets than with constant magnetic fields. By pulsing the magnetic field and combining the data with information about the recording time it is possible to investigate how the sample reacts to much stronger fields, although the limited flux on neutron spectrometers have so far reduced the impact of this technique. Often, the investigated process is running such a short time that it is impossible to get sufficient data in a single data acquisition and so the process is repeated stroboscopically and data recombined until sufficient statistics is reached.

X-rays are especially suited for time resolved studies, as the flight time uncertainty is minimal due to the x-ray moving with the speed of light and the high flux counters the challenge of getting enough statistics for these kinds of studies. Using lasers as the external switch on the sample, it is possible to perform time resolved studies in the pico-second range.

For neutrons, the time resolution is much more limited than for x-rays. The uncertainty in scattering position and detection position alone is of the order 1 cm due to the thickness of sample and detector. Hence for a speed in the order 1 km/s the best possible resolution will be of the order 10  $\mu$ s. At the same time, the challenge of getting sufficient statistics is much larger for neutrons than for x-rays. At most parametric studies only a low number of parameter values are recorded at positions of specific interest in order to reduce the impact of limited flux. In time resolved studies it is not possible to fast forward to the times of interest in the same way so the limited flux becomes an even larger issue. However, the unique measuring abilities of neutrons mean that there is still a great potential in time resolved neutron scattering.

### 3.1.10.1 Event mode Data

Most neutron scattering instruments use histogram mode data recording. Here, the detector electronics collect all neutron detection events in a given time period into a histogram before exporting the histogram to the instrument computer. The size of such histograms means that it takes up to seconds for old electronics to transfer these histograms and this puts a lower limit to the time resolution of the instrument.

As the developments in computers have been substantially faster than the development in neutron beam intensities it is, however, now possible to shift to event mode data where each neutron detection event is reported individually to the instrument computer and stored as separate entries in the data file. A single experiment will in this way produce gigabytes of data, putting pressure on the data handling routines but it does have substantial advantages:

- It enables time resolved studies.
- It enables a continuous change of experimental setup (for example sample orientation) thereby increasing the accuracy and removing unwanted down

time compared to the classical setup where the sample is rotated in small steps.

- As we shall see: Having the raw data makes it possible to track down errors much more efficiently and correct for many problems.

Because of that event mode data acquisition is becoming common and will probably be the standard at least at pulsed sources in the near future.

### 3.1.11 Other Neutron Techniques

There are many other experimental uses of a neutron beam. Disciplines such as imaging, reflection, and small angle neutrons scattering (SANS) can be used to answer different scientific questions. Likewise the backscattering and spin-echo spectrometer techniques increase the achievable energy resolutions within neutron spectrometry.

### 3.1.12 X-ray Instruments

As most of the basic scattering laws are the same for x-ray and neutrons many basic design elements above can also be used for x-rays. Both monochromatic diffractometers and Laue diffractometers are constructed in the same general way and TAS can also be constructed in the same way. TOF instruments will not work at x-ray sources since all x-rays travel with the speed of light.

Soft x-rays (low energy x-rays) do not penetrate more than a few micrometer of sample. Hard x-rays can penetrate a sample but provide considerably worse resolution. Many x-ray techniques are thus surface techniques that do not look at the entire volume of a sample.

## 3.2 Increasing the Performance of Instruments

As mentioned in 3 it is important to increase the count rate of neutron scattering instruments. A lot of effort is put into constructing brighter sources and better guides and recent ideas have also been developed on how to construct more instruments at each source [74, 75]. However, a classic TAS is detecting less than  $10^{-6}$  of all potential scattering events in the horizontal scattering plane, so it seems obvious to attempt to improve on instrument designs as well.

### 3.2.0.1 Increase the Efficiency of the Components

An obvious way to increase the count rate in neutron instruments is to make sure that as many of the desired neutrons are counted as possible. Until the introduction of ballistic guides in neutron scattering there was some obvious gain factors to pursue here but for cold neutron scattering the gain factors are now limited. Today it is possible to construct cold neutron scattering experiments where both guide brilliance transfer, monochromator and analyser peak reflectivity, and detector efficiencies are above 80% . This leaves a limited room for further improvement for simple cold spectrometers but there are still potential

for big gain factors for thermal instruments, and for focusing instrument designs, background reduction and price.

### 3.2.1 Focusing

It is possible to increase the count rate substantially by reducing the resolution along specific directions in the parameter space. For example a TAS might want to have a good energy resolution but can accept a more relaxed angular resolution, especially in the vertical direction. By constructing the monochromator and analyser so that they are focusing in both the horizontal and vertical directions towards the sample and detector respectively one can for example relax both the incoming and outgoing angular resolution from  $1^\circ$  to  $5^\circ$ . This can in principle lead to a gain factor of 25 from both monochromator and analyser, thus increasing the count rate with a factor 625. The cost in this case is that the angular resolution gets relaxed from  $1.4^\circ$  to  $7^\circ$  in both directions.

The gain factors will depend on the number of parameters where a relaxed resolution can be accepted. For diffractometers, the horizontal angular resolution is very important, so here only the vertical resolution will normally be relaxed leading to a gain factor of the order 5.

#### 3.2.1.1 Rowland Geometry

The Rowland geometry is a very important geometry for focusing monochromators and analysers. It uses a geometrical result that all triangles with one fixed side length and a fixed opposing angle will have the same circumscribed circle (see figure 3.4). That means that when the distance between sample and detector

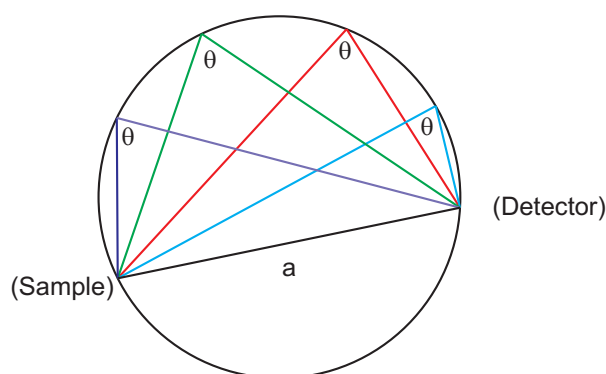


Figure 3.4: **The Rowland circle.** All triangles with the same side length ( $a$ ) and opposing angle ( $\theta$ ) will have the same circumscribed circle.

(or some virtual source and sample) is fixed and the desired Bragg angle is fixed there exists one circle going through both sample and detector upon which any analyser with the right orientation will reflect the same energy from the sample to the detector (see figure 3.5). Note that the Rowland circle describes the optimal position of the crystals - not the optimal orientation. The needed curvature of the orientation is different from the curvature of the position [123, 67] so it

is not possible to obtain perfect focusing with a single bent piece of crystal, although the problem is small if sample the analyser and analyser detector distances are equal. For practical purposes, instrument constructors opt for either a finite number of crystals with a small enough width that this does not dominate the resolution or a bent perfect crystal.

Other geometries evolve around focusing a parallel beam to a point with almost the same energy reflected everywhere, or (time, energy) focus as seen at the TOSCA instrument at ISIS[106].

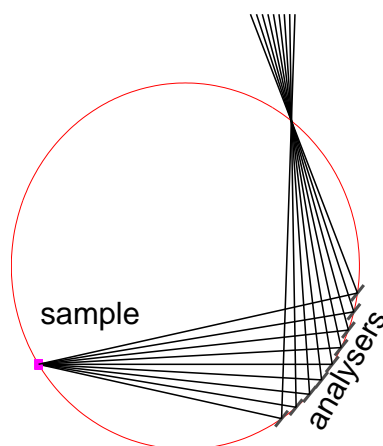


Figure 3.5: *The Rowland Geometry.* It is possible to produce energy and position focusing simultaneously if all analysers are placed on the same circle that also intersects the sample and the detector. The same can be achieved using a virtual source, monochromator crystals and a sample.

### 3.2.2 Mapping

Another way to increase the count rate is by measuring several points in the parameter space simultaneously. This can for example be done by multiplexing or ToF. In multiplexing, a number of different analysers each reflect a different part of the scattered beam to different detectors or a PSD (see for example [112, 81, 79, 91, 96]). Normally the different analysers will be placed at different  $2\theta$  values but they can also be placed behind each other and cover different energies. Multiplexing instruments can achieve a performance in each detector channel that is comparable to a single detector spectrometer. It can however, be a challenge to construct the analyser and detector mount in a sufficiently general way that all analysers can be used in a meaningful way, so the actual gain is often smaller than the number of analyser blades.

ToF is described in section 3.1.7 and greatly increases the number of channels that can be measured at the same time. Since the technique relies on pulsed beams, it is normally necessary to reduce the intensity in each channel in order to chop the signal into pulses. At pulsed sources the flux loss in the primary spectrometer is small or even zero but if ToF is used for the secondary spectrometer there will always be a substantial flux loss in the secondary spectrometer.

The advantage of using ToF in the secondary spectrometer is, however, not only the possibility to measure many outgoing energies simultaneously. It is also possible to cover large solid angles with position sensitive detectors. In some cases, considerable parts of  $4\pi$  are covered by detectors.

Although mapping can in principle achieve huge gain factors, the performance increase is often smaller, since part of the instrument will often look at parts of the scattering space of little interest to the experiment. It is, however, better to measure the areas of limited interest and confirm that there was nothing to see or achieve unpredicted results than not to investigate it. Nonetheless, if the gain in coverage is achieved by sacrificing flux in each channel, as is the case for secondary instrument designs using ToF, it will be a disadvantage for many experiments.

### 3.3 Examples of Existing Instruments

#### 3.3.1 RITA II

Rita II[29, 91, 38] is a multiplexed cold TAS at PSI. It has a curved guide to reduce the fast neutron background, a vertically focusing monochromator, and 9 analysers that reflect neutrons towards a common PSD. Each analyser can be individually rotated and furthermore the analysers are placed on an arm that can rotate changing the relative positions of the analysers. This allows some freedom in the 9 recorded positions in  $(\mathbf{q}, \omega)$ . A schematic drawing of RITA II can be seen in figure 3.6.

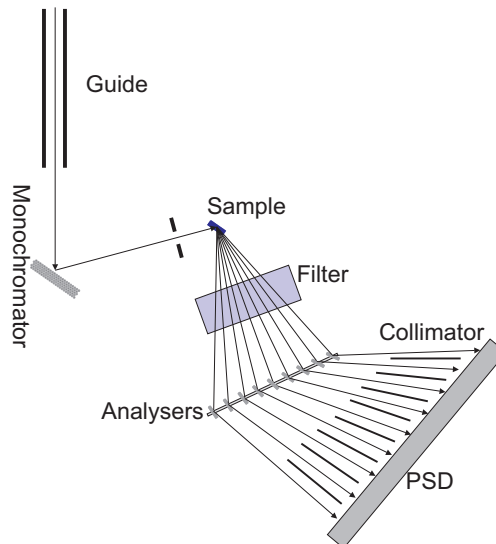


Figure 3.6: *Sketch of RITA-II. RITA-II uses 9 analysers to record 9 points in  $(\mathbf{q}, \omega)$  space simultaneously. Top view, not to scale.*

### 3.3.2 ToFToF

ToFToF is a cold neutron direct ToF spectrometer at FRM II. The instrument is placed in the Neutron Guide Hall, relatively far from the source, and has a long s-shaped guide that removes any high energy neutrons. As the source is continuous, it uses choppers to pulse the incoming beam as well as to monochromate the incoming pulses. Although this leads to a lower flux than on a pulsed source it does add flexibility in that the frequency can be tailored to fit the wanted energy range. Between the pulsing and monochromating choppers, a set of frame overlap choppers removes unwanted neutrons, and allows the main choppers to operate at a frequency that is a multiple of the main frequency of the instrument, thereby increasing the energy resolution (see section 4.4.4.1). Between sample and detectors an oscillating radial collimator is placed, to reduce the background. The detectors covers the angles between  $-15^\circ$  to  $-7^\circ$  and  $7^\circ$  to  $140^\circ$  in the horizontal plane, and a large vertical angle. The detector consists of arcs of up to 4 detector tubes without position sensitivity arranged so that each arc follow a single Debye Sherrer cone from the sample. This makes the instrument ideal for measurements on powders, while the vertical resolution for single crystal measurements is very limited.

## 3.4 Monte Carlo Simulations of Instruments

Although some overall instrument performance can be deduced by analytical calculations, the problems of predicting the exact performance of instruments are often too complicated for analytical solutions. Instead a number of Monte Carlo ray tracing packages exists: McStas[25, 92, 35], VITESS[94] and Restrax[116]. The packages coexist in friendly competition, where they are used to validate each other and have slightly different strengths. All instruments simulations in this work were done using McStas.

The Monte Carlo method is a numerical way to solve complicated mathematical problems by simply picking random numbers and evaluating the problem for each of them. In this case we want to deduce some performance numbers for an instrument by solving an integral over all possible flight paths from the moderator to the detectors, weighted with the probability of such a flight path. This is done by picking a large number of random flight paths and adding the results together. The amount of flight paths needed will depend on the problem. However, it is possible to establish error bars for Monte Carlos simulations and thereby determine when a sufficiently accurate result is achieved.

### 3.4.1 McStas

McStas was developed at Risø National Laboratory in the late 1990'ies for simulation of TAS, and have later been expanded to be able to handle most neutron instrumentation problems. McStas does not simulate individual neutrons but neutron rays. This means that in cases where a Monte Carlo choice needs to be made and where only a limited number of choices are of relevance to the simulations, McStas is able to choose between this limited sub-space rather than the

full space and adjust the intensity of the ray accordingly. This saves considerable computational time simulating neutrons that are lost anyway. For example, when a neutron ray hits a neutron mirror, there is a probability that it will get reflected and a probability that it will continue through and get absorbed in the shielding behind. Since the latter is of low interest (unless one tries to estimate background) the reflected state is always chosen and the ray intensity is multiplied with the reflectivity of the mirror. More complicated examples include only generating rays at the moderator that will actually hit the guide and only scattering rays from the sample that will actually reach the next part of the instrument.

McStas is modular in the sense that an instrument is built from a large library of independent codes, describing each component[135]. The rays are now propagated from component to component by McStas, while the individual components handle what happens to the ray while it is inside the component. Arrangement and parameters of the components can be handled with c-code inside McStas. This makes McStas very flexible as users can build instruments from a wide range of components and place and arrange the components as they wish. Furthermore, it is possible to write homemade components for additional flexibility.

## Chapter 4

# CAMEA

*The CAMEA concept was first proposed by Henrik Rønnow for the Eiger instrument [4] at PSI ~ 10 years ago. It aims to improve the backend of a triple axis instrument to a new degree of multiplexing. This is done by arranging analyser crystals in arcs around the sample, reflecting the neutrons to position sensitive detectors above the horizontal scattering plane, much like at Flatcone[81], ILL. As analysers are transparent to neutrons outside the reflected energy range, several analysers will be placed behind each other in order to reflect several energies towards several detectors. The idea was never implemented on Eiger. It was however not discarded and later I was asked to do simulations showing that the idea could actually work. While I was undertaking this task, the idea of installing it as an inverse ToF spectrometer at ESS was conceived by Kim Lefmann and my focus shifted towards designing such an instrument. A consortium of Copenhagen University, The technical University of Denmark, PSI, and École Polytechnique Fédérale de Lausanne was formed to design the instrument.*

*A complicated instrument like CAMEA will include many different issues that in this case are investigated by a combination of kinematic calculations, simulations, prototyping, and engineering considerations. Presenting the work in a traditional way, method by method would involve covering the same more than 20 subjects up to 4 times in separate chapters from different perspectives and probably leave the reader without an overview of each topic. Instead I have chosen to provide an overview of the instrument, present the methods used in general, and then cover each subject thoroughly, including results from all relevant methods used in the investigation, before finally collecting the result into the proposed instrument. When nothing else is mentioned, simulations and calculations are done for the parameters in the proposed instrument (see table 4.7).*

*CAMEA has been envisioned for several different instruments with very different frontends. In this work however, CAMEA will denote the proposed instrument on ESS, while other implementations of the idea will be given a unique name to distinguish them from the ESS version.*

## 4.1 Instrument Overview

CAMEA is designed to use some of the best features of ToF mapping spectrometers and TAS focusing spectrometers. The idea is to keep a count rate in each channel comparable to that of a TAS while improving the mapping capability by incorporating as many channels as reasonably possible. The channels will be concentrated in the horizontal plane since many sample environments limits the possibilities of out of plane scattering. These sample environments are often used for parametric studies where the extra dimensions of the parameter space requires fast data acquisition to be feasible. The high count rate and in-plane coverage thus makes ESS CAMEA ideal for extreme sample environment measurements and CAMEA is a high priority that it works well in such experiments.

Schematic drawings of ESS CAMEA can be seen in figure 4.1. ESS is a pulsed

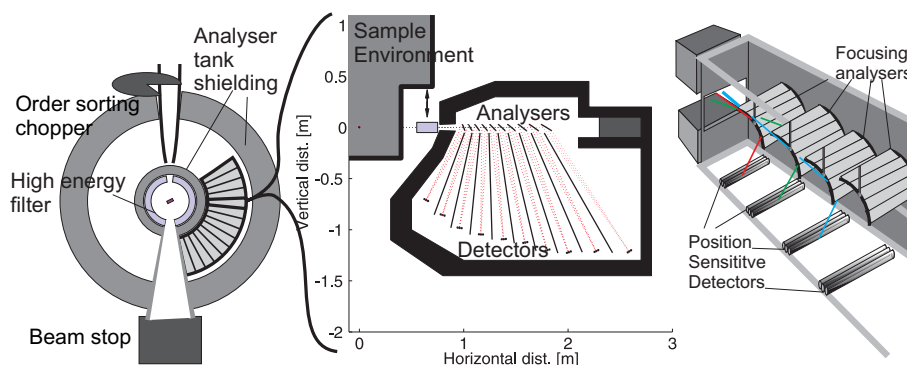


Figure 4.1: *Schematic drawings of ESS CAMEA backend* Left: Top view. Middle: Side view of the secondary spectrometer. Right: 3d illustration.

source so it is possible to use ToF to resolve the incoming energy and provide incoming flux in each energy channel comparable to that of a TAS but for many energy channels within each pulse. This also adds the possibility to tune the incoming energy resolution by the use of choppers. The length of the instrument is chosen to fit the natural length where a pulse just fills the entire frame at all resolutions. Since ESS is a long pulsed source with a frequency of 14 Hz and a first chopper 6.5 m after the moderator, this is 165 m and correspond to a resolution of  $\Delta E/E = 3.5\%$  at  $E_i = 5$  meV. Though slightly worse than on many TAS instruments it is possible to achieve normal TAS resolutions or better with the choppers and still keep a comparable intensity in each channel. 165 m is longer than any existing neutron guide but it is foreseen for several ESS instruments. The guide will allow high divergences on the sample ( $\pm 1^\circ$  vertical and  $\pm 0.75^\circ$  horizontal) in order to increase the flux but has divergence jaws to reduce the incoming divergence when needed. The full flux in a  $1.7 \text{ \AA}$  wavelength band on sample can be up to  $1.8 \cdot 10^{10}$  neutrons/s/cm<sup>2</sup>, considerably higher than on existing spectrometers.

Just before the sample an order sorting chopper system is inserted. This chopper system allows the instrument to distinguish first and second order scattering

from the analysers thus increasing the dynamic range of the instrument.

Around the sample a 45 cm radius cylindrical space is reserved for sample environments.

After the sample a Be filter can be inserted to remove neutrons above 5.2 meV. This will provide higher count rates in the channels below the Be edge than using the order sorting chopper. A radial collimator removes noise from the sample environment and the filter.

The analyser tank will be in vacuum or Argon atmosphere. It will cover scattering angles between  $3^\circ$  and  $135^\circ$  on one side. The other side is left for future upgrades. Inside the tank 15 wedges of  $9^\circ$  in a modular design secures easy maintenance and reduces crosstalk. Each wedge will have a  $6^\circ$  active analyser area. The analysers will consist of a number of crystals arranged in a Rowland geometry. The foremost will cover  $\pm 2^\circ$  in the vertical direction since this is a typical opening angle of strong superconducting magnets[1, 2]. The later analysers will have an opening angle corresponding to the same  $\Delta k_{\text{Vertical}}$ . There will be 10 analysers behind each other, covering the energy spectra  $2.5 \text{ meV} \leq E_f \leq 8 \text{ meV}$  or  $2.5 \text{ meV} \leq E_f \leq 32 \text{ meV}$  including second order signals from the analysers. Each analyser will reflect downwards towards 3 linear position sensitive detectors. The position sensitivity allows a large  $\Delta\theta$  resolution while the 3 detectors enables detection of 3 different energies from the analyser.

The high reflectivity of the analysers will ensure that each channel has a count rate comparable to that of a TAS at an equally bright source. However, the number of channels will be up to about  $2e4$ , considerably higher than for any multiplexed TAS ever constructed. An example of how the many channels will be distributed in  $(\mathbf{q}, \omega)$  space can be seen in figure 4.2. The intense mapping of the horizontal scattering plane will not only mean far more precise spectrometric measurements of already existing systems but also allow users to perform spectrometry of sub  $1 \text{ mm}^3$  crystals. This will facilitate experiments on samples that are impossible to grow in big crystals and new systems before methods have been developed to grow large crystals. It will also enable experiments in sample environments with a very limited sample space such as pulsed magnets and pressure cells. It is believed that this will bring advances in both solid state physics and geoscience.[63, 64]

## 4.2 The Prototype

The CAMEA design incorporates several new concepts that had only been described on paper. When the project was started there were some controversies about whether they would actually work in reality. Especially there were concerns that it would not be feasible to arrange many analysers behind each other, that the geometry was to open for a low background and that it would be impossible to reduce the data from the many different channels to a meaningful dataset. As the design went on and the ideas of using distance collimation and collecting several energies from a single analyser was invented (see section 4.4.10.10), and these were also met with scepticism. In order to answer these questions and provide comparison for our simulations and calculations, prototyping was

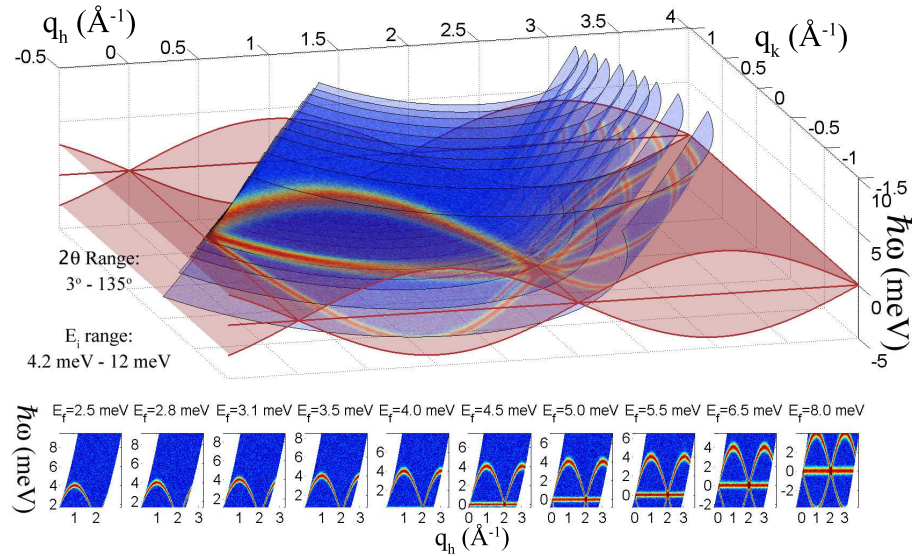


Figure 4.2: *Illustration of data from a single CAMEA data acquisition.* Data from a system with an elastic line and a magnon dispersion is displayed. The simulation is done for the full ESS pulse. For clarity only 10 surfaces, corresponding to 10 analyser-detector groups are shown and displayed below. When including the 3 energies from each analyser, the number would be as high as 30 (and 60 when including the order sorting chopper). Dark angles are omitted, but can be covered in two data acquisitions.

undertaken.

#### 4.2.1 Preliminary Prototyping

Before the actual prototype was constructed a short demonstration experiment was performed on RITA II, PSI. The aim was to place a large number of analysers behind each other and prove that the signal from the backmost analysers will not get ruined by attenuation, small angle scattering, incoherent scattering, and thermal diffuse scattering.

To investigate this, the analyser arm on Rita was moved so that all 9 analysers were placed behind each other, reflecting different energies to the PSD. Figure 4.3 shows the experimental setup (left) and the result of a scan of  $E_i$  (right). It can be seen that it is possible to record a well-defined energy distribution from each analyser. The peaks were deliberately placed at different spacings in angle to investigate how close together reflected energies could be arranged. The results shows that the last energies are dampened since part of the reflectable bandwidth have already been reflected. The effect is small if the angles of different analysers ( $\theta_1, \theta_2$ ) are chosen so  $|\theta_1 - \theta_2| > \eta$  and it can be disregarded if  $|\theta_1 - \theta_2| > 2\eta$ . Using  $\eta = 30'$  mosaicity and energies between 2.5 meV and 8 meV one reach a maximum number of 60 or 30 analysers respectively for the two demands.

The results do not take attenuation into account. In order to compare the exact intensity and find the attenuation a more thorough normalisation of the

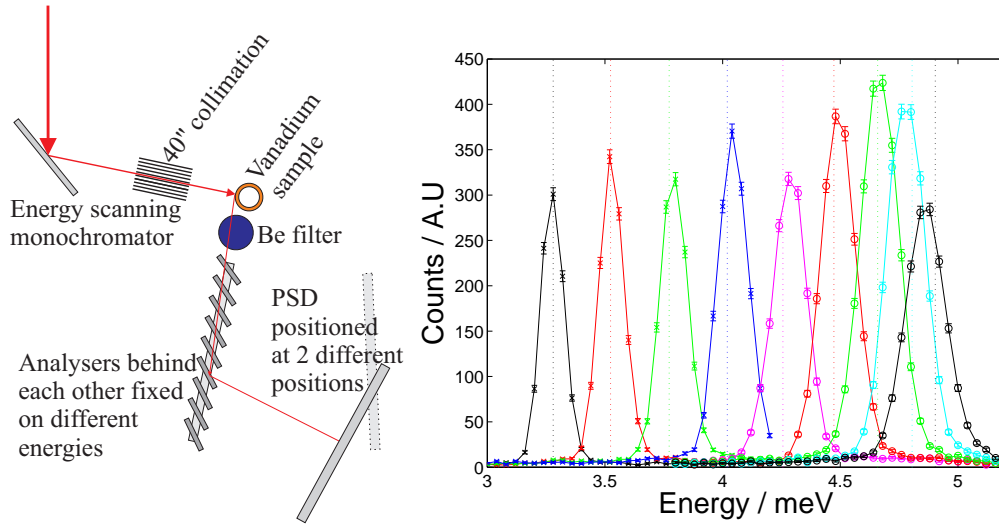


Figure 4.3: *Demonstration Experiment on Rita II* Left: For the experiment the 9 analyser blades were placed behind each other, reflecting different energies towards the PSD. To cover the entire region the detector was shifted between two different positions during the measurements. Right: When scanning  $E_i$  and using a V sample each blade produced a well-defined peak at the detector.

detector sensitivity and analyser reflectivity would be needed. However, since the experimental time was limited a simpler experiment was performed. The central analyser was positioned to reflect elastically scattered neutrons at 3.65 meV from a V sample to the detector. Data acquisition were done in 2 settings: One where 4 analysers were placed in front of the analyser at an angle of  $\alpha=90^\circ$  and one where the analysers were rotated out of the beam path (see figure 4.4). The measurements gave 10251 counts when counting through 4 2 mm analyser blades and 11865 without analysers in front constituting a  $3.6 \pm 0.3\%$  loss from each analyser blade. The Si wafers have comparable incoherent scattering and absorption cross sections to the PG analysers. However, these only account for a fraction of the attenuation (see also 4.4.10.1). Since Si are perfect single crystals, and does not have the same soft phonon modes as graphite have it is reasonable to assume that the main contributor to the attenuation is PG. Assuming this lead to an attenuation of  $1.8 \pm 0.2\%$  per mm graphite. The measurement only shows the attenuation of one energy in one orientation of graphite and later a more advanced study of the attenuation was performed by Marton Marko[88] to produce an overview of more settings. The later experimental setup was however not ideal to determine absolute values of attenuation in the low attenuation regions. So in this region the 1.8% per mm is used as a standard value.

#### 4.2.2 Design of the Prototype

The prototype was designed and constructed as a collaboration between Copenhagen University, the Technical University of Denmark, and PSI. A technical drawing can be seen in figure 4.5. The prototype was primarily designed with

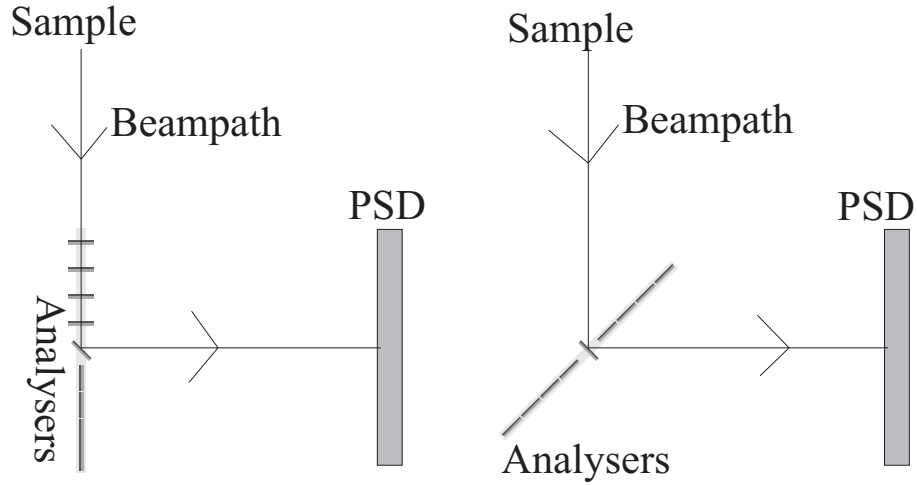


Figure 4.4: **Transmission measurement** Left: The RITA II analyser is rotated so 4 analysers block the line of sight from sample to the central analyser. Right: For comparison the 4 analysers are rotated out of the scattering direction while the central analyser is kept at exactly the same spot as before.

flexibility in mind. It needed to be able to test many different experimental setups and be easy to modify to address any problematic issues found during the testing or continued design study. It thus contains many movable parts and motors compared to the final instrument. Most things are moved by hand to allow maximal flexibility. However, a degree of automation was needed for scans of positions and rotations - especially during the alignment procedures. This is even more important as the working prototype was hard to access due to radiation protection issues and is impossible to access when experiments in Ar atmosphere were performed.

The main frame is built in Kanya Al profile [7] which allows flexible and solid mounting of extra parts wherever it is found useful. It consists of a box on rails that can be moved away from the sample to allow more space for work. The box is approximately 70 cm wide, 2 m tall and 2 m deep. Inside the box two rails hold wagons where analysers and detectors can be mounted and translated to specific locations.

The 3 analyser wagons are moved manually to the desired positions, thus varying the sample-analyser distance ( $d_{as}$ ) from 0.9 to 2.3 m, though the outer setting will only work for some energies. The wagons hold a frame that can be rotated by motors to change  $E_f$  and it is further possible to rotate them manually around the vertical axis to mimic a wider analyser and thus a smaller incident angle. Each frame can hold up to 7 Si wafers that can be rotated manually. 15 cm of analyser crystals can be screwed unto each Si wafer by Al screws for a total of  $7 \cdot 15 \text{ cm}^2 = 105 \text{ cm}^2$  of active area (see figure 4.6 left). 4 different qualities of Graphite was bought from Panasonic (see table 4.1) since simulations suggested that low quality graphite might be preferable for CAMEA.

The 3 detector wagons can be translated to a specific horizontal distance from the sample manually and they do also have the option of a mechanical transla-

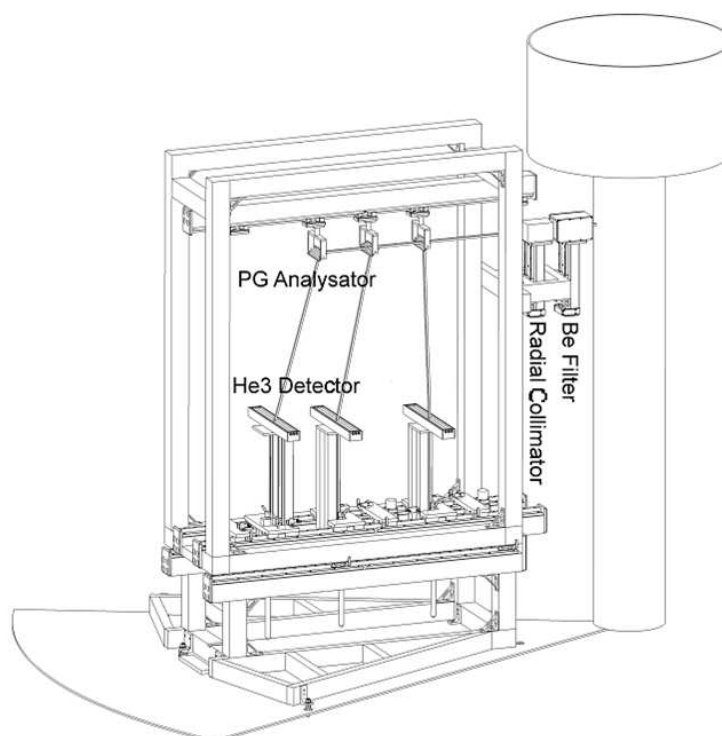


Figure 4.5: *The prototype.* Technical drawing showing the prototype box on its rail to the left together with analysers and detectors. The cylinder to the right is the sample space of MARS. Lines showing typical beam paths are also included.

Badge #	Mosaicity (arch minutes)	# of pieces	Length (mm)	Width (mm)	Thickness (mm)
1	40	15	50	10	1
2	40	15	50	10	1
3	60	10	75	10	1
4	90	10	75	10	1
5	30	15	50	10	1

Table 4.1: *Overview of PG badges.*

tion of up to 20 cm. The height of the detectors can be adjusted manually. Each wagon has 3 parallel  $^3\text{He}$  position sensitive tube detectors with a radius of 0. inch and a position resolution of 0.5 cm. The detectors are mounted in a cradle of Cadmium to shield them (se figure 4.6 right).

In front of the prototype mounting space was prepared for collimators and filters. The shielding can be mounted on the Kanya profile.

One limitation of the prototype is that it only covers an small range of scattering angles around  $a4 = 60^\circ$  and only a limited number of reflections can thus be measured in the relevant energy band. Due to space limitations the vertical distance between analysers and detectors was also more restricted than optimal.

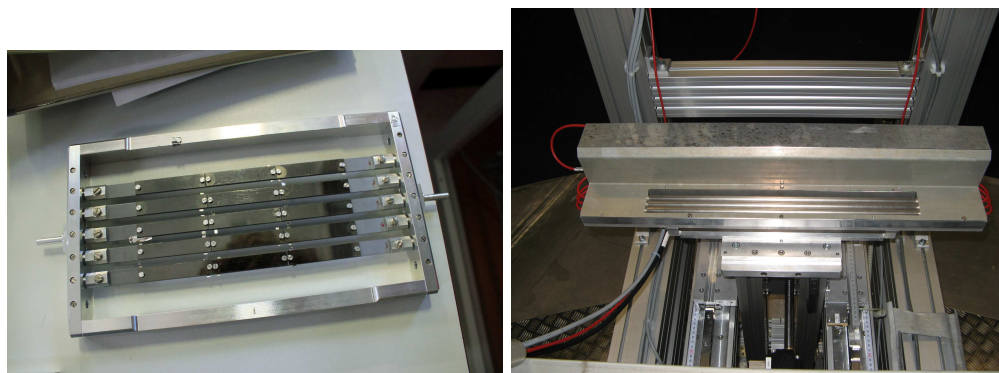


Figure 4.6: **Analyser frame & Detectors.** Left: A photo of an actual analyser frame. Small pieces of Al foil are used to align the crystals on the Si wafers. Right: The detector housing with 3 detectors mounted.

### 4.2.3 Installation of the Prototype

The Prototype was installed in the autumn 2012 at the MARS[132, 5] tank at PSI. Two backscattering sections and a diffraction section was removed and the prototype was lifted down in the tank (see figure 4.7) before the lid was placed back in position. During the installation thorough tests were performed on the graphite and its mounting procedure.

The MARS choppers were reconfigured to increase the possible frequencies from  $n \cdot 50$  Hz to also include a band of 10-20 Hz. The choppers showed considerable problems adjusting to new phases but it could in general be circumvented by applying a common phase shift to all choppers.

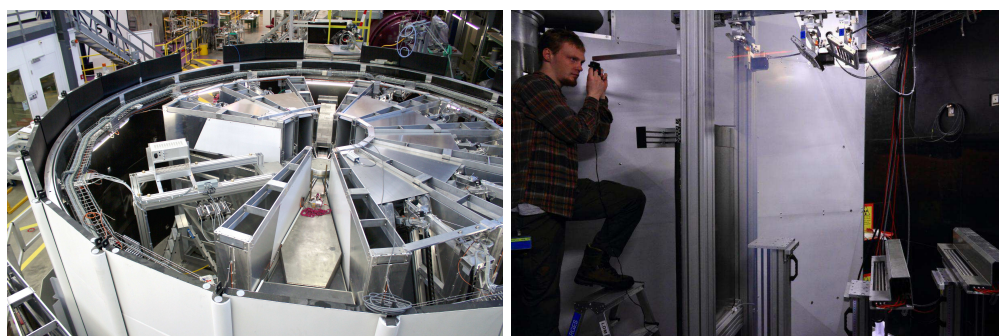


Figure 4.7: **The prototype installed in MARS.** Left: From the top. Right: Alignment of graphite inside the tank. The prototype is moved back on its rails, laser is placed at a position corresponding to the sample and laser light is reflected via the analysers to the detector.

#### 4.2.3.1 Characterisation and alignment of Graphite

The analysers of the final instrument will consist of more than 2000 crystals so some effort was put into producing an efficient alignment procedure.

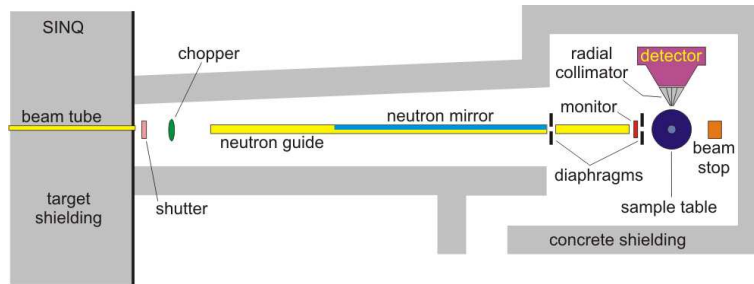


Figure 4.8: *Layout of the Poldi ToF strain scanner at PSI. From the Poldi homepage [31]*

#### 4.2.3.2 Laser Alignment

The first alignment was made by a combination of measurements on Morpheus[6] and laser alignment. Laser alignment assumes that the reflecting (002) plane is parallel to the surface of the graphite. To align the individual crystals, visible laser light is reflected from the analyser to a piece of millimetre paper on a wall some meters away. The reflected spot is marked and a motor translates the analyser frame so the next analyser crystal is in the laser beam. By comparing the position of the laser spots it is possible to find the difference in orientation between the two crystals and align them. Alignment is done by placing small pieces of Al foil between crystal and wafer. Unfortunately this does put some strain on the Si wafer and produce a bending which in turn will disturb the alignment. However a combination of thorough cleaning of the crystals to minimise the need for alignment and careful mounting of the Al screws made it possible to achieve alignment with a spread of 2-3 arc minutes. Since this was much smaller than the mosaicity and we use distance collimation for the energy resolution (as will be described in 4.4.10.9) this result was acceptable.

The alignment was afterwards checked with neutrons before the final placed in a Rowland geometry. To align the wafers in a Rowland geometry the prototype was moved back so that a laser could be placed at a position corresponding to the sample position. The analyser was rotated by a motor so that it was tangential to the desired Rowland circle. The laser was now aimed on one wafer at a time and the wafer was rotated by hand so that the reflected laser spot hit the central detector tube (see figure 4.7 right). The wafer was now fixed with screws and the procedure repeated with the next wafer.

#### 4.2.3.3 Graphite Measurements on Poldi

POLDI[59, 31] is a neutron strain scanner at PSI (see figure 4.8) but can also be used as a powerful 1D Laue camera for characterization of graphite. The instrument has a direct line-of-sight from a thermal moderator at PSI to the sample position, so the sample is strongly illuminated by a white beam. The scattered neutrons are detected by a 1d PSD, simultaneously measuring the entire peak and tail through the different channels, thanks to the white beam. For a strong scatterer like PG the measurement times become very fast and it is possible to

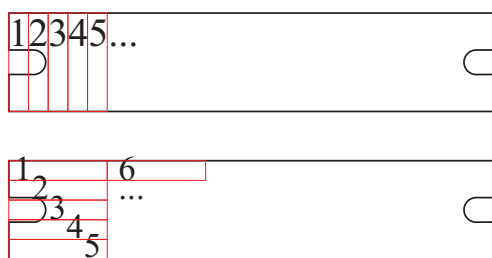


Figure 4.9: *Scanning of the PG.* Schematic illustration of how the PG was scanned in the horizontal (Top) and vertical (bottom) direction.

measure the reflection through a  $2 \times 10\text{mm}^2$  slit opening just before the sample in 5 seconds and record sufficient statistics. This made it possible to scan across the PG crystal as described in figure 4.9 and measure the quality, homogeneity, and alignment of each piece of graphite in a short time. 3 batches of graphite were investigated through 2250 individual measurements in less than 24 hours. In each measurement the  $\sum_n(0, 0, 2n)$  reflection was fitted to a Gaussian and the results investigated as a function of the scan number. The results from the first frame are can be seen in figure 4.10

The position variation is a combination of two things: The crystals are not perfectly aligned with each other and thus a jump is often seen between crystals. Within each crystal the center point increases systematically with higher scan points for the horizontal scan and show a systematic behaviour with a period of 5 for the vertical case. This is because the frame has not been perfectly aligned with the robotic translation system and so the position of the Graphite changes between measurements, changing the angles slightly. It is however still possible to extract the precision in alignment from the data. For this the mean orientation of each crystal is calculated from the point measurements and the variances of these mean values were computed. In the vertical case all crystals can be compared whereas only crystals in the same horizontal position can be compared in the horizontal case. In both cases the result is a spread of 2 arch minutes.

The intensity is seen to have variations below 5% if one disregard the points where holes or edges reduces the total PG volume. These variations are mainly due to non-perfect calibration of crystal positions with the translation arm and should not raise any concerns in a study of the crystal quality.

The width variation of the reflections displays some interesting effects. It is clear that some crystals are a few percent coarser than others, showing the non-uniformity of the manufacturing process. The width also increases close to the edges of the crystals. This is believed to be an artefact of the way the holes for mounting the crystals were drilled. While this does not pose a serious risk to the instrument performance it is worth considering other ways to produce these holes in the future, for example using lasers or acids instead of drills.

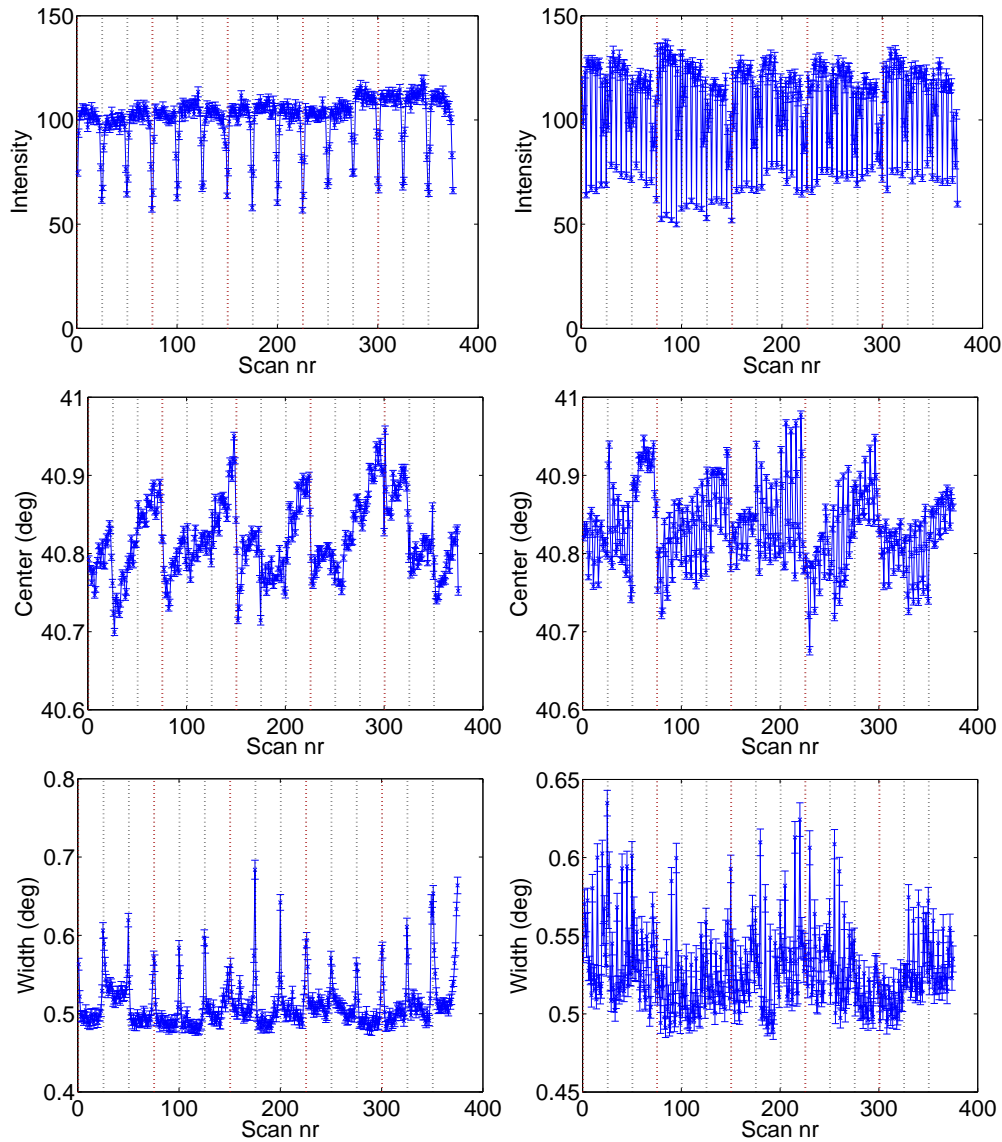


Figure 4.10: *Summary of Poldi measurements.* The intensity(top), position(middle) and width(bottom) of the measured reflection for one batch from Panasonic of nominal 40" PG. both measured horizontally (left) and vertically (right) The black dotted lines indicate a new crystal and the red dotted lines a new wafer.

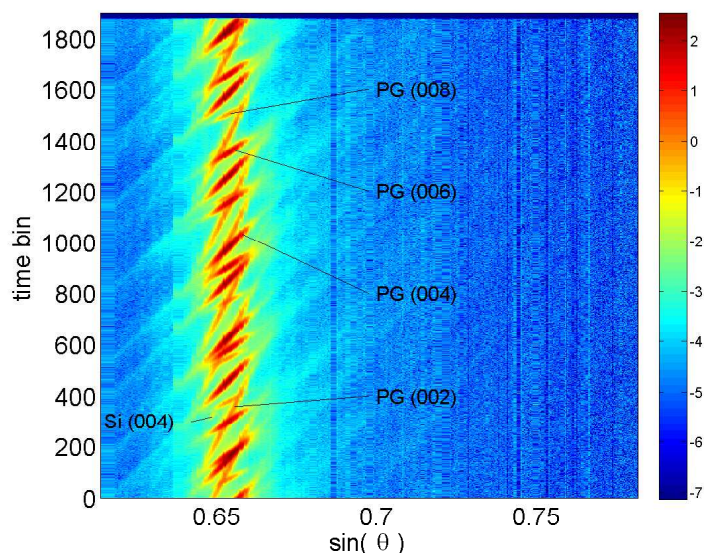


Figure 4.11: *Poldi measurement with the choppers rotating.* The choppers allow one to distinguish the different order reflections from ToF but the instrument loses the advantage of being fast, so other instruments designed for scanning single reflections becomes more advantageous. It does however show how 4 different orders can be distinguished in the reflected beam at Poldi.

#### 4.2.3.4 The other Graphite Batches

Two other batches (another 40" and a 60" batch) were also investigated. The general behaviour is comparable to the first batch, however. The spread in alignment is 3 arch minutes rather than 2 and the general reflectivity of the 60" mosaicity is seen to be about 10% lower. It is understandable that the precision of an alignment procedure that relies on the orientation of the surface is mosaicity dependent. The change in intensity however, is not trustworthy. Poldi provides an excellent fast overview of the graphite and the resolution is only 2% of the typical width of the measured PG performance, however the instrument is not designed for this. The white thermal beam means that the (002), (004), (006) and (008) reflections are seen on top of each other (see figure 4.11). This should not influence center position or width of the peaks but it can make differences in intensity larger than what is observed only for the (002) reflection since warmer neutrons have a higher penetration depth and thus will be more influenced by a lower reflectivity than cold neutrons where reflectivity saturation is almost reached. So while we can trust the behaviour of the intensity graph we should not trust the actual numbers. We can however say that the loss is less than 10%.

#### 4.2.3.5 Isolating the Bragg Tail Problem

*During the construction of an instrument or a prototype many unforeseen issues arise and many resources are used finding the cause of different problems. I will here describe the most time consuming problem with the prototype, both to illustrate the problem with new instrumentation and show that the error detection can lead to new possibilities.*

In the first experiments the signal did not look entirely as expected. The most serious issue was that any Bragg peak had an inelastic tail at the same detector position channel but at all times where inelastic background occurred (see figure 4.12 top). A number of other odd behaviours were also seen but they were less severe and were not immediately realised to originate from the same source.

- The bins on the detector can be divided into 2 regions: The central region that is illuminated by an analyser and the outer regions that are not directly illuminated by an analyser but does correspond to some outer region of the detector with neutron background. The elastic line as a function of time could be seen in both areas.
- In the same way the time channels could be divided into 3 regions: The elastic line, the inelastic part where the choppers allowed illumination of the analysers, and the dark region where choppers blocked neutron access all together. Here the shape of the elastic line as function of detector position could be found in all 3 regions.

At the time the shielding was not yet finished so the signal outside the areas that were supposed to be illuminated were of smaller concern but the quite strong inelastic tail was a problem. Since it was constant in position and thus in  $a_4$ , it's shape in  $(q, \omega)$  space did not resemble any magnon or phonon. It did thus not seem to be inelastic signal from the sample but rather some spurion.

Many things were tested, like whether the signal originated from imperfect chopper attenuation, double counts in the detectors or elsewhere. Especially important were two discoveries: When a shielding plate was installed to block the direct line of sight from the sample to the detectors the background went down and the inelastic tail was dampened by the same factor. This proved that the signal took the direct flight path from sample to detector, not hitting the analysers. On the other hand when the analyser was rotated so that the Bragg peak was no longer reflected towards the detector the tail disappeared together with the peak, proving that the neutrons in question travelled from the sample via analyser to the detector. Disregarding quantum effects, both could not be true at the same time and thus it seemed reasonable that it was some effect of the electronics.

During the testing, technicians traced single neutrons in event mode throughout the data processing, and the files showed no signs of wrong data treatment. Expanding on the technique I developed a program to read the event mode data and translate it into histogram data. With access to event mode data a number of systematic errors in the data handling could be tested. Amongst

the tested hypotheses were that the combinations of time and position stamps were messed up. If the  $j$ 'th event in the  $i$ 'th detector generate a timestamp  $t_{i,j}$  and a position stamp  $x_{i,j}$  the electronics could instead of recording  $(x_{i,j}, t_{i,j})$  record  $(x_{i,j}, t_{i,j+1})$  which would explain the observed problems. Testing this by applying the opposite transformation to the event mode data improved the data quality considerably (see figure 4.13). Given these the result the technicians went through the electronics again and knowing what to look for they realized that a signal cable between the detector and an amplifier produced a 5 ns longer delay than expected, provoking the electronics to look up the position before it had been updated to the newest value.

Other than proving that the errors in neutron instrumentation can be similar to

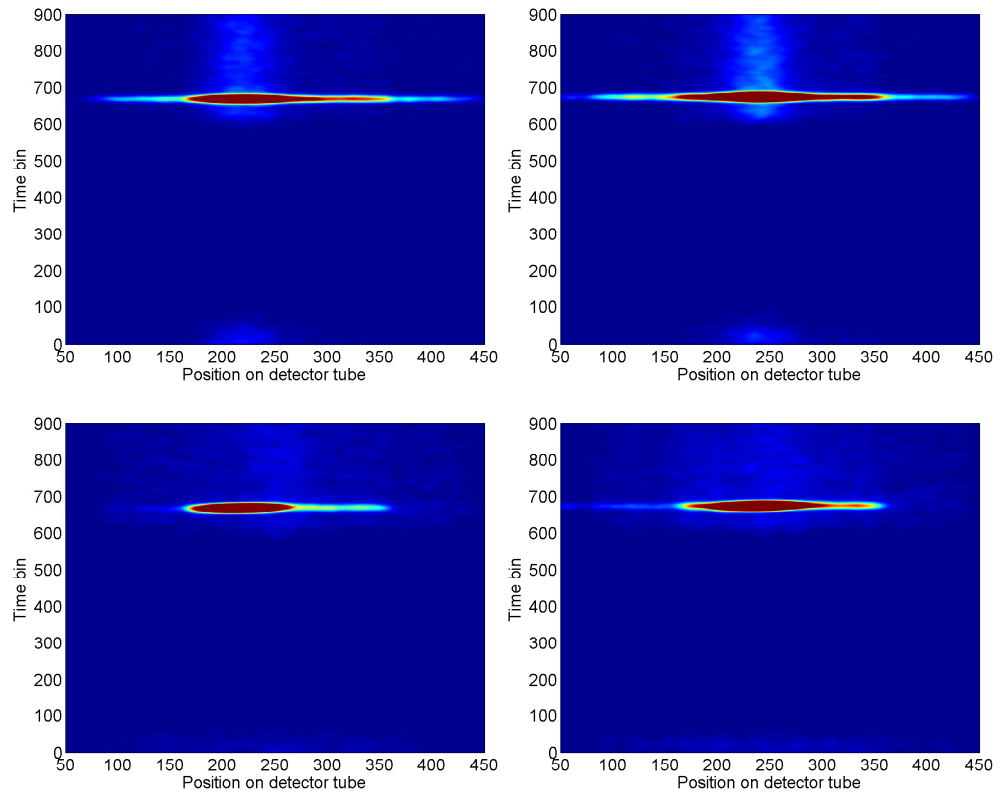


Figure 4.12: *Bragg tail Colormaps of tube 7 (left) and 8 (right) before (top) and after (bottom) correction.*

those in neutrino science, the error hunt did produce a method for event data recording at ToF instruments at PSI. Although the method is not suitable for complicated experiments or user programs it can be used to test hypotheses and time resolutions for the instruments in question and does in fact bring the ambition of doing time resolved studies of quantum phase transitions with the PSI sample environments one step closer to fulfilment (see chapter 6.2). Unfortunately it did take months to find the error so a lot of the first data were recorded with this wrong binning. Although it in principle means that every data point is

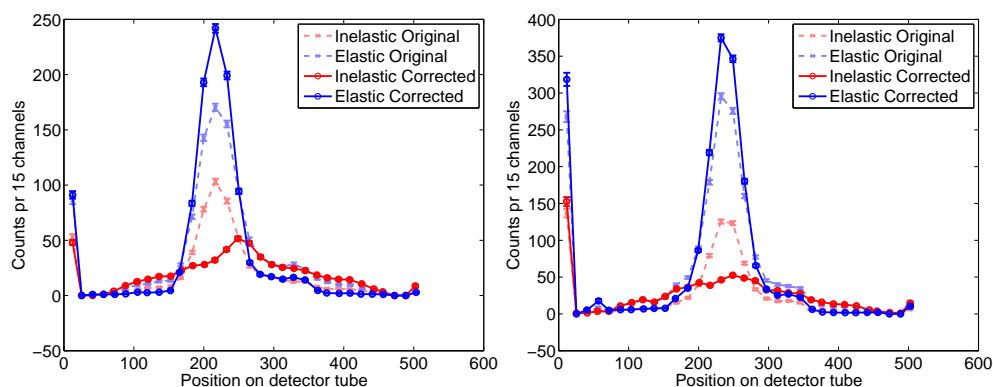


Figure 4.13: **Bragg tail Correction.** The inelastic time channels summed (red) and the elastic time channels summed (blue) before (dashed) and after (full line) correction. Left shows tube 7 and right shows tube 8.

wrong, most of the data are anyway collapsed either in the time or the position direction and when that is done the error disappears. This means that a clear majority of the results are still valid and only a few needed correction.

## 4.3 Simulations

The ray-tracing simulations of the CAMEA were performed in McStas. One key strength of simulations is that they allow the simulator to divide the instrument into small sections and investigate the performance of each part individually, rather than trying to deduce the different contributions from the full signal. This is especially important for resolution functions, where the convolution makes it hard to see changes in the finer of two resolutions. The modular structure of McStas was utilized to simulate the frontend and backend individually. Thus most backend simulations are made with a source illuminating a sample directly, and a narrow wavelength band is simulated so that  $\sigma E_i \ll \sigma E_f$ . The source is also placed at a distance so the secondary divergence dominates the primary. Of course full simulations of the entire instrument were also done to check for any unpredicted correlations. This was thoroughly done for the prototype where such results could be checked against actual data.

### 4.3.1 Detectors

To save simulation time, most backend simulations were further done with one big PSD looking at each analyser. Afterwards the data from the PSD was analysed in Matlab where "detectors" of the desired size and pattern could be extracted from the recorded data. When this was done the different efficiency in different part of the detector cylinders were included, though no direction data was saved and thus all data was assumed to hit the detector from the main direction of analyser. This introduces a small angular error that translates to a very small error in actual flight path. For the full simulations, a new detector

component was written that describes a cylindrical one dimensional PSD with time resolution. The component assumes a simple  $1/v$  relation between absorption cross section and neutron energy, calculates the probability for absorption from the length of the neutron path through the detector and selects a weighted random position along this trajectory for the time and position recording.

### 4.3.2 guide\_bot

guide\_bot is an automated guide optimization tool for McStas written by Mads Bertelsen[41]. It allows the user to specify a string of guide components (*for example EGEKE for an elliptic feeder followed by a gap for choppers, and two elliptic guides with a kink between them*) and some parameters (*for example WaveLmin=1, WaveLmax=5, Mod\_sample=165, ...*) and the code will then write a corresponding McStas file and optimize it on for example the ESS computing cluster[3]. The code also allows the user to write a number of different strings and let the optimizer work on each of those, allowing us to optimize and test more than 150 different guide geometries for CAMEA in a reasonably short time. Furthermore it is possible to place specific restrictions on instrument components and scan many of the parameters. So for the most interesting geometries it is possible to scan for example the divergence at the sample position and make an optimization for each divergence comparing the different results. An especially difficult demand to optimize is losing line-of-sight (LoS) to the moderator at a given position in the guide since the needed bending of the guide will depend on the width and length of several guide elements that the optimizer should be allowed to change. To correct for that guide\_bot writes a ray-tracer in the McStas file that once the optimizer has suggested dimensions of the guide, bends the guide sufficiently to avoid LoS at a predefined point. For each result guide\_bot produces divergence, wavelength and position diagrams as well as phase space acceptance diagrams allowing the user to determine whether the found neutron distributions would be acceptable for an actual instrument.

### 4.3.3 Potential errors in the Simulations

All instruments have a diffuse background of neutrons passing through the shielding, incoherent scattering from/off active components, scattering from supposedly inactive components, or a combination of the above. This is not yet possible to simulate in McStas. Instead the background is generally zero. Background determination should thus not be done by simulations but by prototyping.

PG is a single crystal in the (002) direction and a powder in the plane orthogonal to this direction. This leads to strong scattering in the (002) direction and much weaker reflections in other directions. However, the reflections are there if the angle to the c-axis is correct no matter how the analyser is orientated in the  $(a, b)$  plane. The reflections in question do however all have a relatively high angles to the (002) reflection. Due to the 2.7 times longer c-axis than a-

or b-axis and thus shorter  $\mathbf{c}^*$  vector than  $\mathbf{a}^*$  and  $\mathbf{b}^*$  vectors, even a potential (1,0,16) reflection have an angle of  $11^\circ$  to the (002) reflection. The (1,0,16) reflection will reflect neutrons with energies more than 64 times higher than the (002) reflection if  $a_6$  is similar. Neutrons with so high energies will however, not be transported to the sample. Since PG is not a powder in the (002) direction the angle between a reflection and the (002) reflection must be uphold, so the reflections of concern will have large angles to the main direction of reflection. Even rough collimation will thus remove any side peaks.

Furthermore the peak shape of the analyser/monochromator component is a perfect Gaussian, whereas actual experiments show Lorentzian tails (see section 4.4.15.2). A McStas component addressing these two issues is in production.

### 4.3.4 Errors in the guide\_bot Results

There are three obvious contributions to errors in the guide\_bot optimizations: Statistical errors from the simulations, limitations in the McStas model, and the possibility that an optimizer have not found the global optimum in the many dimensional parameter space.

The first is in this case negligible due to the high statistics of the simulations. The second is harder to test but generally the simulations were always done using pessimistic numbers for mirror reflectivity at high m-values. This means that the actual guide can be expected to perform at least as good and probably slightly better at the more demanding geometries where the full m-value is needed to transport the desired phase space. So when guide\_bot *e.g.* return a low source height and thus small incoming phase space as the optimum we have reason to believe that actual guides would favour this solution even more if anything.

Concerning the optimum all optimizations have been run several times and the maximum have been chosen to minimize the effect but even so some data points are clearly too low, showing that the global optimum have not always (if ever) been reached. To reduce the noise in scans all points more than 20% below both neighbours have been removed as examples of an unsuccessful optimization. Still local minima in scans of for example moderator height and loss of line of sight should not be trusted unless there are some physical reasons to expect a minimum at a certain position.

## 4.4 Instrument Design

*With the methods described I will now describe the individual parts of the instrument. I will start at the source and work my way towards the detectors.*

### 4.4.1 Moderator

Instruments at ESS will use either a cold, thermal or a new so called bispectral moderator concept[60, 61, 102]. The bispectral extraction system has a guide looking at the thermal moderator and a mirror that reflects neutrons from the cold moderator into the guide while the thermal neutrons generally have too

short wavelengths to be reflected and are thus mostly coming from the thermal moderator. This leads to a source that is almost as good as the cold and thermal sources in their main regions and somewhat below in the intermediate region[77]. Since ESS CAMEA is designed mainly for cold neutrons but is also foreseen to use some thermal neutrons both the cold and the bispectral extraction solutions were considered. In the end the cold was preferred for two reasons.

- The cold performs better in the main focus area of the instrument, i.e. mainly cold and intermediate neutrons. ( $\lambda \leq 2.5\text{meV}$ )
- The mirror in the bispectral moderator will be very close to the source and neutron mirrors have previously experienced strong radiation damage. Although new mirror types should reduce this risk they have yet to be used in a facility for many years. If they break down they will be impossible to change and the instrument will be stuck with a thermal source. Though the risk is small and acceptable to instruments that plan to use both wavelength ranges equally often, it was considered too large a risk for CAMEA where thermal neutrons are only foreseen to be used infrequently. Therefore the consequences of a destroyed mirror are too large a risk to take.

#### 4.4.2 Instrument Length

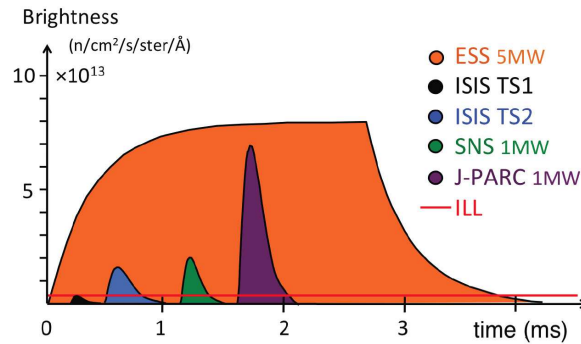


Figure 4.14: **ESS pulse shape.** The ESS pulse shape compared to the major pulsed spallation sources and to ILL. The other pulsed sources have a higher frequency than ESS making the, ESS advantage smaller, though still considerable if a significant part of the ESS pulse can be used. On the other hand ESS might improve the intensity during the final moderator design. Figure from [107]

The ESS source will have a frequency of 14 Hz and a pulse length of  $\tau = 2.86$  ms plus a ramp-up time and a tail[107] (see figure 4.14). If the full pulse is used, any distance between moderator and sample, often called the instrument length ( $L$ ), can be chosen. In this case  $L$  is mainly used to establish a compromise between resolution and bandwidth, since:

$$\delta\lambda = \frac{2\pi\hbar}{m_n} \frac{\delta t}{L} \quad (4.1)$$

where  $\delta\lambda$  is the wavelength uncertainty and  $\delta t$  is the time uncertainty. Likewise the bandwidth ( $\Delta\lambda$ ), i.e. the range of neutron wavelengths that the sample will be exposed to in each period of the instrument becomes:

$$\Delta\lambda = \frac{2\pi\hbar T}{m L} \quad (4.2)$$

where  $T = 71.4$  ms is the period of the source.  $\delta t$ , is dominated by the pulse length. However, many instruments including CAMEA benefits from a variable resolution and uses choppers to control  $\delta t$ . If this is done by producing a single narrow pulse the maximal bandwidth will become a function of the distance from moderator to the pulse shaping chopper ( $l_0$ ) and the opening time of the chopper ( $t_0$ ). Since most instruments wants the flexibility to choose  $t_0 \ll \tau$  we can define a natural length ( $L_n$ ) of the instrument where two neighbouring pulses just touch each other when  $t_0$  is infinitively small:

$$L_n = l_0 \frac{\tau}{T} + l_0 \quad (4.3)$$

(se figure 4.15). If a shorter distance is chosen there will be periods where no neutrons can reach the sample, whereas instruments can be made longer if a finer resolution and shorter bandwidth is desired. If  $L = L_n$  and a longer opening time is desired the pulses will overlap and more choppers will be needed to keep the pulses separate.

It is possible to split a single pulse into several pulses to achieve a wide band-

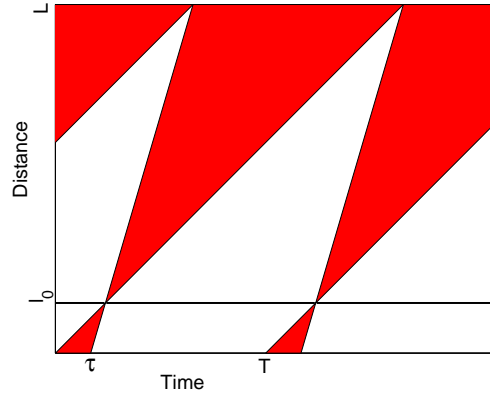


Figure 4.15: **Natural length of instrument.** The natural length is the distance where the different pulses from the moderator touches each other if they have to pass through an infinitively narrow chopper at distance  $l$ .

width and a better resolution in the so called wavelength frame multiplication (WFM) mode[114]. In this way one can pick shorter instruments, increase the bandwidth, and influence how the resolution depends on wavelength, however it will reduce the intensity in each channel. Further the wider range of the frame rate multiplication instrument can be achieved on a natural length instrument either by blocking some pulses from the moderator with a chopper if relaxed resolution is desired, or recording several intervals after each other, whereas

the high intensity in each channel of the natural length instruments cannot be achieved on a WFM instrument. Since a key priority in CAMEA is the high intensity in each channel a natural length instrument is chosen.

Due to radiation shielding, the first possible position of the first chopper  $l_0$  is somewhere between 6 and 6.5 m after the moderator giving a natural length between 155 m and 167 m. Since the first possible placement of the first chopper changed several times during the instrument design some CAMEA design work are done at 155 m, some at 167 m and some later at 165 m. Though it might change bandwidth and resolution a few percent it does not change the performance of the instrument in any fundamental way. 165 m corresponds to a bandwidth of 1.71 Å and an incoming energy resolution of 4% at 5 meV, when the full pulse is used. Though this is slightly coarse it is useful for rough mapping and it is possible to produce a finer incoming resolution with choppers if desired. A longer instrument where the full pulse would give resolutions of 2% though the bandwidth would be reduced to half could also hold some merit. However, it would become far more expensive, both in guide materials and because it will require a separate building for the instrument.

#### 4.4.3 The Neutron Guide

*The CAMEA guide was used as an example when `guide_bot` was developed by Mads Bertelsen. During this process he made scans of the acceptable phase space and performance of different guides with me as main contact to the CAMEA team. I later inherited the optimizations and optimized line-of-sight loss,  $m$ -values, and moderator height.*

To transport the neutrons from the moderator to a sample 165 m away modern guide geometry is needed.

The guide can start 2 meters after the moderator and will have a gap for pulse

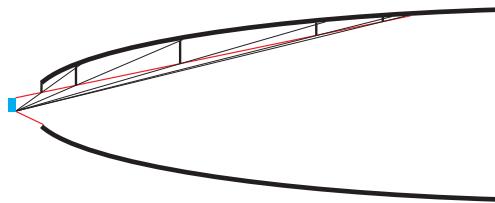


Figure 4.16: **Divergence jaws.** *By inserting a number of slits into the guide it is possible to reduce the divergence on sample (top) compared to when the slits are open (down). Y-axis rescaled.*

shaping choppers about 6 m from the moderator. No gaps for the other choppers are included in the guide. This is because the first choppers are inside the moderator shielding and needs a 10 cm gap to be possible to replace without stopping all instruments for days, whereas the later instruments needs much more narrow gaps (for example the gaps for choppers in the MARS guide at PSI are 1.5 cm wide). Furthermore, the open and closing time of the first chopper is crucial to the instrument performance and it is thus important that the first

choppers are in a narrow part of the guide which makes the gap more difficult to handle. Different widths of the guide just after the gap were investigated. A width of 3.0 cm found to deliver almost the same performance as 3.5 cm but 15% better performance than 2.5 cm. The height of the opening is free since the chopper is sweeping horizontally through the opening and is thus not very sensitive to the height.

To reduce the high energy background the guide should avoid direct LoS from moderator to sample. This can be done with either a kink or a bending section. The guide will not have a perfect cut off at one energy but we wanted to remove neutrons below 1 Å (82 meV) and keep as many as possible above. The actual optimizations was done for energies between 6 and 80 meV (3.65 and 1 Å) since experiences have shown that if the region just above 6 meV is optimized then everything below will also be optimized and the optimizer does a better job in the high energy region if the lower energies are not included.

We agreed with ESS to optimize the instrument for  $0.5 \times 0.5 \times 0.5 \text{ cm}^3$  samples but working up to  $1 \times 1 \times 1 \text{ cm}^3$ . In order to accommodate rotation of slightly bigger samples without big normalisation problems we wanted slightly bigger sample spaces. `guide_bot` was thus used to scan different sample spaces and it was found that the brilliance loss when focusing on  $1.5 \times 1.5 \text{ cm}^2$  was very small while the flux falls off above that. We thus settled on the  $1.5 \times 1.5 \text{ cm}^2$  sample sizes.

We plan to use a number of slits inside the guide to control the incoming divergence on the sample as it is known from the divergence jaws on WISH[22, 51] at ISIS (see figure 4.16) so in principle the higher incoming divergence before the jaws the better. It would be great if we could achieve divergences of  $\pm 2^\circ$ . However `guide_bot` scans were performed and it was realised that above were a divergence of  $\pm 1^\circ$  vertically and  $\pm 0.75^\circ$  horizontally, the increased divergence led to a decreased brilliance so that the total flux on sample stayed almost constant. The difference is due to the asymmetry in the gap for the pulse shaping chopper. Between the guide end and sample a 60 cm open space is left for sample environments.

In order to find the best possible guide `guide_bot` was used to simulate more than 150 different geometries with  $1.0 \times 1.0 \text{ cm}^2$  sample size and  $\pm 1^\circ$  divergence and afterwards the remaining investigation was done with the 4 most promising guides. In the end the geometry in figure 4.17 was chosen. It consist of a parabolic feeder, reducing the horizontal width of the guide before the first chopper. This has been proven to be advantageous to many ESS guide solutions[42]. After the chopper two ellipses separated by a kink transports the neutrons towards the sample. Around the kink two sections of tapering guides are inserted.

#### 4.4.3.1 Line-of-Sight

In the original scans the loss of LoS to the moderator only occurred in the very end of the guide, mainly because `guide_bot` did not support other options. Stopping the fast neutrons just before the sample would however still produce a high background so when `guide_bot` was upgraded to investigate other positions

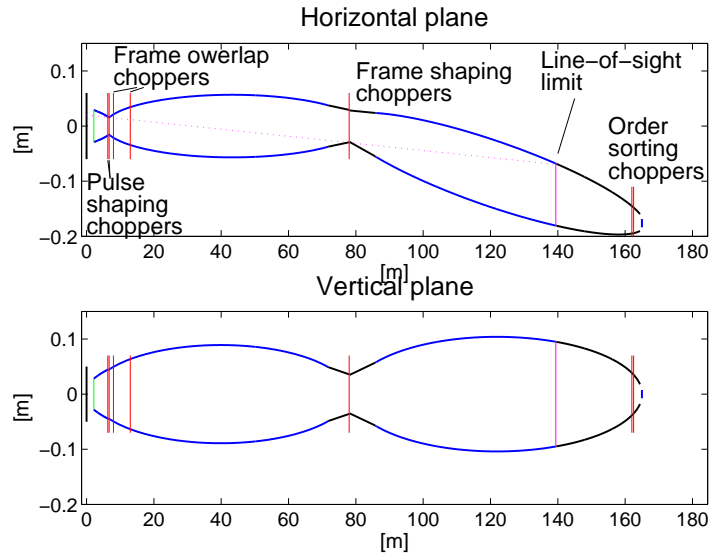


Figure 4.17: **The final guide.** Cross sections of the final guide seen from above (top) and the side (bottom). The pink lines illustrate the line-of-sight and the red lines choppers.

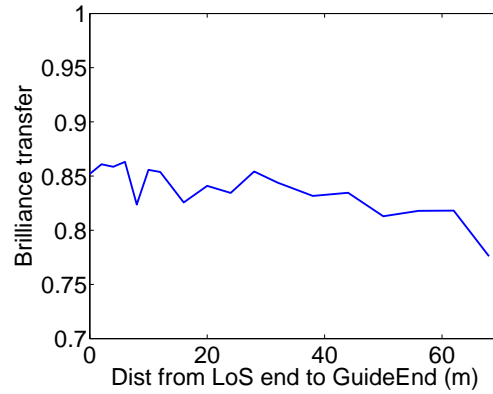


Figure 4.18: **Line-of-sight Distance.** Brilliance transfer as a function of the distance from the end of the guide to the loss of line-of-sight from the moderator. The optimization is done for the standard parameter space for guide optimizations. I.e. a  $1.5 \times 1.5 \text{ cm}^2$  sample area, a horizontal divergence of  $\pm 0.75^\circ$ , a vertical divergence of  $\pm 1^\circ$  and a wavelength range of  $1 - 3.6 \text{ \AA}$ .

a scan was performed to test how far from the guide end the loss of LoS could occur. The results can be seen in figure 4.18. As it can be seen the guide is very robust to movement of the last LoS point. We settled on 25 m as this should be long enough to reduce the high energy neutrons significantly and still only have little impact on the brilliance transfer.

#### 4.4.3.2 Mirror Quality

During the optimization of the guide all mirrors was set to a  $m=3.5$ . The  $m$ -value of the mirrors, however, have great implication for the cost of the guide and if all reflections in a particular part of the guide was performed at low  $q$  due to low angles of incidence the low  $m$ -values would produce the best results[77]. This is in particular the case in the middle of the elliptic guides. In order to investigate this the 5 guide element (feeder, ellipse 1, tapering guide just before the kink, tapering guide just after the kink, and ellipse 2) was split in to 5 sub parts each and a scan of guide performance as a function of  $m$ -values was performed for all 25 guide parts. In all cases the remaining 24 guide parts was left at  $m=3.5$ . Examples of these simulations can be seen in figure 4.19. In many cases like figure 4.19 right the effect is rather subtle. This is because only few neutrons are reflected by this  $\sim 1$  m long guide segment. Adding the effect of all 10 guide segments around the kink would however produce a loss in the order  $\sim 7\%$  of the brilliance transfer, so in this case the maximum  $m=2$  point was still chosen over the slightly cheaper  $m=1$  mirror. Using these results it was determined that a guide with the  $m$ -values specified in table 4.2 would reduce the cost significantly. The exact costs of guides are a trade secret of super mirror suppliers and we were only able to get a quote for the final guide. The resulting brilliance transfer was within 1% of the brilliance transfer from the  $m=3.5$  guide.

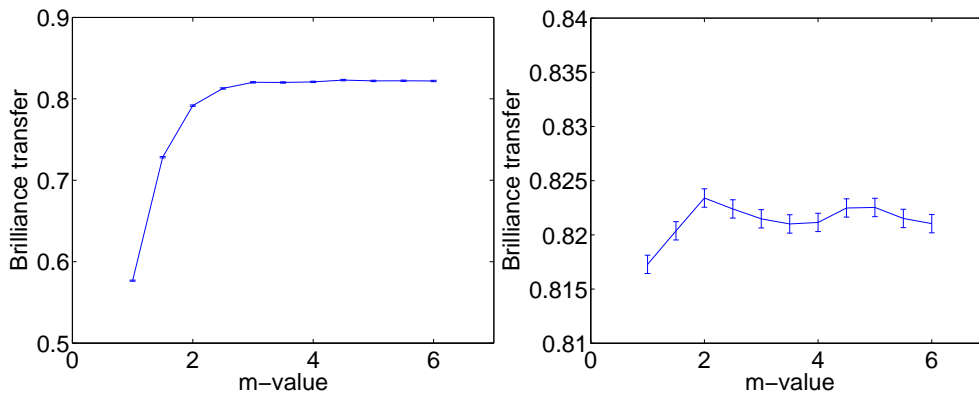


Figure 4.19: *Guide dependence on mirror quality.* The brilliance transfer of the CAMEA guide as function of the  $m$ -value in different sections. Left: The end of the last ellipse. Right: the last part of the straight section around the kink.

#### 4.4.3.3 Moderator Height

As the design of the instrument neared its end the ESS moderator group released data showing how the brilliance of the moderators could be increased by reducing the moderator height[40]. This effect was investigated for the 4 most promising guide geometries. It was found that the chosen guide geometry would also be preferable at lower moderators. Figure 4.20 shows the performance of this guide. Though the brilliance keeps increasing with smaller height the smaller height

Component	length of segment	coating value	position relative to moderator
Parabolic feeder	1.74 m	3	2.16 m - 3.90 m
Parabolic feeder	1.74 m	3.5	3.90 m - 5.63 m
Parabolic feeder	0.87 m	3	5.63 m - 6.5 m
Ellipse 1	6.52 m	3.5	6.6 m - 13.12 m
Ellipse 1	6.52 m	2	13.12 m - 19.64 m
Ellipse 1	39.12 m	1.5	19.64 m - 58.78 m
Ellipse 1	6.52 m	2	58.78 m - 65.28 m
Ellipse 1	6.52 m	3	65.28 m - 71.80 m
Kink section	13.94 m	2	71.80 m - 85.74 m
Ellipse 2	15.73 m	2	85.74 m - 101.47 m
Ellipse 2	47.20 m	1	101.47 m - 148.67 m
Ellipse 2	7.87 m	2	148.67 m - 156.53 m
Ellipse 2	7.87 m	3.5	156.53 m - 164.4 m

Table 4.2: Overview of the guide coating and position of each guide section measured from the surface of the moderator.

demands that higher divergences are accepted in the start of the guide in order to accept a phase space volume of the same size as the one we desire at the sample position. At a certain point the incident angles becomes too high and the brilliance transfer drops countering the increased source brilliance. The point where this happens depends on the desired phase space on the sample. For CAMEA the brilliance starts to drop below about 6 cm and the maximum gain factor of 1.8 can be achieved by going from 10 to 2 cm moderator height. Even at 10 cm the flux is the double of what it was at 12 cm. This is both due to the new better moderator model provided by the moderator group and the fact that the flux here is not displayed in a 1.7 Å wavelength band but for the entire band of interest. Since the official ESS policy is that the old 12 cm moderator will be the reference until all consequences of the new moderator design have been fully investigated all work in this project are done with the old 12 cm moderator. It does however seem likely that a  $\sim 4$  cm moderator will be constructed, increasing the average performance of the instrument with a factor 2 (compared to the 12 cm moderator). The smaller moderator size will also mean a shift towards slightly higher energies so the performance increase will be larger for higher energies but all energies will experience an increase. On the other hand the decreasing brilliance transfer will impact the higher energies reducing the brilliance at the sample position for the very highest energies in the spectra.

#### 4.4.3.4 Performance of the Guide

The performance of the chosen guide can be seen in figure 4.21. The guide has a brilliance transfer close to the best achievable down to 3 Å and a good performance down to the desired 1 Å. Below that the brilliance transfer drops rapidly to 0, limiting the high energy background. Furthermore it is very robust to reduced mirror quality. At 80 meV the profile becomes uneven and a shadow of the kink can be seen the horizontal position profile. Other than that the

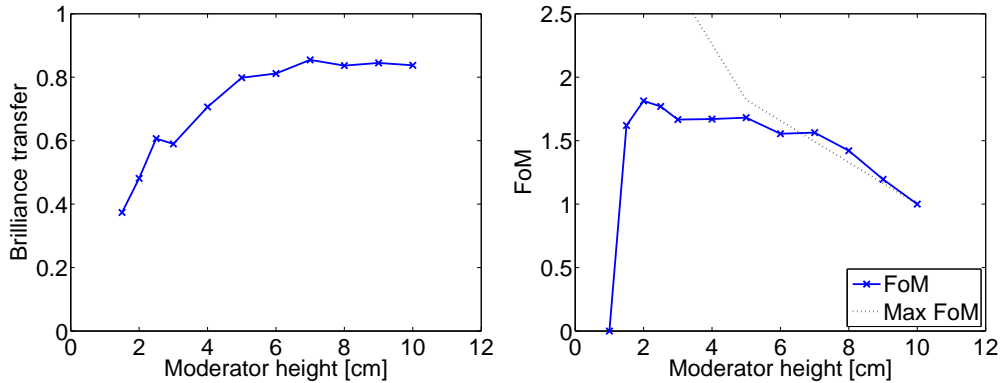


Figure 4.20: **Moderator height dependence.** *Left: Brilliance transfer. Below 6 cm moderator height the brilliance transfer start to decrease, countering the increased brilliance of a smaller moderator. Right: Figure of Merit (FoM) defined as flux at sample for a moderator of height  $h_m$  divided with flux at sample for a 10 cm high moderator, or 0 if the divergence profile becomes unsuitable for the instrument. The black dotted line shows the FoM if the brilliance transfer of 10 cm moderator heights could be achieved at all moderator heights.*

profiles looks acceptable.

The full flux in an  $1.7 \text{ \AA}$  wavelengthband can be seen in figure 4.22. If the full pulse is used CAMEA can reach fluxes of  $1.8 \times 10^{10} \text{ n/s/cm}^2$  on the sample with the old 12 cm moderator or in the most extreme case  $8 \times 10^{10} \text{ n/s}$  from a narrow moderator on the full  $15 \times 15 \text{ mm}^2$  sample space.

#### 4.4.4 The Chopper System

CAMEA will need choppers to fulfil a number of different functions: Pulse shaping, pulse removal, frame shaping, and order sorting. ESS plan to use disc choppers with a standard radius of 35 cm. Choppers cannot be placed closer to the moderator than about 6.5 m and choppers within the first 12 meters need to be robust as they are hard to provide maintenance for.[9]

As part of the design of the chopper system a Matlab function was written that traces the possible neutron paths through a ToF diagram for any given chopper sequence and wavelength interval (see figure 4.24 and 4.25). This gives a fast illustration of the possible traces through the system and makes it easy to spot any problems in the chopper sequence. It does, however, not give any information about intensities or resolutions and it does not consider opening and closing times of the choppers so all sequences should also be thoroughly simulated in McStas. The function is now also used in the design of the ESS backscattering and the vibrational spectrometers.

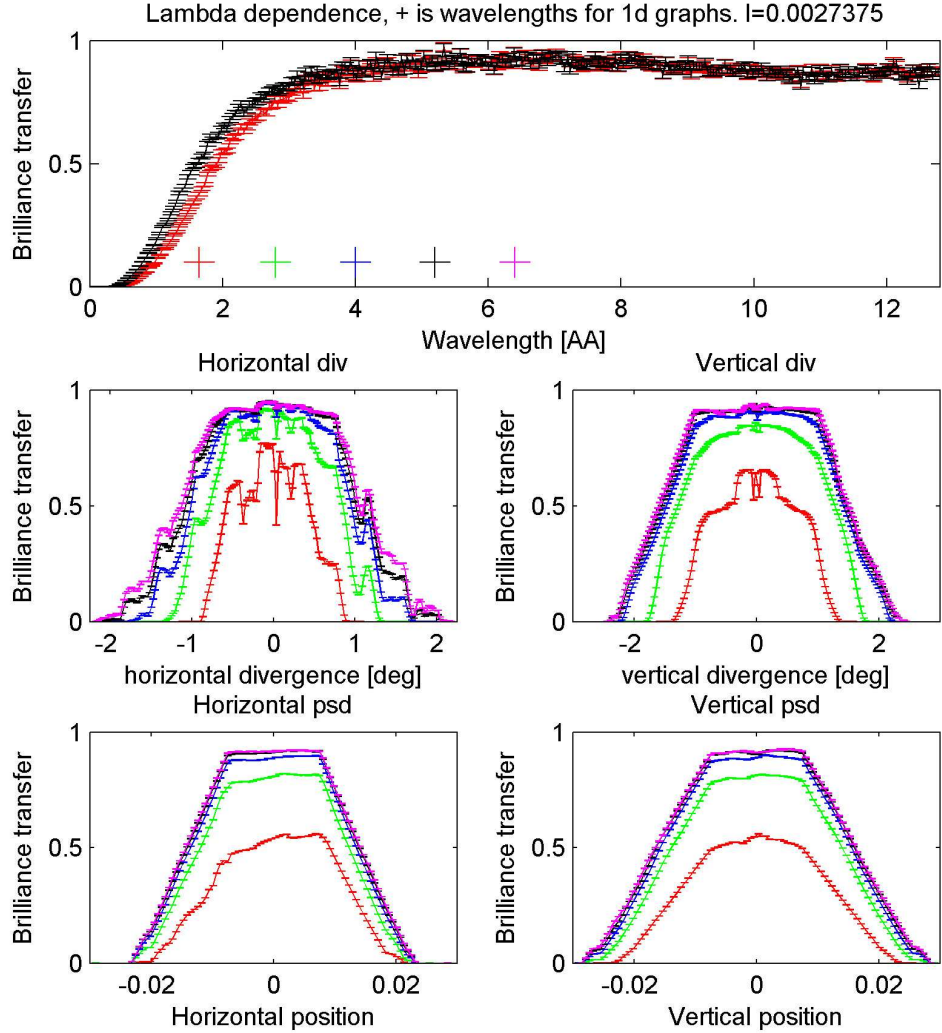


Figure 4.21: *Performance of guide.* *guide\_bot* generated figures showing brilliance transfer as function of wavelength, spatial distribution and divergence distribution in terms of brilliance transfer. The red line in the brilliance transfer as function of wavelength plot shows the performance of the guide in case of a reduction mirror quality. The wavelength snapshots below show the profile and divergence of the beam at specific wavelengths. The displayed wavelengths can be found in the top figure.

#### 4.4.4.1 Pulse Shaping

As we shall see in section 4.4.10.10 the secondary resolution at 5 meV is 1.1% or 55  $\mu\text{eV}$ . The primary resolution can be found from  $v = L/t$  and  $E = m_n v^2/2$  to be:

$$\delta E = \sqrt{\frac{E^3}{2m_n} \frac{\delta t}{L}} \quad (4.4)$$

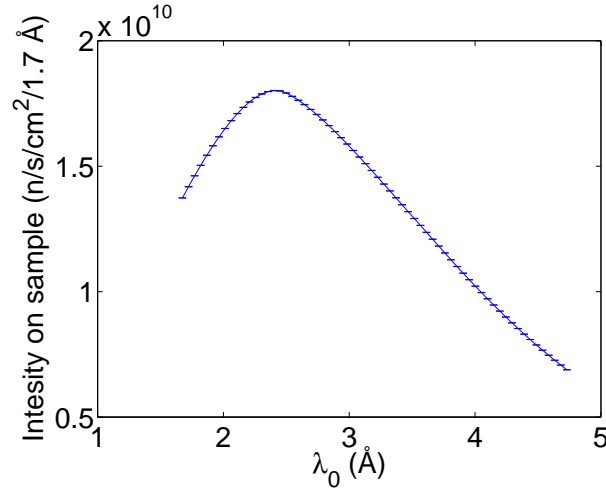


Figure 4.22: **Flux on sample.** The integrated flux from a 12 cm moderator in a 1.7 Å wavelength band from  $\lambda_0$  to  $\lambda_0 + 1.7\text{Å}$  delivered by the guide. Maximum flux is found for the  $\lambda$  interval [2.3;4.0]Å.

Inserting values we find the primary energy resolution without pulse shaping at 5 meV to be 3.5 % or 175  $\mu\text{eV}$ . In order to match the energy resolution at 5 meV elastic scattering it is necessary to reduce  $\delta t$  to 0.9 ms. The instrument will, however, often be used to investigate down scattering. If we look at  $E_i = 80$  meV and  $E_f = 32$  meV energy resolution matching will require  $\delta t = 0.1$  ms.

To reduce  $\delta t$ , a pulse shaping chopper system is required. This pulse shaping chopper system will consist of two choppers rotating out of phase to control the pulse width. The open or closing time of a disc chopper can be found from figure 4.23. In order for a chopper to open or close it have to rotate an angle  $\omega$ . From the blue triangle one sees that  $\tan \omega/2 = w/(2b)$ , and from the red  $b = \sqrt{R_c^2 - (w/2)^2} - h$ . Together the time it takes to open+close is:

$$T_{\text{open+close}} = \frac{2T}{\pi} \arctan \left( \frac{w}{2(\sqrt{R_c^2 - (w/2)^2} - h)} \right) \quad (4.5)$$

where  $R_c$  is the radius of the chopper and  $h$  and  $w$  are the width and height of the beam. Inserting  $T = 71$  ms,  $R_c = 35$  cm,  $w = 3$  cm, and  $h = 8.8$  cm one gets: 0.55 ms. This could be tolerated for 2 ms pulses but for the higher resolutions it will lead to a massive decrease in performance so it is necessary to improve the open/closing time. Though it is technically possible to increase  $R_c$  or decrease  $w$  or  $h$  the influence of this will be limited for technical achievable sizes and it would lead to severe complications. Instead we opt to spin the choppers faster and remove some of the resulting extra pulses with additional choppers. The open and closing time is proportional to the rotation speed so rotating the choppers with a frequency of  $15 \cdot 14 = 210$  Hz reduces the open/closing time to 37  $\mu\text{s}$ , acceptable for the desired pulse length range. The frequency of 210 Hz is an acceptable operating speed for choppers so close to the moderator. If the choppers operate much faster, the risk of instability becomes considerable.

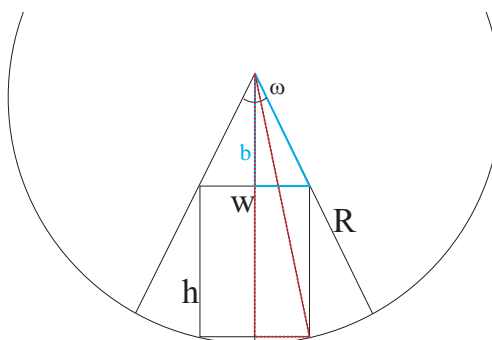


Figure 4.23: **Chopper opening times.** The time it takes for a chopper to open or close is given by the time it takes the edge of the chopper window to pass through the entire guide cross section. This time is proportional to the angle  $\omega$ .

Most choppers operating at these speeds use Cadmium for neutron absorption so we need to be aware that the absorption in these choppers falls off rapidly for neutron energies above a few hundred meV [65]. As the guide transports neutrons up to about 0.5 eV we will need some slower moving choppers using Boron absorbers to remove the high energy background.

#### 4.4.4.2 Pulse Removal Choppers

Figure 4.24 shows a ToF diagram of the first 15 m of CAMEA. At 6.5 m the fast spinning pulse shaping choppers divide the signal into a large number of pulses. Further crosstalk between the different moderator pulses (here called higher order pulses) leads to a very complicated signal. In order to remove all excess pulses two choppers are required. The first chopper rotating at 14 Hz placed 8 m from the moderator is mainly required to remove all but one sub pulse created by the pulse shaping chopper from each pulse. The required pulse has already been shaped by the pulse shaping chopper so the slow opening and closing times are of little consequence as long as they are shorter than the spacing between neighbouring pulses. This requires the chopper to be close to the pulse shaping chopper where the guide is narrow and the sub pulses are still well separated. At the same time it is advantageous to move it some meters back to separate higher order pulses from first order pulses. A number of positions were tested with the Matlab ToF diagram tool and 8 meters was found to be a good compromise that delivers both results.

Some higher order pulses will make it through the sub pulse removal chopper and a fourth chopper is inserted to remove those. Axes and thus maintenance becomes much easier after 12 m so the chopper is placed at 13 m which is close enough to remove all remaining unwanted pulses. This chopper will also rotate at 14 Hz and will not influence the main pulse. Both choppers can thus include Boron and will be able to function as a beamstop plus remove high energy neutrons before the guide leaves the outer moderator shielding at 24 m.

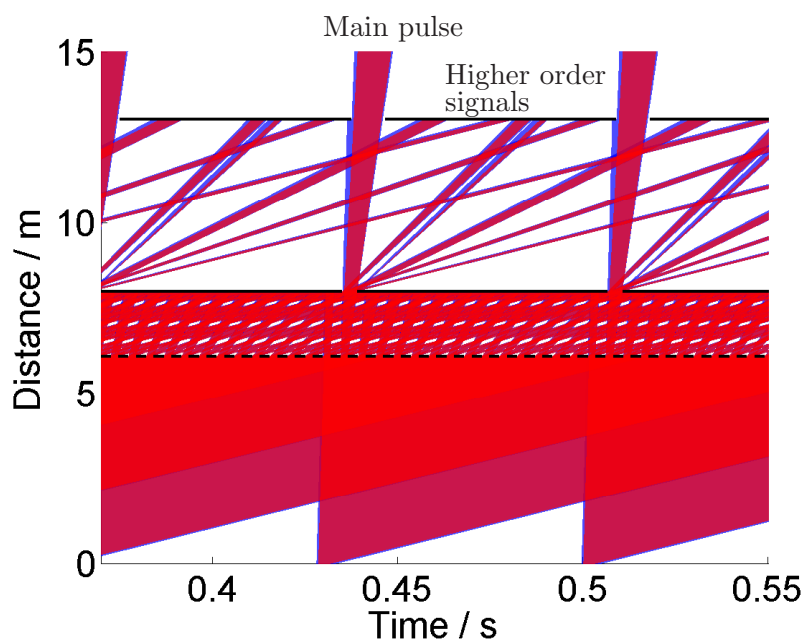


Figure 4.24: **First choppers.** True to scale Time-of-flight diagram of the first choppers planned at CAMEA. The red indicates the signal from the main ESS pulse while the blue is the signal from the tails of the ESS pulse. Neutrons with wavelengths between 1 and 150 Å are displayed.

#### 4.4.4.3 Frame Overlap Chopper

With all excess pulses removed the remaining choppers focus on shaping the main pulses. For infinitely short pulses, the length of the instrument serves to avoid overlap between neighbouring pulses. However, for finite pulse widths, the pulses will overlap. Furthermore, the tails of the moderator pulse will also lead to some overlap between the pulses as a the larger T from the tails will correspond to a shorter natural length in (4.3). In order to remove this overlap, a frame overlap chopper running at 14 Hz is placed further down the guide. The closer the chopper is to the sample the smaller is the shadow from the tails on the moderator pulse but the chopper also needs to be close enough to the pulse shaping chopper that it will remove the overlap between pulses at any opening time of the pulse shaping choppers. A combination of the Matlab ToF diagram tool and simulations showed that a position close to the middle of the guide was optimal, and the kink position is chosen since this is where the guide is narrowest and open/closing times are fastest. In this case, the opening and closing times will not influence the resolution but change how fast each pulse ramps up to its full strength. At the kink position the ramp will cover 1.5 % of the full frame whereas it will cover 4 % if the chopper was placed in the middle of the second guide due to the larger cross section of the guide at this position.

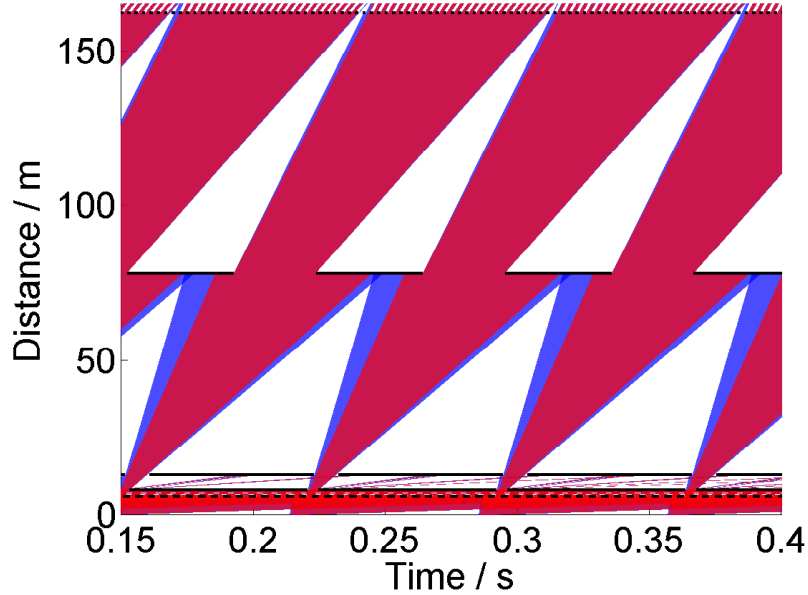


Figure 4.25: *CAMEA chopper solution*. Top: True to scale time-of-flight diagram of the chopper solution planned at CAMEA. The red indicates the signal from the main ESS pulse while the blue is the signal from the tails of the ESS pulse. Neutrons with wavelengths between 1 and 150 Å are displayed.

#### 4.4.4.4 The Order Sorting Chopper

PG analysers will reflect neutrons from all  $(0, 0, 2n)$ ,  $n \in N$  reflections towards the analysers. Usually neutrons from higher order reflections,  $n > 1$ , are handled with a Be or BeO filter and it is also planned to install such a filter at CAMEA. However, it is also possible to use the several allowed reflections to increase the dynamic range of the instrument if they can be distinguished. This can be done by time-of-flight if the beam is chopped in an appropriate way further up-stream (see figure 4.26). Ideally, this should happen after the sample however the space here is tight and the beam of interest wide meaning it is only possible to chop the beam before the sample. If the secondary distance for the  $j$ th analyser is  $d_{sec,j}$  and its (002) reflection selects neutrons with energy  $E_{j,(002)}$  or speed  $v_{j,(002)}$  then the separation of first and second order neutrons that hits the sample at the start of one pulse is  $\Delta t = d_{sec,j}/v_{j,(002)} - d_{sec,j}/v_{j,(004)} = d_{sec,j}/(2v_{j,(002)})$ . This is thus the longest possible opening time of the order sorting chopper, assuming a perfect time resolution. Knowing  $E_{j,(002)}$  for all detectors it is possible to find a relation between  $d_{sec,j}$  for all detectors that will ensure that all detectors are illuminated at all times without crosstalk between first and second order neutrons. Third and higher order analyser reflections can produce background. These require high  $E_f$  values and will not always be present, however if they pollute the signal the two choppers in the order sorting chopper system can be dephased to separate more than the two first orders. If this is done the total

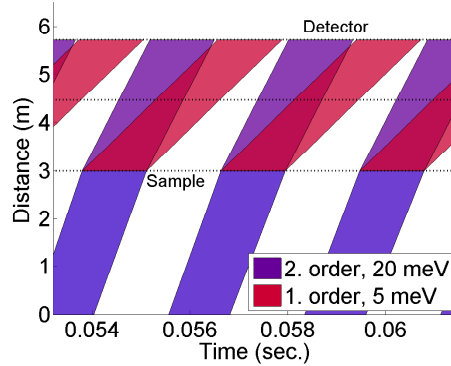


Figure 4.26: **Order sorting chopper.** *ToF diagram of the principle behind the order sorting chopper. Here illustrated by a limited part of the time pulse and the 7th analyser (5 meV). Before the sample the neutrons are chopped into specific pulses that will travel to the sample where inelastic scattering will happen. After the sample only neutrons with energies of 5 (red) or 20 meV (blue) are displayed (corresponding to the (002) and (004) reflections). If the pulse is shaped correctly the two pulses will cover most of the time at the detector position without overlapping.*

efficiency of the instrument will fall.

The pulse will broaden on its way from order sorting chopper to detector. This broadening will cause overlapping tails where it is impossible to distinguish first and second order scattering. Neutrons in periods with overlapping tails will have to be discarded. We required that the two pulses are fully separable, and not that they are separated by one  $\sigma$ . The pulse broadening will come from three main components:

- Time resolution of secondary spectrometer. The uncertainty in flight path and velocity in the secondary spectrometer will cause a widening of the pulses. The relevant numbers can be found in 4.4.14. However, the results given here are the FWHM. If a clear separation between the two pulses is wanted then longer separation time should be chosen. In this case we chose to set each tail equal to one FWHM.
- Broadening of the pulses between chopper and sample. This time is given as  $(t_{pulse} + t_{order}) \frac{d_{os}}{d_{po}}$  where  $d_{po}$  is the distance from the pulse shaping chopper to the order sorting chopper,  $d_{os}$  is the distance from order sorting chopper to sample, and  $t_{order}$  is the open time of the order sorting chopper.
- Chopper opening+closing time of the order sorting chopper system. This time is given in (4.5)

Since we want complete separation of the pulses the contributions are added directly rather than in quadrature to obtain a full width of the tails before or after each pulse ( $t_{tail}$ ).

As the tails before and after a pulse are symmetric in the above calculations it

is advantageous to keep the dead times before and after the (002) pulse equally big. This is done by keeping the frequency that would allow a fully filled time frame if the chopper opening was 50 % and reduce the opening time. Figure 4.27 illustrates different ways to compensate for the tails. Method b) and c) are the most interesting. b) gives a time  $t_{tail}$  where the signals cannot be distinguished, and the neutrons thus must be discarded, corresponding to a loss of signal of  $I * t_{tail}$  where  $I$  is the intensity of the signal. c) gives a time  $2t_{tail}$  where the signal is reduced but distinguishable. If a linear decent is assumed this leads to  $2 * 0.5 * I * t_{tail} = I * t_{tail}$ . Since the tails correspond to several independent contributions the actual tail shape will be Gaussian like and thus the integrated transmission will be highest if a combination of b) and c) is chosen.

The distances in CAMEA can be adjusted so all analysers will be able to sepa-

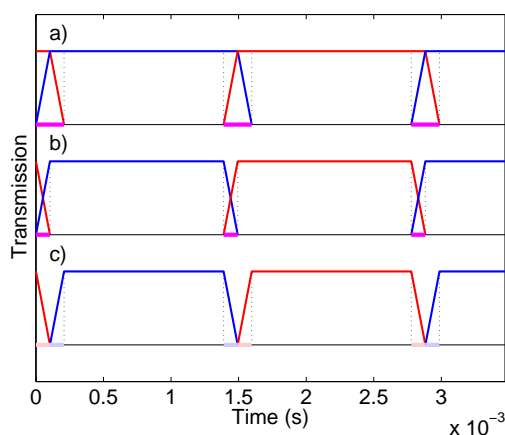


Figure 4.27: **Overlap between order sorting pulses.** The base frequency is kept constant and chopper opening times adjusted. Red symbolises (002) pulses and blue (004) pulses at the detector position. The slopes are kept straight though they will be Gaussian like. a) The base frequency is used and the choppers are open 50% of the time. The detectors will not be able to tell the signals apart for the time  $t_{tail}$  per cycle (marked in magenta). b)  $t_{tail}/2$  is subtracted from the opening time. This reduces the overlap time to  $t_{tail}/2$  per cycle. c)  $t_{tail}$  is subtracted from the opening time. Here the overlap is gone, however the signal is reduced in a region of width  $t_{tail}$ .

rate the pulses if the order sorting chopper frequency is 360 Hz. For a chopper of standard radius,  $R=35$  cm, placed 1.8 m before the sample this leads to a downtime of 5%. However 360 Hz is at the edge of chopper technology and running so close to a potential 25 T magnet could cause problems. Hence in order to increase the reliability it was investigated how the closing time would change if the chopper was moved further away from the sample and the chopper was produced with two openings running at 180 Hz. An added advantage of the 180 Hz setting is that the opening time is large so a chopper with a single opening would be very asymmetric, which would make its center of rotation far away from its natural center of mass and thus potentially put strong demands on the holding technology. The 180 Hz chopper, however, is symmetric and will thus

run far more stable. Figure 4.28 shows the performance of the 360 Hz chopper and 180 Hz chopper as a function of distance to the sample. Given these results it was decided to propose a 180 Hz chopper placed 3 m from the sample (where the stray field from the 25T magnet should be below 0.1 T) in order to guarantee a stable performance. This leads to a downtime of 9%. It should however be investigated if the chopper can be moved closer to a 25T superconducting magnet once one exists.

The frequency of 360 Hz is not a multiple of the 14 Hz of the source. Adjusting

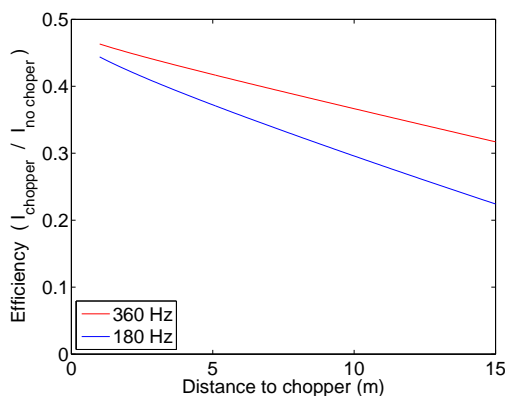


Figure 4.28: **Order sorting efficiency.** Calculated max efficiency of order sorting choppers running at 360 Hz and 180 Hz at various distances.

the frequency to  $26 * 14 \text{ Hz} = 364 \text{ Hz}$  would split each pulse into 26 sub-pulses of length 1.1 ms with 1.6 ms pause between them. The pulse shaping chopper will be used to reduce the incoming pulse to 1 ms (needed for elastic resolution matching) or lower (needed for inelastic resolution matching in the down scattering region). These gaps produced by the order sorting chopper will thus be resolvable, leading to gaps in the coverage. By choosing a frequency that is not a multiple of 14 Hz, this is countered as long as the measurement last for a large number of pulses, corresponding to more than one second.

#### 4.4.4.5 Other Possible Choppers

A number of extra choppers could be included to improve the performance of the instrument: A  $t_0$  chopper could be useful to remove the prompt pulse but may not be needed as we bend the guide out of line of sight. ESS is working on combined simulations of guides in McStas and moderator and guide shielding in MCNPX to clarify this subject.

#### 4.4.4.6 Performance of the Chopper System

The chopper system has been simulated and is shown to block all unwanted neutrons in the range from 0.1 to 100 Å for a range of different wavelength bands, opening times and pulse shaping chopper speeds. An example of such a test can be seen in figure 4.29. Simulations were performed at a number of different chopper settings and the neutron rays recorded at the sample position

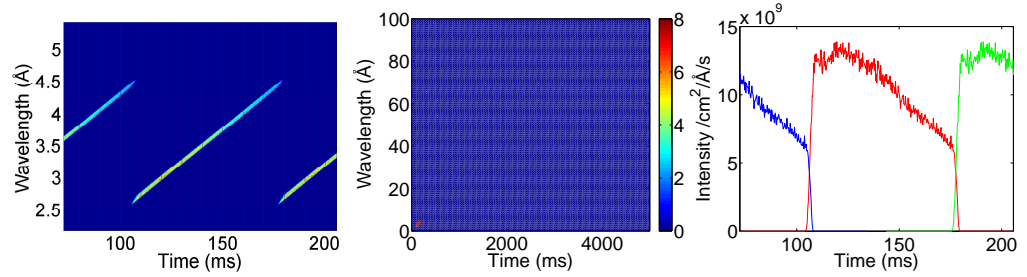


Figure 4.29: **Simulated chopper performance.** Left: McStas simulation of the pulse shape in a  $(t, \lambda)$  diagram. Middle: Zoom out on log scale showing that only the desired  $sim4\text{\AA}$  neutrons reach the sample up to  $100\text{\AA}$ . Right: Collapsing the data to the time axis it is clear that two neighbouring pulses can be distinguished well. The small overlap can be avoided with a slightly smaller opening of the frame overlap chopper however, just as for the order sorting chopper signal this does not improve the total performance. Note that McStas as default only generates one pulse so this pulse have been repeated in Matlab with a frequency of  $14\text{ Hz}$  in the left and rightmost figure, while the middle only shows a single pulse. All simulations are done at a lowest transmitted energy of  $4\text{ meV}$  ( $4.5\text{\AA}$ ) and the full ESS pulse.

as function of  $E_i$  and  $t$ . For each time bin the recorded  $E_i$  dependence was fitted to a Gaussian. The fitted width as function of fitted center value can be seen in figure 4.30 for a number of chopper settings. The simulations show that  $\delta E_i/E_i$  can be varied from  $3.5\%$  at  $E_i = 5\text{ meV}$  with open choppers down to  $0.3\%$  at  $0.2\text{ ms}$  opening times.

#### 4.4.4.7 Reliability of the Chopper System

All chopper specifications have been chosen conservatively so the requirements are considerably below what is running at facilities today. The risk of downtime due to chopper failure is thus low. It is, however, still possible to experience problems with the precision of the chopper phases. The long pulse of ESS and corresponding long primary flight path makes the instrument more resilient to phase uncertainties than at many other facilities. One can either relax the chopper frequency to the pulse frequency of  $14\text{ Hz}$ , accepting long opening+closing times or produce choppers with larger openings. The choppers most sensitive to phase uncertainties are for CAMEA chosen with big openings, and that reduces the phase uncertainty problems significantly.

**Pulse shaping choppers** Phase uncertainties in the pulse shaping choppers can in principle both lead to a lower intensity and a wrong determination of  $\lambda_i$ . Both effects will be very small due to the large opening of the choppers. A phase uncertainty of  $1^\circ$  leads to a drop in flux of less than one percent and a wrong determination of  $\lambda_i$  of the order  $0.01\%$ . Actual chopper phase uncertainties depends on manufacturer, stray fields, rotation speed, and many other

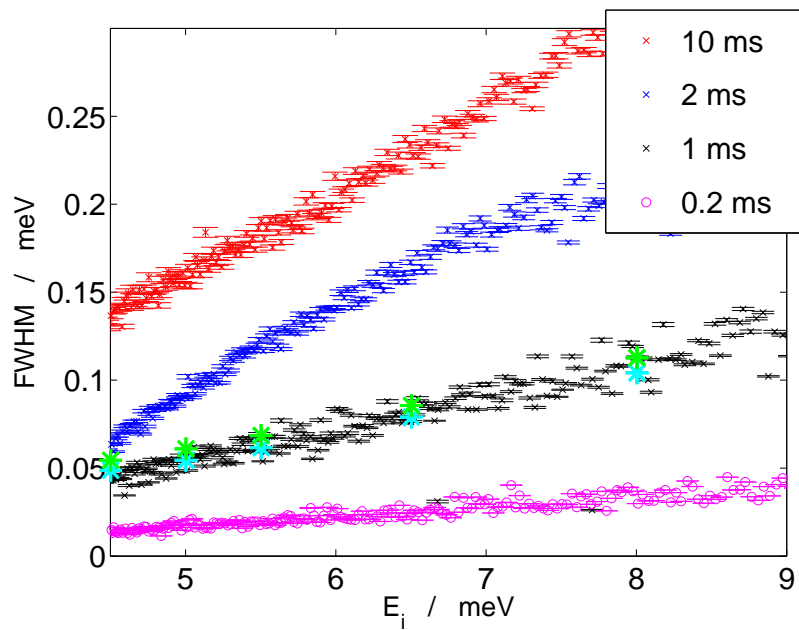


Figure 4.30: *Simulated energy resolution.* Energy resolution of the chopper system for varying opening times of the pulse shaping choppers. Red: full open, Blue: 2 ms, Black: 1 ms, Magenta: 0.2 ms. The secondary energy resolution is included as stars to illustrate the elastic resolution matching at 1 ms opening times. Blue stars: simulated resolution, Cyan stars: Analytical resolution calculations by Marton Marko.

parameters but for the 300 Hz "Res1" and "Res2" choppers at LET realistic phase uncertainties are in the order  $0.04^\circ$ . [85]

**Pulse removal choppers** The pulse removal choppers are independent of phase uncertainties up to about  $5^\circ$ , since they are not shaping the actual beam but only removing unwanted pulses.

**Frame overlap chopper** Phase errors in the frame overlap chopper will shift the wavelength band. The shift can, however, be determined and will not influence the resolution and intensity at a given wavelength considerably. A shift of  $1^\circ$  on the chopper will lead to a shift of the wavelength band of about 0.5 % of the lowest selected wavelength. For the narrowest resolutions the width of the wavelength band can be reduced. However, for the standard resolutions, this will only happen when the chopper is  $10^\circ$  out of phase, and can thus be ignored.

**Order sorting chopper** A phase shift in the order sorting choppers will shift each pulse and can in principle lead to a loss of flux of 1.5% for a  $1^\circ$  phase error if the phase shift is unknown. Since phase shifts can be determined by both direct measurements and data analysis, the effect becomes negligible.

#### 4.4.5 Diffraction Resolution

In high pressure experiments a powder with a well-defined compression rate is included in the pressure cell. The  $d$ -spacing can now be measured by diffraction and be used to determine the actual pressure inside the cell. This demands that the  $d$ -spacing can be determined with great precision. In order to achieve this a diffraction quality beam divergence and a wavelength resolution of  $\delta\lambda/\lambda < 1\%$  is required [8]. The divergence requirement will be achievable with the divergence jaws. Furthermore a small set of dedicated diffraction detectors will be located behind some of the analysers. The exact positions need to be determined. At 10 meV  $\delta\lambda/\lambda < 1\%$  corresponds to  $\delta t < 1.2$  ms, easily within the capabilities of the instrument.

#### 4.4.6 Sample Area

A key performance area for CAMEA is extreme sample environments and space for this equipment is needed. CAMEA is foreseen to have access to a 25 T superconducting split coil magnet as well as a 100 kbar Paris-Edinburgh pressure cell. Although no 25 T superconducting magnet exists, manufacturers believe that such a magnet will be available before the commissioning of CAMEA and that it will have a radius of 35 cm in the sample plane [11]. To leave room for error and extra equipment, the sample area is designed with a radius of 45 cm, and more space is secured above the scattering plane. It is further foreseen to be possible to remove the Be Filter and radial collimator completely if even bigger sample areas are desired.

On the incoming side, the guide ends 60 cm before the sample to leave space for slits and monitors.

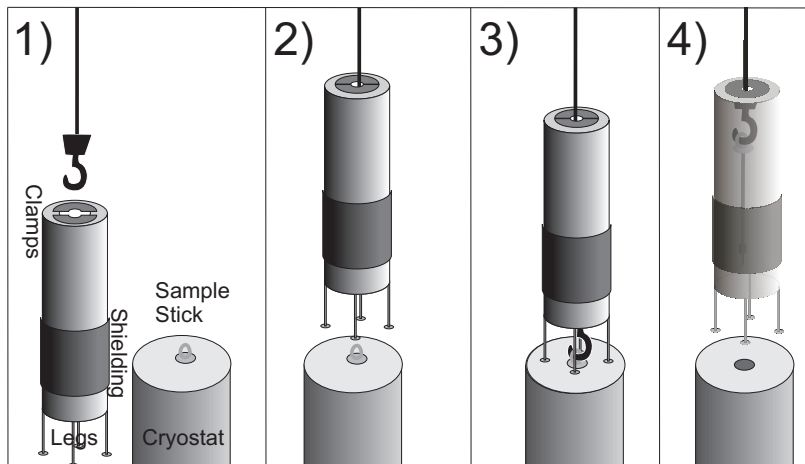


Figure 4.31: **Sample changer system.** 1) The crane is lowered down through the sample changer cylinder and the cylinder is fixed to the crane with clamps. 2) The cylinder is lifted to the top of the sample environment. 3) The crane is lowered and fixed to the sample stick. 4) The sample stick is lifted so that the sample is within the shielding (dark) and everything is moved to a storage space near the instrument.

#### 4.4.6.1 Activation

The incoming flux on the sample is up to  $2 * 10^{10}$  n/s/cm<sup>2</sup>, 30 times higher than the  $6.5 * 10^8$  n/s/cm<sup>2</sup> maximal flux of IN8, ILL[54, 71]. Hence activation of sample and sample surroundings becomes an important issue. The instrument will be shielded from the surroundings, so the main issue is sample changes. Large sample surroundings like magnets will be restricted not to include any isotopes that can get activated into radioactive isotopes with long lifetimes close to the scattering plane. Short lifetimes are less critical. If isotopes with half times below 15 minutes are produced in the sample surroundings it is possible to wait for them to cool down. After 75 minutes the radiation level in a material with 15 minutes halftime will be at the level seen in an experiment on IN8. It is thus possible to use many materials including Al in the sample surroundings. For samples the same restrictions are not possible and it is thus necessary to design a safe way to remove a sample containing elements with halftimes in the hours to weeks region from the instrument. Ideally ESS will develop a robotic system for sample changes since other instruments will have the same problems. However as a fall back option a sample change tube was designed. This tube works much like systems to move used fuel rods at reactors. A cartoon of a sample change can be seen in figure 4.31. The idea is to move sample and sample stick to a storage facility located close to the instrument where the sample can cool down before the sample is removed and the sample stick reused. It might also be necessary to install shielding on top of magnets and cryostats to allow access during experiments.

#### 4.4.7 Polarisation Analysis

In order to enable polarization analysis a number of different solutions were considered:

- **Heussler Crystals.** Since the instrument does not use a monochromator and the attenuation in the useful Heussler Crystals is considerably larger than PG, Heussler will not be ideal. It could however be used as a permanent last analyser or on the side of the sample where no analysers are yet planned. Both solutions will be very expensive and make polarization analysis more than an order of magnitude slower than the standard setting.
- **$^3\text{He}$  Cell.** Although this would allow the user to record data with the entire instrument a  $^3\text{He}$  cell cannot be combined with high magnetic fields, which is foreseen to be a primary use of the instrument. It also works only for a limited wavelength range, reducing the dynamic range of CAMEA considerably.
- **Proton crystals.** A new solution in development is organic crystals where a desired polarization is transferred to hydrogen protons by the spin orbit coupling[58, 66]. The hydrogen will scatter one polarization isotropically while letting the opposite polarization pass through. The solution will work on a broader wavelength range than super mirrors and be completely independent on angles. The polarization of the crystals will have a lifetime of about a week and be insensitive to the stray fields foreseen from the magnet. At present the crystals are too small for CAMEA. However, if the technology improves before the actual construction time it will be an ideal solution for the incoming polarization where the largest wavelength band is needed. For the secondary instrument the required crystal area will probably be too large to be polarizable in realistic times.
- **Polarized super mirrors.** This solution will occupy some space both before and after the sample and also limit the dynamic range, however it can work with magnetic fields and with the full instrument. (The exact configuration of the mirrors is left for the final design study but this is the proposed overall solution.)

Though no final design of the polarization is available PSI have previously done a study of polarizing super mirror benders.

#### 4.4.8 Collimation and Slits

In order to reduce the background, collimation and slits are required, especially on an instrument designed for extreme environments. In the vertical direction, slits will be used to minimize the visible sample environments both seen from guide and analysers. The same will be the case for the horizontal incoming beam. However, for the secondary spectrometer it is not possible to use slits due to the large angular coverage, and a radial collimator will be required.

Figure 4.32 shows simulations of the transparency of radial collimators. The

transparency is defined as the intensity at the analyser position (1.5 m from the sample) with collimator divided with the intensity without collimator. The simulations are done for collimators starting at different distances from the sample and having different lengths of collimator blades. All collimators are required to remove signal originating from more than 50 mm away from the center of a sample with a radius of 15 mm. The data shows that, the collimator should start close to the sample, 20 cm, and have very long blades. However, a sample space of 45 cm is reserved for sample surroundings and the instrument would be too expensive if it starts too long from the sample. A collimator with an inner radius of 50 cm and blade length of 40 cm is thus the best achievable option, corresponding to a transmission of 62%. It could be considered to make a second narrower radial collimator for smaller sample environments. The transmission is not the final FoM for a collimator. For a radial collimator the FoM should be the relative change in signal to noise of the instrument when a collimator is inserted. In order to calculate such numbers specific knowledge of both layout and scattering strength of the background producing sample environments are required as well as knowledge of the sample. Although these numbers do not exist simulations with some generic environments showed a decrease in signal to noise for the longest collimator lengths. The maximal signal to noise was, however, not achievable within the constraints of the instrument. Once more knowledge of the ESS sample environments exists the radial collimator should be redesigned.

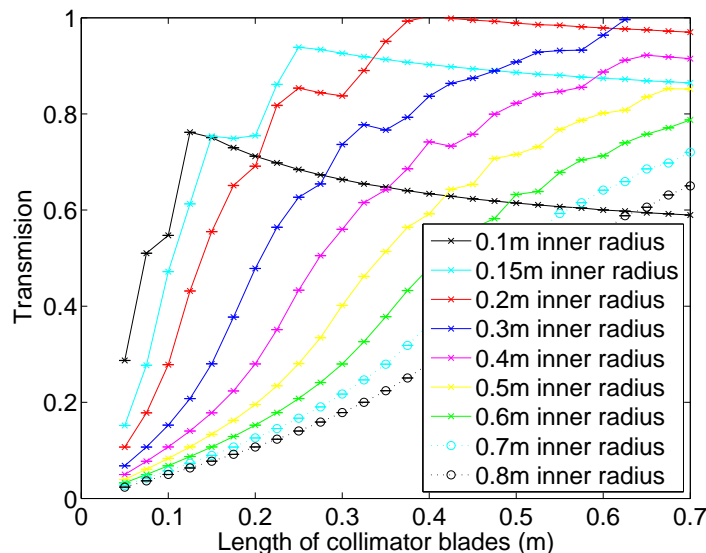


Figure 4.32: *Collimator transmission.* Simulations of the Intensity from a 15 mm sample with a radial collimator divided with the intensity without a collimator. The simulations are done for a number different collimators designed to remove signal more than 50 mm from the center of the sample.

#### 4.4.9 High Energy Filter

If no  $E_f$  values above 5 meV are required, a Be filter will be inserted after the sample. The Be filter have a higher transmission than the order sorting chopper and will thus increase the intensity in the  $E_f < 5.2$  meV channels. The filter will have to be combined with or placed before a radial collimator to remove the neutrons scattered by the filter. Since the collimator needs to be relatively close to the sample it is foreseen to have a collimator with filter inserted and one without. The two can be placed on a wheel and rotated around the sample so either collimator or collimator including filter is in position between sample and analysers, while the other is on the backside of the instrument.

#### 4.4.10 Analysers

The analyser-detector geometry is central to the CAMEA idea and needed careful studies. A number of different choices needs to be made, like material, geometry, number of analysers, and energies. Many parameters are correlated making it hard to describe the choices in a logic way.

##### 4.4.10.1 Analyser Material

Several materials were considered for the analysers: PG, Si, and Ge. A traditional advantage of Si and Ge is that they do not have second order reflections. This means that a Be filter is not needed and, since the filter have a transmission of about 90%, a slightly increased count rate. However, since the order sorting chopper is best combined with second order reflections this will at the same time limit the dynamic range of the instrument. 3rd order reflections from the analyser could be used, however, these cannot be connected with first order reflections unless very low  $\alpha$  angles are chosen. Such angles would have a low transmission and a very coarse energy resolution. Furthermore the low scattering angles would increase the diameter of the detector tank and the cost of detectors and vacuum tank considerably.

PG does have problems with low energy phonons creating energy tails in the measurement, a problem more significant than in other materials. However many successful spectrometers work with the PG tails.[91, 68, 96, 71, 46]

Table 4.3 shows some parameters for the 3 materials. Attenuation and scattering is solely calculated from the relevant cross-sections and does not thus not include thermal diffuse scattering. The actual attenuation will thus be higher than the listed values. However, already from the listed values it is clear that Ge have too high attenuation factors to be suitable if 10 analysers behind each other is desired. In order to get a high peak reflectivity for Si it is necessary to produce analysers that are about 2 cm thick. This means that the attenuation becomes considerable and even though it is possible to construct a setup with several analysers behind each other the total number would be lower than for PG. Furthermore, Si will still have a limited peak reflectivity of roughly half the value of PG. The increased attenuation and reduced reflectivity compared to PG would reduce the count rate in each channel while the lower number of feasible

Material	Attenuation through 1 blade at 45° (%)	Reflectivity (%)	Thickness (mm)
PG	0.01	~80	1.0
Si	5.34	~40	20.0
Ge	17.5	~40	6.0

Table 4.3: **Analysers materials.** Attenuation calculated from data from [55] at 0 K. At room temperature 2 mm PG has been measured to have an attenuation of 2% at 5 meV. Above this energy, the attenuation increases strongly.

analysers would reduce the mapping capabilities. Together this meant that PG was chosen as the most promising analyser material.

#### 4.4.10.2 Analyser Geometry

Initially it was considered whether to bend the analyser crystals so that they would be focusing, both in the energy direction (vertical) and a4 direction (horizontal).

CAMEA will reflect neutrons out of the plane. This means that the analysers relies on a well-defined  $\mathbf{q}_z$  component to determine  $E_f$ . By using vertical focusing analysers it is possible to correct for the distribution of  $\mathbf{q}_z$  and thus get a finer  $E_f$  resolution. Furthermore it is possible to increase the count rate as the crystals will keep the correct angle to the scattered beam. The drawback of vertical focusing is the loss of any information about the scattering dependence on  $\mathbf{q}_z$ , however since CAMEA is designed as an inplane spectrometer this is acceptable. It was thus decided to make CAMEA vertically focusing.

The advantage of bending the analysers horizontally would be smaller dark angles. Dark angles are discussed in section 4.4.13 and have two main components. The reflected beams from the analysers, continue expanding when reflected by a flat analyser and will cross into neighbouring wedges or be absorbed by shielding. Furthermore analyser mounting, shielding, and detector electronics can cause dark angles. Since the reflected neutrons from a horizontally focusing analyser are focused into the available detector space the first contribution would disappear. The analyser mountings would still produce dark angles.

Horizontally focusing the beam on a smaller detector would, however, produce a coarser a4 resolution. This problem would be largest for low  $E_f$  values where the reflect signal is focused on a smaller detector due to the higher reflection angle. At  $E_f = 2.5$  meV  $\delta a_4$  would be doubled, compared to a flat analyser. Double focusing analysers would, also, demand a more complicated analyser mounting. The double focusing analyser could either be produced by bending perfect single crystals of Si or placing small pieces of flat analyser on a machined mounting. The bend Si would reduce the reflectivity and increase the beam attenuation in each analyser, more than countering the gain by the reduced dark angles. In order to keep the analysers bend the holders would need to be more massive and have some supporting beams above and below the scattering plane. This could potentially increase both background and distance between analysers. If

Analyser Nr	1	2	3	4	5	6	7	8	9	10
Energy (meV)	2.5	2.8	3.1	3.5	4.0	4.5	5.0	5.5	6.5	8.0
$\eta = 30'$	5.2°	5.7°	6.1°	6.5°	7.0°	7.3°	7.6°	8.0°	8.4°	9.0°
$\eta = 60'$	7.3°	8.0°	8.6°	9.2°	10.0°	10.3°	10.8°	11.2°	11.9°	12.7°
$\eta = 90'$	9.0°	9.9°	10.5°	11.3°	12.0°	12.7°	13.2°	13.7°	14.5°	15.6°

Table 4.4: **Limits on the coverage of each analyser.** The table shows the maximum angle (in degrees) a flat analyser of a given mosaicity can cover horizontally before the reflectivity drops by 10% for different analyser mosaicities.

small PG analyser crystals mounted in a holder was chosen, the holder would introduce some extra scattering and increase the attenuation compared to the 1 mm thick flat Si holders for the flat crystals.

The flat analyser solution promised the highest count rates and lowest background, combined with the simplest mounting. This outweighed the reduced  $a4$  coverage so it was decided to use flat analyser crystals arranged in a Rowland geometry in the energy direction while remaining flat in the horizontal plane.

The flat analysers means that the analysers will not be completely orthogonal to the scattered beam in the horizontal plane but will have an incident angle of several degrees, changing the reflected energy, reflectivity, and getting slightly out of the Rowland geometry. If the  $x$ -axis points from the sample towards the center of an analyser and  $z$  is vertical, a neutron reflected in the plane from the sample with an angle  $\Delta a4$  to the  $x$  axis will have the flight direction  $(\cos(\Delta a4), \sin(\Delta a4), 0)$ . An analyser with an angle of  $a5$  to the horizontal plane will have a normal vector  $(\cos(a5 + \pi/2), 0, \sin(a5 + \pi/2))$ . The effective angle between scattering angle ( $2 * a5'$ ) can now be described by:

$$\sin(a5') = -\cos(a5' + \pi/2) = -\begin{pmatrix} \cos \Delta a4 \\ \sin \Delta a4 \\ 0 \end{pmatrix} \cdot \begin{pmatrix} \cos(a5 + \pi/2) \\ 0 \\ \sin(a5 + \pi/2) \end{pmatrix} \quad (4.6)$$

$$= \cos(\Delta a4) \sin(a5) \quad (4.7)$$

Table 4.4 shows the maximal angular coverage of flat analyser slab if the peak reflectivity is required to stay above 90% of the maximum value. The coverage is in general good enough for meaningful modular pieces. Although the change in  $E_f$  is measurable, the continuous  $E_i$  coverage means that it is still possible to make a constant  $\hbar\omega$  map out of the data. CAMEA will record a huge number of slightly different resolutions and intensities that will need automated refinement so a small change in  $E_f$  is of little concern refinement wise.

Considering the validity of the Rowland geometry, a McStas simulation was performed. See figure 4.33. The results shows that a flat analyser slab with a coverage of up to 10 degrees is feasible at  $E_f = 5$  meV, a sample to analyser distance ( $d_{sa}$ ) of 1.5 m, and an analyser to detector distance ( $d_{ad}$ ) of 1.0 m.

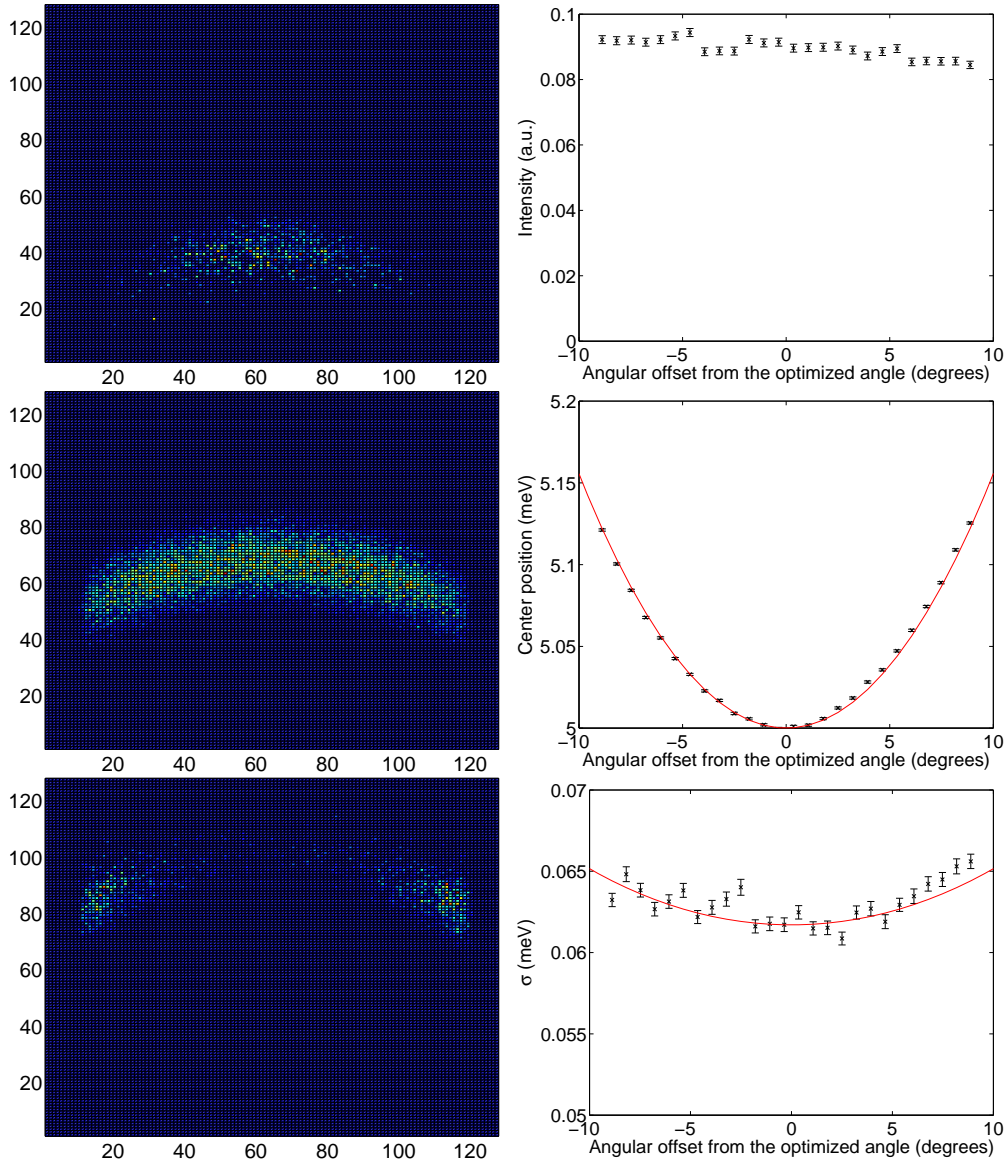


Figure 4.33: **Angular coverage of analyser.** *McStas* simulations of the reflected signal from an analyser set at  $E_f = 5$  meV. A scan was performed using a narrow  $E_i$  band.  $d_{sa} = 1.5$  m,  $d_{ad} = 1.0$  m, and analyser width = 2.5 cm. Left: PSD view of the reflected signal with energies  $4.775\text{meV} < E_f < 4.825\text{meV}$  (top),  $4.975\text{meV} < E_f < 5.025\text{meV}$  (middle), and  $5.275\text{meV} < E_f < 5.325\text{meV}$  (bottom). Right: The Intensity (top), Measured Energy (middle), and Energy resolution (bottom) as a function of angular offset. The small change in resolution is consistent with the change in measured energy. The red lines indicate the theoretical development as seen from (4.7).

#### 4.4.10.3 Reflection Direction

Several different ways of reflecting neutrons out of the plane were considered. All analysers could reflect upwards or downwards. Additionally more complicated

geometries were investigated: Every second analyser arch could reflect upwards and every second downwards. Every second analyser wedge could reflect upwards and every second downwards. Finally a single backscattering analyser behind the others could reflect in a different direction than the rest.

If upwards reflections were chosen this would either limit the lowest possible energy, the size of sample environments, or force the analysers further away from the sample, increasing the price with several million euros. It was thus decided that at least all analysers in the first arc should reflect downwards, ruling out two of the above solutions. A setup with every second arc reflecting upwards was tested. However this forced the gaps between the analysers to be bigger and increased the instrument size and complexity for a limited gain in detector shielding. Finally, the idea of a single backscattering analyser behind the other analysers reflecting upwards proved too expensive and complicated construction wise for the limited gain of such an analyser. The conclusion was thus that if A6 angles above  $90^\circ$  are desired, scattering down to detectors below the analysers are preferable. This does demand considerable space below the scattering plane, and since the beam height and green field liberties of ESS allow such a geometry it was chosen.

#### 4.4.10.4 Rotating Analysers

During the early design process some thought were given to how the instrument would cover  $(q, \omega)$  space and the most advantageous scan possibilities. At this point 7 analyser arcs were envisioned.

At a given energy transfer the 7 analyser arcs will draw 7 rings in reciprocal space. In order to map out substantial parts of reciprocal space inside the scattering plane it is necessary to perform a scan of some parameter. The most obvious scan parameters are A3 and  $E_f$ . Figure 4.34 displays examples of such scans. It was considered if it should be possible to control A5 and A6 of each analyser so that the  $n$ 'th analyser could scan  $E_f$  from  $E_{n,0}$  to  $E_{n+1,0}$ . The advantage of such a setup is that it leads to a much more smooth coverage of reciprocal space since the scan point at a given energy transfer will correspond to rings in reciprocal space and touch each other in one point and thus never crosses, whereas the alternative A3 scan corresponds to rotating rings, that will cross each other. Although the  $E_f$  scan mode has clear merits it does introduce a lot of extra complication to the instrument and it was thus omitted.

#### 4.4.10.5 Vertical Opening

Many sample environments such as strong split coil magnets have a limited vertical opening angle of down to  $\pm 2^\circ$  [1, 2]. We opted to match the vertical coverage of the frontmost analysers to this value and reduce the vertical coverage of each analyser thereafter to cover the same vertical momentum transfer range ( $\Delta k_z$ ). This means that no normalisation is needed in the outgoing direction when only first order reflections from the analysers are considered. Since the actual width in  $k_z$  of a signal may not be known it is advantageous to minimize the effect of such an uncertainty. The incoming  $k_z$  resolution will depend on

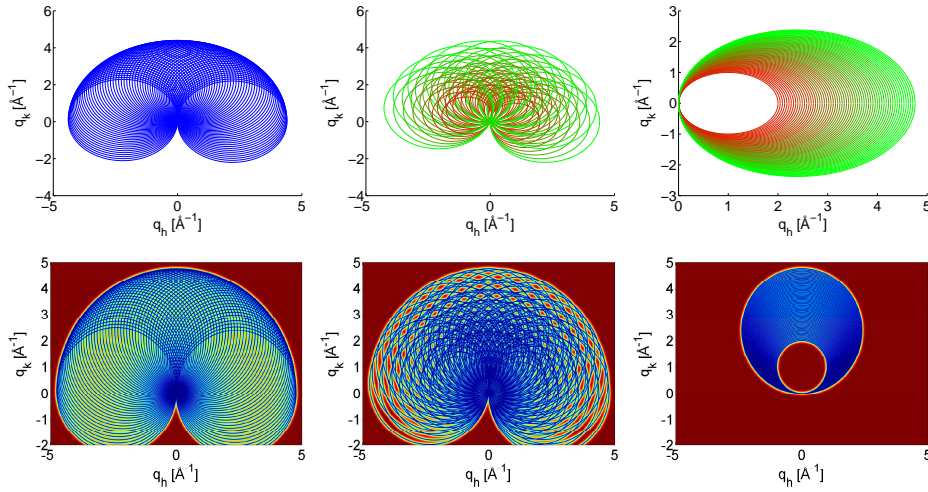


Figure 4.34: **Coverage illustrations** Idealised coverage of an ESS CAMEA module at different energy transfers ( $\hbar\omega$ ). First row illustrates the signal at  $\hbar\omega = 0$ . Left shows a flat-cone-like instrument with a single analyser arc performing a sample rotation scan in 70 steps while the middle shows the same scan performed by a CAMEA system with 7 analysers but only in 10 steps. Finally the same 7 analysers scan  $E_f$  and keeps the sample still. As it can be seen the homogeneity is best for the  $E_f$  scan and worst for the CAMEA A3 scan. To further investigate this, a calculation of the distance to the closest measured point was done for all 3 setups the distance is plotted on an equal color scale for all 3 setups. The results are displayed in the second row, again confirming that  $E_f$  scans are preferable. Dark angles and blank region at small and large  $a_4$  are not included.

energy but in a limited way since the transmitted divergence decreases with increased  $E_i$ . If normalization is critical this can be done by rotating the sample so different analysers cover the same point in  $(q, \omega)$  space.

#### 4.4.10.6 Distance between Analysers

As the necessary area of PG to cover a given solid angle increases with  $d_{sa}^2$ , it is a priority to keep the analysers close together in order to reduce the cost. However, if the analysers are placed too close together it will increase the background and risk of spurious signals from crosstalk. Experience from RITA-II shows that it is a clear advantage if each detector can only "see" the analyser that is meant to reflect neutrons towards it. Hence this was chosen as a boundary for how close the analysers could be spaced (see figure 4.35 Left).

It is possible to insert a rough radial collimation in the vertical direction in order to move the analysers slightly closer together (figure 4.35 Right) but it will only reduce the average distance 10% and it will reduce the flux, introduce an asymmetry to scattering slightly above and below the scattering plane, and make maintenance more complicated. It was thus decided not to use this collimator.

Table 4.5 shows the distances between the analysers for the proposed CAMEA as well as the total graphite area from each analyser, assuming a total active

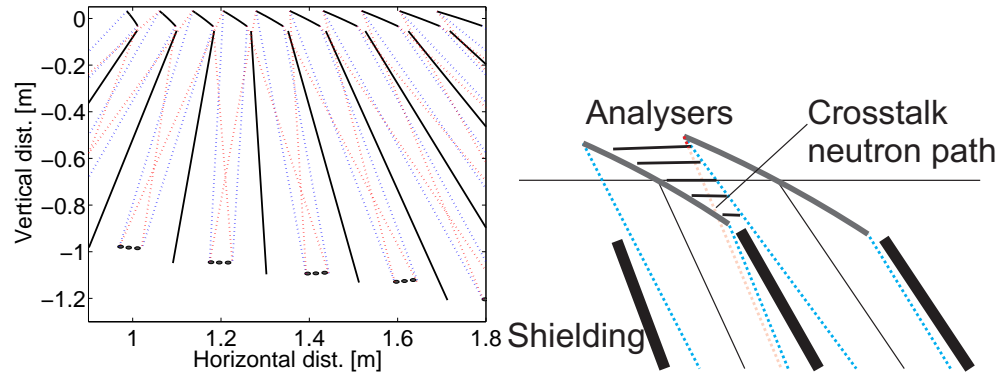


Figure 4.35: **Crosstalk.** Left: The analysers are shown in the top (black arcs), shielding is illustrated with black lines and detectors black circles in the bottom. In order to minimize background any line from the  $n$ 'th detector to any other analyser other than the  $n$ 'th should be blocked (red lines) while any line from the  $n$ 'th analyser to  $n$ 'th detector should be undisturbed (blue lines). Right: A coarse vertical radial collimator between the analysers can eliminate crosstalk that can not be removed by the shielding below the analysers. This enables a denser analyser arrangement.

Analyser Nr	1	2	3	4	5	6	7	8	9	10
Energy (meV)	2.5	2.8	3.1	3.5	4.0	4.5	5.0	5.5	6.5	8.0
Distance from previous analyser (cm)	-	6.2	6.7	7.3	7.8	8.5	9.3	10.5	11	12
Distance from sample (m)	1.0	1.08	1.16	1.23	1.31	1.39	1.47	1.56	1.65	1.74
Area (cm <sup>2</sup> )	413	534	627	736	820	873	898	921	929	907

Table 4.5: *Position and area of the analysers.*

angle of  $90^\circ$  in the horizontal plane.

#### 4.4.10.7 Number of Analysers

From section 4.2.1 it is known, that it is possible to fit 60 analysers into the secondary spectrometer however, each new analyser will have a larger area and thus the cost will increase. Furthermore the beam will be attenuated in each previous analyser. Figure 4.36 (left) displays the total amount of graphite needed to intersect a given neutron flux (disregarding reflected energy bands). This is found as  $d_{sa}^2/0.982^{n-1}$ , where  $0.982^{n-1}$  is the transmission through the previous graphite pieces found in section 4.2.1, and  $d_{sa,n}$  can be approximated by  $d_{sa,n-1} * 1.05$ . Note that the actual distance between the analysers and their attenuation of the beam will vary with the reflected energies of the analysers. Furthermore the necessary solid angle to cover and the resolution functions will also vary with reflected energy. The detector cost and cost of vacuum tank and shielding also

changes in a non-trivial way with number of analysers. This is thus not an exact calculation of how much an extra analyser of higher energy than the previous will cost. It is rather an approximation of the cost in graphite of including an analyser more in the middle of the energy range and pushing all following analysers backwards.

Although the 10'th analyser is  $\sim 3$  times less efficient than the 1st in that it

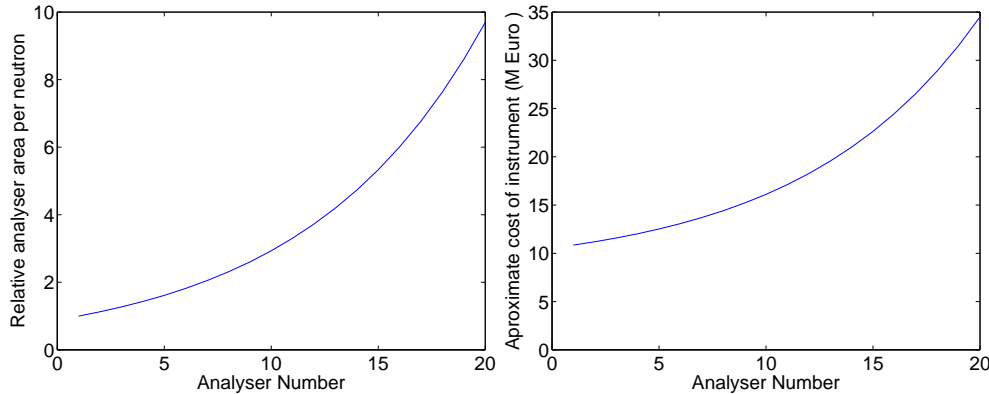


Figure 4.36: *Number of analysers.* Left: Area of analyser needed to cover a given solid angle at the position of the different analysers divided with the transmission of the beam to the given analyser position. Right: Approximate cost of instrument with a given number of analysers.

takes 3 times more graphite to intersect the same solid angle the full price of the instrument does not scale as strongly with number of analysers. Figure 4.36 (right) approximates the full cost of the instrument as function of the number of analysers. Here the price of the secondary spectrometer, after the radial collimator is chosen to scale with the analyser cost and the remaining costs are constant. Prices are taken from [110]. The prices are divided with the flux at the analyser position to account for the attenuation in the analysers so the performance in this model is directly proportional to the number of analysers. It was decided to use 10 analysers for CAMEA.

#### 4.4.10.8 $E_f$ Values

There are several different considerations when choosing the  $E_f$  values of the analysers:

- **Spacing:** As we saw in section 4.2.1, the minimal distance between two energies changes with energy. It is still possible to make the 9 steps of equal size required for 10 analysers, if mosaicity and energy range is chosen correctly. This could be relevant if only a single incoming energy was recorded in one setting and a scan of  $E_i$  was needed to make a dense coverage. However, with continuous incoming energy coverage, there will be no gaps in the energy coverage anyway. The distance between the different  $E_f$  values will instead decide the density of measured points at different energy transfers. Since low energies have a finer resolution, they

will produce less statistics if equal  $E_f$  steps are chosen. It is thus worth concentrating the analyser energies at low  $E_f$  values to get more equal statistics at different energy transfers.

- **Spread:** Choosing a non-equal energy spacing it was shown in section 4.2.1 that 30-60 analysers can be fitted inside a meaningful energy band, depending on mosaicity and overlap. With only 10 analysers available a choice between density and coverage has to be made. In general CAMEA seeks to maximise density and get as good coverage as that allows. However since CAMEA will have an order sorting chopper and large gaps in the coverage is suboptimal it is necessary to have the coverage going from the energy of the first analyser ( $E_1$ ) to almost the second order energy of the first analyser ( $4E_1$ ).
- **Band position :** A low  $E_1$  will mean a more dense coverage and more analysers, that are usable with the Be filter. However, it will also reduce the dynamic range and decreasing  $E_1$  also result in increasing dark angles and less space for sample environments/shielding because of the higher A6 angle. The limit of acceptable consequences was found to be at  $E_1 \approx 2.5$  meV.
- **Number of energies below the filter :** Since the energy of the analysers are fixed, a number of analysers and detectors will not produce a useful signal when the Be-filter is inserted. This number should be kept as low as possible while not producing gaps in the coverage. In order to obtain this, the individual spacing was adjusted slightly to push an extra energy below the Be-edge. Because of Be-filters, 5 meV is one of the most popular  $E_f$  values in TAS measurements and having that specific energy will also be useful for comparison with other experiments.
- **Flight time:** In order for the order sorting chopper to work optimally it is advantageous if the difference in flight time between first and second order neutrons remains constant for all analysers. This can be achieved by adjusting the energies and/or distances.

The chosen values will be described in section 4.5.

#### 4.4.10.9 Mosaicity and Distance Collimation

In many TAS instruments mosaicity is used to produce the desired energy resolution[121]. Coarser mosaicity means coarser resolution and reduced graphite cost (see figure 4.37), and vice versa. In order to find the right compromise simulations were performed of different analyser mosaicities and detector sizes. The results can be seen in figure 4.38.

The results suggest that for small detectors the resolution becomes independent of the mosaicity while the intensity even increases with coarser mosaicity. The latter is, however, misleading. The McStas model does not take the reduced peak reflectivity of the coarser graphite into account, since this depends

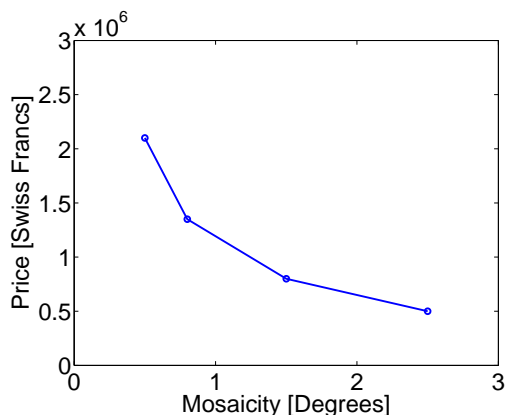


Figure 4.37: **Graphite price.** Example of prices of PG from Panasonic for an entire instrument. Figure from [80].

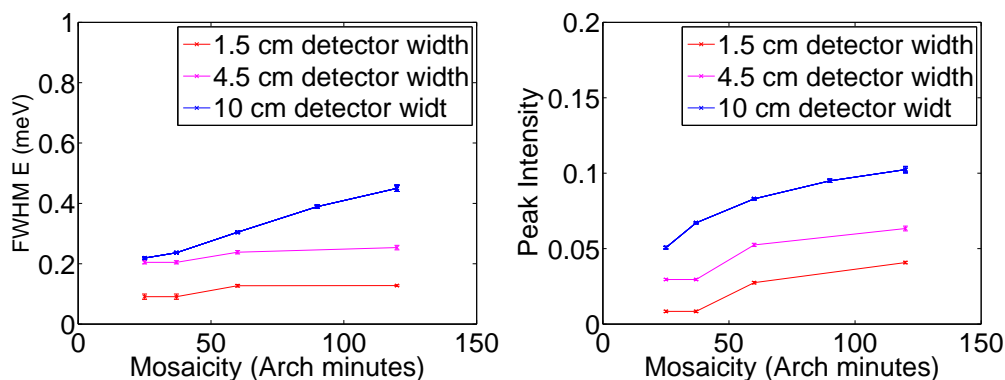


Figure 4.38: **Mosaicity dependence of  $\delta E_f$  and intensity.** McStas simulations performed for a setup with: 5 analyser crystals in a Rowland geometry in the energy direction,  $E_f = 5$  meV,  $d_{sa} = 1.2$  m,  $d_{ad} = 1.0$  m, and a sample height of 1.0 cm. Left: The resolution. Right: The integrated intensity

on mosaicity, analyser thickness, and manufacturer. If this is corrected, the intensity is almost independent of mosaicity, depending on the chosen values for peak reflectivity. The lack of dependence on mosaicity was first met with some scepticism in the CAMEA team. However the reason is simply that distance collimation dominates the mosaicity resolution.

Distance collimation is the limit on possible divergences imposed by geometric restrictions. This is not a new phenomenon and have been used to achieve well collimated beams in other instruments[38, 82, 105]. Here we look at the special case, where the geometrical restrictions limits the possible reflection angles for paths from the sample via the analyser to the detector and due to the small samples, long distances and small detectors this becomes better than the limits on these reflection angles imposed by the mosaicity. At first there was some confusion about whether it was a disadvantage not to match the contributions to the resolution from mosaicity and distance collimation. This is not the case:

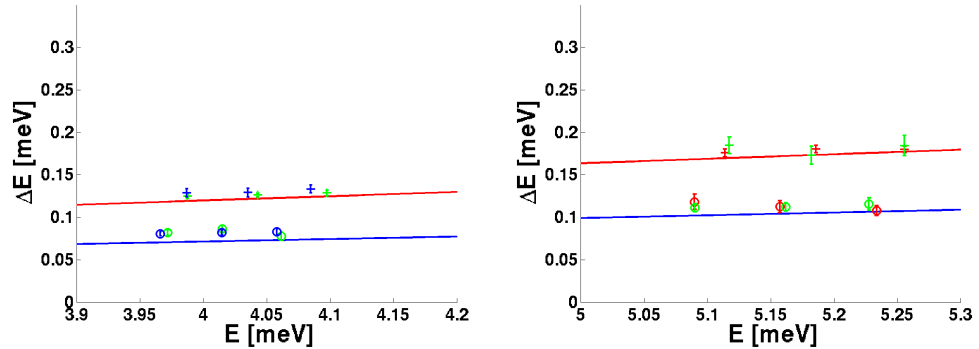


Figure 4.39: *Mosaicity dependence measurements.* The lines indicate analytical calculations of the energy resolution when the prototype runs in a 14 Hz (red) and 50 Hz (blue) setting. Prototype measurements were taken at both 14 Hz (Bars) and 50 Hz (circles) with analyser mosaicities of  $0.65^\circ$  (green) and  $1^\circ$  (blue) and  $1.3^\circ$  (red). Figure produced by Marton Marko.

Matching resolutions should be sought if two contributions to the final resolution are independent, *e.g.* the primary and secondary resolution of a spectrometer. In this case, however, the restrictions on the possible beam paths are strongly correlated with the paths that are dampened by the mosaicity and the resolutions are thus not added in quadrature (See figure 4.40). When one dominates the other the resolution becomes the minimum rather than the maximum as it is the case for independent resolution contributions. The mosaicity independent energy resolution was later confirmed with analytical calculations by Marton Marko and by prototype results (see figure 4.39).

It should be noted that distance collimation makes the resolution dependent on

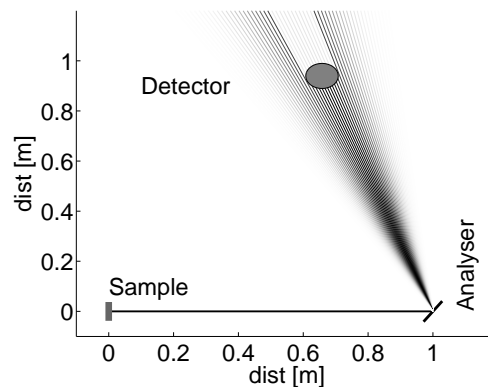


Figure 4.40: *Correlated resolutions.* The intensity of the reflected beams are indicated by the greyscale. Black most intense, white least intense. The reflected neutrons away from the central reflected energy are both suppressed by the mosaicity and by distance collimation.

the sample height. However, for the small samples CAMEA is designed for, the

distance collimation is limited by the detector width and not the sample height so the dependence will be weak (see figure 4.46). Furthermore, distance collimation does also contribute to the resolution for most existing analyser spectrometers. The angular resolution will decrease with coarser mosaicity. However the angu-

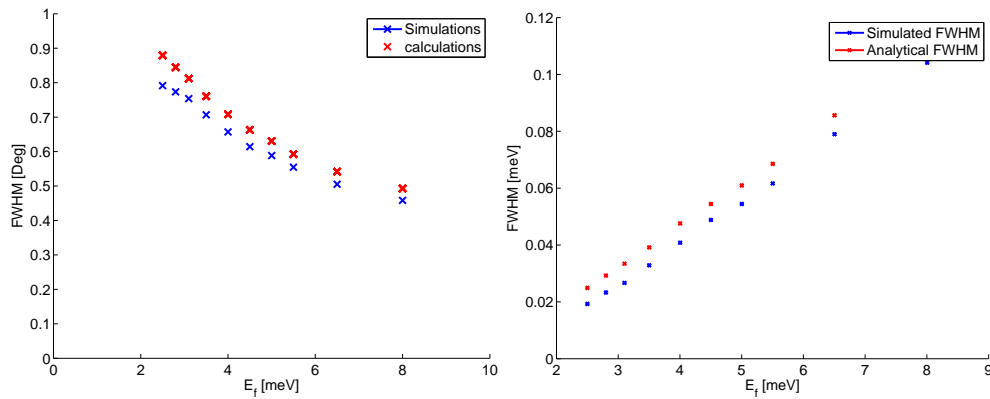


Figure 4.41: **Resolutions.** Simulated (Blue) and calculated (Red) angular resolutions (left) and energy resolution (right) of the CAMEA backend. The energy resolution of the 3 frontmost analysers can be improved further by changing the binning of the detectors (see 4.4.11.3).

lar resolution are going to be better than acceptable (see figure 4.41) and better than the default incoming resolution.

#### 4.4.10.10 Prismatic Analysers

While testing the mosaicities and understanding the results in the frame of distance collimation I got the idea that the unmatched resolutions could actually be an asset. This led to the development of the prismatic analyser. A thorough description of the ideas can be found in the attached article. Here I will just give a short overview.

When distance collimation dominates the energy resolution, a broader energy spectrum is reflected than the recorded spectrum. The remaining spectrum simply misses the detector due to the Bragg law. If extra detectors are placed next to the main detector they will record these neutrons. In this way the same flux will be recorded as with one big detector but the energy resolution will be improved thanks to the distance collimation. Experimental proof of the idea is displayed in figure 4.42.

In practice it is not reasonable to install detectors recording the very tail of the reflected signal due to the difference in flux, and thus statistics, in detectors placed in the center and tails of the reflected beam. The amount of detectors that have acceptable statistics can be increased by using coarser graphite (see figure 4.43).

Typical gain factors achieved with this method would be in the order 2 in finer resolution and 1.5-2 in total recorded flux, corresponding to a total gain factor in the order 3-4. For CAMEA 60' mosaicity and 3 detectors per analyser were

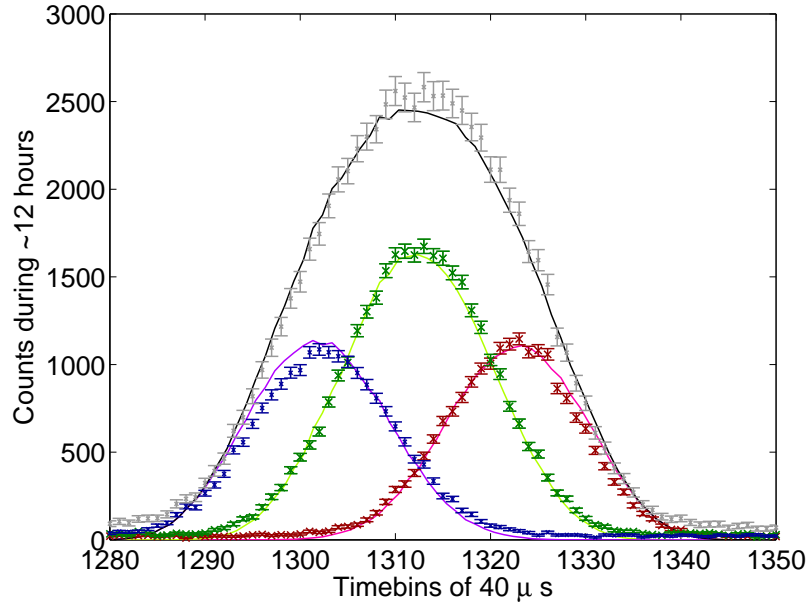


Figure 4.42: *Prismatic analysers.* Simulated (lines) and prototype (crosses) data of three 0.5 inch  $^3\text{He}$  tube detectors recording data from 5 analysers arranged in a Rowland geometry on the prototype. Data are taken on a 2.3 cm high  $V$ -sample and kept in original time bins. The simulated data have been rescaled with a common intensity renormalisation factor. The grey line represents a sum of the 3 signals and represent what would be seen in a traditional setup with a single detector.

chosen, corresponding to halving  $\delta E_f$  and increasing the total count rate a factor 1.5 compared to a more traditional analyser with 30' mosaicity reflecting neutrons to a detector width a width of 1.5 inch.

#### 4.4.10.11 Analyser Dimensions

Most PG analysers are 2 mm thick. The reflectivity of graphite as a function of thickness can be described by Darwin equations. In order to investigate the effect of a reduced thickness a simple Monte Carlo simulation of the equations was performed. The simulated neutrons were traced through a number of thin layers in a graphite crystal. For each layer it was randomly determined if the neutron should be absorbed, reflected, or pass unhindered. By simulating a large number of neutrons and recording the number of neutrons that exited the crystal on the reflected side it was possible to estimate the reflectivity of the crystal. The model was adjusted to fit a number of reflectivities obtained from literature[104]. Figure 4.44 shows the results of the simulations. The simulations does not take the different manufacturing processes of graphite into account and can only be used as a rough estimate of the actual reflectivity.

At 2 mm the reflectivity have reached attenuation for cold neutrons. Reducing the thickness to 1 mm will produce a small reflectivity decrease but half the

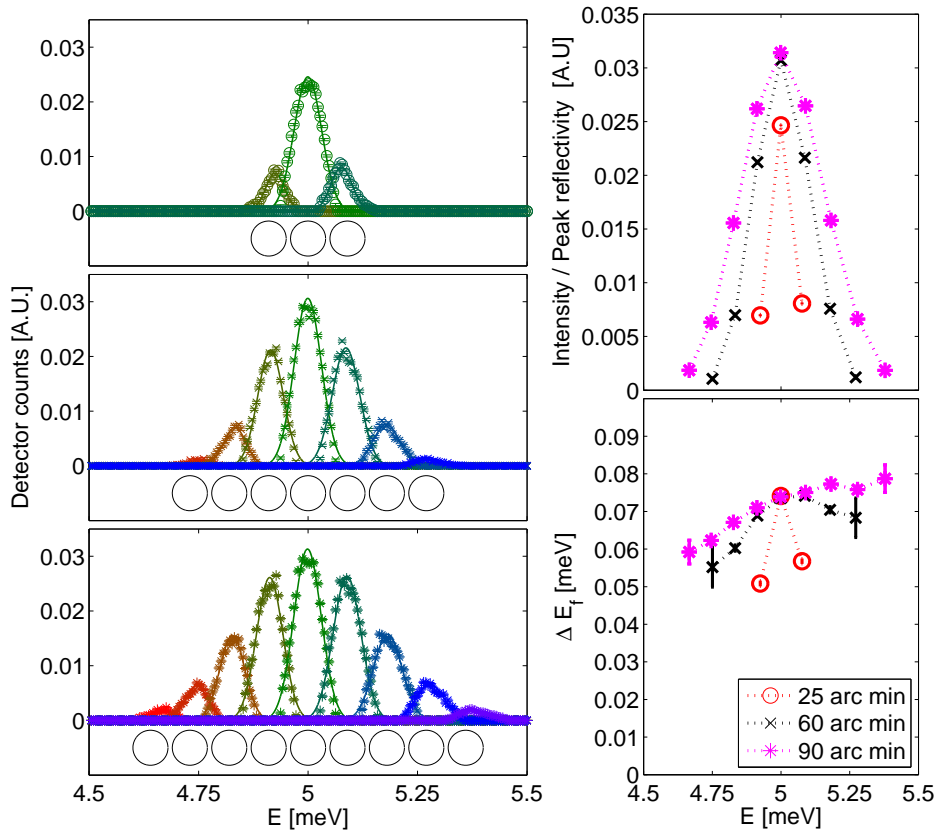


Figure 4.43: *Simulated recordings of several energies from a single analyser illuminated with a white beam.* Each peak in the left column represents the counts in a single detector tube as function of  $E_i$  (The detector tubes are represented by circles below the data). The mosaicity of the analyser is 25' (top), 60' (middle), and 90' (bottom). The top right panel shows the corresponding intensities before correcting for peak reflectivity and bottom right panel displays the energy resolution (FWHM) of the detectors for the three different mosaicity values.

graphite cost. For most instruments the cost of graphite is a small contribution to the final cost and there are only small disadvantages of increasing the thickness. For CAMEA the amount of graphite is relatively large and the increased attenuation through 2 mm graphite counters the slightly improved reflectivity. Furthermore 2 mm will produce more background than 1 mm. It was thus decided to go with 1 mm graphite.

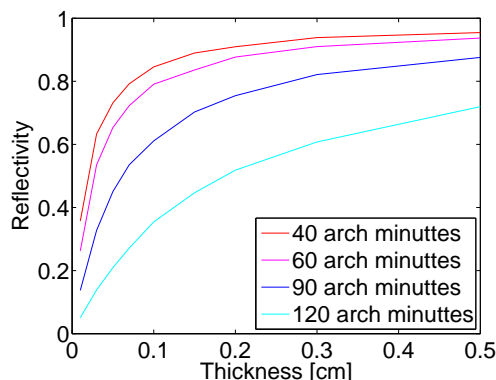


Figure 4.44: *Approximate analyser reflectivity.* The results are found by Monte Carlo simulations.

#### 4.4.10.12 Cooling the Analysers

As mentioned in 4.4.10.1 an energy scan with a PG analyser produce Lorentzian tails on the Gaussian resolution function, causing an increased background close to the elastic line. The reason for these tails is currently debated. However work at ISIS suggest that they are an effect of phonons and can be reduced in a backscattering setting if the PG is cooled[50, 125, 126]. Experiments on the CAMEA PG, however, suggested that the tails were independent of cooling at the (a5,a6) values used in CAMEA. An investigation of the effect of cooling was thus undertaken by Jacob Larsen but was inconclusive as to the effect of cooling for the CAMEA settings[88]. Later unpublished experiments by Felix Groitl indicate that cooling does not have the desired effect in the CAMEA setup. As mentioned in 4.3.3 further work is undertaken, but for now it is not envisioned to cool CAMEA.

#### 4.4.11 Detectors

##### 4.4.11.1 Distance to Detectors

It is possible to construct great CAMEA-like mapping instruments with flat analysers of relaxed mosaicity and short analyser to detector distances, like it is done on Flatcone. This produces a coarse energy-resolution. However for mapping purposes this will often be satisfying and both FLEXX[18, 89, 68], HZB and Panda[26, 96], FRM II will get CAMEA-like upgrades with this aim. CAMEA, however, is a standalone instrument designed for high quality spectrometry data

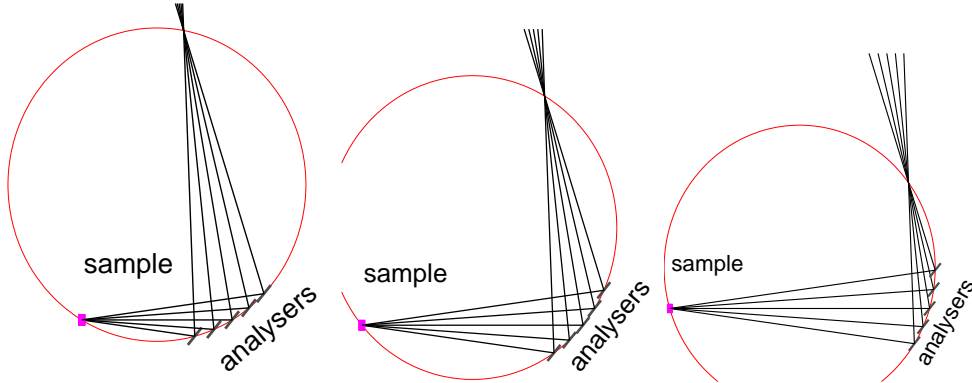


Figure 4.45: **Analyser shadowing.** Rowland geometries with  $E_f = 3.1$  meV and  $d_{sa} < d_{ad}$  (left),  $d_{sa} = d_{ad}$  (middle), and  $d_{sa} > d_{ad}$  (right). Shadowing effect in the Rowland geometry increases with the difference between  $d_{sa}$  and  $d_{ad}$ .

and will need superior energy resolution. In order to achieve this, the piecewise flat analyser is curved and the distance from analysers to detectors are increased. If the Rowland geometry is employed and  $d_{ad}$  is considerably different from  $d_{sa}$ , shadowing problems between analysers increases, reducing the effective covered solid angle considerably (see figure 4.45). Since  $d_{sa}$  is large, especially for the backmost analysers, long detector distances are also required. Larger  $d_{ad}$  also provides considerably better distance collimation (see figure 4.46 left), improving the energy resolution beyond what is possible with a simple Rowland geometry and mosaicity driven energy resolution from PG. This does increase the problems with dark angles from the expanding reflected beam and reduce the angular resolution, due to smearing from mosaicity. It is possible to keep both within a tolerable level by keeping  $d_{ad}$  slightly smaller than  $d_{sa}$ . The exact distances are chosen in a way so that the order sorting chopper works best possible and the dark angles are kept below 1/3 of the a4 range covered by the instrument.

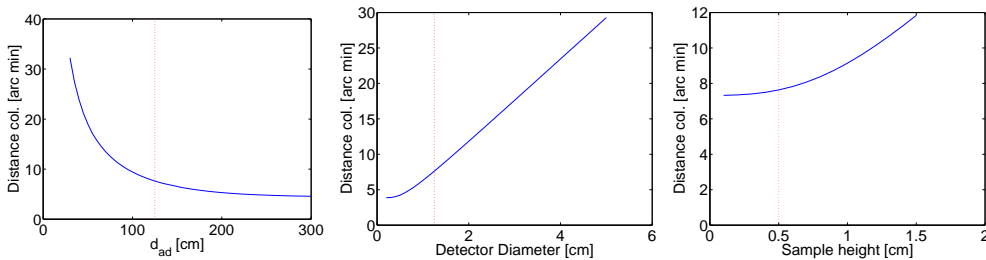


Figure 4.46: **Distance collimation.** Distance collimation (FWHM) for the 5 meV analyser detector setup on CAMEA found by numeric integration as a function of  $d_{ad}$  (left), detector diameter (middle) and sample height (right). The red lines indicate the values chosen/standard for CAMEA. The two first is equivalent as the change in detector solid angle observed from the analyser is the same if  $d_{ad}$  is doubled or the detector radius is halved.

#### 4.4.11.2 Detector Type

In recent years,  $^3\text{He}$  shortage have led to development of new detector types. CAMEA does, however, need a relatively small amount of  $^3\text{He}$  compared to other ESS spectrometers, so  $^3\text{He}$  is still presumed to be viable, and all work so far has been done assuming that  $^3\text{He}$  will be used. New technologies are not ready yet, and it is therefore hard to do real design work let alone prototyping using these. Furthermore the  $^{10}\text{B}$  solid state detectors technology that ESS plans to use for the large detector areas will have a considerable depth that makes the prismatic analyser concept less efficient. Hence at present  $^3\text{He}$  seems to be the best solution.

#### 4.4.11.3 Detector width and Orientation

The width of the proposed 0.5 inch detector tubes are the main contribution to  $\delta E_f$  (see figure 4.46). However, 0.5 inch is the thinnest commercially available detector tubes so if the width should be reduced new tubes should be developed or a 2d PSD system used. Both solutions are too costly, given the 150 detector arrays of CAMEA.

So far we have only considered detector tubes that are positioned tangentially

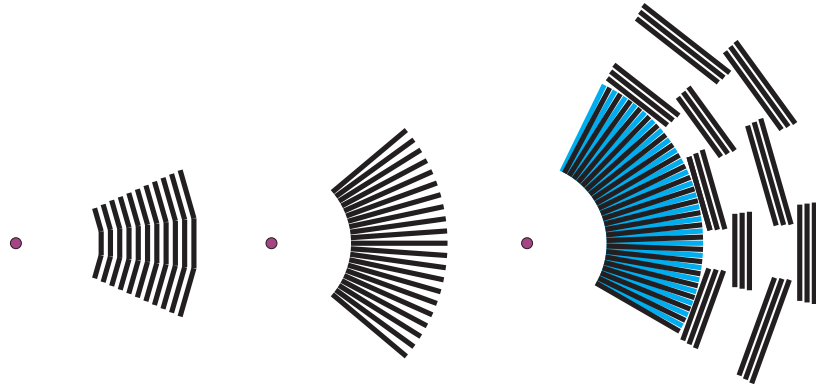


Figure 4.47: **Arrangement of detectors.** Top view of different arrangements of detectors (black lines). Left: Tangential arrangement. Middle: Radial arrangement. Right: The CAMEA detector arrangement. The blue detectors are placed below the black detectors. Not all detectors are shown and the illustrations are not to scale.

with respect to the sample. Another option would be to turn the detectors so that they are radial and making each detector tube look at several analysers (see figure 4.47). This solution improves the finest potential energy resolution while making the angular resolution coarser. However the angular resolution is limited by other factors so the impact from the rotated analysers is limited. This is a beneficial solution for the innermost detectors where the reflected signals are very close. However, further out several issues occur: In order to be economical feasible, the detectors need to cover many analysers and this will reduce the freedom in selecting  $d_{ad}$  in a critical way, reducing performance in other parts

of the instrument. Furthermore, the larger spacing between the reflected signals from the 7 outermost analysers will increase the cost of such a solution substantially. It is therefore only deemed beneficial for the frontmost analysers, where it is even needed due to lack of space. This means that the energy resolution for the 3 frontmost analysers can be reduced even further than the results displayed in 4.41. If the position resolution is taken to be half the diameter of the detector the energy resolution  $\delta E_f$  is corrected by a factor 0.61 for a sample height of 0.5 cm and 0.82 for a 1 cm high sample. The proposed layout of the detectors is thus as seen in figure 4.47 (right).

#### 4.4.11.4 Detector Pressure

Early in the process it was investigated, whether it would make sense to work with lower than usual 6–8 bar  $^3\text{He}$  pressures in the 0.5" detector tubes, since this reduce the detection efficiency for high energy neutrons more than low energy neutrons and could thus improve the signal to noise ratio. The effect can be seen in figure 4.48. It was however deemed too small to be worth the lower count rate and when the order sorting chopper was introduced, increasing the demand for detection of neutrons with medium energies the idea was completely disregarded. Instead, a high pressure of 7 bar was chosen (corresponding to an efficiency at 5 meV of  $\sim 88\%$ ) to optimize the efficiency. The instrument will have to rely on other methods to reduce the background.

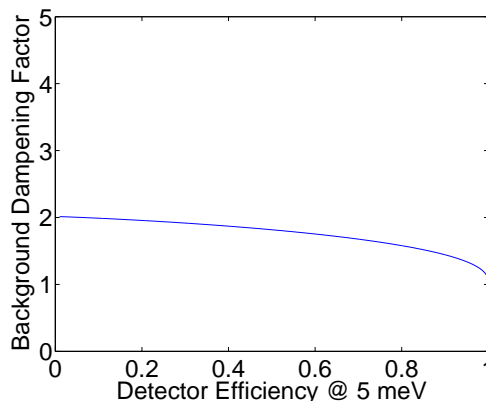


Figure 4.48: **Detector background dampening factor.** Calculated detection efficiency for background neutrons in thermal equilibrium with the room temperature surroundings compared to the efficiency at 5 meV. The detection cross section is assumed to follow a simple  $1/v$  dependence.

#### 4.4.11.5 Detector Saturation

The intense beam at the sample means the detectors can saturate and even be permanently harmed if Bragg peaks are reflected towards them. In order to resolve this problem it is foreseen too lower the voltage on any detector with to high count rates. Together with the ESS Technical teams, it is planned

to investigate if this can be done by electronics that simply limits the current through each detector disabling it temporarily. It is possible that the voltage reduction can be done fast enough that the detectors can stay active at the part of the incoming wavelength band that does not reflect Bragg peaks towards the detector. As a fall-back option, a system of attenuators that can be pushed up to attenuate specific  $a_4$  directions are envisioned. This system will be tested at PSI. If intense Bragg peaks needs to be investigated it is in principle possible to insert attenuators before the sample like it is done on a classic TAS. However, a more elegant solution will be to improve the incoming energy resolution with the use of choppers, thereby reducing the incoming flux, and possibly also the incoming divergence with the use of the divergence jaws.

#### 4.4.12 $a_4$ Coverage

As the secondary spectrometer will be almost stationary, it is important to cover a wide angular range in order for the instrument to be as flexible as possible. Especially the small angles are very important since information at low  $q$  give insight into correlations, that are longer than a typical unit cell and are *e.g.* often used to isolate magnetic signals from structural signals. Figure 4.49 illustrates the area in  $(q, \omega)$  space 2 of the CAMEA analysers will cover if the minimal  $a_4$  angle is  $3^\circ$  and  $10^\circ$ . In order to go to  $3^\circ$  in  $a_4$  the first wedge will need to use a modified mounting system. Furthermore, the direct beam that did not react with the sample will continue through the analyser tank and down through a get-lost tube on the backside of the tank. Although this does imply a risk of increased background in the first wedge, the unscattered beam will enter the tank through a thin Al window, continue in a evacuated guide and leave through another window. It should thus have a minimal impact on the background. Any increased background will be kept in the first wedge by shielding between the wedges. If  $a_4$  angles below  $10^\circ$  are ignored it is possible to keep the direct beam outside the analyser tank and use the same analyser mounting for all analysers. In the end, it was decided that the low  $q$  values are sufficiently important that a minimal  $a_4$  of  $3^\circ$  should be pursued. The maximal recordable  $a_4$  determines the maximal  $q$  values each analyser can record. However, CAMEA can already access relatively large  $q$ -values for a cold neutron spectrometer so the maximum is less critical for most spectrometry applications. In order to leave space for the order sorting chopper, guide, divergence jaws and shielding the coverage is foreseen to go to  $135^\circ$ .

#### 4.4.13 Dark Angles

The CAMEA dark angles can be caused by several different contributions like walls between the analyser-detector modules, mounting of analysers, and dead areas at the end of the detectors and expanding beams from the analysers. The latter is the most uncommon and will be described in more detail here. For simplicity we will consider a coordinate system where  $\boldsymbol{x}$  lies in the direction from the sample towards the center of the investigatd analyser,  $\boldsymbol{z}$  is vertical and  $\boldsymbol{y}$  is orthonormal to  $\boldsymbol{x}$  and  $\boldsymbol{z}$ . When a neutron traveling in the direction

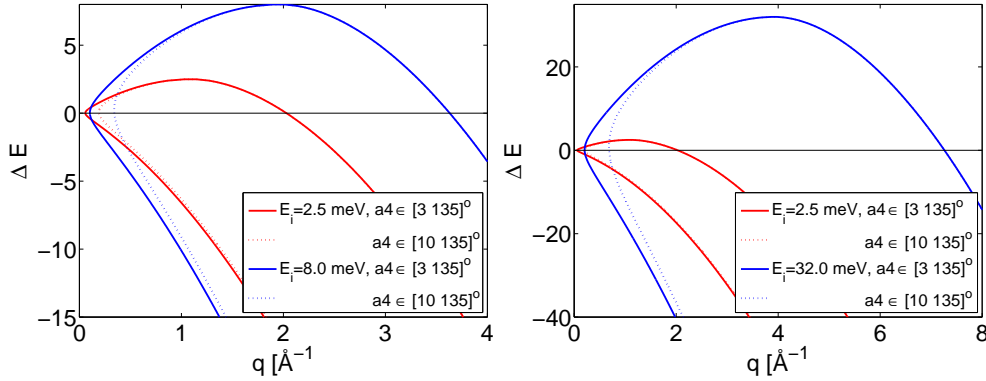


Figure 4.49:  $q$  range dependence of  $a_4$ . The accessible  $q$  range for a number of different analysers and  $a_4$  angles. Left: Examples of first order scattering. Right: Examples of first and second order scattering.

$\mathbf{v} = (\cos(\Delta a_4), \sin(\Delta a_4), 0)$  where  $\Delta a_4$  is the angle between the neutron travel path and the path towards the center of an analyser with surface normal  $\mathbf{n} = (\cos(a_5 + \pi/2), 0, \sin(a_5 + \pi/2))$  the reflected beam will have the direction:

$$\begin{pmatrix} \cos(\Delta a_4) \cos(2a_5) \\ \sin(\Delta a_4) \\ \cos(\Delta a_4) \sin(2a_5) \end{pmatrix} \quad (4.8)$$

So it will continue its travel along the  $y$  direction while the velocity along the  $x$  directions is reduced and might even be negative. That means that the reflected beam will expand across the wedge wall spanned by  $(\cos(\pm \Delta a_{4max}), \sin(\pm \Delta a_{4max}), 0)$  and  $z$  thus reaching the detector of the neighbouring analyser-detector setup (see figure 4.50). At the detector position the width of the reflected beam becomes  $2 \tan(\Delta a_4)(d_{sa} + d_{as})$ . If the detector is kept within a wedge with a width of  $2\Delta a_4$  it has a maximal active area of  $2 \tan(\Delta a_4)(d_{sa} + \cos(2a_5)d_{as}) - d_{dead}$  where  $d_{dead}$  is the dead area in the end of the detectors. Thus the fraction of the beam that cannot be detected becomes:

$$\theta_{dark} = 1 - \frac{2 \tan(\Delta a_4)(d_{sa} + \cos(2a_5)d_{as}) - d_{dead}}{2 \tan(\Delta a_4)(d_{sa} + d_{as})} \quad (4.9)$$

The problem is of limited consequences in instruments like Flatcone or the new CAMEA-like FLEXX upgrade where  $d_{sa}$  is considerably larger than  $d_{ad}$ . However, choosing such settings with small  $d_{ad}$  for CAMEA would have a severe impact on time resolution, energy resolution, and the performance of the order sorting chopper. At CAMEA the dark angles becomes acceptable for small  $2a_5$ , however for large  $2a_5$ , like the 2.5 meV analyser at CAMEA the dark angles becomes more than  $2/3$  even without dead layers in the end of the detectors.

In order to minimize the problem, a strict split of the analyser-detector setup into completely independent wedges was abandoned (though the ideas of crosstalk blocking and modular design for easy maintenance were kept) and several geometries investigated. In the proposed geometry, the analysers and detectors are

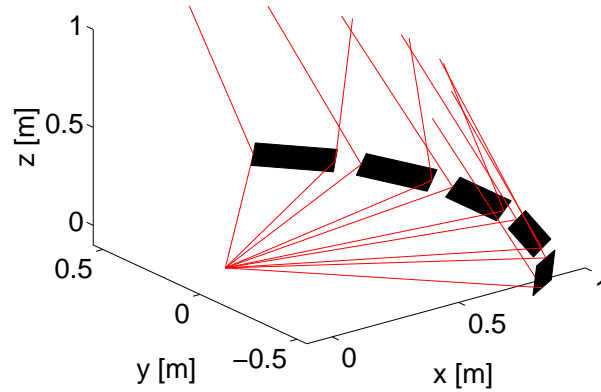


Figure 4.50: **Analysers crosstalk.** Flat analysers (black) arranged on a circle will have crossing neutron trajectories (red). Wedge size is exaggerated.

arranged in a Zig-Zag pattern. Every second analyser-detector wedge is shifted some centimetres back so that the detectors can be prolonged without overlapping the detectors of the neighbouring wedge (See figure 4.51). By doing this it is possible to reduce the dark angles to  $1/3$ , which is anyway required for mounting of analysers and crosstalk blocking. However for the frontmost detectors the dead area on the detectors takes up to much space and the detectors are thus rearranged into one big cone of detectors where each analyser reflects to a limited part of the full detector.

To avoid crosstalk, vanes of Al with a neutron absorbing inner cladding are

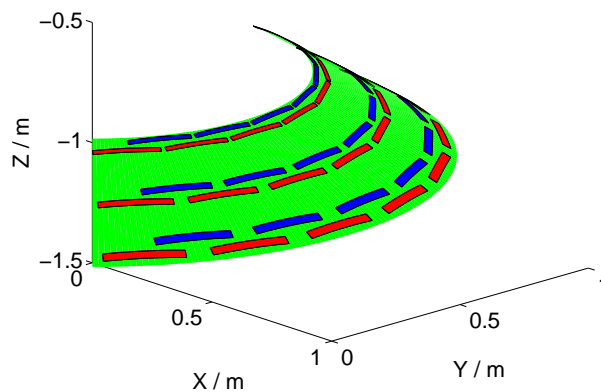


Figure 4.51: **The active area of the first detectors.** The green area shows the cone produced by a number of linear position sensitive detectors arranged with every second partially covered by the others in the narrow end of the cone. The blue areas the reflected signal of the 3 foremost analysers in every second wedge and the red are the signal from the 3 frontmost analysers in the other wedges.

installed between each analyser and corresponding detector. In this way each detector area can only see the analyser that it is associated with. In addition the solid angle visible for each detector is greatly reduced, reducing the general background. It has been checked in a technical drawing program that the vanes will fit with the zigzag pattern, though the drawing is impossible to reproduce in 2d and thus omitted from this thesis. The vanes can be upgraded with coarse radial collimators, reducing the background further.

#### 4.4.13.1 Wedge Size

The size of each wedge is a compromise between two dark angle effects:

- A finite space is taken up by walls between the wedges and mounting for the analysers. The smaller the angular coverage of each wedge, the larger a fraction will become dark angles due to this effect.
- The length of detectors inside a neighbouring wedge grows with wedge size, as does the angle between the detectors of two neighbouring wedges. In order to avoid detector overlap the wedges are thus required to stay within a certain angle or the analysers will need to be moved further apart.

For the proposed instrument a value of  $6^\circ$  active area and  $3^\circ$  dark angles per wedge could be achieved. However it is possible that this will change with ESS regulations of for example spare parts for analyser mounting and shielding.

#### 4.4.13.2 Covering the Dark Angles

Two different methods are foreseen in order to cover the dark angles. The entire analyser detector setup is mounted on rails inside its vacuum tank and can thus be rotated. Since the dark angles correspond to  $1/3$  of the full arc all points can be covered twice in 3 data acquisitions if the analyser is shifted  $1/3$  of the coverage of a single box at a time so the rails are designed to be able to rotate the analyser-detector setup by a total of  $6^\circ$ .

It is, however, also possible to cover the plane by simply rotating the sample ( $a_3$ ) slowly around. This method will lead to a non-uniform statistical and resolution coverage but will still be useful for many experiments.

This analysis was done before any technical drawings were made. The actual implementation may have a slightly different distribution of dark angles, but this will not change the overall principle.

#### 4.4.13.3 Discrete Rotation of $a_3$

In many cases scans are foreseen to be done with a series of discrete  $a_3$  steps. If that is the case the coverage will look as in figure 4.52. The covered area is without gaps, but some areas have gaps in the fine resolution data (red lines in the figure). It is however hard from the figure to quantify the gaps. Hence we will continue to the case of continuous  $a_3$  scanning in section 4.4.13.4 as it makes the coverage clearer and the results can be generalized to the probably

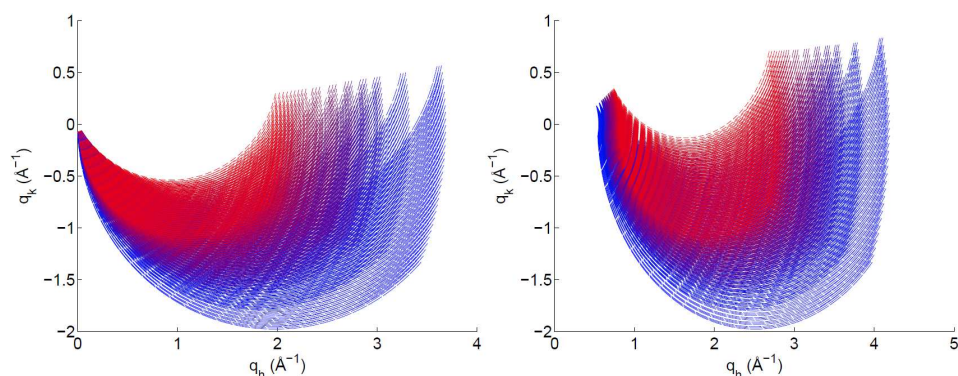


Figure 4.52: *Examples of how the scattering plane is covered by a discrete sample rotation.* Left: 0 meV energy transfer. Right: 5 meV energy transfer. Each line represents the centre of the measurement from one specific analyser. The red lines are low  $E_f$  (fine resolution) and the blue high  $E_f$  (coarse resolution). The sample is rotated  $30^\circ$  in discrete steps of  $1^\circ$ .

more frequently used discrete case.

Not all data in figure 4.52 will be recorded simultaneously. The  $1.7 \text{ \AA}$  wavelength band does not allow all detectors to record the elastic line from the same pulse, unless every second moderator pulse is removed by the chopper system. The number of analysers that can see the elastic line depends on the choice of wavelength band. All analysers can see the  $\hbar\omega = 5 \text{ meV}$  energy transfer at the same time if the wavelength band is chosen with that in mind.

#### 4.4.13.4 Continuous Rotation of a3

With the high flux and event mode data acquisition of ESS-CAMEA it is foreseen that some experiments will be done rotating the sample slowly around while counting. This will lead to a coverage as shown in figure 4.53. The gaps in the coverage from the first analysers are now clearly visible but it is also clear that all gaps are covered by analysers behind the frontmost ones. Only the small gaps in the regions exclusively covered by the backmost analyser are left open. It can be seen that the analyser overlap changes with both the scattering angle and energy transfer. Hence it is impossible to design the dark angles and energies in a way so no gaps will be seen between the first two analysers for all energy transfers. This means that some areas will have lower statistical weight and a coarser resolution than others when the dark angles are only covered by a3 rotation. Note that the 7th analyser is at 5 meV - the most used energy for cold TAS. Hence, if just one of the first 7 analysers covers the region, then the resolution will be better than in many cold TAS experiments since the prismatic analyser improves the energy resolution compared to normal TAS.

If the prismatic analyser is taken into account and 3 energies are recorded per analyser the gaps between the analysers becomes smaller, although they are still there for the frontmost analysers (see figure 4.54).

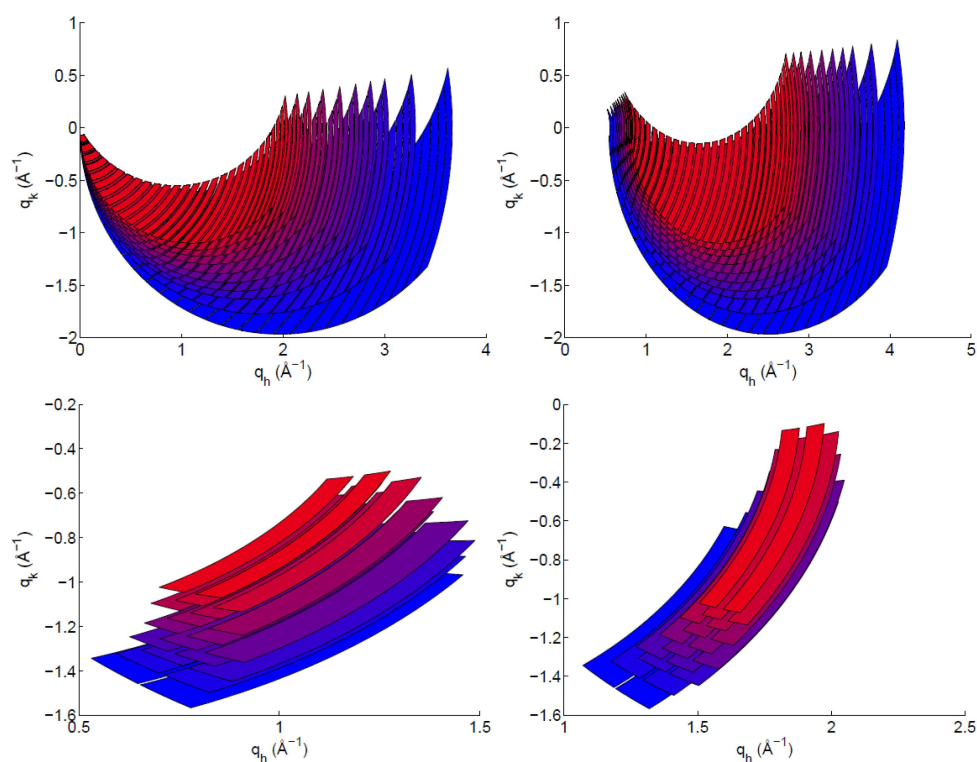


Figure 4.53: *Examples of how the scattering plane is covered by a continuous sample rotation. Left: 0 meV energy transfer. Right: 5 meV energy transfer. Each coloured area represents the area covered by one analyser when the sample is rotated continuously through 30 degrees. The red lines are low  $E_f$  (fine resolution) and the blue high  $E_f$  (coarse resolution). The top row shows all analyser segments whereas the bottom row only shows two. As the coverage changes with energy the same wedges are not displayed for all  $E_f$  values but instead wedges covering approximately the same area in reciprocal space are chosen.*

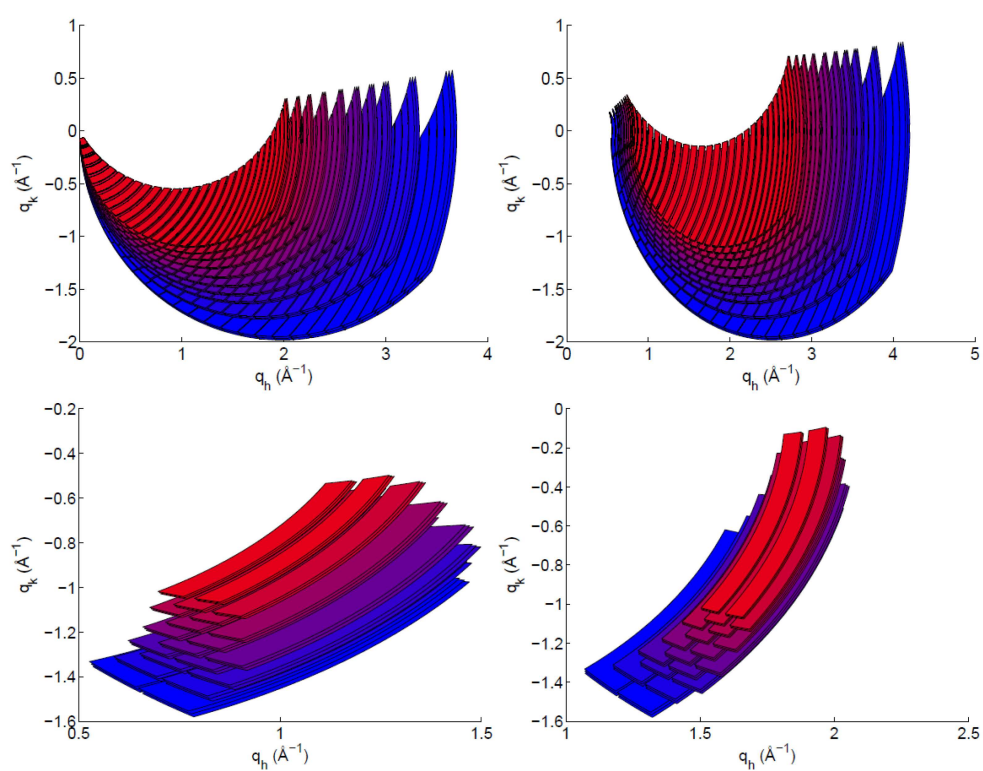


Figure 4.54: *Examples of how the scattering plane is covered by a continuous sample rotation with 3 energies from one analyser. The same as in figure 4.53 but with 3 half-inch tube detectors 0.5 mm apart looking at the same analyser.*

Although the a3 scan mode does have limitations it will be useful for many experiments when the users need the a3 scan anyway, which most mapping experiments will. Should the generated map show interesting features particularly in the regions where the resolution are limited the user can afterwards rotate the analyser-detector module and redo the scan.

#### 4.4.14 Secondary time Resolution

The time resolution of the secondary spectrometer is important in three ways:

- It sets a limit on the primary energy resolution since this depends on the determination of the primary flight time, which is calculated from the total flight time and the secondary flight time. Since ESS is a long pulsed source and CAMEA is a 165 m long instrument this is not expected to be a problem, even for inelastic measurements. However, it needs to be considered.
- The high flux in each channel makes CAMEA ideal for parametric studies, including time-resolved studies and studies using a pulsed magnet. In both cases, the time resolution is crucial.
- In order for the order sorting chopper to work well the time resolution needs to be good enough that the different pulses can be distinguished.

For the  $j$ 'th analyser, the secondary flight time ( $t_{sec,j}$ ) will be:

$$t_{sec,j} = \frac{d_{sec,j}}{c\sqrt{E_{f,j}}} \quad (4.10)$$

where  $d_{sec,j}$  is the secondary distance (i.e. the flight path from sample via the  $j$ 'th analyser to the detector) and  $c = 437.4m/(s\ meV^{\frac{1}{2}})$  is a constant. It follows that:

$$(\delta t_{sec,j})^2 = \left( \frac{1}{c\sqrt{E_{f,j}}} \delta d_{sec,j} \right)^2 + \left( \frac{d_{sec,j}}{2c(E_{f,j})^{\frac{3}{2}}} \delta E_{f,j} \right)^2 \quad (4.11)$$

where the correlation between  $\delta E_{f,j}$  and  $d_{sec,j}$  is set to 0 since the energy resolution is only correlated to the small transverse component in the flight path uncertainty.  $\delta E_{f,j}$  is known from simulations, however  $\delta d_{sec,j}$  needs to be determined.  $d_{sec,j}$  can be split in 4 components: The travel distance in the sample, the flight path due to the Rowland geometry, the travel path inside the analyser and the travel path inside the detector.

The uncertainty on the travel path inside the analyser can immediately be discarded as 1 mm thick PG analysers are used while the detectors are 1.27 cm thick, however, for a 2 cm thick Si analyser it will be a significant contribution. A cylindrical sample with a radius of 0.5 cm giving a flight path uncertainty of  $\sigma = 0.25$  cm.

The maximum uncertainty difference in travel path in the detector is 1.27 cm, disregarding the small contribution from neutrons with a direction not completely orthogonal to the length direction of the detector cylinder. However, as

Analyser Nr	1	2	3	4	5	6	7	8	9	10
Energy (meV)	2.5	2.8	3.1	3.5	4.0	4.5	5.0	5.5	6.5	8.0
Time resolution from $\delta E$ ( $\mu s$ )	9.9	11.0	12.0	13.0	14.0	14.8	15.0	15.5	16.5	17.0
Time resolution from $\delta d$ ( $\mu s$ )	12.2	9.6	8.4	7.9	7.3	6.9	6.5	6.2	5.8	5.1
Total secondary time resolution ( $\mu s$ )	15.7	14.6	14.7	15.2	15.8	16.3	16.3	16.7	17.5	17.8

Table 4.6: *Time resolution of secondary spectrometer.*

the neutron beam intensity is exponentially decreasing through the detector and as travel path through the detector becomes shorter the further the neutron trajectory is from the center of the detector a numerical integration was performed and a  $\sigma$  between 0.28 cm and 0.30 cm was found depending on neutron energy. It is not possible to focus an analyser so that it selects a constant energy and travel time and focuses it towards a single point. If  $d_{sa} = d_{ad}$ , however, the uncertainty in travel length becomes a second order effect. It was not possible to get complete agreement between distances because of order sorting limits, dark angles and crosstalk minimization, however, the distances are close to each other making the travel path uncertainty small. The actual numbers were found by numerical integration of the different travel paths.

Adding the different travel length contributions in quadrature and inserting them in (4.11) gives the numbers seen in table 4.6. For small energies where the neutron speed is small and the energy resolution is good, the uncertainty in travel length dominates while the energy resolution dominates for high energies where the energy resolution is coarse. For most analysers the contribution from the flight path is below the contribution from energy resolution, making the benefits of moving toward equal  $d_{sa}$  and  $d_{ad}$  minor. The time resolution remains below 20  $\mu s$  for all channels. It is worth to note that the improved energy resolution due to the prismatic analyser method does contribute to a better time resolution as well.

#### 4.4.15 Background

With a high incoming flux, relatively open geometry and many active components, some concerns have been raised regarding background levels at CAMEA. Ideally, at any given time the sample is illuminated by a narrow wavelength band, much like a TAS but without higher order noise from the monochromator. In principle, the background from the secondary spectrometer should thus be TAS-like, while the primary spectrometer will produce a ToF-like background. However correlations between the primary and secondary spectrometer could result in placing background at critical places in  $(\mathbf{q}, \omega)$  space.

#### 4.4.15.1 Background from the Primary Spectrometer

The background from the primary spectrometer will arise from the same sources as for other ESS instruments. ESS is presently studying the best way to reduce these effects[52]. A major concern is the shower of high energy particles that are generated when the proton pulse hits the spallation target and travels at relativistic velocities towards the instruments. This pulse of intense background called the "prompt pulse" is clearly visible at SNS instruments like HYSPEC[136]. The long length of CAMEA and the kinked guide is aimed at reducing the problems with the prompt pulse, as are the relatively low detector area ( $2.5 \text{ m}^2$ ) with high count rates, however if the background becomes too high it will be necessary to remove the signal during the 2.86 ms prompt pulse from the dataset.

#### 4.4.15.2 Background from the Secondary Spectrometer and Sample Area

The backend is essentially a large multiplexed instrument so it can in principle reach background levels comparable to that of other multiplexed instruments. For example RITA-II, PSI has a background level of less than 0.2 count pr. minute pr.  $2.5 \times 12.5 \text{ cm}^2$  channel in the deep inelastic background. Of course, CAMEA will have a higher flux on sample, so the absolute background will be higher. However 50% of the deep inelastic background on RITA-II is electronic noise which does not scale with intensity, so the relative background can be lower. Furthermore higher statistics increase the signal to noise ratio even at constant signal to background.

To reduce the background, the secondary instrument is designed so that each detector only "sees" the analysers that are meant to reflect neutrons towards it, the rest of the solid angle is covered with neutron absorbing materials. It is further planned to place analysers and detectors in a common vacuum or Argon tank to remove air scattering. This is important due to the long secondary flight paths and relatively open geometry.

Collimators and slits will reduce the background from sample surroundings, although it is impossible to remove the background completely from all sample surroundings. This is, however, also a problem for TAS experiments where extreme environments are used routinely. Although the background can cause spurious and shadow important features, TAS instruments are helped by analysers that record most of the background from sample surrounding in the elastic line where both signal and background from the sample are relatively high and not in the inelastic region where the signals can be very weak.

**Energy tails:** As discussed in section 4.4.10.12 a quasi-elastic background from the energy tails in PG can also be expected. The background will not disturb deep inelastic measurements but it will contribute to the background at low energy transfers. We still hope to find ways to reduce this problem.

**Bragg reflections from Si, PG and Al:** Both Si and PG are excellent scatterers and will produce background events.

For Si, the perfect single crystals with very fine mosaicity means that any Bragg reflections will require perfect fulfilment of the Bragg conditions. This combined with cutting the Si wafers along a low symmetry axis will reduce the risk of background from Si considerably.

As described in section 4.3.3, PG will have some reflections with contributions from the  $(a, b)$  plane. However due to the considerably longer  $c$  axis than  $a$  and  $b$  axes,  $l$  needs to be much larger than  $h$  and  $k$  for the reflection to be close enough to make it to the detectors. This is of lesser concern since only very high energy neutrons will be able to reflect towards the detectors of these high indices.

Most Al will be covered in neutron absorbing materials. However, some will be visible to neutrons and produce Debye-Sherrer cones that can potentially make it to some detectors. A way to reduce spurious contamination is presented in section 4.4.15.5.

#### 4.4.15.3 Background from Correlations between Primary and Secondary Instrument

A problem in direct ToF spectrometers is background due to wrong flight path determination of neutrons scattered from the sample surroundings. Figure 4.55 displays examples of such backgrounds from LET[43], ISIS and CNCS[57], SNS. The signals close to the elastic line are from the sample surroundings and stronger than the inelastic signal from the sample. The displayed background at CNCS has later been reduced significantly by applying radial collimation outside the sample environment. At ISIS, specialized sample environments have proven able to reduce background by reducing the amount of material in the beam. However, for certain kinds of environments such as very strong magnets or pressure cells it is impossible to reduce the material in the beam significantly, and for the small samples envisioned at CAMEA the background dampening level of a collimator might not be enough to counter the reduction in signal from the sample. With the high flux on sample, there were considerable concerns about background from the secondary spectrometer or from multiple scattering in the sample surroundings, polluting the inelastic signal. Scattering events in the CAMEA sample surroundings are easily limited to the horizontal scattering plane by slits. It is thus easier to shield off sample surroundings with slits and radial collimators. However some multiple scattering events will make it through and can potentially lead to wrong energy determinations and inelastic background (see figure 4.56). Although the probability for multiple scattering is low, sufficient amounts of material in the sample surroundings can cause the elastic signal from these events to shadow inelastic scattering. The exact distribution of such background will depend on the precise layout of the sample surroundings, but it is possible to calculate limits on the background distribution. Assuming that the multiple scattering respectively adds or subtracts a distance  $\Delta l$  from the flight path, the

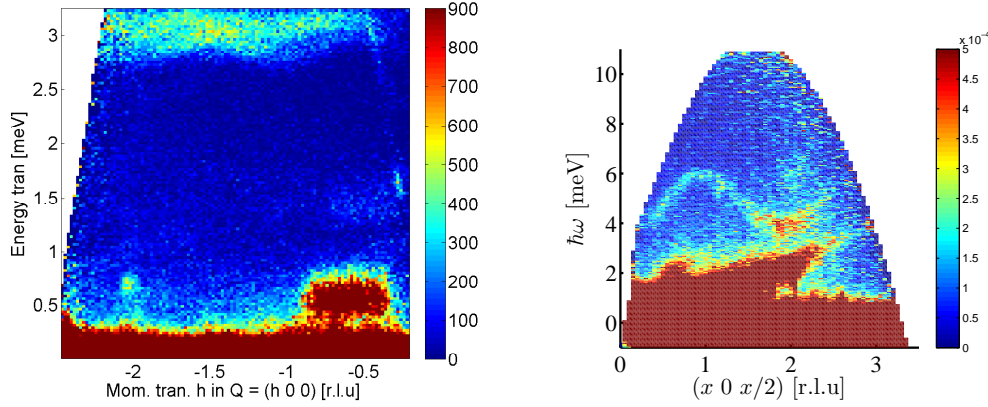


Figure 4.55: **Examples of background from sample surroundings.** Left: LET[43], ISIS data of  $\text{SrCu}_2(\text{BO}_3)_2$  in an orange cryostat[23] ( $E_i=12$  meV). Right: CNCS[57], SNS data on  $\text{CoCl}_2 \cdot 2\text{D}_2\text{O}$  with the 16 T magnet "Fat Sam"[14] that has a radius of 40.5 cm ( $E_i=12$  meV). In both cases the background can be reduced by the right choice of collimation/cryostat. (Figures from Paul Freeman and Jacob Larsen.)

recorded neutron energy ( $E'$ ) will be:

$$E' = E \left( \frac{l}{l \pm \Delta l} \right)^2 \quad (4.12)$$

where  $l$  is the flight path used for the ToF measurements and  $E$  is the actual energy of the neutron. However, whereas this extra flight path on a direct ToF spectrometer is compared with a secondary flight path of  $\sim 4$  m it will be compared to the 165 m flight path of the primary spectrometer on CAMEA, making the broadening a factor 40 smaller. Inserting these lengths leads to the distribution seen in figure 4.57 left.

In principle, infinitely long flight paths can be imagined by allowing an infinite number of scattering events in the sample surroundings. However, to make a qualitative analysis I will at first only look at paths including two elastic scattering events and consider inelastic scattering and paths involving more than two scattering events higher order corrections, since they have substantially lower probabilities.

The extreme values for  $\Delta l$  that will make it through a radial collimator can be found from figure 4.56. The minimum will be

$$\Delta l = R(\sqrt{2(1 + \cos(a4))} - 2) \quad (4.13)$$

where  $R$  is the radius of the sample environments and  $a4$  is the recorded scattering angle. The maximum path including two scattering events is:

$$\Delta l = R * (\sqrt{2(1 + \cos(a4))} + 2) \quad (4.14)$$

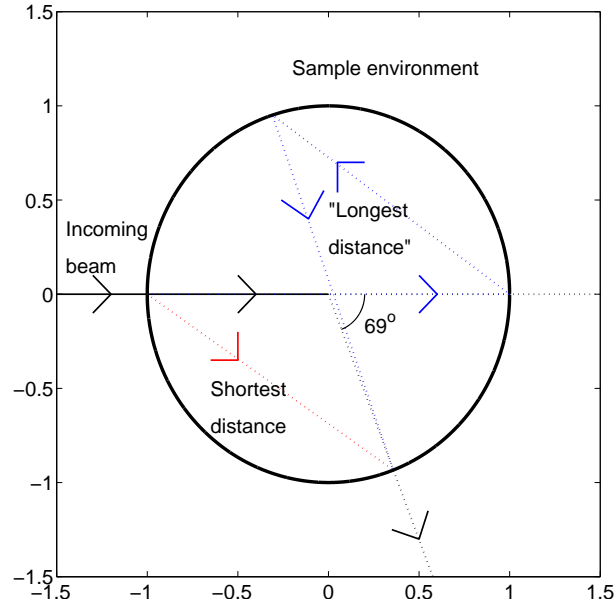


Figure 4.56: *Neutron flight paths in sample surroundings.* The longest (blue) and shortest (red) paths a neutron can travel to the middle of the CAMEA detector ( $a4 = 69^\circ$ ) with maximum 2 scattering events if radial collimation removes neutrons that do not come from the sample direction.

or a difference of  $4R$ . At CAMEA, the minimum path will be recorded as down scattering, while the maximum will appear as up scattering. It is opposite for direct ToF. These boundaries for multiple scattering from sample surroundings are displayed in figure 4.57 (right) for the centre of the CAMEA detector ( $a4 = 69^\circ$ ). In the down-scattering region, where CAMEA is designed to deliver its optimal performance, the extend of the scattering is less than  $\Delta E/E \approx 0.5\%$ . So multiple scattering will be contained in the elastic line, while it for direct ToF can cause problems for low lying excitations and quasi-elastic scattering with  $\Delta E/E < 50\%$ . On the up scattering side the maximum deviation can get close to  $2.5\%$  so in the most extreme cases it might cause a small widening of the elastic line on CAMEA. At direct ToF machines it is  $\Delta E/E < 8.5\%$ . Fortunately, the down-scattering region is of most interest on CAMEA since many experiments are done at low temperatures where only few excitations exists in the sample, suppressing the upscattering.

Equation (4.13) and (4.14) do not predict that big inelastic regions will be overshadowed by multiple scattering events. They merely place a limit on what region can potentially be overshadowed by double scattering events. Figure 4.55 does, however, confirm that the effect can be a real issue on direct ToF spectrometers, although the measurements in these cases were taken without a radial collimator.

It is possible to subtract parts of this background by measuring without the sample but if the multiple scattering events involved the sample, subtraction

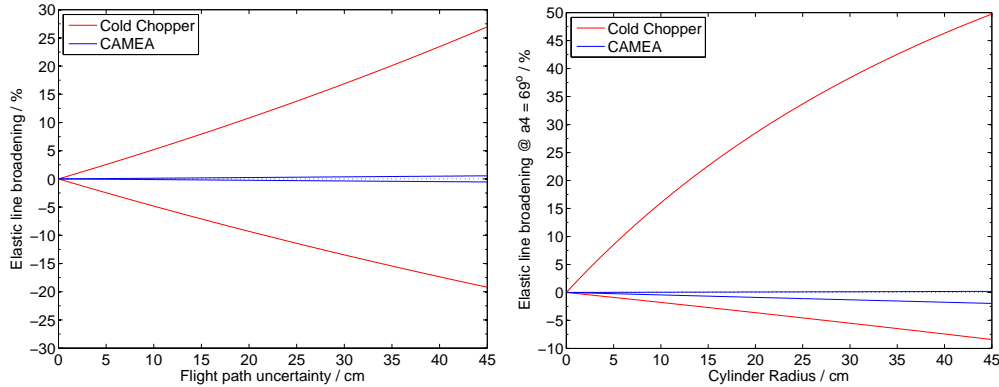


Figure 4.57: *Boundaries for line broadening from multiple scattering in the sample surroundings with maximum two scattering events. Left: calculated from the travel path uncertainties. Right: Calculated from the longest  $\Delta l$  possible within a cylinder of a given radius, as described in figure 4.56. The relative broadening is independent of  $E$ , see (4.12).*

will be inaccurate. This can, however, only happen for  $\Delta l > 0$  so it is possible to map out all contribution from multiple scatterings without the sample on the down scattering side on CAMEA and up scattering side on direct ToF. Note that in the examples from figure 4.55, the background is much stronger than the inelastic signal from the sample so even if it is mapped out it might not be possible to reliably retrieve any actual data hidden below it.

If we look at paths with a higher number of scattering events, it is possible to produce longer but not shorter traveling paths. This means that additional broadening from this effect can occur in the up-scattering region on CAMEA and down scattering region on direct ToF. Inelastic scattering in sample surroundings can produce noise in both the up- and down-scattering regions although the signal would usually be weak and removable by background subtraction.

Another concern we have investigated is that the uncertainty in the secondary energy could influence the determination of the primary energy. The time resolution of the secondary spectrometer was described in 4.4.14 and found to be lower than the relevant pulse widths for CAMEA so the secondary spectrometer will not pose any problems to the ToF determination.

#### 4.4.15.4 Background Measurements

Background measurements were performed by Marton Marko at the prototype. A V sample was inserted and counts performed for  $\sim 3$  hours in each setting. The intensity at different time channels was normalized to the maximum counts at the elastic line. A number of different measurements was performed (see figure 4.58): One at room temperature where incoherent phonon scattering in V is the major contribution to the background. One where the V sample is cooled to

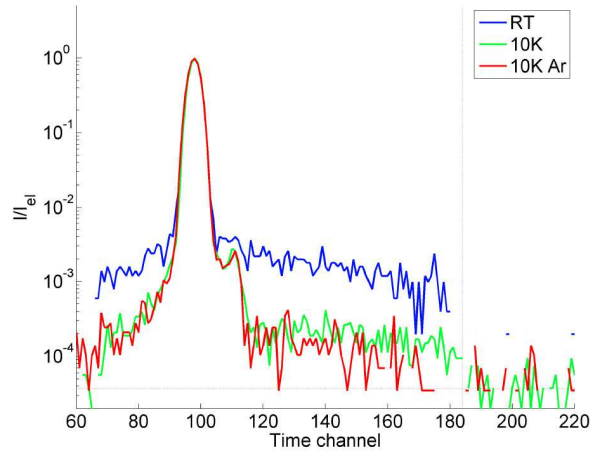


Figure 4.58: **Background measurements.** Energy scans across the elastic line of Vanadium for room temperature (blue) and 10 K (green) Vanadium samples and 10 K vanadium sample and Argon in the analyser tank (red). After time channel 185 the choppers are closed and only noise from the primary spectrometer and electronic noise from the detectors are recorded. Figure taken from [100].

10 K and one where the air in the analyser tank was replaced with Ar. The results prove that a relative background level of  $5 \times 10^{-5}$  can be achieved in the deep inelastic region when compared to the elastic line of cooled Vanadium. All measurement was taken with Cadmium shielding around the analyser holdings and rough Cadmium slits between analysers and detectors. In the 10 K data sets a small excitation can be observed at slightly higher time stamps (lower  $\hbar\omega$ ) than the elastic line. As this was the last measurement before PSI shut down for winter the source of this signal was never found.

It is possible that a lower relative background level could be achieved at CAMEA since the Argon atmosphere of the prototype will be exchanged with vacuum, the shielding between sample and detectors will be much heavier, the electronic noise will be smaller compared to the signal, and there will be less material in the beam height as *e.g.* no motors are needed to rotate the analysers.

#### 4.4.15.5 Detecting Spurious

When a scan is performed at CAMEA, most recorded points in  $(\mathbf{q}, \omega)$  space are measured several times by different analysers. Since  $E_i$ ,  $E_f$ ,  $a_3$ , and  $a_4$  varies between the different measurements most spurious will only occur in one of the measured channels. It is thus possible to compare the results and remove channels with spurious in them. Software should be produced that automatically detects any channels with a higher count rate than other channels measuring the same  $(\mathbf{q}, \omega)$  volume and flags these channels if the result cannot be explained by statistics or different resolution functions.

#### 4.4.15.6 Reducing the Background Further

It is possible to install coarse radial collimators just before the detectors to reduce the solid angle seen by the detectors and thus reduce the background further. This will remove most spurions and probably also reduce the energy tails from PG. Simulations and measurements of this is in preparation.

## 4.5 Optimizing CAMEA

The parameter space of CAMEA is more than 100 dimensional while the performance space, *i.e.* the space spanned by the 10  $E_f$  resolutions, 10 a4 resolutions, 10 efficiencies of the different analyser arcs, the price the guide brilliance transfer, the background, and so forth, is more than 40 dimensional, even if the prismatic analyser is not considered. Describing the transformation between the two requires a combination of calculations, simulations, prototyping, and obtaining cost numbers that are not publically available, like guide prices. Furthermore, in order to find a global performance optimum a one dimensional measure should be computed from performance space. While the second transformation could in principle be described mathematically it is unrealistic to describe the first transformation in a single mathematical function. This makes any attempt at reliably identifying a global optimum for the parameter space impossible.

What can be done is mapping the most important correlations and using the knowledge to produce a very well performing instrument. This is generally what is done in instrument designs, also when the instruments are far less complicated than CAMEA. I have already described most choices and the chosen parameters in the previous section.

For the more complicated choices, *e.g.* the exact  $E_f$  distribution, a choice that delivered the desired performance was produced by a combination of calculations and trial and error. So solutions that would fulfil the requirements in section 4.4.10.8 was produced and they were tested to see if distances with these energies could be found that satisfied the order sorting chopper, kept the dark angles below 1/3, allowed space for 3 detectors per analyser, allowed the first 3 detectors groups to be on a single cone, and kept the dimensions and thus the cost realistic. If such numbers existed, the energy resolution, angular and time resolution, and approximate cost was found. By trying different values and using the knowledge described in previous sections, it was possible to design an instrument that fulfilled the different requirements and promised great performance. It is possible that slightly different energies could increase *e.g.* the relative energy resolution or performance of the order sorting chopper however gains would most likely be minor.

When ESS have reached a decision regarding moderator height, the results from investigation of guide background and PG tail dampening are ready, and technical constraints from general ESS design choices are known, the parameters should be re-examined to see if a change could improve the instrument further.

## 4.6 Final Design and Performance

An overview of the proposed instrument parameters can be found in figure 4.7. More detailed data are available in the specific sections. The resolution of the secondary spectrometer is collected in table 4.8.

### 4.6.1 Comparison to a TAS at ESS

An alternative to CAMEA could be a classic TAS, using a doubly focusing monochromator and a doubly focusing analyser. The solid angle covered by double focusing monochromators and analysers will depend on  $a1$  ( $E_i$ ) and  $a5$  ( $E_f$ ) respectively. Here we will assume a  $4^\circ$  coverage in both horizontal and vertical direction and an energy resolution of  $\Delta E_i/E_i = \Delta E_f/E_f = 3.5\%$ .

Both instruments have access to the same guides. However, the TAS has slightly better focusing options but requires the neutrons to reflect from a monochromator with reflectivities below 1. We assume that two effects cancel out and the total flux on sample in a narrow  $E_i$  band is approximately equal. The TAS will pick out one narrow  $E_i$  band and reflect that towards the sample, whereas CAMEA will use the entire  $1.7 \text{ \AA}$  wavelength band, corresponding to a gain of a factor of 30 for CAMEA.

In the secondary spectrometer both instruments use analyser crystals and would thus in principle perform equally well. The analyser of a doubly focusing TAS will collect a solid angle of  $4^\circ \times 4^\circ$  into a single channel, while the average vertical coverage of CAMEA is  $3^\circ$  and the average horizontal resolution is  $0.6^\circ$ . The TAS thus records a 9 times large solid angle into a single channel. The TAS will also record a double as wide wavelength band in the detector channel. However, CAMEA will record most of the same neutrons and just split them into 3 energy channels times 7 a4 channels adding extra information. To make comparison easier we first consider a setup where CAMEA rebins the data to match the resolution of a double focusing TAS. In this case the 10 analyser arcs of CAMEA and  $90^\circ$  active a4 coverage compared to the one analyser with a coverage of  $4^\circ$  gives a total gain factor of  $\sim 170$  for CAMEA when the average vertical coverage of  $3^\circ$  for CAMEA is included. The flux in the frontmost detectors will be slightly above that of the TAS due to the combination of relaxed mosaicity and distance collimation while the backmost will be below due to attenuation through the analysers. We approximate the average reflected flux per solid angle from the analysers to be equal for CAMEA and TAS. Collecting the numbers CAMEA will have a comparable flux to the doubly focusing TAS, however in  $30 * 170 = 5 * 10^3$  channels.

If the resolution of the TAS should be comparable to CAMEA it would require that both analysers and detectors reduce their horizontal coverage to  $2^\circ$ , giving CAMEA a factor 4. In order to reach an energy resolution of  $dE_i/E_i = dE_f/E_f = 1.1\%$  at 5 meV the TAS would in a best case scenario need to reduce the signal a factor 9 while CAMEA only needs to reduce the incoming flux a factor 3. In this case CAMEA would thus win with a factor  $6 * 10^4$ . If CAMEA Furthermore uses the divergence jaws to reduce the incoming a4 resolution to  $0.6^\circ$ , thereby matching the secondary resolution, an additional factor 3 could be

<b>Primary Spectrometer</b>	
ESS Moderator	Cold
Wavelength range (Energy range)	1 Å to 8 Å (81.8 meV to 1.3 meV)
Bandwidth at sample position	1.7 Å
Guide length and shape	165 m - Parabolic feeder to double elliptical guide
Line-of-sight removal	Kink between elliptical guide sections
Number of choppers	7, operating from 840 rpm to 12600 rpm
Incoming divergence	2.0° vertical, 1.5° horizontal
Divergence control	5 divergence jaws integrated in guide
Incoming energy resolution	Adjustable from 0.1 % to 3 % at 5 meV
<b>Sample</b>	
Maximum flux on sample position	$1.8 * 10^{10}$ n/s/cm <sup>2</sup> /1.7 Å
Wave vector range at elastic position (including PG(004) reflections)	PG(002) reflections: 0.058 Å <sup>-1</sup> to 3.6 Å <sup>-1</sup> PG(004) reflections: 0.12 Å <sup>-1</sup> to 7.26 Å <sup>-1</sup>
Background count rate	< 5*10 <sup>-5</sup> compared to elastic signal of vanadium (result from prototype testing)
Beam size at sample position	1.5 cm * 1.5 cm
Beam size optimization	0.1 cm * 0.1 cm - 1 cm * 1 cm
Sample environment space	90 cm diameter, side access possible
Magnetic fields	>20 T, >10 T with 10 GPa, 0.1 K-350 K
Pressure	30 GPa with 5 mm <sup>3</sup> sample, T=3-2000 K 10 GPa with 50 mm <sup>3</sup> sample, T=0.1-1800 K
<b>Secondary Spectrometer</b>	
Collimation	Radial collimation after sample. Cross talk collimation in secondary spectrometer.
Filter	Removable cooled Be-filter before analysers
Analyser crystals	2 m <sup>2</sup> cooled PG - 60" mosaicity, using (002) and (004) reflections
Detectors	2.5 m <sup>2</sup> Position sensitive <sup>3</sup> He at 7 bar
Number of analyser arcs	10
Number of analyser-detector segments	15 (9° per segment, 6° active)
Sample to analyser distances	1.00 m to 1.79 m
Analyser to detector distances	0.80 m to 1.45 m
Horizontal angular coverage	3°-135°
Horizontal angular resolution	0.79° to 0.46°
Vertical angular coverage	±1.4°
Final neutron energy range	PG(002): 2.5 meV to 8.0 meV PG(002)+PG(004): 2.5 meV to 32 meV
Secondary energy resolution	0.77 % to 1.3 % (2.5 to 8.0 meV)
Time resolution	≤ 20 μs
Neutron polarization and analysis	Polarizing super mirrors

Table 4.7: Important CAMEA design parameters

Analyser No	1	2	3	4	5	6	7	8	9	10
$E_f$ (meV)	2.5	2.8	3.1	3.5	4.0	4.5	5.0	5.5	6.5	8.0
$\delta E_f/E_f$ (%)	0.77	0.83	0.85	0.94	1.02	1.08	1.09	1.12	1.21	1.30
Secondary angular resolution ( $^\circ$ )	0.79	0.77	0.75	0.71	0.65	0.61	0.59	0.55	0.51	0.46
Secondary time resolution ( $\mu\text{s}$ )	15.7	14.6	14.7	15.2	15.8	16.3	16.3	16.7	17.5	17.8

Table 4.8: *Secondary spectrometer performance.*

gained over TAS for a total of  $2 * 10^5$ .

Most experiments will not find every channel equally useful but it is impossible to predict the actual number of useful channels in a typical experiment.

#### 4.6.2 Comparison to a Cold Chopper Spectrometer at ESS

*The direct ToF cold chopper and CAMEA spectrometers are the ESS instrument closest to CAMEA in performance. Even though there are many differences they are both spectrometers with great mapping capabilities and medium resolution. This means that they compete for the same spots in the ESS instrument suite. This section is a rewrite of a report that I produced for ESS about their comparison. The original report is available online[44].*

The two spectrometers are in many ways equivalent. The cold chopper spectrometer (CCS) uses several incoming energies from repetition rate multiplication[113] combined with a continuous outgoing energy band, while CAMEA uses a continuous incoming band and several outgoing energies, and both have large angular coverage. They do, however, also have some key differences. CAMEA has a higher flux in each channel while the CCS has a bigger angular coverage, bigger resolution flexibility, and more freedom in choosing its energy range.

Since the CCS has a larger parameter space than CAMEA there are many experiments where a cold chopper spectrometer would be preferable. The main question is thus if there are experiments where CAMEA would be preferable. The main strength of CAMEA is 1.4% energy resolution down-scattering from a cold sample in an extreme environment. Hence we will investigate whether CAMEA performs better than a CCS here. A study by the CAMEA group have shown that 1/3 of all experiments at some of the best performing triple axis instruments in Europe are done with magnetic fields[63]. Although it is not included in the statistic, it is reasonable to expect that most of these are done with cold samples where down-scattering is the relevant measuring technique. We assume similar guide systems with the same wavelength band. A wavelength band of 3.1 Å to 4.76 Å was chosen for the simulations, corresponding to the CAMEA  $E_f$  energies.

### 4.6.2.1 Kinematic flux Calculations

It is possible to get an idea of how the two instruments will compare from simple kinematic considerations:

- CAMEA uses the full 71 ms pulse at the sample while the cold chopper for similar resolution use 8 pulses of approximately 25  $\mu$ s. This gives CAMEA a factor  $\sim 360$ .
- The reflectivity of the CAMEA analysers are on average about 50% if all 30 detectors are counted and beam attenuation is included. This gives CCS a factor 2.
- CAMEA has 33% dark angles giving CCS a factor 1.5.
- CAMEA has 30 detectors with a 1.4% resolution giving a total covered EF bandwidth of about 2 meV. The cold Chopper goes in  $E_f$  from 0.2  $E_i$  to  $E_i$  giving on average a 4 meV energy band. This gives a factor 2 to CCS.
- We have so far only disregarded up scattered neutrons from the cold chopper. Approximately half information from the sample lies in the up scattering giving the cold chopper a factor 2.
- As we only regard down-scattering CAMEA will get limited coverage from the analysers with the coarsest resolution (highest count rate) whereas the CCS will get the highest coverage from the shortest wavelength where the resolution is coarser and the countrate higher. The exact effect on countrates needs simulation but a factor 2 is estimated in favour of CCS.
- CAMEA has a vertical opening of  $\pm 2^\circ$ , while CCS is assumed to have an opening angle of  $\pm 30^\circ$ , giving CCS a factor  $\sim 15$  if the full opening angle can be used.

Combining these factors one find that CAMEA will win with a factor 15 if only in-plane scattering is considered. But if out of plane scattering is also included, the  $\pm 30^\circ$  coverage of the cold chopper will mean that the two instruments are comparable. The approximate calculation does, however, have several shortcomings (*e.g.* that the flux varies with the wavelength and that there exists small gaps between the analyser crystals). In order to reach a more accurate number, simulations have been performed.

### 4.6.2.2 Flux Simulations

In order to compare the flux and coverage of the two instruments we performed a simulation with as equal settings as possible. Both instruments used the same source, guide, chopper settings before the monochromating chopper at the direct ToF spectrometer, and same sample. The incoming and outgoing energy resolutions were chosen to match the outgoing resolution of CAMEA. This resulted in a factor 380 in favour of CAMEA at the incoming flux.

A sample with a scattering cross section of  $\frac{d\sigma^2}{d\Omega dE} = \frac{k_f}{k_i} s(q, \omega)$  with constant

$s(q, \omega)$  was chosen as to not favour one instrument that *e.g.* happened to match a certain excitation curve. The signal just before the analysers was compared to the signal in the CAMEA detectors to measure the fraction of the beam from the sample that each detector records. For CCS the full signal was recorded. Afterwards the data was corrected for beam attenuation through the analysers and an average graphite reflectivity of 70% was chosen. Finally, dark angles and the smaller vertical coverage of the backmost analysers of CAMEA were included. Only-down scattering was considered.

#### 4.6.2.3 Results

Comparing the two instruments gives a factor 22 to the CAMEA instrument if a  $\pm 2^\circ$  opening angle is considered. If one considers the full  $\pm 30^\circ$  detector coverage, the two instruments are almost equal, CAMEA having 50 % more counts. This agrees approximately with the back of the envelope calculations in the previous section.

It is thus clear that CAMEA in its key performance is more powerful than the cold chopper. This is however not a full and fair comparison as other experimental considerations will also be important in the choice of instrument for a specific experiment.

#### 4.6.2.4 Other Experimental Issues

- **Background** As described in section 4.4.15.3 the background in the two instruments behaves very different. If inelastic measurements with extreme sample environments are desired, CAMEA will perform best.
- **Coverage.** The cold chopper spectrometer looks at the elastic line with all repetition rate frames whereas the amount of analysers looking at it in CAMEA will be different. Usually, only the high  $E_f$  frames will be recording the elastic line; the others will be concentrating on the down scattering region. This means that CAMEA will have a worse resolution at the elastic line but a much higher coverage in the inelastic than the elastics while the CCS will have the highest coverage at the elastic line and lowest in the deep inelastic. (It is possible for CAMEA to have high coverage and good resolution at the elastic line too but in that case the coverage will shift towards the up scattering region.) This difference emphasises the CAMEA strength in low temperature inelastic measurements.
- **High Resolution.** CAMEA can reach a  $\frac{\Delta E}{E}$  resolution of just above 1.1% at 5 meV by using unmatched primary and secondary resolutions, but will lose a substantial part of its flux doing so (the matched value is  $\frac{\Delta E}{E} = 1.4\%$ ). The cold chopper can not only reach these levels with a smaller loss by matching the resolutions, it will also be able to surpass it.
- **Time Resolution.** Both CAMEA and the cold chopper can in principle have good time-resolution for time-dependent experiments. However, the monochromating chopper of the CCS means that the time where a

certain energy transfer is recorded will be comparable to the time resolution of 30  $\mu\text{s}$  while it will be 100 times longer (3 ms) on CAMEA. This means that CAMEA will be able to resolve many processes with constant experimental settings while this can only be reached by running a stroboscopic measurement with a different frequency than the ESS pulse at a cold chopper instrument. The later will make for much longer experiments and together with the lower count rates makes many experiments unrealistically long on a CCS while manageable on CAMEA.

- **Thermal Measurements.** For up-scattering the cold chopper will at first glance win a lot since the outgoing bands can be increased to any energy for almost no cost in time and it will thus be possible to reach any energy coverage. Of course much of this gain is insubstantial since the resolution will worsen considerably.
- **Bragg peaks.** The high intensity of CAMEA means that the problem with Bragg peaks saturating the detectors will be most severe on CAMEA.

#### 4.6.2.5 Conclusion

The Cold chopper spectrometer has an impressively large achievable parameter space compared to most other spectrometers and will be an excellent flexible spectrometer that can handle most challenges but will not be able to compete with more specialised instruments within their optimal field of operation. CAMEA will have 22 times higher count rates and lower inelastic background when cold samples and extreme environments are needed. The two instrument types are thus in many ways complementary.

#### 4.6.3 Comparison to Existing Instruments

Paul Freeman did a study comparing CAMEA and existing TAS and ToF instruments [62]. The conservative results show gain factors between 20 and 1500. The numbers are below what will be expected from the above comparisons. This is because the comparisons are done in slightly different ways. In the comparison to existing instruments the difference in resolutions are accepted since no middle ground can be found between the different resolutions of the existing instruments. Also the intensity at the brightest incoming energy is used for the TAS instruments whereas an average over the brightest wavelength range is used for CAMEA. However even this conservative estimate points to CAMEA as an essential development in neutron spectroscopy.

### 4.7 Demonstration Experiments

To demonstrate how CAMEA would record actual scientifically relevant data and to gain experience a measurement of  $\text{YMnO}_3$  was performed on the prototype.  $\text{YMnO}_3$  is a multiferroic system that recently have attracted much attention[76, 122, 130, 133]. The sample was a single crystal of  $\sim 1 \text{ cm}^2$ . Unfortunately it

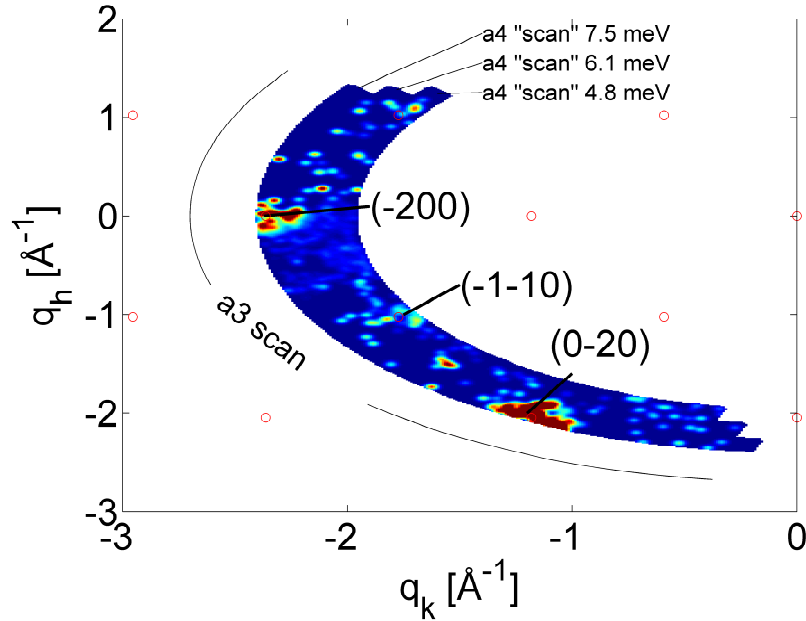


Figure 4.59: *YMnO<sub>3</sub> measurements from the prototype.* Map of  $(q_h, q_k)$  produced by an  $a_3$  scan for  $\hbar\omega = 6$  meV. The  $a_4$  "scans" are results of the position sensitive detector tubes. All 9 tubes are treated individually in the prismatic analyser principle. If only the central energies were used, the 3 resulting slices would not be connected. The  $a_3$  scan covers  $120^\circ$ .

was twined and aligned along a smaller crystallite approximated to be  $\sim 200$  nm<sup>3</sup>. The aim of the experiment was to measure magnetic excitations around the (1,1,0) reflection. A severe limitation on the prototype is the very limited coverage in  $a_4$ . This was countered by moving the analysers as close to the sample as possible to maximise the  $a_4$  coverage of each and adjusting their energy so that the  $\mathbf{q}$  space covered by each of them just overlap for any relevant  $\hbar\omega$ . The shortest possible distances at the prototype is  $d_{sa,1} = 0.90$  m and 15 cm between the analysers so this was chosen. Adjusting the energies to 4.8, 6.1 and 7.5 meV meant that they would cover the (-1,-1,0) reflection for  $\hbar\omega = 0$  and just overlap if the prismatic analyser principle was included to get 3 energies from each analyser. As  $\hbar\omega$  increased, the (-1,-1,0) reflection would move through the covered region and disappear at  $\hbar\omega = 7$  meV. Figure 4.59 illustrates the coverage at  $\hbar\omega = 6$  meV.

The data from all 9 detectors looking at the 3 analysers were converted from (detector number, Position on detector, recording time, sample rotation) into  $(\mathbf{q}, \omega)$  space and corrected for the following effects:

- **Monitor.** A time-of-flight monitor is installed before the sample, so by back-tracing the neutrons it is possible to find the energy and time dependent intensity, when the monitor's efficiency as function of energy is known[10].

- **$(d\Omega, dE)$  volume:** Each recorded time, position combination corresponds to a different solid angle and energy bin size. These  $\Omega \times \hbar\omega$  volumes were calculated and the signal normalized to the volume size.
- **Analyser reflectivity & Detector sensitivity.** To account for varying detector sensitivity and analyser reflectivity a measurement of vanadium was performed. The data was normalized to the  $(d\Omega, dE)$  volume as described above and the elastic line fitted for each detector channel. The integrated intensity was now taken as a measure of the sensitivity of the detectors and peak reflectivity of the analysers, so all measured signals were normalized to these values.

The refined data was stored in a 3 dimensional matrix with previously defined bin sizes and from this fast slicing and plotting could be performed. The written Matlab routines will need lots of development and can be made considerably faster for the final instrument. However it does prove that data reduction from a complicated instrument like CAMEA can be performed and useful data extracted.

The experiment was performed at 20 K and an a3 scan of  $120^\circ$  was performed (corresponding to 2 reciprocal unit cells, since  $\text{YMnO}_3$  has a  $60^\circ$  symmetry in the  $(a, b)$  plane). Data from the experiment can be seen in figure 4.60. The signal around the  $(-1, -1, 0)$  position is very weak at best, however the great mapping abilities of the CAMEA has made the excitations at the  $(-200)$  position clearly visible. Although this peak have already been mapped out the main purpose of this experiment was to record data with the prototype and learn from the experience so further scans were performed around the  $(-200)$  position to increase the statistics.

The chosen analyser energies did not make it possible to record the  $(-200)$  position at  $\hbar\omega = 0$  meV. However, the excitations above are visible. The results can be compared with measurements on RITA-II[117] and theoretical calculations from the Spin-w program[129], se figure 4.61. The coverage and statistics are limited. However, the results show agreement with both previous measurements and theory.

Though statistics might seem disappointingly low, one needs to consider the limitations of the prototype. First, the summed solid angle coverage from the 3 analysers is 0.0176 steradians whereas it will be 0.7659 steradians for the proposed CAMEA, so the prototype can be regarded as 2.3% of the final CAMEA instrument. Further, the intensity on sample is  $4 \cdot 10^5$  N/s/cm<sup>2</sup> compared to the predicted  $2 \cdot 10^{10}$  N/s/cm<sup>2</sup> at CAMEA. Hence CAMEA is a factor  $2 \cdot 10^6$  more efficient than the prototype. So the recording time of 1.3 days will correspond to 2 seconds on 2.3% of CAMEA. In addition the twining of the crystal means that a limited volume of at most 200 mm<sup>3</sup> was investigated. If the data is regarded as 2 seconds measurement from 2% of the instrument at a 200 mm<sup>3</sup> sample it is actually very impressive that a magnon excitation can even be seen. The entire instrument will not be able to focus on the same subspace of  $(\mathbf{q}, \omega)$  space. However, a factor  $\sim 5$  gain could be achieved in each channel by having the full instrument (as well as a factor  $\sim 10$  gain in coverage) so the same statistics

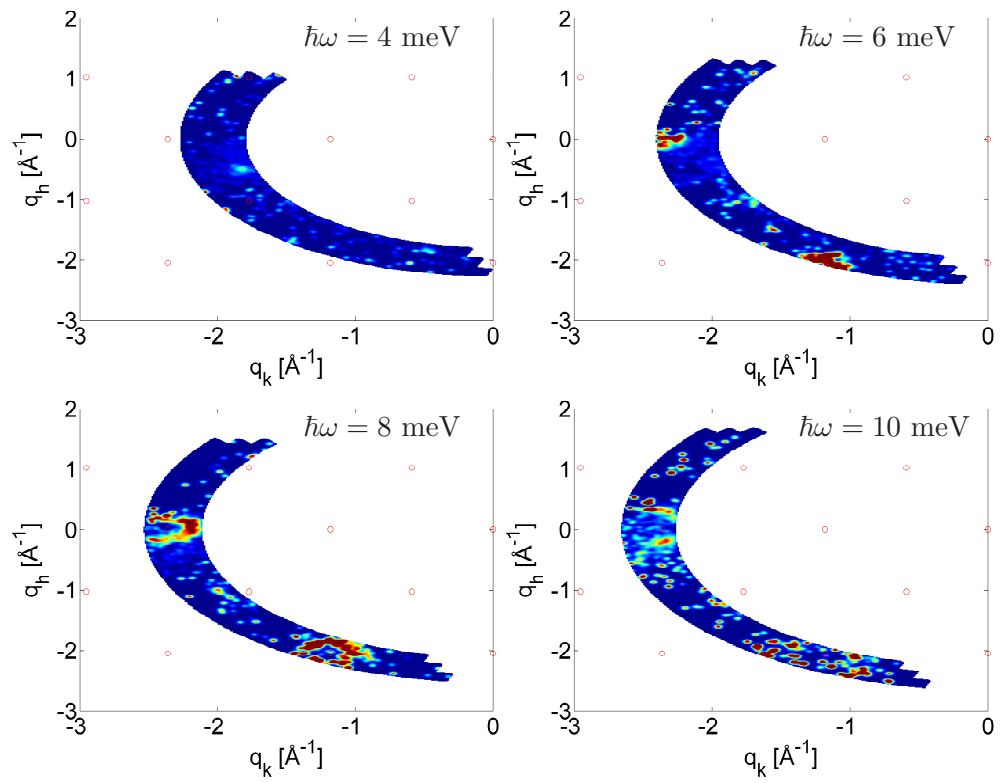


Figure 4.60: *Constant  $\hbar\omega$  maps of  $YMnO_3$ . Map of  $(q_h, q_k)$  for constant  $\hbar\omega$  at 20 K taken at the prototype. From top left to bottom right:  $\hbar\omega = 4$  meV, 6 meV, 8 meV and 10 meV.*

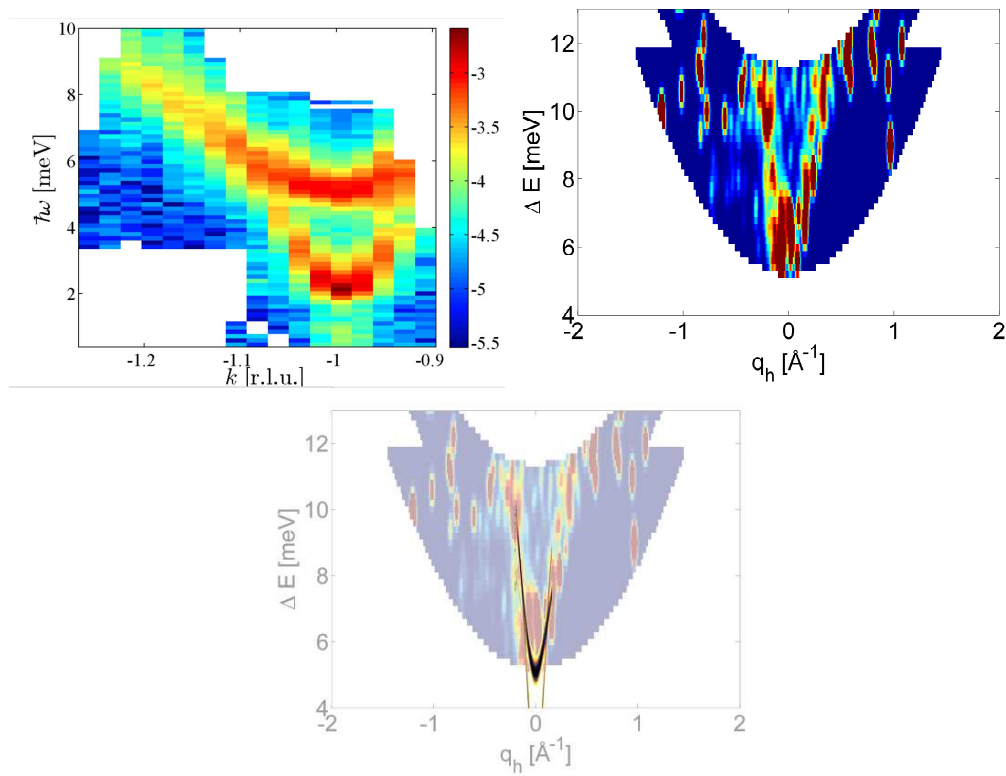


Figure 4.61: *Excitations around  $(-200)$  in  $YMnO_3$  taken at 20 K at the prototype.* Maps of  $(q_k, \hbar\omega)$  for  $q_h = 2.3 \text{ \AA}^{-1}$ . Measurements taken around  $(100)$  on RITA-II at the same crystal $[11\bar{7}]$  (left), the prototype (right), and prototype measurements overlaid with SpinW calculations (bottom).

could be achieved in a  $\sim 10$  times larger  $(\mathbf{q}, \omega)$  space in less than 100 seconds on a  $1 \text{ mm}^3$  sample. This supports the claim that CAMEA will be able to do spectroscopy on  $1 \text{ mm}^3$  samples (even if better statistics will clearly be needed). The experiment also demonstrated that visualization and analysis of data from the CAMEA setup has been solved. Once the data refinement routines are written, the combination of the many different detection channels runs automatically and produces meaningful data.

An experiment on  $\text{LiHoF}_4$  was also undertaken by Marko Marton[99, 100] and showed that for a large sample even the prototype delivers excellent data and can deliver complementary knowledge to the information generated by measuring the same sample on FOCUS.

## 4.8 Uncertainties

During the instrument design process a combination of calculations, simulations and prototype measurements were used to validate each other. The main new principles were verified experimentally to work, so the risk of the instrument failing to deliver a predicted functionality is minimal. The errors in energy and angular resolutions are estimated to be below 5% by comparing calculation, simulation and prototyping results. The time resolutions are less thoroughly checked and should be assigned uncertainties of up to 50%. The intensity is heavily dependent on the final ESS moderator solution and will thus have uncertainties of a factor 2. Although much effort went into determining the background, on the prototype the final instrument will have a different source spectrum, a different instrument length, different guide, different neighbouring instruments, and a secondary instrument with different dimensions and shielding instead of flexibility. The uncertainties in the background will thus be relatively high. There is a possibility that the background will eventually be lower than that of the prototype. However there are still too many uncertainties to guarantee this.

## 4.9 Comming CAMEA Instruments

A proposal for construction of CAMEA at ESS was delivered to ESS in March 2014[110]. The proposal has a substantial contributions from work described in this thesis. It was recommended for construction by the ESS Scientific Advisory Committee and accepted for construction by the ESS Steering Committee. A contract between ESS, Denmark, and Switzerland is being drafted.

### 4.9.1 Other CAMEA Implementations

As mentioned, ESS will not be the only facility constructing a CAMEA type instrument. PSI is already constructing a similar instruments and FLEXX at the Helmholtz-Zentrum Berlin is constructing an upgrade that will be use many of the same ideas as used on CAMEA. Panda at FRM II are planning a similar

upgrade. Furthermore, the design has generated some interest at SNS and J-Parc.

#### 4.9.1.1 The PSI CAMEA Design

ESS CAMEA benefits from a pulsed source and will be able to perform energy scans and in general get a dense coverage of part of the reciprocal space in a single data acquisition, thanks to its continuous incoming energy coverage. Conversely, PSI is a continuous source and PSI CAMEA will use a monochromator to reflect a single energy towards the sample. Hence if the ESS CAMEA was just copied to PSI, it would record a number of unconnected paths in the scattering space that would need to be connected through scans. In order to minimize the demand for scans, the analyser energies of PSI CAMEA will be compressed to the energy interval between 3.5 and 5 meV so that they almost overlap. In this way, a quasi- $E_f$ -scan is performed in one setting. If this is not deemed accurate enough, a more precise scan can be performed in just two settings of  $E_i$ . This also means that all analysers are below the Be edge and can be used together with a Be filter. The downside is that the dynamic range is reduced significantly, compared to ESS CAMEA. However, since many cold TAS rarely uses  $E_f$  values outside the interval covered by PSI CAMEA it is an acceptable restriction.

The same trick could be performed at ESS CAMEA to give an even denser coverage of a smaller subspace of the scattering space. If a second CAMEA instrument were to be built at ESS this would probably be an interesting option. However, with the already unprecedented high count rates within the chosen subspace of the scattering space it was decided that the higher dynamic range would be more useful for ESS CAMEA as it allows the instrument to be applied to more scientific questions.



# Chapter 5

## NiMn<sub>2</sub>O<sub>4</sub>

NiMn<sub>2</sub>O<sub>4</sub> is spinel system with a rich magnetic phase diagram that has shown strong dependence of the manufacturing process[95, 36, 56, 48, 120]. In this particular project, a chemical manufacturing process was chosen in order to produce a pure and uniform powder. The powder was investigated with x-rays, SEM and neutron diffraction. A description of the process can be found in the attached article where it is shown that the sample is pure and uniform. The synthesised material ordered as (Ni<sub>0.20</sub>Mn<sub>0.80</sub>)<sub>tet</sub>[Ni<sub>0.84</sub>Mn<sub>1.16</sub>]<sub>oct</sub>O<sub>4</sub>, where the *tet* and *oct* subscript denotes whether it is ordered in a tetrahedral or octahedral system. The lattice parameter of 8.392 Å. Two magnetic phase transitions  $t_t = 40$  K and  $t_c = 96$  K is observed in the zero field cooled system.

### 5.1 Measurements

An experiment was performed at the ToFToF neutron spectrometer in order to investigate magnetic excitations in NiMn<sub>2</sub>O<sub>4</sub>. The experiment was performed at an incident wavelength of  $\lambda_i = 5$  Å (or 3.27 meV). We used a chopper frequency of 16,000 rpm (265 Hz), meaning that only one in 4 generated pulses could be used in order to avoid frame overlap. Count times were 4 hours per temperature. A few grams of sample were placed in a hollow Al cylinder in order to increase the sample material to travel path through sample ratio, while keeping it isotropic in the scattering plane. The data was normalized to Vanadium and an empty can measurement was subtracted.

#### 5.1.1 Elastic Data Treatment

The elastic line was found by summing data with energy transfers  $-0.1 \text{ meV} < \hbar\omega < 0.1 \text{ meV}$ . At low temperature 8 different contributions to the total signal was identified (see figure 5.1).

**Peak 1** is very broad and does not correspond to any lattice reflection but was interesting due to a possible quasi-elastic scattering contribution at the peak. However, due to the small size of the crystals the **SANS** signal overshadows this region and is probably also the cause of peak 1. Any attempts to investigate this further would need a SANS measurements to understand the general behaviour

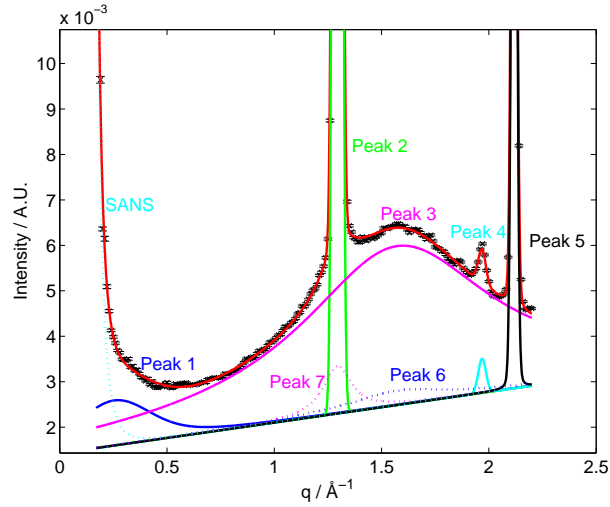


Figure 5.1: *The elastic line.* 4 K time-of-flight data from *TofToF* summed for energy transfers  $-0.1 \text{ meV} < \hbar\omega < 0.1 \text{ meV}$ .

in this region.

**Peak 2** is the NiMn<sub>2</sub>O<sub>4</sub> (111) reflection. It contains both a structural and a magnetic component. A small Voigt tail (**peak 7**) on the otherwise Gaussian peak 1 is needed to describe the peak in a satisfactory way.

The broad **Peak 3** constitutes some short range order in the system around the (200) reflection position with a correlation length of 5.2 Å, or less than a unit cell. The signal is, however, not well fitted with a single Voigt so a second Voigt (**peak 6**) has been added with the same position but half the Lorentz width, corresponding to the double correlation length.

The small **peak 4** were originally identified as a weak antiferromagnetic peak since it disappears at 50 K. It was, however, later realised that it was an anti-ferromagnetic signal from an impurity in the sample container.

**Peak 5** is the NiMn<sub>2</sub>O<sub>4</sub> (220) reflection.

### 5.1.2 Inelastic Data Treatment

A map of the inelastic signal at 40 K can be seen in figure 5.2. Apart from the elastic line and Bragg peaks an excitation signal can be seen at the position of the (111) Bragg peak. In order to subtract the background and map out the behaviour of the excitation, cuts with constant energy transfer were made and the signal fitted to two Voigt functions at (111) and (220). A sloping background and a SANS signal ( $c \cdot q^{-4}$ , where  $c$  is a fitted constant) was used for background. As the statistics in each cut was limited the position and Gaussian width of the excitations were kept constant at the values found from the elastic fit.

The fitted Lorentzian width of the (111) excitation as a function of energy transfer can be seen in figure 5.3. Apart from very close to the elastic line where the Bragg peak overshadows any signal, the width development falls in two separate

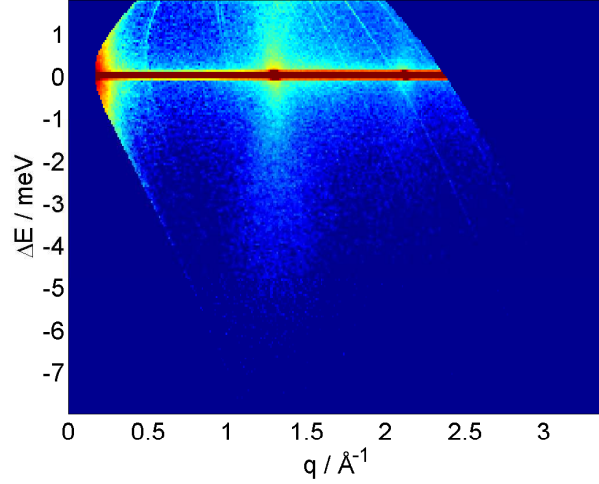


Figure 5.2: **Inelastic scattering.** 40 K time-of-flight data from ToFToF on logarithmic c-axis. The elastic line, the (111) reflection ( $q=1.29 \text{ \AA}^{-1}$ ), and the (220) reflection ( $q=2.11 \text{ \AA}^{-1}$ ) can be seen as well as some inelastic signal around the (111) reflection.

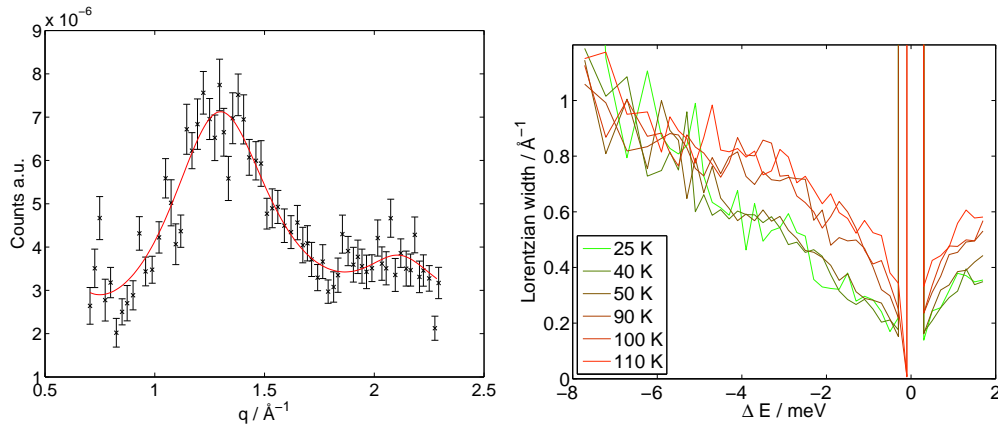


Figure 5.3: **Fit to single phonon model.** Left: Example of inelastic data from ToFToF fitted to a sloping background, two phonons at the (111) and (220) positions with a Voigt shape, and a SANS signal. The example is taken at 25 K and  $-3 \text{ meV} < \hbar\omega < -2.8 \text{ meV}$ . Right: The development of the fitted Lorentzian width as a function of energy transfer and temperature in case of the single phonon model.

categories: low temperature data and data from 90 K and above. Since the (111) peak both contains a structural and a magnetic component that passes into a paramagnetic phase at 90 K the excitation data above 90 K are interpreted as a phonon dispersion. Such a dispersion should also be existing at lower temperatures, however, it is expected to have a T-independent width.

We do, however, observe that the  $q$ -width in the magnetic phase is much lower.

Hence magnetism must play a role. The hypothesis is thus that some magnetic excitation with a lower width is present below 90 K and that the limited statistics means that the fitting routine can fit both using the same Voigt with a reduced width. The fitted intensities as function of temperature was also investigated but was less conclusive than the width development. In order to extract the magnetic excitation signal a new model with two Voigts at the (111) position is fitted to the constant energy transfer cuts. One Voigt, representing the phonon, have all parameters locked: Position and Gaussian width to the elastic line fit. The Lorentzian width was found by fitting the 110 K width development to a powerlaw. The intensity was calculated from the Bose occupation factor, normalized to the intensity in the  $-8 \text{ meV} < \hbar\omega < -6 \text{ meV}$  region where no separation between the two signals can be observed. With the phonon contribution determined the magnetic excitation was fitted to a second Voigt. The position and in Gaussian width was locked to the fit of the elastic signal while the intensity and Lorentzian width is fitted. Finally a sloping background, SANS signal and the (220) peak is built into the model.

The intensity of the magnetic signal can be seen in figure 5.4 (Right). The signal

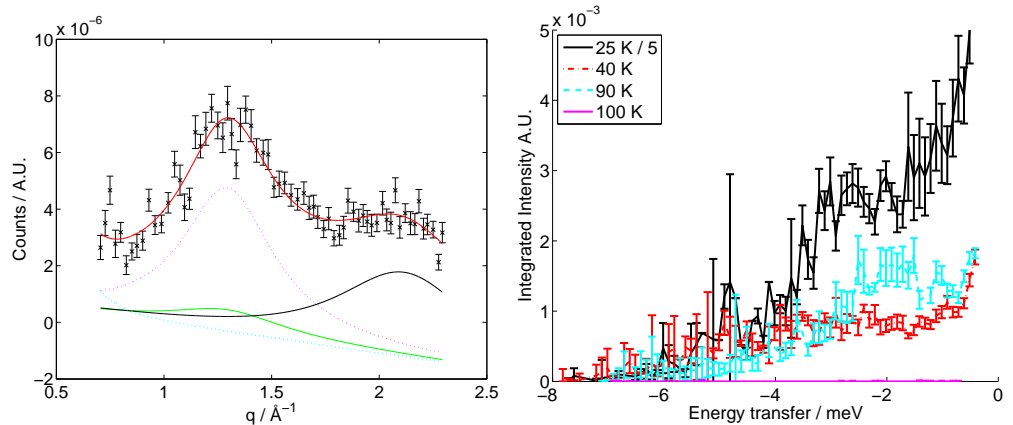


Figure 5.4: *Fit to the two excitations model.* Left: Example of fitted inelastic data. The Voigt shaped phonon at (111) is shown in green, the SANS signal in blue, and the magnetic excitation in magenta. The inelastic signal at (220) is only fitted to one Voigt and shown in black. All signals are shown on top of a sloping background. The total fit is shown in red and seems to fit the data well. The example is like in figure 5.3 left taken at 25 K and  $-3 \text{ meV} < \hbar\omega < -2.8 \text{ meV}$ . Right: The development of the fitted intensity of the magnetic excitation as function of energy transfer and temperature in two excitations model.

includes a quasi-elastic broadening of the (111) peak as well as indications of an excitation at  $-2 \text{ meV}$  for 90 K and  $-3 \text{ meV}$  for 25 K with a width of about 1 meV. This could be a magnetic gap that broadens with T. If an excitation exists at 40 K it is considerably broader. The signal disappears completely above 100 K.

### 5.1.3 Neutron Spectroscopy Results

Figure 5.5 displays the development of the different recorded signals as a function of temperature. At 91 K magnetization experiments have shown that the ferromagnetic component disappears. The loss of magnetic signal from the ToFToF data confirms that this is indeed the Curie Temperature of the system. This is in the low end of the broad region of temperatures between 100 K and 140 K reported by literature[48, 49, 56, 108] but as the system is very dependent on the manufacturing process, the value seems reasonable.

Below  $T_c$  both a quasi-elastic signal and an inelastic excitations can be observed though at 40 K the excitation seems to broaden or disappear. The integrated inelastic intensity also seems to be reduced before increasing strongly at 25 K. This agrees with other observations that some spin rearrangement occurs between 30 K and 50 K (see appendix A). Furthermore the broadening of the excitation could indicate that the spins in this phase are canted which have been observed to lead to a sort of dynamic spin-frustration effect in other spinel systems[128]. The results were published in an article, together with data from magnetisation

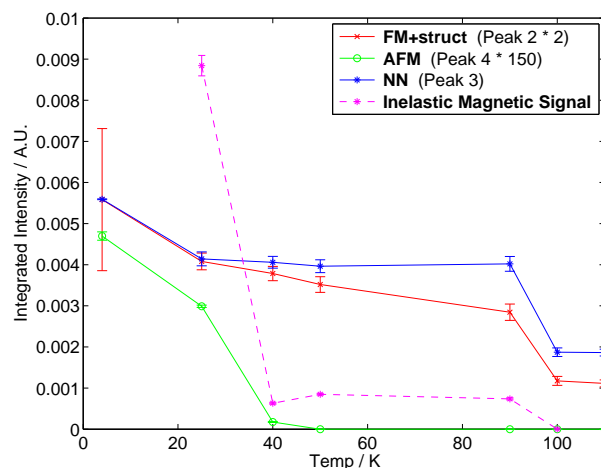


Figure 5.5: **Signal development.** The development in integrated intensity for some of the measured signals. The red is the elastic intensity of the ferromagnetic (111) peak, the green is the antiferromagnetic peak from the sample holder, the blue is the short range (nearest neighbour) signal at (the 200) reflection with a correlation length of  $5.2 \text{ \AA}$ , and the magenta signal is the inelastic magnetic signal at the (111) peak.

and powder diffraction experiments. (see appendix A).



## Chapter 6

# LiNiPO<sub>4</sub>

LiNiPO<sub>4</sub> is a magnetoelectric material. The magnetoelectric coupling can be described by a linear coupling constant of  $\alpha_{i,j} = 4 * 10^{-5}$  in rationalized Gaussian units[134] or  $1.7 * 10^{-12}$  s/m in SI units. This couples an electric field along the a(c) axis with an magnetic field along the c(a) axis by  $M_i = \sum_j \alpha_{i,j} E_j + \sum_{j,k} \beta_{i,j,k} E_j E_k$ , where  $M$  is the magnetisation,  $E$  is the Electric field and the nonlinear term is disregarded.

In recent years, great effort have been made to determine the spin configuration of this material at low temperature[78, 109]. The phase diagram for LiNiPO<sub>4</sub> in a magnetic field can be seen in figure 6.1. At low temperatures, when the field is increased above 12.1 T the spins rearrange from a commensurate antiferromagnet with a (0,1,0) reflection into an incommensurate phase with a (0,1+q,0) reflection, where  $q$  is approximately 0.16 but dependent on field and temperature.

Our hope was to study the quantum phase transition in this material. The original idea was to place the sample in a magnetic field just below the phase transition at the lowest possible T and use an electric field to generate the extra perturbation to move the sample across the phase transition through the magnetoelectric coupling in the sample.

The long term goal was to use this to do time resolved studies of quantum phase transitions since an electric field in principle can be changed faster than the time resolution of neutron spectrometers and reliable enough to allow stroboscopic measurements. It was, however, during the project realized that the detector electronics at PSI did not allow event mode recording. Instead RITA-II spends several seconds exporting each detector histogram to the instrument computer so it was not possible to perform actual time resolved studies at PSI with the existing setup. Instead the chapter documents the (unpublished) results that we were able to obtain with the present setup.

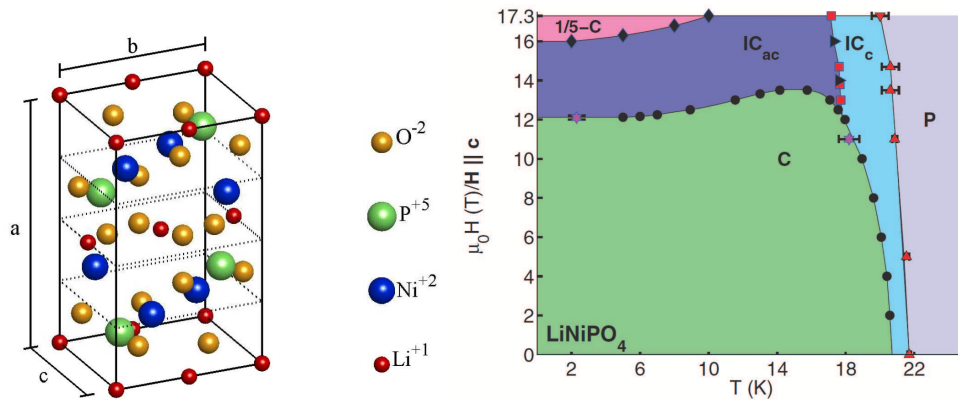


Figure 6.1:  $\text{LiNiPO}_4$ . Left: Crystal structure of  $\text{LiNiPO}_4$ .  $a=10.02 \text{ \AA}$ ,  $b=5.83 \text{ \AA}$ ,  $c=4.66 \text{ \AA}$  (from [78]). Right: Phase Diagram for  $\text{LiNiPO}_4$  (from [127]).

## 6.1 Measurement

### 6.1.1 Experimental Setup

In order to measure in a combined electric and magnetic field at low temperatures, a special sample stick was developed. The stick is compatible with all magnets at PSI, including the 15 T vertical split coil magnet needed for the experiment. Two wires provide the electric field and are led through a thermal anchor before the sample to stop heat transfer from the high voltage generator to the sample. The sample holder was a piece of sapphire, that conducts heat

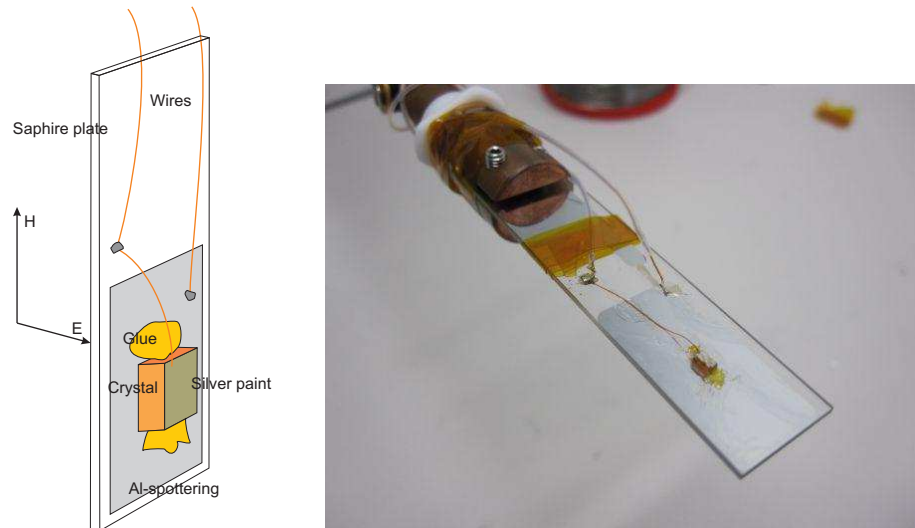


Figure 6.2: *Experimental Setup.*

but is electrically insulating with an area of silver sputtered on it (see figure 6.2). The sample was now glued onto one silver surface and painted with silver paint on the opposite side to form two conductor plates. One wire was soldered to silver surface and a second wire was fixed to the silver painted side of the sample

with silver paint. A power supply that could go to  $\pm 10$  KV was obtained.

In order to provide a uniform field in the entire sample a rectangular sample was needed. Two samples were aligned using x-ray Laue diffraction and cut along the (100), (010), and (001) axes. The crystals were afterwards  $1.7 \times 1.1 \times 1.3$  mm<sup>3</sup> and  $1.4 \times 1.3 \times 2.6$  mm<sup>3</sup>, respectively.

The experiment was performed at RITA II, PSI. The 15 T vertical magnet was used. The monochromator was set at  $E_i = 5$  meV. The analysers were also set to  $E_f$  meaning elastic scattering and a Be filter was used.

### 6.1.2 Experimental Results

When the E-field was raised above 4.5 KV, sparks could be observed by studying the current and temperature of the crystal. This limited the fields below these values for the remaining experiment.

During the experiments a hysteresis loop with a width of 0.4 T was observed in the magnetic phase transition at 1.5 K and 12.1 T. In order to cross this hysteresis the induced magnetic field would need to be more than 0.4 T, corresponding to  $0.4\text{T}/(1.7 * 10^{-12}\text{s/m})/(10^{-3}\text{m}) = 2.4 * 10^5$  KV, which would not be possible. It was thus decided to move across the phase transition and try to make the final push with the electric field. However, it was observed that close to the phase boundary the intensity of the antiferromagnetic (100) peak decreased with time, making such measurements unreliable. Instead, the hysteresis loop was investigated repeatedly at different electric fields (See figure 6.3). It can be seen that a hysteresis loop can be reproduced nicely by repeating the same scan at the same electric field, though it does change when the field is changed. It does however not shift but rather become narrower. One explanation for that is that the increased electrical field may have induced a small current in the sample that heats the sample, in turn narrowing the hysteresis. Unfortunately, the high E-fields had earlier produced sparking that had destroyed the sample thermometer so only the temperature at the cold anchor was available and did not show any change.

#### 6.1.2.1 Relaxation Times

The behaviour of the (010) peak was observed as a function of time at a temperature of 1.5 K and magnetic field of 11.83 T. The behaviour was fitted to an exponentially decreasing function but this did not seem to model the observations (see figure 6.4). The best fit ( $\chi^2 = 5.6$ ) was obtained with a logarithmic function, however the power law also showed a good fit ( $\chi^2 = 7.2$ ) with an exponent of  $\beta = 0.20$ . The exponentially decaying model fits very badly ( $\chi^2 = 76$ ) and saturates at a considerably lower level of 0.140 than the expected value of 0.185, found by measuring the intensity of the antiferromagnetic phase when the magnetic field was reduced and the magnetic phase transition was completed. The exponential decreasing behaviour can thus be discarded. None of the models can be a full description of the relaxation since they diverge at  $t \rightarrow \infty$ , though it

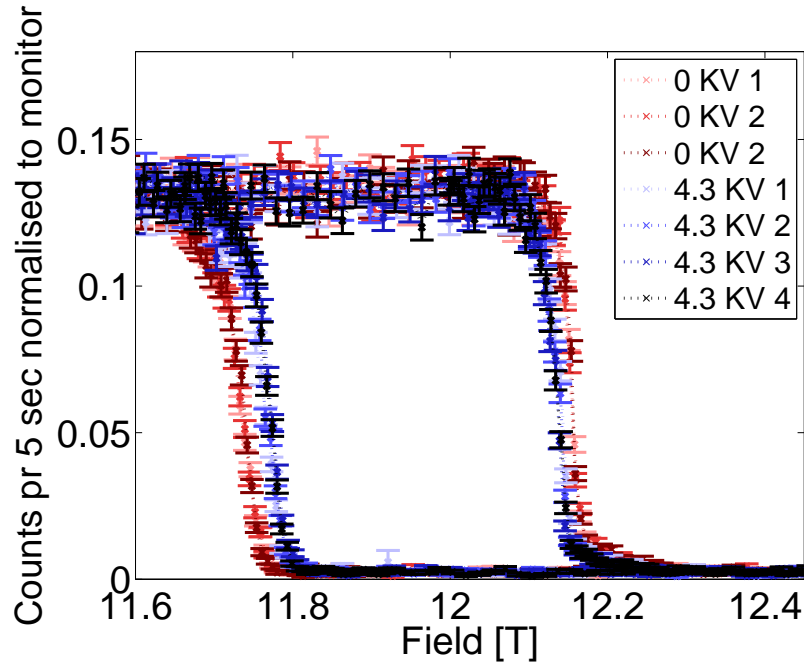


Figure 6.3: **Hysteresis loops for LiNiPO<sub>4</sub>**. The intensity of the commensurate (010) reflection recorded through 3 loops at  $E=0$  KV (red) and 4 loops at  $E=4.3$  KV (blue). The magnetic field of 12.3 T is parallel to the  $c$ -axis and the electric field parallel to the  $a$ -axis.

is possible that they will be true almost until saturation is reached. It is however very time consuming to map out the remaining part of the transition (the power law and logarithmic model will reach a full transformation after 106 and 156 hours respectively). It would be interesting to map at stronger fields where the relaxation is expected to happen considerably faster.

The respective equations of motion for the logarithmic and power law fit become:

$$A = a * \ln \left( \frac{t - t_0}{\tau} \right) \quad (6.1)$$

$$\Rightarrow \frac{dA}{dt} = \frac{a}{\tau} \frac{\tau}{t - t_0} \quad (6.2)$$

where  $A$  are the amount of material in the paramagnetic phase,  $a$  is some constant,  $\tau$  is a characteristic time, and  $t_0$  is the starting time. By inserting  $A = \frac{a}{\tau} * \ln \left( \frac{t-t_0}{\tau} \right) \Rightarrow e^{\frac{A}{a}} = \frac{t-t_0}{\tau}$  in (6.2)

$$\frac{dA}{dt} = \frac{a}{\tau} e^{-\frac{A}{a}} \quad (6.3)$$

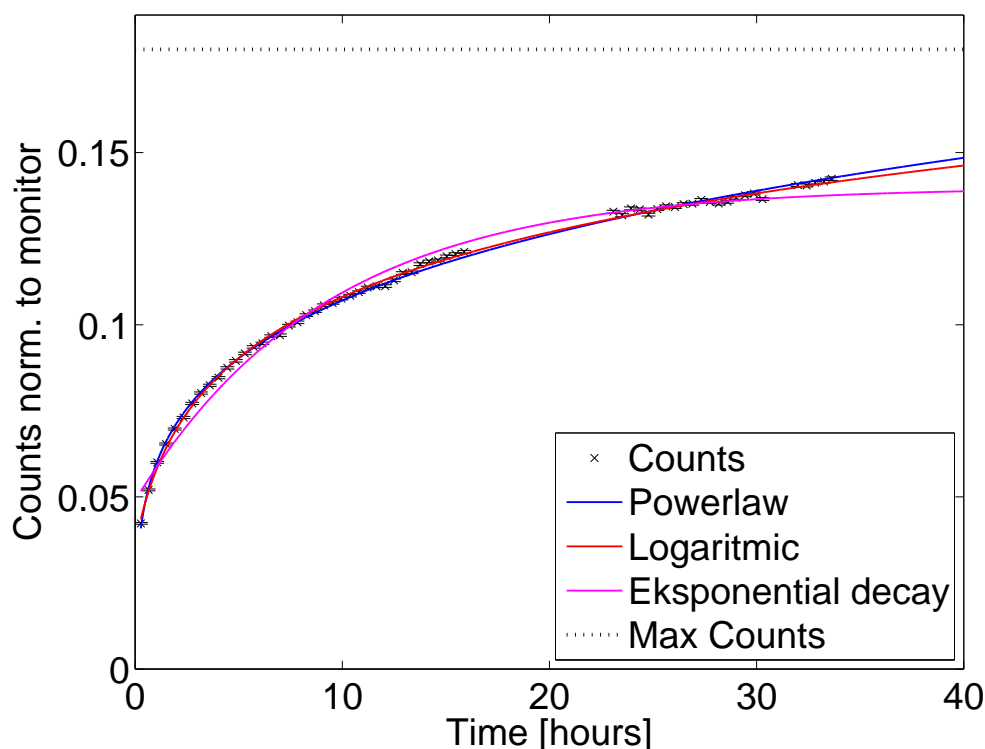


Figure 6.4: **Relaxation time.** During the measurement the detector experienced some instability leading to the holes in the dataset.

Equivalently:

$$A = a * \left( \frac{t - t_0}{\tau} \right)^\beta \quad (6.4)$$

$$\Rightarrow \frac{dA}{dt} = \frac{\beta * a}{\tau} * \left( \frac{t - t_0}{\tau} \right)^{\beta-1} = \frac{\beta a}{\tau} \left( \frac{A}{a} \right)^{\frac{\beta-1}{\beta}} = \frac{a^5}{5\tau} \frac{1}{A^4} \quad (6.5)$$

The reaction shape does not fit the two most obvious driving forces for such relaxations:

- At such low temperatures an obvious driving force would be quantum mechanical tunnelling through the potential barrier, or rare thermal fluctuations. This is known from textbook spin-lattice relaxation theory and follow a exponentially decreasing pattern.[45]
- If the process is self-reinforcing by releasing energy that makes it more likely for the remaining reactants to cross the potential barrier the process should be accelerating until equilibrium with the cooling of the system is potentially reached.

It is possible that the results are some combination of different contributions, though it is surprising that this leads to a simple logarithmic behaviour over

long time and a considerable part of the reaction. It is also possible that one needs to investigate the full spin arrangement instead of the independent spins. The energy barrier a spin is required to pass to rearrange is a function of the arrangement of neighbouring spins. When spins rearrange this will thus change the relaxation time of their neighbours. This could explain the process happening faster than described by a single exponential decay, though a more thorough investigation is needed to see if the observed behaviour can be explained by this model. At the time, these results were not the main point of the experiment and they have thus not been pursued afterwards but a thorough literature study potentially followed by more experiments could potentially bring new knowledge on time dependence of phase transitions.

## 6.2 Conclusion

The experiment showed that the project of using electric fields to move a sample across a quantum phase transition could not be performed on LiNiPO<sub>4</sub>. Though it is still a very interesting project it needed new samples to be grown as well as investments in new options for event mode recording at PSI. At the time it was not believed that event mode recording could be implemented at PSI without new electronics, which was far above the budget of the project. It was of course an option to make the experiment at another facility. However, this would involve exporting PSI know-how to other facilities and since the project was partly PSI funded this was not reasonable. Instead the project moved towards designing new instrumentation that would enable time resolved studies. A work that eventually leads to possibilities of time resolved studies on PSI. Mainly by using the coming CAMEA upgrade for RITA II but also through development of new data analysis software. Hence, the goal of performing such experiments is closer to fulfilment than before the project.

## Chapter 7

# Concluding Remarks

The majority of this PhD project evolved around the design of the CAMEA instrument for ESS. During the project I also participated in the several smaller experimental and simulation projects. Two are described in the LiNiPO<sub>4</sub> and NiMn<sub>2</sub>O<sub>4</sub> chapters.

### CAMEA

CAMEA is an inverse time-of-flight spectrometer with a multiplexing backend. It takes advantage of the long ESS pulse and transports a flux of up to  $1.8 \times 10^{10}$  neutrons/s/cm<sup>2</sup> in a 1.7 Å wavelength band to the sample position, with an energy resolution of  $\Delta E_i/E_i = 3.5\%$  at  $E_i = 5$  meV but can improve the primary energy resolution down to 0.1% by the use of choppers. The flux is transported by a guide consisting of a parabolic feeder, and two ellipses with a kink between them to ensure that line of sight from the moderator is lost 25 m before the sample. The backend consists of a number of concentric analyser arcs that reflects the neutrons down towards position sensitive detectors. This ensures analyser angular coverage of 90° out of the instrument tank's 135° in the scattering plane. This coverage can be multiplied with 30 simultaneously recoded  $E_f$  values, due to the 10 analyser arc and the new prismatic analyser concept that allows detection of 3 energies from each analyser. The backend has resolutions of  $\delta a_4 = 0.6^\circ$  and  $\Delta E_f/E_f = 1.1\%$  at  $E_f = 5$  meV. An order sorting chopper enables the instrument to distinguish first and second order scattering and record up to 60 energies simultaneously. The background level is by prototyping found to be in the order  $5 \times 10^{-5}$  compared to the elastic line of Vanadium and the inverse time-of-flight design together with the long primary flight path ensures that elastic scattering from sample environments will end up in the elastic line, keeping the inelastic background at very low levels. This together with the up to 20 times higher count rate in the horizontal scattering plane than on a direct time-of-flight spectrometer at ESS makes CAMEA a very powerful instrument for extreme environment studies.

The design of a CAMEA spectrometer for ESS was a large project, involving 4 institutes, 12 scientists and a number of technicians. Kinematic calculations were performed to investigate what the instrument could measure dependent on

the overall layout. Simple demonstration experiments were undertaken and a prototype constructed and installed in the MARS backscattering spectrometer at PSI. Prototype data, simulations and thorough calculations was used to determine the performance and its dependence on parameters thoroughly. From this a final instrument was proposed. Demonstration experiments on  $\text{YHoF}_4$  and  $\text{YMnO}_3$  further demonstrated that the instrument principles work and can produce useful data. The project has so far concluded with the final acceptance from the ESS Steering Committee to build the instrument, on recommendation from the EES Scientific Advisory Committee.

During the project a new prismatic analyser concept was invented. This concept uses distance collimation to record several different energies from a single analyser. In this way the same amount of neutrons can be recorded with a finer energy resolution and by relaxing the analyser mosaicity it is possible to increase the total recorded flux while keeping a finer energy resolution. The prismatic analyser can be used on both inverse time-of-flight spectrometers and traditional triple axis instruments.

### **$\text{LiNiPO}_4$**

The magneto-electric system  $\text{LiNiPO}_4$  was a candidate for time resolved neutron scattering studies of quantum phase transitions. During the project it becomes clear that a large hysteresis around the phase transition coupled with spin relaxation would complicate such measurements considerably. The spin-relaxation associated with the (1st order) quantum phase transition did however show unusual behaviour that could deserve further investigation.

### **$\text{NiMn}_2\text{O}_4$**

$\text{NiMn}_2\text{O}_4$  is a system where the magnetic phase diagram has shown strong dependence on the manufacturing process. In this project a powder was produced by a chemical process to ensure a uniform sample. Neutron spectrometry performed at ToFToF showed agreement with previous measurements with neutrons and other techniques and showed some evidence of a new magnetic phase transitions at 40-50 K.

## **Additional work during the PhD enrolment**

In addition to the work described in the thesis I participated in a number of other projects. The Studies of Goethite and the time-structure for ESS are explained in the attached articles.

### **Goethite**

The magnetic excitations around the (200) reflection in two samples of Goethite nano crystals were investigated with neutron scattering. A  $\mathbf{q} = 0$  spinwave with an energy of  $\hbar\omega \sim 1.0$  to  $1.5$  meV was observed in the excitation spectrum

and described as function of temperature. A magnetic anisotropy constant of  $K \sim 0.6 * 10^5 \text{Jm}^{-3}$  was derived from the data behaviour of the excitation.

### **The pulse structure of the future European Spallation Source**

The performance of a generic instrument suite for ESS was investigated as a function of pulse structure and the data combined into a single performance number. This helped ESS decide on a pulse structure for the coming source to be 14 Hz and a pulselength of 2.86 ms.



# Chapter 8

## List of Publications

### Published/Accepted

#### **A Prismatic Analyser concept for Neutron Spectrometers**

Jonas O Birk, Marton Marko, Paul G Freeman, Johan Jacobsen, Niels B Christensen, Christof Niedermayer, Henrik M Rønnow, and Kim Lefmann. Review of Scientific Instruments, accepted (2014).

#### **Simulation of a suite of generic long-pulse neutron instruments to optimize the time structure of the European Spallation Source.**

K Lefmann, JO Birk, KH Klenø, BR Hansen, SL Holm, E Knudsen, K Lieutenant, L von Moos, M Sales, PK Willendrup, and KH Andersen, 2013, Review of Scientific Instruments, vol 84, nr. 5, 055106., <http://dx.doi.org/10.1063/1.4803167> (2013).

#### **Ferrimagnetism and spin excitation in a Ni-Mn partially inverted spinel prepared using a modified polymeric precursor method.**

Rafael A. Ferreira, Julio C.G. Tedesco, Jonas O. Birk, Walter Kalceff, Fabiano Yokaichiya, Nina Rasmussen, Octavio Pena, Paul F. Henry, Giovanna G. Simeoni, Heloisa N. Bordallo, and Paulo N. Lisboa-Filho, Materials Chemistry and Physics 07/2014; 146(s 1-2):58-64. (2014).

#### **Magnetic properties of ultra-small goethite nanoparticles**

E. Brok, C. Frandsen, D.E. Madsen, H. Jacobsen, J. O. Birk, K. Lefmann, J. Bendix, K. S. Pedersen, C. Boothroyd, A.A. Berhe, G.G. Simeoni, and S. Mørup. Journal of Physics D: Applied Physics 47 365003 (2014).

#### **CAMEA ESS - The Continuous Angle Multi-Energy Analysis Indirect Geometry Spectrometer for the European Spallation Source.**

Paul G Freeman, Jonas O Birk, Marton Marko, Johan Jacobsen, Niels B Christensen, Christof Niedermayer, Henrik M Rønnow, and Kim Lefmann. QENS/WINS 2014 proceedings, accepted (2014).

**In Preparation:****Nano-criticality in small CoO Particles**

Jonas Okkels Birk, Jari i Hjöllum, Thorbjørn Lourcing Koch, Jacob Lass, Elisabeth Ulrikkenholm, Niels Bech Christensen, Erik Brok, Cathrine Frandsen, Christof Niedermayer, Luise Theil Kuhn, Lukas Keller and Kim Lefmann.

**The CAMEA Prototype**

Marton Marko, Jonas O Birk, Paul G Freeman, Johan Jacobsen, Niels B Christensen, Christof Niedermayer, Henrik M Rønnow, and Kim Lefmann.

**Non Peer reviewed publications:**

In addition, a number of reports were produced for ESS during the design of CAMEA. The ESS Technical Design Report was a grand undertaking by everyone included in the ESS design project and my contribution in this scheme is minor. The ESS Instrument Construction Proposal CAMEA was produced in collaboration in the CAMEA design work-unit. I was main author of the Instrument Description and Technical Maturity chapters and participated to all other chapters except the Executive summary. Building and Testing a Prototype for CAMEA was written in collaboration between Marton Marko and me. The CAMEA: Guide Report was a collaboration between Mads Bertelsen and me. CAMEA: Simulations and Kinematic Calculations and CAMEA: Comparison to the Colder Chopper Spectrometer was mostly done by me.

**ESS Technical Design Report**

S. Peggs et al,

[http://eval.ess.lu.se/DocDB/0002/000274/015/TDR\\_online\\_ver\\_all.pdf](http://eval.ess.lu.se/DocDB/0002/000274/015/TDR_online_ver_all.pdf) (2013).

**ESS Instrument Construction Proposal CAMEA.**

Freeman, Paul; Rønnow, Henrik M.; Niedermayer, Christof; Jurányi, Fanni; Markó, Márton; Lefmann, Kim; Larsen, Jacob Okkels; Bertelsen, Mads; Christensen, Niels Bech; Larsen, Jacob <http://infoscience.epfl.ch/record/190509?ln=en> (2014).

**Building and Testing a Prototype For CAMEA.**

Márton Markó, Jonas Okkels Birk, <http://infoscience.epfl.ch/record/197952?ln=en> (2014).

**CAMEA: Simulations and Kinematic Calculations.**

Birk, Jonas Okkels <http://infoscience.epfl.ch/record/190505?ln=en> (2014).

**CAMEA: Guide Report.**

<http://infoscience.epfl.ch/record/190503?ln=en> (2014).

**CAMEA: Comparison to the Colder Chopper Spectrometer.**

<http://infoscience.epfl.ch/record/190496?ln=en> (2014).

# Bibliography

- [1] <http://lns00.psi.ch/sinqwiki/wiki.jsp?page=ma15specifications>.
- [2] <https://www.ill.eu/instruments-support/sample-environment/equipment/high-magnetic-fields/vertical-field-magnets/>.
- [3] <http://www.ess-dmsc.eu/computing-centre>.
- [4] <http://www.psi.ch/sinq/eiger/description>.
- [5] <http://www.psi.ch/sinq/mars/description>.
- [6] <http://www.psi.ch/sinq/morpheus/description>.
- [7] Kanya homepage: <http://www.kanya.ch/wdeutsch/index.php>.
- [8] Personal communications with Stefan Klotz.
- [9] Ian sutten, personal communication, 2013.
- [10] Marton marko, personal communication, 2013.
- [11] Oxford instruments, personal communication, 2013.
- [12] <http://europeanspallationsource.se/>, 2014.
- [13] <http://neutrons.ornl.gov/>, 2014.
- [14] <http://neutrons.ornl.gov/equipment/equip-detail.cfm?recordid=mag-002&facility=sns>, 2014.
- [15] <http://www-llb.cea.fr/en/>, 2014.
- [16] <http://www.ansto.gov.au/aboutansto/opal/index.htm>, 2014.
- [17] <http://www.frm2.tum.de/en/>, 2014.
- [18] [http://www.helmholtz-berlin.de/forschung/oe/em/transport-phenomena/flex/index\\_en.html](http://www.helmholtz-berlin.de/forschung/oe/em/transport-phenomena/flex/index_en.html), 2014.
- [19] [http://www.helmholtz-berlin.de/quellen/ber/index\\_de.html](http://www.helmholtz-berlin.de/quellen/ber/index_de.html), 2014.
- [20] <http://www.ill.eu/en/>, 2014.
- [21] <http://www.isis.stfc.ac.uk/>, 2014.

- [22] <http://www.isis.stfc.ac.uk/instruments/wish/technical/wish-technical-information7362.html>, 2014.
- [23] <http://www.isis.stfc.ac.uk/sample-environment/low-temperature/cryostats/files/orange-cryostat-operating-procedures11594.pdf>, 2014.
- [24] <http://www.j-parc.jp/index-e.html>, 2014.
- [25] <http://www.mcstas.org/>, 2014.
- [26] <http://www.mlz-garching.de/panda>, 2014.
- [27] <http://www.ncnr.nist.gov/>, 2014.
- [28] <http://www.psi.ch/sinq/>, 2014.
- [29] <http://www.psi.ch/sinq/ritaii/description>, 2014.
- [30] <http://www.swissneutronics.ch/>, 2014.
- [31] Poldi homepage: <http://www.psi.ch/sinq/poldi/description>, 2014.
- [32] H. Abele, D. Dubbers, H. Hase, M. Klein, a. Knopfler, M. Kreuz, T. Lauer, B. Markisch, D. Mund, V. Nesvizhevsky, a. Petoukhov, C. Schmidt, M. Schumann, and T. Soldner. Characterization of a ballistic supermirror neutron guide. *Nuclear Instruments and Methods in Physics Research Section A: Accelerators, Spectrometers, Detectors and Associated Equipment*, 562:407–417, 2006.
- [33] L. Alianelli, M. S. del Rio, and R. Felici. Characterization and modelling of germanium assembled crystals for the diffraction of thermal neutrons. *J. Appl. Cryst.*, 37:732–742, 2004.
- [34] J. Als-Nielsen and D. McMorrow. *Elements of modern x-ray physics*. Wiley, New York, NY, 2001.
- [35] P. Andersen, K. Lefmann, L. T. Kuhn, P. Willendrup, and E. Farhi. Monte carlo simulations as a part of the configuration for neutron instruments. *Physica B: Condensed Matter*, 350:E721 – E724, 2004. Proceedings of the Third European Conference on Neutron Scattering.
- [36] S. Åsbrink, A. Waskowska, M. Drozd, and E. Talik. Physical properties and x-ray diffraction of a nimn2o4 single crystal below and above the ferrimagnetic transition at  $t_c = 145$  k. *Journal of Physics and Chemistry of Solids*, 58(5):725 – 729, 1997.
- [37] N. W. Ashcroft and N. D. Mermin. *Solid State Physics*. 1976.
- [38] C. R. H. Bahl, P. Andersen, S. N. Klausen, and K. Lefmann. The monochromatic imaging mode of a rita-type neutron spectrometer. *Nuclear Instruments and Methods B*, 226:667–681, 2004.

- [39] R. J. Barlow. *Statistics, A Guide to the Use of Statistical Methods in the Physical Sciences*. John Wiley & Sons, 1999.
- [40] K. Batkov, A. Takibayev, L. Zanini, and F. Mezei. Cold moderators for long pulse neutron sources: unperturbed brightness. Technical report, ESS, 2013.
- [41] M. Bertelsen. Optimizing neutron guides using the minimalist principle and guide.bot. Master's thesis, Niels Bohr Institute, University of Copenhagen, 2014.
- [42] M. Bertelsen, H. Jacobsen, U. Bengaard Hansen, H. Hoffmann Carlsen, and K. Lefmann. Exploring performance of neutron guide systems using pinhole beam extraction. *Nuclear Instruments and Methods in Physics Research A*, 729:387–398, Nov. 2013.
- [43] R. Bewley, J. Taylor, and S. Bennington. Let, a cold neutron multi-disk chopper spectrometer at ISIS. *Nuclear Instruments and Methods in Physics Research Section A: Accelerators, Spectrometers, Detectors and Associated Equipment*, 637(1):128 – 134, 2011.
- [44] J. O. Birk. Camea - comparison to cold chopper. <http://infoscience.epfl.ch/record/190496?ln=en>, 2014.
- [45] S. Blundell. *Magnetism in Condensed Matter*. Oxford University Press, 2006.
- [46] M. Boehm, S. Roux, A. Hiess, and J. Kulda. Thales - towards the next generation cold neutron three-axis spectrometer. *Journal of Magnetism and Magnetic Materials*, 310(2, Part 3):e965 – e967, 2007. Proceedings of the 17th International Conference on Magnetism The International Conference on Magnetism.
- [47] P. Böni. New concepts for neutron instrumentation. *Nuclear Instruments and Methods in Physics Research Section A: Accelerators, Spectrometers, Detectors and Associated Equipment*, 586(1):1 – 8, 2008. Proceedings of the European Workshop on Neutron Optics NOP '07.
- [48] B. Boucher, R. Buhl, and M. Perrin. Etude cristallographique du manganite spinelle cubique  $\text{NiMn}_2\text{O}_4$  par diffraction de neutrons. *Acta Crystallographica Section B*, 25(11):2326–2333, Nov 1969.
- [49] C. Boudaya, L. Laroussp, E. Dhahrp, J. C. Joubert, and A. Cheikh-Rouhou. Preparation and characterization of the spinel series  $\text{Co}_{6+x}\text{Ni}_{4-x}\text{Mn}_8\text{O}_{24}$  ( $0 \leq x \leq 4$ ). *Phase Transitions*, 68(4):631–642, 1999.
- [50] C. Carlile and M. Adams. The design of the IRIS inelastic neutron spectrometer and improvements to its analysers. *Physica B: Condensed Matter*, 182(4):431 – 440, 1992. Quasielastic Neutron Scattering.

- [51] L. C. Chapon, P. Manuel, P. Radaelli, C. Benson, L. Perrott, S. Ansell, N. Rhodes, D. Raspino, D. Duxbury, E. Spill, and J. Norris. Wish: the new powder and single crystal magnetic diffractometer on the second target station. *Neutron News*, 22:22:2, 2011.
- [52] N. Cherkashyna, K. Kanaki, T. Kittelmann, U. Filges, P. Deen, K. Herwig, G. Ehlers, G. Greene, J. Carpenter, R. Connatser, R. Hall-Wilton, and P. M. Bentley. High energy particle background at neutron spallation sources and possible solutions. *Journal of Physics: Conference Series*, 528(1):012013, 2014.
- [53] J. Christ and T. Springer. Über die entwicklung eines neutronleiters am frn-reaktor. *Nukleonik*, 4:23–25, 1962.
- [54] G. Cicognani, editor. *The ILL Yellow Book*. ILL, 2008.
- [55] A.-J. Dianoux and G. Lander. Ill neutron data booklet, 2003.
- [56] A. Diez, R. Schmidt, A. E. Sagua, M. A. Frechero, E. Matesanz, C. Leon, and E. Moran. Structure and physical properties of nickel manganite  $\text{NiMn}_2\text{O}_4$  obtained from nickel permanganate precursor. *Journal of the European Ceramic Society*, 30(12):2617 – 2624, 2010.
- [57] G. Ehlers, A. A. Podlesnyak, J. L. Niedziela, E. B. Iverson, and P. E. Sokol. The new cold neutron chopper spectrometer at the spallation neutron source - design and performance. *Rev. Sci. Instrum.*, 82:085108, 2011.
- [58] T. Eichhorn, N. Niketic, B. van den Brandt, U. Filges, T. Panzner, E. Rantsiou, W. Wenkebach, and P. Hautle. Proton polarization above 70states, a first step towards a broadband neutron spin filter. *Nuclear Instruments and Methods in Physics Research Section A: Accelerators, Spectrometers, Detectors and Associated Equipment*, 754(0):10 – 14, 2014.
- [59] A. Evans, S. Van Petegem, and H. Van Swygenhoven. Poldi: Materials science and engineering instrument at sinq. *NEUTRON NEWS*, 20:17, 2009.
- [60] F.Mezei and M.Russina. Patent: Neutronenoptische bauelementenanordnung zurgezielten 242 spektralen gestaltung von neutronenstrahlen oder pulsen, 2002.
- [61] F.Mezei and M.Russina. Patent: Neutron-optical component array for the specific spectral shaping of neutronbeams or pulses, 2006.
- [62] P. Freeman. Benching Mark CAMEA Against Present Inelastic Neutron Spectrometers. Technical report, 2014.
- [63] P. Freeman. Camea - concept and science case. <http://infoscience.epfl.ch/record/190011?ln=en>, 2014.

- [64] P. Freeman. Continuous Angular Multiple Energy Analysis Spectrometer Report on Instrument Concept and Scientific Case. Technical report, 2014.
- [65] D. L. Garber and R. R. Kinsey. Neutron cross sections, vol. ii, curves. *Brookhaven National Laboratory report*, page 325, 1976.
- [66] M. Haag, B. van den Brandt, T. Eichhorn, P. Hautle, and W. Wenckebach. Spin filtering neutrons with a proton target dynamically polarized using photo-excited triplet states. *Nuclear Instruments and Methods in Physics Research Section A: Accelerators, Spectrometers, Detectors and Associated Equipment*, 678(0):91 – 97, 2012.
- [67] K. Habicht and M. Skoulatos. Optimization of virtual source parameters in neutron scattering instrumentation. *Journal of Physics: Conference Series*, 340:012029, 2012.
- [68] K. Habicht, R. Toft-Petersen, M. Kure, L. Mäde, F. Groitl, M. D. Le, and D. L. Quintero-Castro. The upgraded cold neutron triple-axis spectrometer flexx - enhanced capabilities by new instrumental options. *QENS / WINS conference proceedings*, in printing, 2014.
- [69] K. Haldrup, M. Christensen, and M. Nielsen. Analysis of time-resolved x-ray scattering data from solution-state systems. *Acta Crystallographica. Section A: Foundations of Crystallography*, 66:261–269, 2010.
- [70] K. Haldrup and M. Nielsen. *Measuring and understanding ultrafast phenomena using X-rays*, pages 91–113. NATO Science for Peace and Security Series A: Chemistry and Biology. Springer Science+Business Media B.V., 2014.
- [71] A. Hiess, M. Jimenez-Ruiz, P. Courtois, R. Currat, J. Kulda, and F. Bermejo. ILL’s renewed thermal three-axis spectrometer IN8: A review of its first three years on duty. *Physica B: Condensed Matter*, 385-386, Part 2(0):1077 – 1079, 2006. Proceedings of the Eighth International Conference on Neutron Scattering.
- [72] H. Hiraka, Y. Miyake, S.-C. Che, N. Murakami, M. Ohkawara, K. Nemoto, K. Horigane, K. Ohoyama, Y. Yamaguchi, and K. Yamada. Application of hot-pressed ge-crystal monochromators for reactor-based neutron beam experiments. *Journal of the Physical Society of Japan*, 80(Suppl.B):SB012, 2011.
- [73] I. I. Hirschman and D. V. Widder. *The Convolution Transform*. Princeton University Press, 1955.
- [74] S. L. Holm. Heimdal a powerful instrument for novel material science. Master’s thesis, Niels Bohr Institute, University of Copenhagen, 2014.
- [75] S. L. Holm, N. Rasmussen, L. Høpfner, M. Bertelsen, J. Voigt, K. H. Andersen, and K. Lefmann. Neutron guide-spilt: A high performance

- guide bundle concept for elliptical guides. *Nuclear Inst. and Methods in Physics Research*, submitted, 2014.
- [76] C. J. Howard, B. J. Campbell, H. T. Stokes, M. A. Carpenter, and R. I. Thomson. Crystal and magnetic structures of hexagonal YMnO<sub>3</sub>. *Acta Crystallographica Section B*, 69(6):534–540, Dec 2013.
- [77] H. Jacobsen, K. Lieutenant, C. Zandler, and K. Lefmann. Bi-spectral extraction through elliptic neutron guides. *Nuclear Instruments and Methods in Physics Research A*, 69 - 76:717, 2013.
- [78] T. B. S. Jensen. *Magnetic structures, phase diagram and spin waves of magneto-electric LiNiPO<sub>4</sub>*. PhD thesis, Risø National Laboratory for Sustainable Energy, Technical University of Denmark, 2007.
- [79] M. Jiménez-Ruiz and A. Hiess. IMPS: A multianalyser detector system for the thermal three-axis spectrometer IN8. *Physica B*, 385-386:1086–1088, 2006.
- [80] F. Jurányi. Pg prices. Technical report, PSI.
- [81] M. Kempa, B. Janousova, J. Saroun, P. Flores, M. Boehm, F. Demmel, and J. Kulda. The flatcone multianalyzer setup for ill’s three-axis spectrometers. *Physica B*, 385-386:1080 – 1082, 2006.
- [82] M. Kenzelmann, A. Zheludev, S. Raymond, E. Ressouche, T. Masuda, P. Böni, K. Kakurai, I. Tsukada, K. Uchinokura, and R. Coldea. Magnetic order and spin-waves in the quasi-1d s=1/2 antiferromagnet BaCu<sub>2</sub>Si<sub>2</sub>O<sub>7</sub>. *Phys. Rev. B*, 64:054422, 2001.
- [83] C. Kittel. *Introduction to Solid State Physics*. Wiley, 2004.
- [84] K. H. Klenø. *Exploration of the challenges of neutron optics and instrumentation at long pulsed spallation sources*. PhD thesis, Copenhagen University, 2014.
- [85] K. Klenø, K. Lefmann, P. Willendrup, P. Christiansen, and R. Bewley. Simulations of chopper jitter at the let neutron spectrometer at the isis ts2. *Journal of Neutron Research*, 17, Number 2:77–85, 2014.
- [86] K. H. Klenø, K. Lieutenant, K. H. Andersen, and K. Lefmann. Systematic performance study of common neutron guide geometries. *Nuclear Instruments and Methods in Physics Research Section A: Accelerators, Spectrometers, Detectors and Associated Equipment*, 696(0):75 – 84, 2012.
- [87] L. Landau and E. Lifshitz. *Statistical Physics*. Elsevier, 1951.
- [88] J. Larsen. CAMEA: Pyrolytic Graphite Experimental Results. Technical report, 2014.

- [89] M. Le, D. Quintero-Castro, R. Toft-Petersen, F. Groitl, M. Skoulatos, K. Rule, and K. Habicht. Gains from the upgrade of the cold neutron triple-axis spectrometer FLEXX at the BER-II reactor. *Nuclear Instruments and Methods in Physics Research Section A: Accelerators, Spectrometers, Detectors and Associated Equipment*, 729(0):220 – 226, 2013.
- [90] K. Lefmann. Neutron scattering: Theory, instrumentation and simulation.
- [91] K. Lefmann, D. F. McMorrow, H. M. Rønnow, K. Nielsen, K. N. Clausen, B. Lake, and G. Aeppli. Added flexibility in triple axis spectrometers: the two ritas at risø. *Physica B*, 283:343–354, 2000.
- [92] K. Lefmann and K. Nielsen. Mcstas, a general software package for neutron ray-tracing simulations. *Neutron News*, 10:20, 1999.
- [93] R. L. Liboff. *Introductory Quantum Mechanics*. Addison Wesley, 2003.
- [94] K. Lieutenant, G. Zsigmond, S. Manoshin, M. Fromme, H. N. Bordallo, D. Champion, J. Peters, and F. Mezei. Neutron instrument simulation and optimization using the software package vitess, 2004.
- [95] P. Lisboa-Filho, M. Bahout, P. Barahona, C. Moure, and O. Pena. Oxygen stoichiometry effects in spinel-type  $\text{NiMn}_2\text{O}_{4-\delta}$  samples. *Journal of Physics and Chemistry of Solids*, 66(7):1206 – 1212, 2005.
- [96] M. Loewenhaupt and N. M. Pyka. The ultrahigh flux polarized cold neutron spectrometer PANDA of the FRM-II reactor. *Journal of Applied Physics*, 85:5145, 1999.
- [97] H. Maier-Leibnitz and T. Springer. The use of neutron optical devices on beam-hole experiments. *J. Nucl. Energy*, 17:217, 1963.
- [98] W. Mampe, P. Ageron, C. Bates, J. M. Pendlebury, and A. Steyerl. Neutron lifetime measured with stored ultracold neutrons. *Phys. Rev. Lett.*, 63:593–596, Aug 1989.
- [99] M. Markó. Building and Testing a Prototype For CAMEA. Technical report, 2014.
- [100] M. Markó, J. O. Birk, P. G. F. K. Lefmann, N. B. Christensen, C. Niedermayer, F. Jurányi, and H. M. Rønnow. Building and testing of prototype for continuous angle multiple energy analysing spectrometer. *in preparation*, 2014.
- [101] F. Mezei. Novel polarized neutron devices: supermirror and spin component amplifier. *Comm. Phys.*, 1:81–85, 1976.
- [102] F. Mezei. Advances by innovation and building on experience. *The ESS project, New Science and Technology for the 21st Century*, II, 2002.
- [103] F. Mezei and P. Dagleish. Corrigendum and experimental evidence on neutron supermirrors. *Comm. Phys*, 2:41–43, 1977.

- [104] A. Moore, M. Popovici, and A. Stoica. Neutron reflectivity and lattice spacing spread of pyrolytic graphite. *Physica B: Condensed Matter*, 276-278(0):858 – 859, 2000.
- [105] M. P. Nieh, Z. Yamani, N. Kucerka, and J. Katsaras. Adapting a triple-axis spectrometer for small angle neutron scattering measurements. *Journal of Physics: Conference Series*, 251, 2010.
- [106] S. Parker, C. Carlile, T. Pike, J. Tomkinson, R. Newport, C. Andreani, F. Ricci, F. Sacchetti, and M. Zoppi. Tosca: a world class inelastic neutron spectrometer. *Physica B: Condensed Matter*, 241-243(0):154 – 156, 1997. Proceedings of the International Conference on Neutron Scattering.
- [107] S. Peggs, R. Kreier, C. Carlile, R. Miyamoto, A. Paahlsson, M. Trojer, and J. G. Weisend II. ESS technical design report. Technical report, ESS, 2013.
- [108] O. Pena, X. Cailleaux, B. Piriou, M. del Canto, S. Abarca, E. Rios, J. Ortiz, J. Gautier, P. Lisboa-Filho, and C. Moure. Magnetic properties of  $\text{Cu}_{1+x}\text{Mn}_{2-x}\text{O}_4$  and  $\text{Ni}_{1+x}\text{Mn}_{2-x}\text{O}_4$  solid solutions. *Journal of the European Ceramic Society*, 27(13-15):3911 – 3914, 2007. Refereed Reports ELECTROCERAMICS X 2006.
- [109] R. T. Petersen. *Magnetic structures of the lithium orthophosphates and the study of the Bragg glass phase of vortex matter*. PhD thesis, RisøNational Laboratory, DTU, 2011.
- [110] H. M. Rønnow, K. Lefmann, N. B. Christensen, C. Niedermayer, F. J. M. Markó, J. O. Birk, M. Brtelsen, J. Larsen, and P. G. Freeman. ESS instrument construction proposal CAMEA. Technical report, ESS, 2014.
- [111] D. M. Rodriguez, S. J. Kennedy, and P. M. Bentley. Properties of elliptical guides for neutron beam transport and applications for new instrumentation concepts. *Journal of Applied Crystallography*, 44:727–737, 2011.
- [112] J. A. Rodriguez, D. M. Adler, P. C. Brand, C. Broholm, J. C. Cook, C. Brocker, R. Hammond, Z. Huang, P. Hundertmark, J. W. Lynn, N. C. Maliszewskyj, J. Moyer, J. Orndorff, D. Pierce, T. D. Pike, G. Scharfstein, S. A. Smee, and R. Vilaseca. Macs - a new high intensity cold neutron spectrometer at nist. *Measurement Science and Technology*, 19(3):034023, 2008.
- [113] M. Russina and F. Mezei. First implementation of repetition rate multiplication in neutron spectroscopy. *Nuclear Instruments and Methods in Physics Research Section A: Accelerators, Spectrometers, Detectors and Associated Equipment*, 604(3):624 – 631, 2009.
- [114] M. Russina and F. Mezei. Implementation of repetition rate multiplication in cold, thermal and hot neutron spectroscopy. *Journal of Physics: Conference Series*, 251:012079, 2010.

- [115] J. J. Sakurai. *Modern Quantum Mechanics, Revised Edition*. Addison Wesley Longman, 1994.
- [116] J. Saroun and J. Kulda. RESTRAX – a program for TAS resolution calculation and scan profile simulation. *Physica B: Condensed Matter*, 234-236(0):1102 – 1104, 1997. Proceedings of the First European Conference on Neutron Scattering.
- [117] T. C. Schäffer. Phonon-magnon coupling in frustrated and multiferroic  $h\text{-ymno}_3$ . Master’s thesis, Niels Bohr Institute, University of Copenhagen, 2014.
- [118] P. Scherrer. Bestimmung der gröse und der inneren struktur von kolloidteilchen mittels röntgenstrahlen, nachrichten von der gesellschaft der wissenschaften, göttingen. *Mathematisch-Physikalische Klasse*, 2:98–100, 1918.
- [119] A. Serebrov and A. Fomin. New analysis of neutron-lifetime experiments. *Crystallography Reports*, 56(7):1248–1252, 2011.
- [120] Y. Shen, T. Nakayama, M. Arai, O. Yanagisawa, and M. Izumi. Magnetic phase transition and physical properties of spinel-type nickel manganese oxide. *Journal of Physics and Chemistry of Solids*, 63(6-8):947 – 950, 2002. Proceedings of the 8th ISSP International Symposium.
- [121] G. Shirane, S. M. Shapiro, and J. M. Tranquada. *Neutron Scattering with a Triple-Axis Spectrometer*. Cambridge University Press, 2002.
- [122] A. K. Singh, S. Patnaik, S. D. Kaushik, and V. Siruguri. Dominance of magnetoelastic coupling in multiferroic hexagonal  $\text{ymno}_3$ . *Phys. Rev. B*, 81:184406, May 2010.
- [123] M. Skoulatos, K. Habicht, and K. Lieutenant. Improving energy resolution on neutron monochromator arrays. *Journal of Physics: Conference Series*, 340(1):012019, 2012.
- [124] G. L. Squires. *Introduction to the Theory of Thermal Neutron Scattering*. Cambridge University Press, 2012.
- [125] M. T. F. Telling. Performance of the cooled pyrolytic graphite analyser bank on the OSIRIS spectrometer at ISIS. part i - preliminary results. *ISIS facility Repport*, 2004.
- [126] M. T. F. Telling and K. H. Andersen. Spectroscopic characteristics of the osiris near-backscattering crystal analyser spectrometer on the isis pulsed neutron source. *Phys. Chem. Chem. Phys.*, 7:1255–1261, 2005.
- [127] R. Toft-Petersen, J. Jensen, T. B. S. Jensen, N. H. Andersen, N. B. Christensen, C. Niedermayer, M. Kenzelmann, M. Skoulatos, M. D. Le, K. Lefmann, S. R. Hansen, J. Li, J. L. Zarestky, and D. Vaknin. High-field

- magnetic phase transitions and spin excitations in magnetoelectric linio<sub>4</sub>. *Phys. Rev. B*, 84:054408, Aug 2011.
- [128] K. Tomiyasu, H. Hiraka, K. Ohoyama, and K. Yamada. Resonance-like magnetic excitations in spinel ferrimagnets FeCr<sub>2</sub>O<sub>4</sub> and NiCr<sub>2</sub>O<sub>4</sub> observed by neutron scattering. *Journal of the Physical Society of Japan*, 77(12):124703, 2008.
- [129] S. Toth and B. Lake. General linear spin wave theory for incommensurate magnetic structures. *arXiv:1402.6069 [cond-mat.str-el]*.
- [130] C. Toulouse, J. Liu, Y. Gallais, M.-A. Measson, A. Sacuto, M. Cazayous, L. Chaix, V. Simonet, S. de Brion, L. Pinsard-Godart, F. Willaert, J. B. Brubach, P. Roy, and S. Petit. Lattice and spin excitations in multiferroic h-YMnO<sub>3</sub>. *Phys. Rev. B*, 89:094415, Mar 2014.
- [131] G. Vankó, A. Bordage, P. Glatzel, E. Gallo, M. Rovezzi, W. Gawelda, A. Galler, C. Bressler, G. Doumy, A. March, E. Kanter, L. Young, S. Southworth, S. Canton, J. Uhlig, G. Smolentsev, V. Sundström, K. Haldrup, T. Brandt van Driel, M. Nielsen, K. Kjaer, and H. Lemke. Spin-state studies with xes and rixs: From static to ultrafast. *Journal of Electron Spectroscopy and Related Phenomena*, 188:166–171, 2013.
- [132] P. L. W., Tregenna-Piggotta, F. Juranyia, and P. Allenspach. Introducing the inverted-geometry time-of-flight backscattering instrument, MARS at SINQ. *Journal of Neutron Research*, 16:1–12, 2008.
- [133] K. Wang, J. Liu, and Z. Ren. Multiferroicity: the coupling between magnetic and polarization orders. *Adv. Phys.*, 58:321–448, 2009.
- [134] W. S. Weiglhofer and A. Lakhtakia, editors. *Introduction to Complex Mediums for Optics and Electromagnetics*. SPIE - the International Society for Optical Engineering, 2003.
- [135] P. Willendrup, E. Farhi, E. Knudsen, U. Filges, and K. Lefmann. *mcstas-2.1-components.pdf*. <http://www.mcstas.org/documentation/manual/>, 2.1 edition, September 2014.
- [136] B. Winn and M. Hagen. Memorandum: Inelastic spurion from the prompt pulse. Technical report, SNS - HYSPEC Instrument Development Team, 2012.

Appendix A

Articles

## Prismatic Analyser Concept for Neutron Spectrometers

Jonas O Birk,<sup>1</sup> Márton Markó,<sup>2</sup> Paul G Freeman,<sup>3</sup> Johan Jacobsen,<sup>1</sup> Rasmus L Hansen,<sup>1</sup> Niels B Christensen,<sup>4</sup> Christof Niedermayer,<sup>2</sup> Martin Månsson,<sup>2,3</sup> Henrik M Rønnow,<sup>3,1</sup> and Kim Lefmann<sup>1</sup>

<sup>1)</sup>*Nano Science Center, Niels Bohr Institute, University of Copenhagen, DK-2100 Copenhagen Ø, Denmark*

<sup>2)</sup>*Laboratory for Neutron Scattering & Imaging, Paul Scherrer Institute, CH-5232 Villigen PSI, Switzerland*

<sup>3)</sup>*Laboratory for Quantum Magnetism, École Polytechnique Fédérale de Lausanne (EPFL), CH-1015 Lausanne, Switzerland*

<sup>4)</sup>*Institute of Physics, Technical University of Denmark, DK-2800-Kgs. Lyngby, Denmark*

(Dated: 15 September 2014)

Developments in modern neutron spectroscopy have led to typical sample sizes decreasing from few cm to several mm in diameter samples. We demonstrate how small samples together with the right choice of analyser and detector components makes distance collimation an important concept in crystal analyser spectrometers. We further show that this opens new possibilities where neutrons with different energies are reflected by the same analyser but counted in different detectors, thus improving both energy resolution and total count rate compared to conventional spectrometers. The technique can readily be combined with advanced focussing geometries and with multiplexing instrument designs. We present a combination of simulations and data showing three different energies simultaneously reflected from one analyser. Experiments were performed on a cold triple axis instrument and on a prototype inverse geometry Time-of-Flight spectrometer installed at PSI, Switzerland, and shows excellent agreement with the predictions. Typical improvements will be 2.0 times finer resolution and a factor of 1.9 in flux gain compared to a focussing Rowland geometry, or of 3.3 times finer resolution and a factor of 2.4 in flux gain compared to a single flat analyser slab.

## I. INTRODUCTION

Most crystal analyser neutron spectrometers such as triple axis spectrometers (TAS) rely on the analyser mosaicity to provide the desired compromise between intensity and energy resolution<sup>1</sup>. Coarse analyser mosaicity means reflection of a larger energy range resulting in higher recorded flux but coarse resolution, while fine mosaicity brings the opposite result. For cold neutron spectrometers the most common analyser material is Pyrolytic Graphite (PG), using the (002) reflection with typical mosaicities of 20' to 40' ( $\frac{1}{3}^\circ - \frac{2}{3}^\circ$ ) FWHM as seen *e.g.* on TASP at PSI<sup>2</sup>, PANDA at FRM II<sup>3</sup>, 4F1, 4F2 at LLB<sup>4</sup> and SPINS at NIST<sup>5</sup>. However as neutron spectroscopy moves towards smaller sample sizes, the natural collimation produced by the distance between *e.g.* sample and analyser can become comparable to, or better than, the mosaicity of standard graphite analysers. It has been shown that relying on distance collimation instead of mosaicity and the conventional parallel beam approximation can lead to better performing monochromators<sup>6</sup> so it would be natural if the same was true for analysers. We will show that this is indeed the case and additionally demonstrate the opportunity to analyse several energy bands simultaneously with a single analyser. First we will describe the geometric effects in scattering from a single analyser slab, and then move to more advanced focussing and multiplexed setups. Finally we show how our ideas are verified by both experiments and simulations leading to simultaneous gains in flux and resolution.

## II. INSTRUMENT AND SIMULATIONS

The concept discussed in this article was developed for the CAMEA inverse time-of-flight spectrometer proposed for the European Spallation Source (ESS)<sup>7</sup>. Although the ideas are applicable to many crystal analyser spectrometer designs, they will be discussed based on the 5 meV CAMEA analyser as this specific setup has been thoroughly investigated. The analyser is placed at  $L_{SA} = 1.46$  m from the sample. It consists of five wafers with three analyser crystals each that are 1.0 cm wide, 5.0 cm long, and reflecting out of the horizontal scattering plane. Neutrons are recorded by several parallel  $^3\text{He}$  1/2" (1.27 cm) linear position sensitive detector tubes at a distance  $L_{AD} = 1.25$  m. The settings are optimised for sample heights up to  $h_S = 1.0$  cm. All the work is done based on these settings unless stated otherwise. Monte Carlo ray-tracing simulations were performed using the McStas package<sup>8,9</sup>.

## III. ELEMENTS OF THE PRISMATIC ANALYSER CONCEPT

The prismatic analyser uses a combination of distance collimation and an auto focussing effect from the analysers to achieve its results. We will here describe these effects before explaining the prismatic analyser itself.

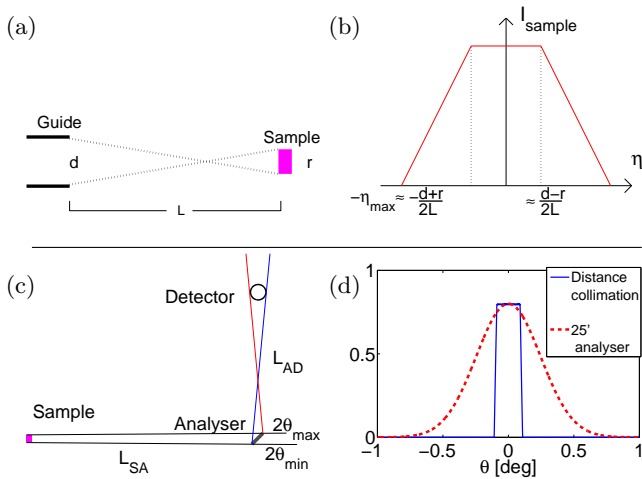


FIG. 1. Distance collimation. a) Geometrical constraints limits the possible paths *e.g.* from guide to sample. This will lead to a divergence distribution on the sample as shown in b), assuming uniform divergence and position distributions with no correlations at the end of the guide. c) The effect of distance collimation on analysers. Due to the geometrical restrictions only polychromatic scattering with a Bragg angle between  $2\theta_{min}$  and  $2\theta_{max}$  can reach the detector independently of the analyser mosaicity. The corresponding rays that cross between sample and analyser have less extreme angles when sample and detector are approximately equal in size and  $L_{SA} > L_{AD}$ . d) Comparison of the resolution from distance collimation (numerically calculated) and a typical PG (002) analyser mosaicity ( $25'$ ) for the reference 5 meV CAMEA analyser.

### A. Distance collimation

Distance is used in neutron instrumentation as a supplement to collimators to achieve a well collimated beam<sup>10–12</sup>. If two parts of an instrument (for example the guide end and the sample) have a maximum size and a certain distance between them then the maximal divergence that can propagate through the instrument is limited (see figure 1 a-b). We denote these geometrical constraints *distance collimation*. In our prismatic analyser setting we compute the correlated distance collimation contributions between sample and analyser and between analyser and detector. We therefore consider the maximum variation in Bragg angle that allows reflection from somewhere on the sample via any spot on the analyser to somewhere on the detector (see figure 1 c). For our reference setup this leads to a distance collimation (shown in figure 1 d) of the order 12' FWHM and thus dominates the mosaicities of most graphite analysers. This makes it possible to relax the mosaicity further with no change in energy resolution.

### B. The auto-focus effect

A monochromatic neutron beam will be focused at a certain distance by a single, flat analyser slab. This "auto-focus" is illustrated in figure 2. Panel a) illustrates how a perfect monochromatic beam is reflected and focused by an analyser with a coarse mosaicity. Simulations of this effect using three narrow energy bands c) - e) confirm the effect by a clear narrowing of the reflected beam at 80-100 cm from the analyser. The exact focussing spot will move further away (and be more focussed) for smaller sample sizes, so it is not possible to define an exact focussing position for a general sample. However it is possible to construct the system so the auto focus point will be close to the detectors for a wide range of sample sizes.

### C. A single prismatic analyser

If distance collimation is the dominant part of the energy resolution, the analyser crystal will reflect a wider energy band than measured by the detector. Neutrons with other energies will be reflected at slightly different angles as described by Bragg's Law, and thus miss the detector. For example the reference 5 meV analyser has a mosaicity of  $60' = 1^\circ$  so the spread in scattering angle is  $2^\circ$  (FWHM) and the real space FWHM of the beam spot at the detector position is 4.4 cm, substantially larger than the 1.27 cm width of the detector tube. However, due to the distance collimation each specific energy will be reflected into a much smaller angular band. Figure 2 shows how three different monochromatic beams are reflected from the same analyser and recorded by three different detectors (b). McStas simulations of three narrow adjacent energy bands are shown in c) - e). Although there is some overlap it is clear that the energy affects the direction of the reflected beam. If a sufficient number of detectors are installed, the entire flux reflected from the analyser will be recorded. In addition, the improved distance collimation provides an accurate determination of the Bragg angle. This provides a better resolution than most mosaicity limited spectrometers together with comparable total count rates from the same analyser.

### D. Simulated performance of the prismatic analyser

Figure 3 shows McStas simulations of reflected intensity and energy resolution for different analyser mosaicities. We see that coarser analysers allow detection of more energies and will even detect slightly more neutrons in the central detector. However coarser graphite will in practice lower the peak reflectivity counteracting this gain. Peak reflectivity depends on analyser thickness, manufacturing process and the reflected energy<sup>13,14</sup> and

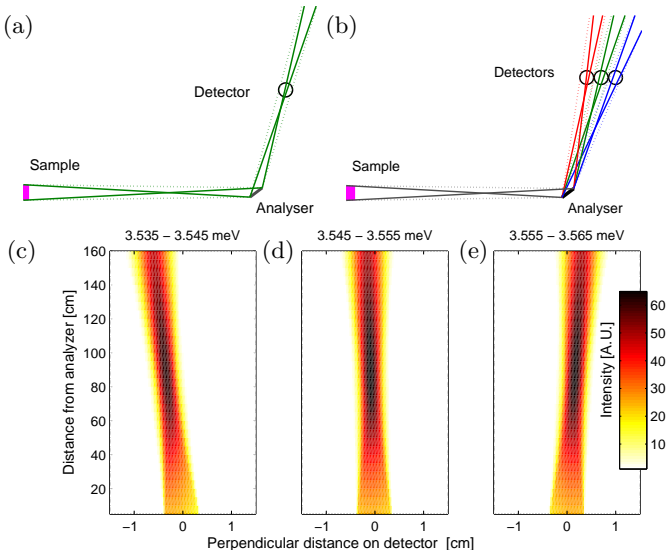


FIG. 2. a): Reflection of a monochromatic beam from a single analyser crystal focussing at a certain distance. The solid and dashed lines represent the limits of the scattered rays. The outer gives the width of the beam while the inner illustrates how focused the beam will be. b) Reflection of three specific energies (red, green, blue respectively) from a single analyser crystal. Each energy is illustrated as in a) and reflected in a specific angle given by Braggs Law. The large difference in focussing distance is due to the exaggerated sample size, analyser size, and angular separation. c-e) McStas simulation of the beam profile as a function of distance from the analyser of three adjacent energy bands, centered at 3.54 meV, 3.55 meV, and 3.56 meV from a single reflecting analyser piece. The horizontal scale has been expanded by a factor 20 for clarity. The autofocus is at 60-120 cm.

can only be applied to the results once these parameters are determined. The resolution broadens with higher energy as expected<sup>1</sup> but is almost independent of mosaicity. The better resolutions at the outer detectors, especially at the 25' analyser, are due to the analyser illuminating one part of the detector tubes more than the other. Thereby the effective detector width decreases, which in turn improves the distance collimation. The outermost detectors will have much smaller intensities than the central and can be omitted to get comparable statistics and signal-to-noise in the different channels.

Even though coarser mosaicity will lower the peak reflectivity, it will increase the total count rate provided there are enough detectors. The same effect can be achieved replacing the detector tubes with a position-sensitive detector. However, in this work we concentrate on a detector setup of thin tubes.

#### IV. ADVANCED INSTRUMENT DESIGNS

In addition to the improved performance offered by the prismatic analyser, there are several other techniques to

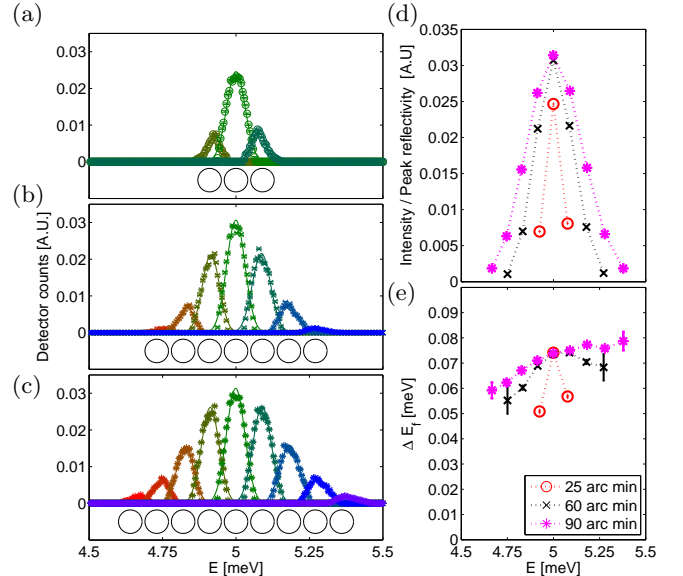


FIG. 3. Simulated recordings of several energies from a single analyser illuminated with a white beam. Each peak in a) - c) represents the counts in a single detector tube as function of  $E_i$  (The detector tubes are represented by circles below the data). The mosaicity of the analyser is 25' for a), 60' for b), and 90' for c). d) Shows the corresponding intensities before correcting for peak reflectivity and e) displays the energy resolution (FWHM) of the detectors for the three different mosaicity values.

improve the performance of triple axis-type spectrometers, such as focussing and multiplexing. The prismatic analyser concept will be most useful if combined with any of these techniques.

#### A. Focussing analysers

An important component in distance collimation is the limited analyser width that unfortunately also limits the covered solid angle. However, like in conventional analyser spectrometers, this can be countered by arranging the analysers in a focussing Rowland Geometry<sup>15</sup>. The Rowland Geometry is robust to small perturbations in energy so the outer detectors will be in almost perfect focussing condition even when the analyser is focused on the central detector. Figure 4 a) displays the optimal Rowland circles for reflecting three different energies towards three different detectors from the same analyser position. At the analyser the distance between the circles is smaller than the width of the analyser crystals so the focussing is almost perfect for all detectors, independent of which of the circles is chosen. Figure 4 b) shows the schematics of how three different energies are reflected and how they can be separated at the detector position. The crystals are chosen to be so close that no gap is seen from the sample, but a small overlap between crystals is seen from the detector. Simulations have shown that

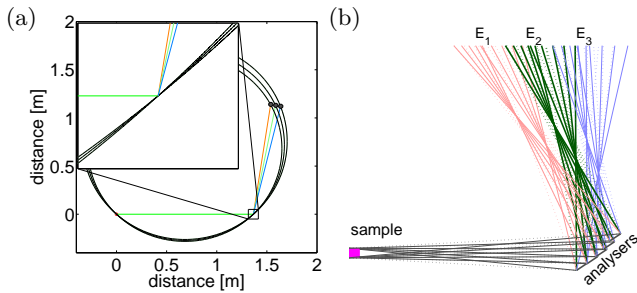


FIG. 4. a) Illustration of the optimal Rowland Circles for three parallel  $1/2''$  detector tubes. At the analyser positions the circles are very close together, making it possible to get almost perfect focussing for all three detectors from one focussing analyser. b) The principle shown in figure 2 for five analysers arranged in a Rowland geometry, the three energies, represented by different colors, are separated at the focussing distance.

this shadow effect is small when  $L_{SA} \approx L_{AD}$  as it is in our example and for practical purposes the finite width of crystals and mounting will force the analysers further apart, eliminating the overlap.

By focussing it is possible to increase the solid angle coverage and thus improve the recorded flux just like with a conventional analyser setup. To confirm that it does indeed work we performed a full simulation with five analyser blades in a focussing geometry. This provided a factor 4.6 in flux gain without sacrificing energy resolution (data not shown).

## B. Multiplexing

Multiplexing spectrometers have become increasingly popular with varying layouts like RITA II at PSI<sup>16,17</sup>, and IMPS<sup>18</sup> and Flatcone<sup>19</sup> at ILL. A challenge when combining multiplexing with prismatic analysers is that many multiplexing instruments have several detectors close together measuring reflections from different analysers. There might thus not be sufficient space for the optimal number of detectors. However by choosing slightly sub-optimal settings it is still possible to combine the two techniques.

For example the proposed ESS CAMEA will have a multiplexing setup with very large analyser coverage. It has 10 concentric rings of analysers reflecting 10 different prismatic energy bands, three of which are seen in Figure 5, to position sensitive detectors below the scattering plane<sup>20</sup>. While this extreme case of multiplexing could be combined with any number of detectors per analyser, a detector number above three would force the innermost analysers further apart than optimal and impose severe extra costs. In contrast, three detectors can be included without any drawbacks<sup>21</sup>.

## V. EXPERIMENTAL VERIFICATION

A prototype of the ESS CAMEA prismatic analyser was built at the Technical University of Denmark and installed on the MARS backscattering spectrometer at PSI<sup>22</sup> in 2012. MARS is an inverse time-of-flight instrument with a flight path between the master chopper and sample of 38.47 m. The prototype consists of 3 vertically focussing analysers behind each other. Each consists of five 15 cm wide, 1 cm tall analysers in Rowland geometry which scatter the neutrons out of the plane to 3 linear position-sensitive detectors. The distance between sample and analyser is 1.2 m and between analyser and detectors 1.0 m. The analysers are centered around a  $2\theta$  value of  $60^\circ$ . Due to spatial restrictions in the prototype, the test was not performed at the exact settings proposed for the final instrument. A more thorough description of the prototype and its testing will be reported elsewhere<sup>23</sup>.

Figure 5 shows data obtained from the prototype experiment at the 5 meV analyser. In c) we used a 2.2 cm tall Vanadium sample to ensure incoherent elastic scattering and recorded the energy separation expressed as neutron time-of-flight in the three detectors. The simulations were done at the same settings and the simulated intensities were rescaled with one common factor to account for imprecise descriptions of source brilliance, sample volume, and analyser peak reflectivity. The data is displayed in the raw time bins in order not to impose any data treatment assumptions. The data confirms that it is indeed possible to separate several energy bands and obtain the good resolution promised by the simulations from a focussing prismatic analyser in a multiplexing inverse time-of-flight spectrometer. The technique has also been tested at other distances and mosaicities and found to work equally well.

To test the prismatic analyser on a triple axis instrument, an experiment was performed on TASP<sup>2</sup>, PSI. TASP is a triple axis instrument with a vertically focussing monochromator, a horizontally focussing analyser with a mosaicity of  $30'$  and a single  $^3\text{He}$  detector tube with a width of  $2' = 5.1$  cm.  $L_{SA}$  and  $L_{AD}$  were both set to 110 cm. The slits before and after the sample were left open and a Be filter inserted after the sample. The sample was a 4 cm high, 1 cm wide V rod, cooled to 10 K. Just before the detector, a slit was inserted to mimic the effect of a narrower detector and the detector arm was rotated to a number of different positions to represent several small detectors. For each position of the detector an  $E_i$  scan was performed around the analyser energy of  $E_f = 4.6$  meV. The results for a 5 mm slit can be seen in figure 6 a). The comparison of different settings can be seen in c). The 5 mm slit corresponds to a position sensitive detector while the 10 mm slit resembles a number of thin detector tubes. Both solutions provide considerably better resolution than the full detector. The similarity of the results from the 5

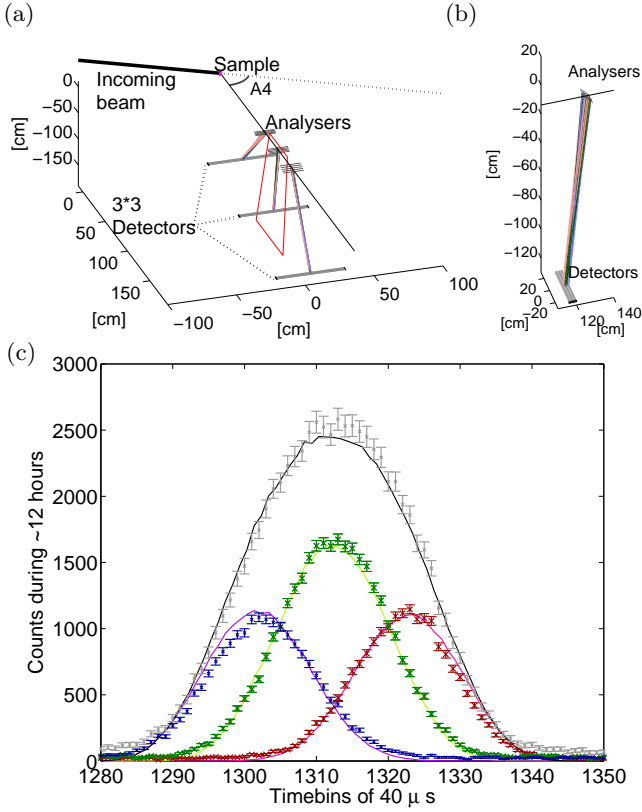


FIG. 5. a): Sketch of the experimental setup of the CAMEA prototype. The analyser-detector setup in the red box is shown in b). Data from this single analyser-detector setup is below. c): Time distribution of neutrons scattered by a 2.2 cm tall Vanadium sample and detected in each of the three detectors recording data from the 5 meV analyser. Measured data are given by data points and simulated data by solid lines. The coloured peaks show the result of using the prismatic analyser while the grey shows the corresponding signal from adding all three detectors together and relying on 30' mosaicity for energy resolution. The simulated intensities have been rescaled by one common factor in order to compare the line shapes. The data is displayed in raw time bins. Each time bin of 40  $\mu$ s corresponds to an energy difference of  $\sim 10$   $\mu$ eV.

and 10 mm slit settings is due to the unmatched energy resolution, the largest contribution being from the monochromator. In this case, however, the unmatched resolution does not reduce the counts since all analysed neutrons are counted, although in different channels. However, the instrument becomes very sensitive to improved incoming energy resolution. In Fig. 6 b) the experiment from Fig. 6 a) was repeated without Be-filter and with the monochromator set at second order 10 meV (first order 2.5 meV) and the analyser at first order 10 meV. This rebalanced the resolutions, the incoming being relatively better. The data shows a clear separation of the peaks from the different detectors. For many experiments on TASP, a slit of variable size is inserted in front of the detector, leading to a smaller

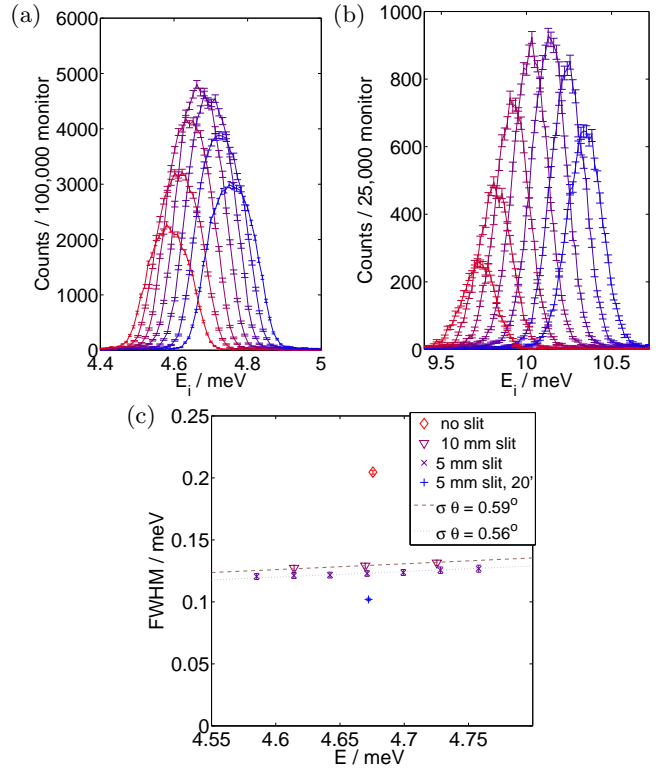


FIG. 6. a)  $E_i$  scans of the elastic V line for 7 different detector positions on TASP with a 5 mm slit in front of the detector and a fixed analyser. b) Using second order reflections from the monochromator and first order from the analyser it is possible to match the energy resolutions. c) Comparison of energy resolutions of TASP depending on slit size. The lines represent the standard resolution dependence on energy found by differentiating Bragg's law and fitting  $\delta\theta$  to the data points. When a 20' collimator is inserted after the monochromator (Blue cross) the resolution is improved further.

resolution improvement for the prismatic analyser. However, the prismatic system will record more neutrons and still have a better resolution than the single detector setup with any slit used at the same instrument.

## VI. COMPARISON TO A CONVENTIONAL SPECTROMETER

Table I shows examples of simulated gain factors for prismatic analysers. The resolution reduction is understood as  $\sigma_r/\sigma_{\text{new}}$  where  $\sigma_{\text{new}}$  is determined from the central 5 meV detector and  $\sigma_r$  is the resolution of the reference setup. The intensity gain is defined as  $(\sum_n I_n) \cdot R_\eta / (I_r \cdot R_{25'})$  where  $I_n$  is the intensity of the n'th tube looking at a given analyser and  $I_r$  is the intensity on the reference detector.  $R_\eta$  is the peak reflectivity of the analyser with mosaicity  $\eta$ . The comparison is done for a vertical Rowland geometry as described in section II, and for a reference using the same geometry but 25' analysers and a single detector

Analyser mosaicity	No. of detector tubes	Resolution reduction	Intensity Gain
25'	3	2.0	0.9
60'	3	2.0	1.4
60'	5	2.0	1.9
90'	3	2.0	1.4
90'	5	2.0	2.0
90'	7	2.0	2.3

TABLE I. Gain factors for different prismatic analyser layouts obtained by simulations, using the standard geometry.

taking up the same space as the full detector setup of the prismatic analyser. Hence the total width is 3.95 cm (including the 1 mm spacing between the detector tubes) when using three detectors and 6.65 cm wide when using five detectors. The Rowland geometry of the reference already gives a gain of 1.7 in flux and 1.7 in resolution reduction compared to a single 5 cm analyser. For this comparison we used typical peak reflectivity values of 0.8, 0.7, and 0.6 for 25', 60' and 90' respectively. The 0.9 in flux gain factor for three detectors and 25" mosaicity is due to the difference between the three round detectors with less efficient edges and spacing between them and the single big square detector of the reference model.

The results demonstrate that it is possible to improve the resolution a factor of 2 while at the same time doubling the intensity compared to a traditional mosaicity driven analysers. This corresponds to a total gain factor of 4 if intensity and secondary energy resolution are assumed inversely proportional. Both gain factors can be increased slightly by using position sensitive detectors.

As discussed earlier there is only space for three detector tubes per analyser on CAMEA. Thus for this setting 60' mosaicity has been chosen for the design. This reduces the resolution a factor 2.0 and increases the flux a factor 1.4 for the ESS version when compared to a traditional Rowland geometry with the same analyser and detector area. Compared to a flat analyser slab one gains a factor of 3.3 in resolution reduction and 2.4 in flux or a total gain factor of 7.9. The same factor would be found if this analyser system was installed elsewhere *e.g.* on a conventional TAS.

## VII. CONCLUSION

We have showed that crystal analyser spectrometers designed for small samples can have a better distance collimation than the mosaicity of standard triple axis spectrometers. Instead of reducing the distance collimation or accept lower count rates the geometric constraints can be used as a benefit by installing several detectors that record different energies from the same analyser. If the mosaicity is relaxed, this can simulta-

neously produce better resolution and higher total count rates than achievable by installing finer mosaicity analyser crystals in standard geometry at the spectrometer or by using Soller collimators. The method is proven by both measurements and simulations to work together with analysers arranged in Rowland geometries and multiplexing setups. The method was developed for indirect time of flight but has also been proven feasible with a traditional TAS setup.

We have further exemplified that a 60' mosaicity setup with three detector channels can lead to a resolution improvement of a factor 2.0 together with a flux increase of a factor of up to 1.4 compared to a conventional 25' mosaicity analyser and single detector with analysers in Rowland geometry. Even bigger gain factors of 3.3 in resolution reduction and 2.4 in flux can be achieved when compared to a flat analyser slab.

## ACKNOWLEDGEMENTS

This project was funded by the Danish and Swiss in-kind contributions to ESS design-update phase. We thank Astrid Schneidewind for insightful comments to the manuscript.

## REFERENCES

- <sup>1</sup>G. Shirane, S. M. Shapiro, and J. M. Tranquada, *Neutron Scattering with a Triple-Axis Spectrometer* (Cambridge University Press, 2002).
- <sup>2</sup>P. Böni and P. Keller, Proceedings of the 4th Summer School on Neutron Scattering, <http://www.psi.ch/sinq/tasp/instrument-references> **96-02**, 35 (1996).
- <sup>3</sup>PANDA, "Panda restrax file," (2014).
- <sup>4</sup>Saclay, <http://www-llb.cea.fr/en/fr-en/spectros-llb.pdf> (2003).
- <sup>5</sup>L. Harriger, SPINS homepage: [www.ncnr.nist.gov/instruments/spins/spins\\_details.html](http://www.ncnr.nist.gov/instruments/spins/spins_details.html) (2014).
- <sup>6</sup>K. Lefmann, U. Filges, F. Treue, J. J. K. Kirkensgaard, B. Plesner, K. S. Hansen, and K. H. Klenø, Nucl. Instr. Meth. A **634**, S1 (2011).

- <sup>7</sup>S. Peggs, R. Kreier, C. Carlile, R. Miyamoto, A. Paahlsson, M. Trojer, and J. G. W. (eds), “ESS technical design report,” Tech. Rep. (ESS, 2013).
- <sup>8</sup>K. Lefmann and K. Nielsen, *Neutron News* **10**, 20 (1999).
- <sup>9</sup>P. K. Willendrup, E. Farhi, and K. Lefmann, *Physica B* **350**, E735 (2004).
- <sup>10</sup>M. P. Nieh, Z. Yamani, N. Kucerka, and J. Katsaras, *Journal of Physics: Conference Series* **251** (2010).
- <sup>11</sup>C. R. H. Bahl, P. Andersen, S. N. Klausen, and K. Lefmann, *Nuclear Instruments and Methods B* **226**, 667 (2004).
- <sup>12</sup>M. Kenzelmann, A. Zheludev, S. Raymond, E. Ressouche, T. Masuda, P. Böni, K. Kakurai, I. Tsukada, K. Uchinokura, and R. Coldea, *Phys. Rev. B* **64**, 054422 (2001).
- <sup>13</sup>A. Moore, M. Popovici, and A. Stoica, *Physica B* **276-278**, 858 (2000).
- <sup>14</sup>M. Adiba, N. Habiba, M. El-Mesirya, and M. Fathallah, *Proceedings of the 8th Conference on Nuclear and Particle Physics*, 81 (2011).
- <sup>15</sup>M. Skoulatos, K. Habicht, and K. Lieutenant, *Journal of Physics: Conference Series* **340**, 012019 (2012).
- <sup>16</sup>K. Lefmann, D. F. McMorrow, H. M. Rønnow, K. Nielsen, K. N. Clausen, B. Lake, and G. Aeppli, *Physica B* **283**, 343 (2000).
- <sup>17</sup>K. Lefmann, C. Niedermayer, A. Abrahamsen, C. Bahl, N. Christensen, H. Jacobsen, T. Larsen, P. Häfger, U. Filges, and H. M. Rønnow, *Physica B* **385386**, 1083 (2006).
- <sup>18</sup>M. Jimnez-Ruiz and A. Hiess, *Physica B* **385-386**, 1086 (2006).
- <sup>19</sup>M. Kempa, B. Janousova, J. Saroun, P. Flores, M. Boehm, F. Demmel, and J. Kulda, *Physica B* **385-386**, 1080 (2006).
- <sup>20</sup>P. G. Freeman, J. O. Birk, M. Marko, N. B. Christensen, J. Larsen, C. Niedermayer, J. Fanni, A. L. R. Hansen, K. Lefmann, and H. Rønnow, *QENS/WINS 2014 proceedings* (2014).
- <sup>21</sup>H. M. Rønnow, K. Lefmann, N. B. Christensen, C. Niedermayer, F. J. M. Markó, J. O. Birk, M. Brtelsen, J. Larsen, and P. G. Freeman, “ESS instrument construction proposal CAMEA,” Tech. Rep. (ESS, 2014).
- <sup>22</sup>P. L. Tregenna-Piggott, F. Juranyi, and P. Allenspach, *Neutron News* **19/1**, 20 (2008).
- <sup>23</sup>M. Markó, J. O. Birk, P. G. Freeman, K. Lefmann, C. Niedermayer, N. B. Christensen, F. Jurányi, A. L. R. Hansen, and H. M. Rønnow, (in progress).

## Simulation of a suite of generic long-pulse neutron instruments to optimize the time structure of the European Spallation Source

Kim Lefmann, Kaspar H. Klenø, Jonas Okkels Birk, Britt R. Hansen, Sonja L. Holm, Erik Knudsen, Klaus Lieutenant, Lars von Moos, Morten Sales, Peter K. Willendrup, and Ken H. Andersen

Citation: [Review of Scientific Instruments](#) **84**, 055106 (2013); doi: 10.1063/1.4803167

View online: <http://dx.doi.org/10.1063/1.4803167>

View Table of Contents: <http://scitation.aip.org/content/aip/journal/rsi/84/5?ver=pdfcov>

Published by the [AIP Publishing](#)

---

### Articles you may be interested in

[Instrument performance study on the short and long pulse options of the second Spallation Neutron Source target station](#)

Rev. Sci. Instrum. **84**, 105104 (2013); 10.1063/1.4823778

[A time-of-flight backscattering spectrometer at the Spallation Neutron Source, BASIS](#)

Rev. Sci. Instrum. **82**, 085109 (2011); 10.1063/1.3626214

[Computer simulations for rf design of a Spallation Neutron Source external antenna H – ion sourcea\)](#)

Rev. Sci. Instrum. **81**, 02A726 (2010); 10.1063/1.3279304

[Mercury Cavitation Phenomenon in Pulsed Spallation Neutron Sources](#)

AIP Conf. Proc. **1022**, 197 (2008); 10.1063/1.2956185

[Simulation of the ion source extraction and low energy beam transport systems for the Spallation Neutron Source](#)

Rev. Sci. Instrum. **73**, 1013 (2002); 10.1063/1.1431417

---



**2014 Special Topics**

PEROVSKITES

2D MATERIALS

MESOPOROUS MATERIALS

BIOMATERIALS/  
BIOELECTRONICS

METAL-ORGANIC  
FRAMEWORK  
MATERIALS

**AIP** | APL Materials

**Submit Today!**

# Simulation of a suite of generic long-pulse neutron instruments to optimize the time structure of the European Spallation Source

Kim Lefmann,<sup>1,2</sup> Kaspar H. Klønø,<sup>1,2</sup> Jonas Okkels Birk,<sup>1,2,3</sup> Britt R. Hansen,<sup>4,5</sup>  
 Sonja L. Holm,<sup>1,2</sup> Erik Knudsen,<sup>4,5</sup> Klaus Lieutenant,<sup>6,7,8</sup> Lars von Moos,<sup>9,5,10</sup>  
 Morten Sales,<sup>1,2</sup> Peter K. Willendrup,<sup>4,5</sup> and Ken H. Andersen<sup>11</sup>

<sup>1</sup>Nanoscience and eScience Centers, Niels Bohr Institute, University of Copenhagen, Universitetsparken 5, 2100 Copenhagen Ø, Denmark

<sup>2</sup>Danish Workpackage for the ESS Design Update Phase, Universitetsparken 5, 2100 Copenhagen Ø, Denmark

<sup>3</sup>Laboratory for Quantum Magnetism, École Polytechnique Fédérale de Lausanne (EPFL), 1015 Lausanne, Switzerland

<sup>4</sup>Institute of Physics, Technical University of Denmark, 2800 Lyngby, Denmark

<sup>5</sup>Danish Workpackage for the ESS Design Update Phase, 2800 Lyngby, Denmark

<sup>6</sup>Institute for Energy Technology, Instituttveien 18, 2007 Kjeller, Norway

<sup>7</sup>Helmholtz Center for Energy and Materials, Hahn-Meitner Platz, 14109 Berlin, Germany

<sup>8</sup>German Work Package for the ESS Design Update, Hahn-Meitner Platz, 14109 Berlin, Germany

<sup>9</sup>Department of Energy Conversion and Storage, Technical University of Denmark, 4000 Roskilde, Denmark

<sup>10</sup>Institute for Energy Conversion, Technical University of Denmark, 4000 Roskilde, Denmark

<sup>11</sup>European Spallation Source ESS AB, 22100 Lund, Sweden

(Received 18 January 2013; accepted 16 April 2013; published online 7 May 2013)

We here describe the result of simulations of 15 generic neutron instruments for the long-pulsed European Spallation Source. All instruments have been simulated for 20 different settings of the source time structure, corresponding to pulse lengths between 1 ms and 2 ms; and repetition frequencies between 10 Hz and 25 Hz. The relative change in performance with time structure is given for each instrument, and an unweighted average is calculated. The performance of the instrument suite is proportional to (a) the peak flux and (b) the duty cycle to a power of approximately 0.3. This information is an important input to determining the best accelerator parameters. In addition, we find that in our simple guide systems, most neutrons reaching the sample originate from the central 3–5 cm of the moderator. This result can be used as an input in later optimization of the moderator design. We discuss the relevance and validity of defining a single figure-of-merit for a full facility and compare with evaluations of the individual instrument classes. © 2013 AIP Publishing LLC. [<http://dx.doi.org/10.1063/1.4803167>]

## I. INTRODUCTION

The European Spallation Source (ESS) is designed to be a long-pulsed spallation neutron source – the first of its kind.<sup>1,2</sup> This opens new territory, including the challenges to design instruments that perform well for a long-pulsed source, to design the optimal moderator for these instruments, and to choose the pulsing time structure that matches these choices. Obviously, these optimizations are coupled, since, e.g., the instrument design depends upon the pulse length and the optimal moderator design depends on both desired pulse length and on the instrument geometries.

In this article, we are concerned with only one part of this optimization problem: the selection of the source time structure, i.e., its pulse length ( $\tau$ ) and repetition time ( $T$ ). The original 2002 design was fixed at  $\tau = 2$  ms, and  $T = 60$  ms ( $f = 16\frac{2}{3}$  Hz),<sup>3</sup> and we have therefore investigated time structures in the neighbourhood of these initial parameters.

In order to perform the time-structure optimization, we have selected a suite of generic instruments, covering a broad range of scientific utilizations. These instruments have then undergone a rough design and optimization for each setting of ( $T$ ,  $\tau$ ), and the relative merits of the instruments at the different time structures have been compiled and compared.

The simulated instrument suite should not be seen as a draft day-one suite, neither should the individual instruments be seen as being close to their final design. Much design work and careful selection of an initial instrument suite is presently in progress. The present work is merely the first step in a long process.

Below, we present our generic neutron long-pulse instrument suite, the optimization procedure, and the obtained overall results. The simulation results of the 15 individual instruments are available online<sup>4</sup> and are or will be published individually in more detailed articles.<sup>5–12</sup>

As a result of this and other studies of the ESS time structure, covering its impact on the performance, reliability, construction cost, and operation of the facility, the time structure has now been fixed at  $\tau = 2.86$  ms and  $T = 71$  ms ( $f = 14$  Hz). The results presented in this paper were an important input to this decision.

## II. THE GENERIC INSTRUMENT SUITE

The instrument suite we discuss here was initiated by the Scientific Advisory Group (SAG) for ESS-Scandinavia, in September 2009. This list was expanded by the slightly different “straw-man-list” of instruments, decided upon by the

TABLE I. Properties of 15 generic ESS instruments, suggested by the ESS-SAG and the ESS SAC.  $L_1$  denotes the length of the instrument for a pulse length of  $\tau = 1$  ms, while  $L_2$  is the instrument length for  $\tau = 2$  ms, and  $\beta$  is the “Frascati exponent,” defined by (1).

Instrument	$L_1$ (m)	$L_2$ (m)	$\beta$
Cold chopper spect.	60	100	0
Therm. chopper spect.	100	100	0
Cold triple axis	40	40	0
Thermal triple axis	40	40	0
TOF triple axis	60	100	0
Backscatter spectrometer	151	302	0
Spin echo spectrometer	30	30	2.5
Short SANS (bio-)	12 + 1–4		2.5
Medium SANS	18 + 1–10		2.5
Long SANS (materials-)	28 + 2–20		2.5
Horizontal reflectometer	52	52	4
Vertical reflectometer	52	52	4
Cold powder diffract.	88	176	0
Thermal powder diffract.	102	102	0
Single crystal diffract.	31	42	0

Scientific Advisory Council for the ESS (SAC) in June 2010. Our starting list was found as a join of these two instrument suites, and is shown in Table I. It should be noted that due to time constraints, neither a tomography instrument, a protein diffractometer, nor a wide-angle spin-echo instrument have been included in these simulations, even though these classes of instruments were present in the straw-man suite. For an artists view on the present version of the straw-man suite, see Fig. 1.

In the optimizations, we have taken into account that neutrons of different wavelengths may not be equally useful for the individual instruments. In particular, spin-echo spectrometers, reflectometers, and small-angle diffractometers strongly prefer long wavelength neutrons. To account for this fact in a simplified way, we parametrize the relative “value,”  $V$ , of each neutron by a simple expression

$$V(\lambda) = \lambda^\beta. \quad (1)$$

The values of  $\beta$  for different instrument types were selected by an expert meeting in Frascati, August 2009,<sup>13</sup> and Table I

contains the chosen values of  $\beta$ . Here, a value of zero indicates that all neutrons are considered equally valuable, while a positive value of  $\beta$  gives preference to long-wavelength neutrons.

### III. DESIGN AND OPTIMIZATION OF INSTRUMENTS

Over the last decade or more, a number of authors have addressed the issue of long-pulse instrumentation.<sup>14–17</sup> The instrument concepts and designs simulated here are in general adapted from the earlier work, except that we have adjusted the instrument lengths as described below and listed in Table I. Most instruments on this list are typical time-of-flight instruments, except the reactor-type triple-axis instruments. One untraditional instrument type, labeled “TOF Triple Axis” has been included in the list. This is a hybrid (or inverted-geometry) spectrometer<sup>11</sup> with a time-of-flight front-end and a triple-axis-like crystal analyzer back-end.

#### A. Instrument length and resolution

To qualify the discussion, let us first recall the equation for the neutron time-of-flight,  $t$ ,

$$t = \alpha\lambda L, \quad (2)$$

where  $L$  is the flight length and  $\alpha = m_n/h \approx 252.7 \mu\text{s}/(\text{m} \text{ \AA})$ . The relative uncertainty of the neutron wavelength can then be expressed by the uncertainty in flight time by

$$\frac{\delta\lambda}{\lambda} = \frac{\delta t}{t} = \frac{\delta t}{\alpha\lambda L}. \quad (3)$$

For long-pulse instruments,  $\delta t$  is either given approximately by the pulse length,  $\tau$ , (at a long pulsed source, the exponentially decaying tail of the pulse can to first order be neglected compared to  $\tau$ ), or by the opening time of a pulse-defining chopper, as described below. In the latter case,  $L$  will be the flight length from the pulse-defining chopper to the detector, in the former it will denote the full instrument length to the detector (for chopper spectrometers, see later).

In analogy, the useful wavelength band,  $\Delta\lambda$ , of neutrons which can reach the detector without creating frame overlap

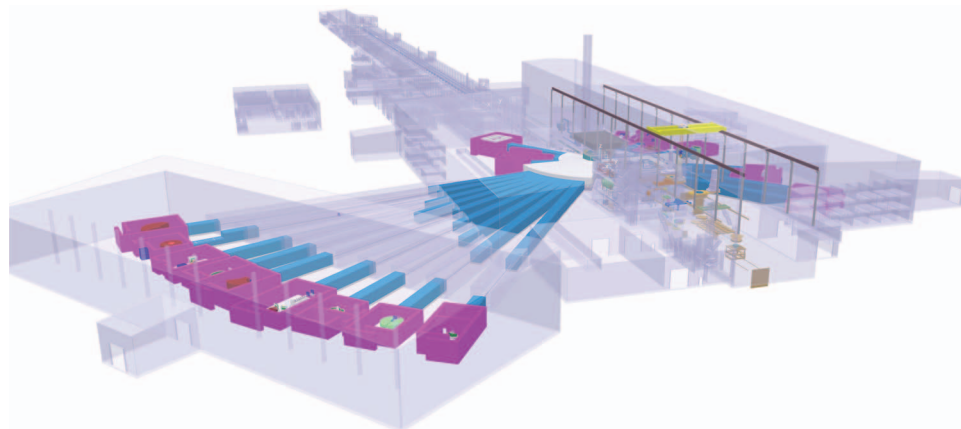


FIG. 1. Artists view of the ESS target/instrument buildings seen obliquely from above. Note that the long instruments are placed in a hall (foreground left) which is separated from the main target building (right). The accelerator is seen stretching into the background.

is given by

$$\Delta\lambda = \frac{\Delta t}{\alpha L}, \quad (4)$$

where for instruments using the full pulse,  $\Delta t = T - \delta t \approx T$ .

A number of the simulated instruments cannot directly utilize the full pulse length,  $\tau$ , since this would result in a too bad resolution (too large  $\delta\lambda/\lambda$ ). Therefore, pulse shaping must be performed at a fast pulse-defining chopper, close to the source. In this work, the distance between source and chopper is set to the smallest realistic value given by the biological shielding of the moderator:  $L_{pc} = 6$  m.) A pulse-defining chopper at the distance  $L_{pc}$  effectively selects a wavelength band, given by  $\Delta\lambda = \tau/(\alpha L_{pc})$ . To let this wavelength band fill the whole time frame,  $T$ , at the detector, the instrument must be very long:  $L = L_{pc}(1 + T/\tau)$ , which for the parameters investigated in this work lies between 126 m and 606 m, since the inverse duty cycle,  $T/\tau$ , lies in the range 20–100.

## B. Wavelength frame multiplication and repetition rate multiplication

At some instruments with pulse-defining choppers, we have used an alternative scheme to having very long instruments: A number of closely spaced shorter pulses is produced at the pulse-defining chopper, which are then kept separated by a number of sub-frame-overlap choppers. This has been denoted “Wavelength Frame Multiplication” (WFM), as first presented by the group of Mezei.<sup>18,19</sup> In the present simulations, the WFM method is used at the thermal powder diffractometer and the thermal chopper spectrometer.

The cold chopper spectrometer uses a similar technique, which bears the name “Repetition Rate Multiplication” (RRM). Here, the full pulse length is used, but a monochromating chopper close to the sample produces up to 15 different monochromatic pulses for each moderator pulse,<sup>14,20</sup> as simulated in Ref. 5. Recently, this technique has been experimentally proven feasible at NEAT, HZB<sup>21</sup> and 4SEASONS, J-PARC.<sup>22</sup> In the present simulations, also the thermal chopper spectrometer employs RRM (in addition to using WFM).

## C. The source

Lacking precise information about the source power and moderator performance for the different time structures, we have initially considered the two following scenarios.

1. The source has a constant time-average neutron flux.
2. The accelerator is limited by a maximum beam current; i.e., the source peak flux is constant.

These two scenarios differ only by a  $\tau/T$  scaling of the source flux, whence we were able to use the same set of simulations/optimizations. As a reference point at the baseline settings, we use the characteristics of a  $12 \times 12$  cm<sup>2</sup> moderator with uniform flux distribution, as given in Ref. 23.

## D. The guide systems

For the short guide systems (below 60 m), we have everywhere used guides with constant cross section, where fast-neutron background from direct line-of-sight to the moderators is avoided by inserting a kink or curved section. At the reflectometers, we have used elliptical focusing in the direction perpendicular to the sample surface, combined with a kink in the other direction.

For instruments of 60 m and longer, and for the 40 m triple-axis instruments, we have employed elliptical guides for beam transport, since recent experiments and simulations have shown this design to be strongly superior over traditional curved guides.<sup>6,24</sup>

For the values of guide reflectivities, we have everywhere used recent information from one supplier.<sup>25</sup> In general, we use  $m = 3$  along the main length of all guides, and  $m = 6$  in the beginning and end of elliptical guides.

Guides have everywhere been assumed to consist of straight sections, with perfect alignment and zero waviness. The effect of waviness and misalignment of (in particular) long elliptical guides is a topic of future simulations.<sup>26</sup> A similar work was carried out earlier for straight guide geometries.<sup>27</sup>

In the optimizations, we have assumed 40 cm as the maximal guide width for the longest guides, relying on information that guides of this width and matching slow frame-overlap choppers can be produced.<sup>25,28</sup> Should it be necessary to place stricter limits on the guide width this will affect the absolute flux values at some instruments,<sup>26</sup> but not the relative comparisons relevant for the present work. This statement is valid for most other design parameters.

For the long guides, no attempt has been made to avoid line-of-sight. The key issue is that bending of the guides, as known from traditional guide systems, would disturb the elliptical focusing properties,<sup>26</sup> whence a solution to this issue is more involved and was postponed to later studies.<sup>29,34</sup>

An additional possibility to reduce the fast-neutron background would be to insert either a crystal filter or a heavy “straight-beam-block” in the middle of the guide, probably early in the guide.<sup>30</sup> Another possibility for guide design is the combination parabolic-straight-parabolic, where the straight section can be curved. This combination transmits almost as well as an elliptical guide.<sup>24</sup>

## E. Optimization of instruments by simulation

All present simulations were performed using the Monte Carlo ray-tracing package McStas v. 1.12,<sup>31</sup> where the instrument designs were typically performed on individual computers, while the final optimization and data taking was performed on the computer cluster of the ESS Data-Management Center in Copenhagen. Typical runs used between  $10^8$  and  $10^{11}$  neutron rays, depending on the type of instrument.

Instruments were first simulated at the baseline time structure settings of  $\tau = 2$  ms and  $T = 60$  ms. The instrument length and chopper settings were adjusted as to obtain a pre-determined instrumental resolution, while remaining above a certain length limit, relevant for the SANS and spin-echo

instruments. Subsequently, the guide system of each instrument was optimized using a Figure-of-Merit (FoM) found from the time average flux,  $\Psi(\lambda)$ , on the sample position in the useful wavelength band,  $[\lambda_{\min}, \lambda_{\max}]$  weighted by  $V(\lambda)$ ,

$$\text{FoM} = \int_{\lambda_{\min}}^{\lambda_{\max}} \Psi(\lambda) V(\lambda) d\lambda. \quad (5)$$

Subsequently, the design of each of the 15 instruments was modified and optimized for each of 20 different time structure settings, in principle 300 optimizations and subsequent simulated data. In order to produce comparable simulations, all optimizations for a given instrument were restricted to have certain resolution characteristics. For spectrometers, this was given as  $\delta\lambda/\lambda$  at the sample position for a certain value of  $\lambda$ . For diffractometers, this was given as a fixed  $\delta\lambda/\lambda$  at the detector for a limited divergence matching this value, to obtain a certain low linewidth in the measured lattice spacing,  $\delta d/d$ , at a given scattering angle. For a few instrument types (spin-echo spectrometer and SANS), the worst resolution was in all cases deemed “sufficient,” so these instruments were not restricted by resolution requirements and were thus simulated at their constant (minimum) lengths.

Since it has been proposed to place triple-axis spectrometers at the long-pulsed ESS, we have included a cold and a thermal instrument in these comparisons. For a triple-axis spectrometer at a pulsed source, the time structure is useful only for filtering of background and higher order harmonics. Hence, the instrument has identical FoM for all time structure settings, and we needed to simulate only one time structure for each of the two triple-axis spectrometers.

#### IV. RESULTS OF INSTRUMENT OPTIMIZATIONS

We now present the results of our optimizations over the time structure range, as described above. To exemplify, we begin with the results for two individual instruments, before describing the combined results of the full instrument suite. Finally, we discuss the validity of our FoM approach.

##### A. Simulation example 1: Cold chopper spectrometer

Let us first consider the simulation of the cold-neutron chopper spectrometer, with a design similar to IN5 at ILL. In this present (simple) version of this instrument, the monochromatization is performed by the (full) length of the pulse, in combination with the opening time of fast choppers just before the sample, as illustrated in Fig. 2. The instrument length is determined by the pulse length, to fulfill a constant  $\delta\lambda/\lambda = 1.6\%$  at  $5 \text{ \AA}$  wavelength. At the baseline time structure settings, the distance between the source and the fast chopper is  $L = 100 \text{ m}$ , and the useful band is  $2.2 \text{ \AA}$  wide (here chosen to be  $3.9\text{--}6.1 \text{ \AA}$ ). This is described in detail in Ref. 5, where, however, a more simple guide system was used. Our results can thus be seen as an update of the previous publication.

The present cold chopper spectrometer uses an elliptical guide with quadratic cross section, which is  $27.3 \text{ cm}$  at its widest place. The guide focuses to the sample, which is defined to be  $2 \times 2 \text{ cm}^2$ . The instrument uses the RRM scheme,

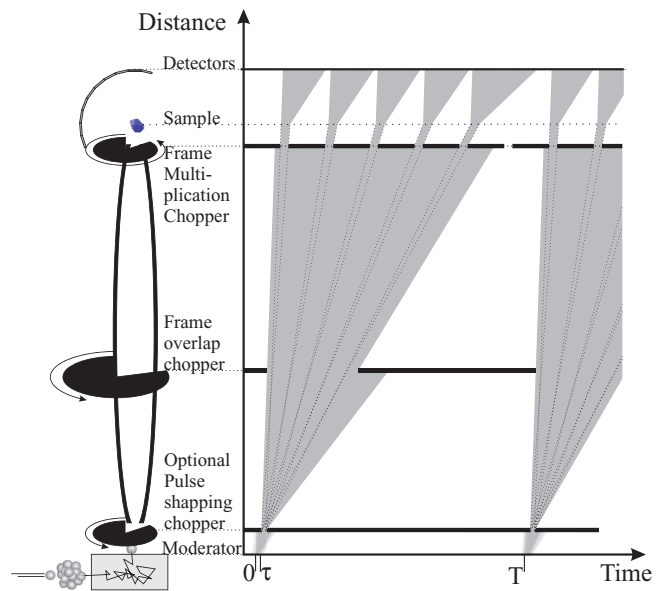


FIG. 2. (left) Sketch of the main elements of the cold chopper spectrometer. Picture is not to scale. (right) Time-of-flight diagram illustrating the selection of neutron pulses by choppers, with the spectrometer running in RRM mode with  $N = 5$ .

as presented earlier. This mode allows for each source pulse 9 monochromatic pulses on the sample, with a wavelength difference between neighbouring pulses of  $0.25 \text{ \AA}$ , and 6 ms between pulses. In this way, the instrument reaches a combined monochromatic flux of  $1.6 \times 10^8 \text{ n/s/cm}^2$  for the wavelength band mentioned above, centered at  $5 \text{ \AA}$ .

A shorter source pulse will allow for a shorter instrument; for pulses of 1.5 ms, 1.25 ms, and 1.0 ms, the instrument length becomes 80 m, 70 m, and 60 m, respectively. (The finite opening time of the monochromating choppers has the consequence that the 1.0 ms instrument is less than a factor two shorter than the 2.0 ms instrument.) A shorter instrument gives rise to a larger bandwidth and thus more neutrons on the sample (for constant time-average flux). For example, when going from 2 ms to 1 ms pulse length, the increase in FoM is more than 50%, as seen in Table II. A rather similar gain is found from lowering the source frequency from  $16\frac{2}{3} \text{ Hz}$  to 10 Hz, also due to the larger useful bandwidth.

Due to the point-to-point-like focusing of an elliptical guide, most neutrons at the sample originate from the

TABLE II. Relative Figure-of-Merit (FoM) values for the simulations of the IN5-like cold chopper spectrometer at ESS, under the assumption of constant time-average flux. Simulations are performed for 20 different settings of the time structure,  $(T, \tau)$ . The RRM scheme is parametrized by  $N$ , which indicates the number of possible monochromatic pulses at the sample per source pulse.

$T$ (ms)	$\tau$ (ms)	1.0	1.25	1.5	2.0	$N$
100 (10 Hz)		2.39	2.24	2.05	1.67	15
80 (12.5 Hz)		2.08	1.83	1.59	1.26	11
60 (16.67 Hz)		1.72	1.48	1.29	1.00	9
50 (20 Hz)		1.35	1.17	0.98	0.76	7
40 (25 Hz)		0.91	0.81	0.68	0.56	5

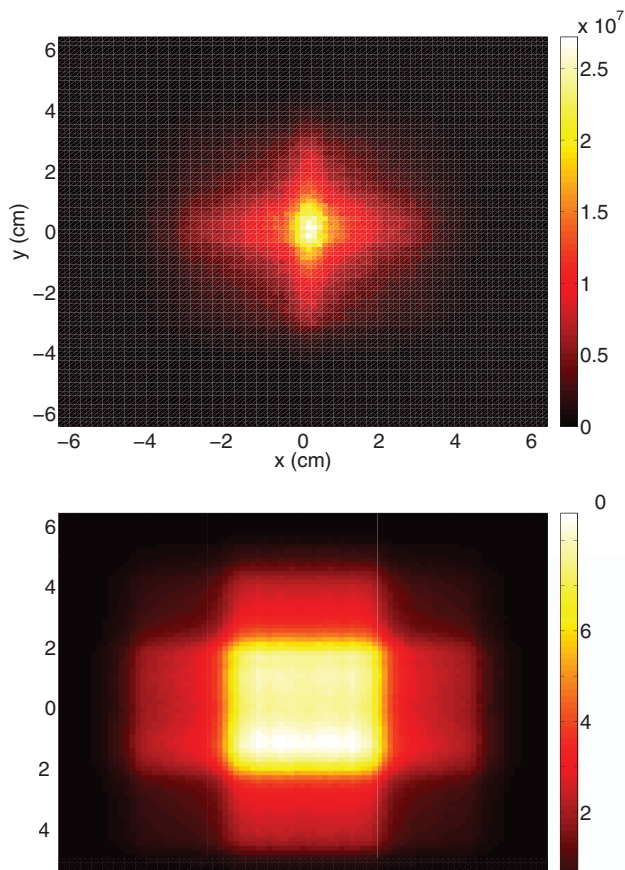


FIG. 3. Simulated plots of the moderator surface showing the number of neutrons which reach the sample at the IN5-like chopper spectrometer. Top panel shows the situation with a 60 m guide ( $\tau = 1$  ms), while bottom panel shows the results for a 100 m guide ( $\tau = 2$  ms).

innermost  $4 \times 4$  cm<sup>2</sup> of the moderator surface, as shown in Fig. 3. Therefore, it would be beneficial if neutrons were emitted preferentially from the center of the moderator. A simulated hot spot with a factor 2.0 intensity gain over a circle of diameter  $d = 3$  cm produces a gain in neutron flux at the sample of 30%.

Taken at face value, the flux number obtained at the base time structure settings represents an impressive factor 200 gain over IN5. However, care should be taken when comparing these numbers. First, the full gain is possible only if neutrons from all monochromatic pulses are equally useful to the actual experiment. Second, much of the flux increase comes from an increased divergence of neutrons in the elliptical guide system (compared to the straight/curved guide at IN5), and this part of the gain would be of value only to particular experiment types. Hence, the mentioned gain is for this instrument a best case scenario, where a worst case scenario (collimating down to IN5 divergence and using only one RRM frame) would lead to a gain factor of “just” 5.

## B. Simulation example 2: Long SANS instrument

We now consider the longest of the three simulated cold-neutron small-angle scattering instruments. In analogy with the cold chopper spectrometer described above, the wave-

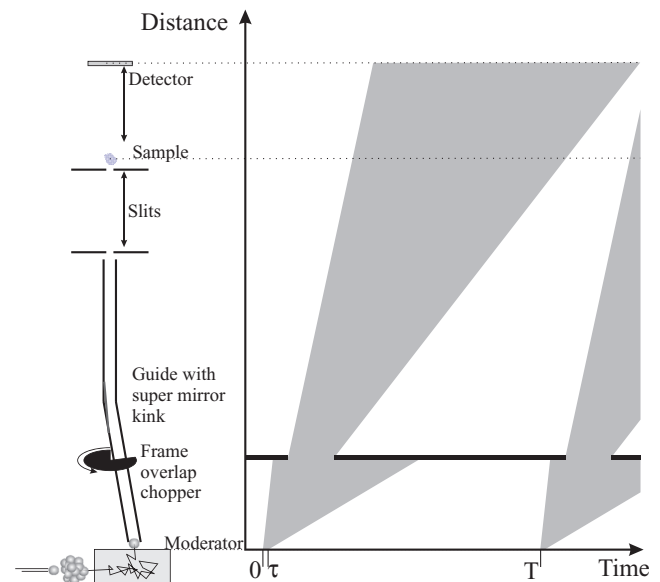


FIG. 4. (left) Sketch of the main elements of the long SANS instrument. Details are not to scale. (right) Time-of-flight diagram illustrating the selection of wavelength band by choppers, with the spectrometer running in the (20 + 20) m setting.

length uncertainty is determined by the full pulse length, since the incoming wavelength is determined by the measured time-of-flight in the detector (assuming elastic scattering at the sample).

The length of the instrument is in practice determined by the 20 m long double-pinhole collimator section, combined with an initial 8 m of guide, which includes a kink to avoid direct line-of-sight. The source-sample distance is thus always 28 m, while the sample-detector distance can vary between 2 m and 20 m. The relevant time-of-flight length,  $L$ , thus varies between 30 m and 48 m. At these lengths, the wavelength uncertainty at the SANS instrument at  $\lambda = 5$  Å and  $\tau = 2$  ms is of the order  $\delta\lambda/\lambda \approx 3\%$ – $5\%$ , which is almost always “too good,” since the double-pinhole collimation of  $d_1 = 10.5$  mm and  $d_2 = 7.0$  mm has the dominating contribution to the  $q$ -resolution.

The bandwidth of the instrument is rather large, of the order 8 Å at the shortest detector setting. In combination with the large angular range covered at the detector, this allows a large  $q$ -range detected in the same setting. A sketch of the long SANS instrument and the corresponding wavelength band selection is found in Fig. 4.

In our optimizations, we have employed three settings of the collimation length and the sample-detector distance: (2 + 2) m, (10 + 10) m, and (20 + 20) m. The results presented are an average of the three results, each normalized by the result at the baseline setting. For the baseline setting, the instrument reaches neutron fluxes of  $1.8 \times 10^8$  n/s/cm<sup>2</sup>,  $9.0 \times 10^5$  n/s/cm<sup>2</sup>, and  $9.7 \times 10^3$  n/s/cm<sup>2</sup> for the three choices of distance, respectively, and the wavelength band centered around 10 Å.

A shorter source pulse will give better wavelength resolution, but the instrument cannot be shortened due to the kink and the collimation section. Therefore, this gives no gain in

TABLE III. Relative Figure-of-Merit (FoM) values for the simulations of the long SANS instrument at ESS under the assumption of constant time-average flux. Simulations are performed for 20 different settings of the time structure, ( $T$ ,  $\tau$ ).

$T$ (ms)	$\tau$ (ms)	1.0	1.25	1.5	2.0
100 (10 Hz)		1.69	1.69	1.69	1.69
80 (12.5 Hz)		1.34	1.34	1.34	1.34
60 (16.67 Hz)		1.00	1.00	1.00	1.00
50 (20 Hz)		0.83	0.83	0.83	0.83
40 (25 Hz)		0.67	0.67	0.67	0.67

bandwidth (or integrated flux), but a small improvement in  $q$ -resolution. If, on the other hand, the source frequency is lowered, e.g., to 10 Hz, at constant time-average flux, the instrument will benefit from an increase in useful bandwidth and hence the FoM will increase. All FoM data are displayed in Table III.

At the longest collimation length, all neutrons at the sample originate from a circle of  $d \approx 2.5$  cm at the center of the moderator surface. This effect is less pronounced at the shorter collimation lengths. This is illustrated in Fig. 5. On average, a simulated hot spot with a factor 2.0 intensity gain

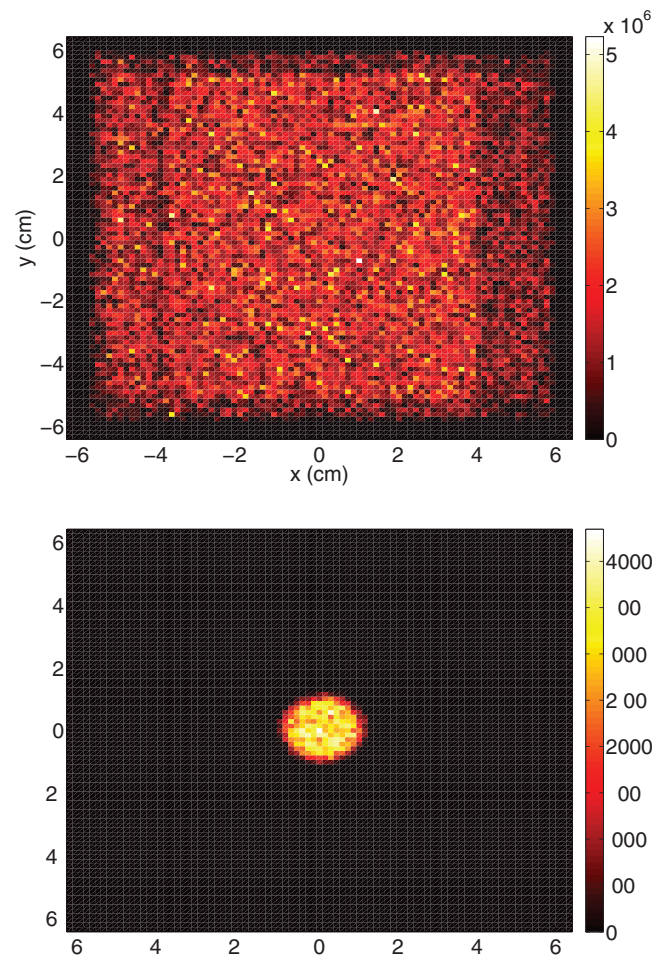


FIG. 5. Simulated plots of the moderator surface showing the number of neutrons which reach the sample for the 20 m SANS instrument. The results are valid for any time structure. (top) data for 2 m collimator-detector setting; (bottom) data for 20 m collimator-detector setting.

TABLE IV. Average relative Figure-of-Merit for the generic ESS instrument suite at different time structures, under the assumption of constant time-average flux.

$T$ (ms)	$\tau$ (ms)	1.0	1.25	1.5	2.0
100 (10 Hz)		2.07	1.81	1.67	1.37
80 (12.5 Hz)		1.89	1.66	1.55	1.19
60 (16.67 Hz)		1.62	1.42	1.24	1.00
50 (20 Hz)		1.53	1.27	1.09	0.88
40 (25 Hz)		1.20	1.05	0.90	0.73

over a circle of diameter  $d = 3$  cm produces a gain in neutron flux at the sample of 73%.

### C. Optimization of the full instrument suite

After the optimization procedures, we record the resulting values of wavelength, bandwidth, flux at sample position, and FoM for each instrument and time structure setting. The results of the individual simulations are in general similar to the simulation results of the chopper spectrometer and the small-angle instrument shown above. (Results can be found from Ref. 4.) The obtained values of FoM have been normalized to the baseline setting of  $T = 60$  ms and  $\tau = 2$  ms.

For constant time-average flux, almost all instruments perform better towards the upper left-hand corner of the performance matrix. This is as expected, since (i) a longer  $T$  will allow for a larger useful wavelength band,  $\Delta\lambda$ , and (ii) a smaller  $\tau$  will either (iia) allow  $L$  to be smaller, giving an increased  $\Delta\lambda$ , or (iib) allow a higher fraction of the total flux through the pulse-defining choppers.

In contrast, for the constant-peak-flux scenario, most instruments perform better towards the lower right corner of the performance matrix. This is most simply explained by the fact that here, more neutrons are produced in total, overcompensating the advantages of short pulses and low frequencies mentioned above.

To perform a global comparison of the different time structure settings, we use the relative instrument performances for each instrument. A simple arithmetic mean value has been used, since no decision on the relative importance of instruments has been taken. The results for the average performances are listed in Tables IV and V for the constant-time-average-flux and constant-peak-flux scenarios, respectively.

We see that the effect of shortening the pulse from 2.0 ms to 1.0 ms is typically around 60% increase at constant time-average flux – or around 20% decrease at constant peak flux. Likewise, the effect of going from 20 Hz to 10 Hz is

TABLE V. Average relative Figure-of-Merit for the generic ESS instrument suite at different time structures, under the assumption of constant peak flux.

$T$ (ms)	$\tau$ (ms)	1.0	1.25	1.5	2.0
100 (10 Hz)		0.62	0.68	0.75	0.82
80 (12.5 Hz)		0.71	0.78	0.87	0.89
60 (16.67 Hz)		0.81	0.89	0.93	1.00
50 (20 Hz)		0.92	0.95	0.98	1.05
40 (25 Hz)		0.90	0.98	1.01	1.09

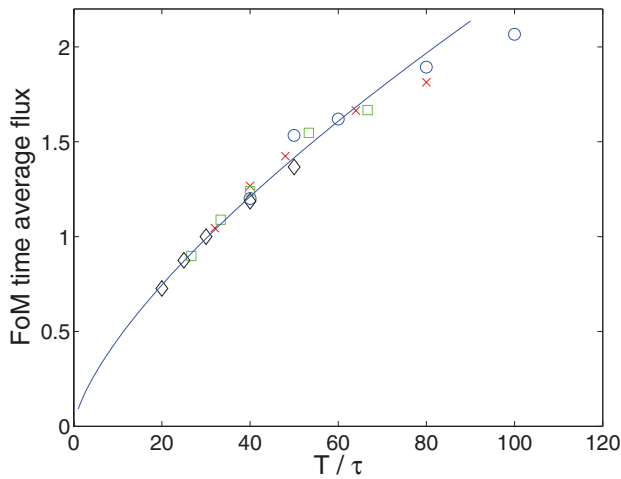


FIG. 6. Average Figure-of-Merit for the generic ESS instrument suite at different time structures, plotted as a function of the inverse source duty cycle, under the assumption of constant time-average flux. Diamonds, squares, crosses, and circles represent pulse lengths of 2.0, 1.5, 1.25, and 1.0 ms, respectively. The solid line is a fit to the power law (6), as explained in the text.

around a 50% increase at constant time-average flux – or around 30% decrease at constant peak flux.

The data for constant time-average flux is shown as a function of the inverse source duty cycle,  $T/\tau$ , in Figure 6. It is seen that, except for the very smallest duty cycles, the data fall almost on a common curve, which can be approximately described by

$$\text{FoM} \approx \Psi_{\text{peak}} \left( \frac{\tau}{T} \right)^{\alpha} = \Psi_{\text{peak}}^{1-\alpha} \Psi_{\text{time av}}^{\alpha} = \Psi_{\text{time av}} \left( \frac{T}{\tau} \right)^{1-\alpha}, \quad (6)$$

with  $\alpha = 0.30$ . This value confirms the trivial result that the long-pulse source of the ESS is intermediate in nature between a short-pulse source and a continuous source. Instruments at short-pulse sources aim to be optimized to benefit from the peak flux, while instruments at steady-state sources are optimized to benefit from the time-average flux. The exact value of the exponent will clearly depend on the chosen instrument suite, but it is interesting to note first that the instrument performance scales more closely with the peak flux than with the time-average flux. Second, Eq. (6) predicts that the global instrument performance depends only on the time-average flux and duty cycle. If both are kept constant, e.g., by changing  $T$  and  $\tau$  simultaneously, the instrument performance should be independent of the time structure.

Our results can be seen as a natural continuation of the discussion on the merits of long-pulse sources, initiated in Ref. 14. While the previous work has used an analytical approach to address the usefulness of long neutron pulses, our results serve to quantify this usefulness, including important features like moderator spectrum and instrument-specific details across the instrument suite.

#### D. Considerations beyond a simple figure-of-merit

The analysis above is based on the assumption that it is possible to reduce the full scientific usefulness of a facility

into one single number, the FoM, and to express its variation by essentially one parameter, the duty ratio  $\tau/T$ , as illustrated in Figure 6. This assumption shares one problem with most numerical optimization work: Details that cannot be compressed into the FoM are easily overlooked. For this reason, we will look more into some of these details. To simplify the argument, we will consider the effect on the instrument performance under the condition that the duty cycle  $\tau/T$  is unchanged. The effect of varying the time structure under this boundary condition depends rather sensitively on the type of instrument.

- SANS, reflectometry and spin-echo instruments will benefit from the increased wavelength range which a longer repetition period will give them. Their performance will not suffer significantly from the degraded wavelength resolution, which an associated increase in pulse length would give. Any increase in bandwidth translates directly into improved performance.
- Crystal-monochromator instruments, such as triple-axis spectrometers, do not make much use of the source time structure at all. In these cases, only the time-average flux counts. The time structure has little or no effect.
- Chopper spectrometers, or other instruments that may employ RRM, have a weak preference for shorter repetition periods. These instruments use the RRM to compensate for the fact that their preferred repetition frequency is higher than the source frequency. Increasing the source frequency reduces the need for RRM and makes their data-collection strategy more similar to existing instruments and simplifies the data analysis.
- Very high-resolution instruments, such as backscattering spectrometers and high-resolution diffraction also have a preference for shorter repetition periods. These instruments cut out only a small fraction of the pulse length to achieve the desired resolution and do not benefit significantly from the increased wavelength range offered by an increase in repetition period.

Overall, it seems clear that an increase in pulse length will translate into an increase in the average length of the instruments, which will, in turn, result in increased costs for guides and shielding along the guides. On the other hand, with modern ballistic-type guides, the transport of neutrons represents no essential problem,<sup>24</sup> while the instrument space becomes less restricted at the same time as the general background level decreases. In addition, certain combinations of  $T$  and  $\tau$  may result in instruments with lengths which allow them to be grouped together in common instrument halls, rather than requiring separate buildings. In such a scenario, the cost savings associated with the reduction in the number of instrument buildings could cancel out the cost increase of the longer guides, as well as providing other benefits in terms of upgradeability and flexibility.

#### E. Optimizing the moderator parameters

The design and simulation of the target/moderator is much more computationally demanding than that of the

instruments. Hence, one aim of the instrument simulations has been to assist the moderator optimizations towards an improved functionality of the full ESS. We here describe the results obtained in this direction.

Often, the figure-of-merit in moderator optimizations is the number of neutrons produced, possibly in a given wavelength interval and for a given moderator size. However, the moderator simulations produce more detailed information than this. The result of each simulation is given as a history of neutron events, each event having 6 parameters: position at moderator surface ( $\mathbf{r}$ ), time of emittance ( $t$ ), wavelength ( $\lambda$ ), and moderator emission angle ( $\eta$ ). By means of instrument simulations it was found possible to represent the transmission probability of a neutron from moderator surface to sample as

$$T(\mathbf{r}, \lambda) \approx T_r(\mathbf{r})T_\lambda(\lambda). \quad (7)$$

Here, the dependence on divergence has been integrated out, since the moderator flux (even with complex geometries) is expected to vary insignificantly over the rather small solid angle of the guide entry. Furthermore, we have neglected the emission time, which corresponds to ignoring the tails from the moderators. For a total target/moderator optimization, the figure-of-merit to optimize is thus for each of the moderators (e.g., a cold and a thermal),

$$\text{FoM}_{\text{mod}} = \sum_j W_j \int N(\mathbf{r}, \lambda, t, \eta) V_j(\lambda) \times T_{j,r}(\mathbf{r}) T_{j,\lambda}(\lambda) d^2\mathbf{r} d\lambda d^2\eta dt, \quad (8)$$

where the summation label,  $j$ , represents the instruments at the moderator,  $W_j$  is a normalization and weighting constant for each instrument,  $N$  is the simulated density of neutrons from the moderator, and  $V_j(\lambda)$  is given in (1).

We have for each instrument calculated the spatial transmission function,  $T_r(\mathbf{r})$ , as shown in the examples above, and listed in Ref. 4. The results show that for most instruments, the transmission peaks strongly in a 3–5 cm diameter circle (or square) in the center of the moderator. This effect results for some instruments from the use of elliptical guides, for others from using tight collimation and straight guides. Thus, it can for these simple guide systems be advantageous to concentrate the flux in a hot spot, while the size of the emitting part of the moderator can be limited, e.g., by reflectors. In this way, it should be possible to simultaneously increase the useful neutron flux and decrease the emission of fast neutrons. For each instrument, we have calculated the effect of producing a circular, 3 cm diameter, hot spot with 100% higher emittance – while maintaining the total emittance of the moderator. This set-up is close to what was presented in Ref. 32. For most instruments, the gain factor of such a hot spot is around 30%, while few instruments show a full 100% gain.

It should be added that more elaborate guide systems, in particular, an optimized guide extraction system for instruments with a pulse shaping chopper close to the moderator, will modify this picture. This problem will be addressed by further simulation work.<sup>29</sup>

## V. CONCLUSION

We have performed a series of systematic ray-tracing simulations of the performance of a generic instrument suite for the ESS. These simulations were carried out for a large number of time structure settings, for constant, typical instrument resolutions. The performance parameters were found to increase with increasing peak flux, as well as with increasing time-average flux, while varying only weakly with the details of the time structure.

The variation with time-average and peak flux can be expressed as  $\text{FoM} \propto \Psi_{\text{peak}}(\tau/T)^\alpha$ , with  $\alpha = 0.30$ . If both the peak flux and the duty cycle are kept constant, the average instrument performance is largely independent of pulse-length or frequency, within the frequency range of the current study.

Since most instruments use tight collimations or (elliptical) focusing guides, most neutrons hitting the sample stem from a central part of the moderator of a diameter 3–5 cm. We suggest to use this knowledge for the optimization of the moderator design, in particular by considering “hot spots” at the moderator. However, this can be finalized only when the guide systems of the instruments are designed.

### A. Implications for design of long-pulsed sources, e.g., ESS

As part of the study which resulted in the decision to fix the time structure of the ESS to  $\tau = 2.86$  ms and  $T = 71$  ms ( $f = 14$  Hz), two boundary conditions were considered: (1) the time-average power is planned to be 5 MW. (2) the peak accelerator current cannot exceed 50 mA. The 5 MW number is judged to be important, so as to at least match the best existing instruments over the largest possible range. The limitation on the peak current results from a judgement, based on the experience of the SNS linear accelerator, as to the optimal compromise between performance, reliability and cost. In the interest of maximizing the instrument performance, it is clearly advantageous to push for the highest peak flux which the accelerator and target assembly can provide. We can therefore consider the 50 mA peak current as our specification, rather than an upper limit. These boundary conditions reduce the number of degrees of freedom when choosing  $\tau$  and  $T$  from 2 to 1, as follows. The peak power on target is given by the product of the peak current and proton energy of 2.5 GeV. At 50 mA peak current, the instantaneous power is 125 MW. In order to achieve a time-average power of 5 MW, the source therefore needs to operate at a duty cycle  $\tau/T$  of  $5 \text{ MW}/125 \text{ MW} = 1/25$ , as a direct consequence of our two boundary conditions. If we set the repetition period to 100 ms (10 Hz), the pulse length will be 4 ms. At  $T = 50$  ms repetition period ( $f = 20$  Hz), the pulse length is 2 ms. The range of  $\tau$  and  $T$  covered in the present study only overlaps partially with the duty cycle  $\tau/T = 1/25$ . In order to study the instrument performance over the 10–25 Hz frequency range, while maintaining a duty cycle of  $1/25$ , we extrapolate based on the data in Tables IV and V and Eq. (6) that the performance of the instrument suite does not depend upon the value of the source frequency.

In general, our results imply that factors other than the flux-related FoM used here should be decisive when determining the time structure for a long-pulse spallation source. For the case of ESS, the time structure has now been locked to  $\tau = 2.86$  ms and  $f = 14$  Hz, as the best compromise between performance, reliability, and cost. The detailed considerations are outside the scope of this article.

## B. Further design and optimization of ESS instruments

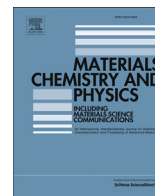
The instrument design work for ESS is currently taking place in a setting which is very different from when the design work described in the present paper was taking place. A large number of the neutron laboratories and university groups working in neutron scattering in Europe are now engaged in the process of designing instruments for the ESS and the number is still increasing. About 40 different concepts for instruments are currently being optimized, some pursued by researchers in partner countries and some by ESS instrument scientists. A subset of these concepts has been assembled into a reference suite of instruments which is described in the ESS Technical Design Report.<sup>33</sup> The reference suite has been chosen to maximize the scientific impact of the ESS by addressing a broad science case, while in each case being fully optimized to benefit from the natural strengths of the long-pulse concept. The choice of instruments to be built at the ESS will take place as a staged process in consultation with the European scientific community and will result in the reference suite gradually evolving into the actual instrument which will be available at the ESS.

## ACKNOWLEDGMENTS

First of all we are strongly indebted to Ch. Vettier for initiating this project and to D. Argyriou for keeping up the urgency of the simulations. We would further like to thank the ESS SAG, the ESS SAC, and H. M. Rønnow for illuminating discussions.

This project was supported by the Danish, Norwegian, and German contributions to the Design Update phase of the ESS. J. O. Birk was supported by PSI and the Danish Research Council through the graduate school C:O:N:T.

- <sup>1</sup>See [www.ess-scandinavia.eu](http://www.ess-scandinavia.eu) for the home page of the ESS project.
- <sup>2</sup>*The ESS Project*, edited by D. Richter (Jülich Research Center, 2002), Vol. I.
- <sup>3</sup>*The ESS Project*, edited by D. Richter (Jülich Research Center, 2002), Vol. IV.
- <sup>4</sup>See [sim.ess.dk](http://sim.ess.dk) for the home page.
- <sup>5</sup>K. Lefmann, H. Schober, and F. Mezei, *Meas. Sci. Technol.* **19**, 034025 (2008).
- <sup>6</sup>K. Lefmann, U. Filges, F. Treue, J. J. K. Kirkensgård, B. Plesner, K. S. Hansen, and K. H. Klenø, *Nucl. Instrum. Methods A* **634**, S1 (2011).
- <sup>7</sup>M. Sales, S. L. Holm, K. Lieutenant, and K. Lefmann, *J. Phys. Soc. Jpn.* **80**, SB018 (2011).
- <sup>8</sup>K. H. Klenø and K. Lefmann, *J. Phys. Soc. Jpn.* **80**, SB004 (2011).
- <sup>9</sup>K. H. Klenø, P. K. Willendrup, E. Knudsen, and K. Lefmann, *Nucl. Instrum. Methods A* **634**, S100 (2011).
- <sup>10</sup>K. H. Klenø, S. Kynde, G. Nagy, K. Mortensen, K. Lefmann, J. Kohlbrecher, and L. Arleth, "A compact time-of-flight SANS instrument optimised for measurements of small sample volumes at the European Spallation Source," *J. Appl. Crystallogr.* (submitted).
- <sup>11</sup>J. O. Birk *et al.*, "Simulations of the inverse-geometry time-of-flight spectrometer CAMEA for the European Spallation Source" (unpublished).
- <sup>12</sup>A. Vickery *et al.*, "Comparing thermal spectrometers for a long-pulse spallation source" (unpublished).
- <sup>13</sup>R. K. Crawford *et al.*, Report of the Long-pulse Neutron Instrumentation Workshop, Frascati, August 2009, 2010.
- <sup>14</sup>F. Mezei, *J. Neutron Res.* **6**, 3 (1997).
- <sup>15</sup>G. Zsigmond *et al.*, *Appl. Phys. A* **74**, S224 (2002).
- <sup>16</sup>H. Schober *et al.*, *Nucl. Instrum. Methods A* **589**, 34 (2008).
- <sup>17</sup>K. Lefmann *et al.*, Report from the Ven 2008 meeting (unpublished).
- <sup>18</sup>K. Lieutenant and F. Mezei, *J. Neutron Res.* **14**, 177 (2006).
- <sup>19</sup>M. Russina and F. Mezei, *Proc. SPIE* **4785**, 24 (2002).
- <sup>20</sup>F. Mezei, M. Russina, and S. Schorr, *Physica B* **276**, 128 (2000).
- <sup>21</sup>M. Russina and F. Mezei, *Nucl. Instrum. Methods A* **604**, 624 (2009).
- <sup>22</sup>M. Nokamura *et al.*, *J. Phys. Soc. Jpn.* **78**, 093002 (2009).
- <sup>23</sup>F. Mezei, *ESS Reference Moderator Characteristics for Generic Instrument Performance Evaluation* (ESS Project, Jülich, 2000), see also [http://rencurel.essworkshop.org/documents/ess\\_itg/ESS-moderators.pdf](http://rencurel.essworkshop.org/documents/ess_itg/ESS-moderators.pdf).
- <sup>24</sup>K. H. Klenø, K. Lieutenant, K. H. Andersen, and K. Lefmann, *Nucl. Instrum. Methods A* **696**, 75 (2012).
- <sup>25</sup>SwissNeutronics AG, personal communication (2012), see also [www.swissneutronics.ch](http://www.swissneutronics.ch).
- <sup>26</sup>K. H. Klenø *et al.*, "Effects of non-idealities in long neutron guides" (unpublished).
- <sup>27</sup>P. Allenspach, P. Böni, and K. Lefmann, *Proc. SPIE* **4509**, 157 (2001).
- <sup>28</sup>Mirrortron Ltd., personal communication (2012), see also [www.mirrortron.kfkipark.hu](http://www.mirrortron.kfkipark.hu).
- <sup>29</sup>M. Bertelsen *et al.*, "Exploring performance of neutron guide systems using pinhole beam extraction," *Nucl. Instrum. Methods. A* (submitted).
- <sup>30</sup>U. Filges, personal communication (2012).
- <sup>31</sup>K. Lefmann and K. Nielsen, *Neutron News* **10/3**, 20 (1999), see also [www.mcstas.org](http://www.mcstas.org).
- <sup>32</sup>Y. Kiyonagi *et al.*, in Proceedings of the ICANS conference, PSI report, 2010.
- <sup>33</sup>*ESS Technical Design Report*, edited by S. Peggs (European Spallation Source ESS AB, 2013).
- <sup>34</sup>L. D. Cussen *et al.*, *Nucl. Instrum. Methods A* **705**, 121 (2013).



## Ferrimagnetism and spin excitation in a Ni–Mn partially inverted spinel prepared using a modified polymeric precursor method



Rafael A. Ferreira<sup>a,b</sup>, Julio C.G. Tedesco<sup>c</sup>, Jonas O. Birk<sup>c</sup>, Walter Kalceff<sup>d,\*</sup>,  
Fabiano Yokaichiya<sup>e,f</sup>, Nina Rasmussen<sup>c</sup>, Octavio Peña<sup>b</sup>, Paul F. Henry<sup>g</sup>,  
Giovanna G. Simeoni<sup>h</sup>, Heloisa N. Bordallo<sup>c,g</sup>, Paulo N. Lisboa-Filho<sup>i</sup>

<sup>a</sup> Programa de Pós-Graduação em Ciência e Tecnologia de Materiais (POSMAT), Universidade Estadual Paulista, Faculdade de Ciências, Caixa Postal 473, 17033-360 Bauru, São Paulo, Brazil

<sup>b</sup> Institut des Sciences Chimiques de Rennes – UMR 6226, Université de Rennes 1, F-35042 Rennes, France

<sup>c</sup> The Niels Bohr Institute, University of Copenhagen, DK-2100 Copenhagen, Denmark

<sup>d</sup> School of Physics and Advanced Materials, University of Technology Sydney (UTS), P.O. Box 123, Broadway, NSW 2007, Australia

<sup>e</sup> Laboratório Nacional de Luz Síncrotron (LNLS), Caixa Postal 6192, CEP 13083-970 Campinas, São Paulo, Brazil

<sup>f</sup> Comissão Nacional de Energia Nuclear (CNEN), Instituto de Pesquisas Energéticas e Nucleares (IPEN), Reactor Multipropósito Brasileiro (RMB), Avenida Lineo Prestes 2242, Bloco A, Cidade Universitária Armando Salles de Oliveira, São Paulo, Brazil

<sup>g</sup> European Spallation Source ESS AB, Box 176, 22100 Lund, Sweden

<sup>h</sup> Heinz Maier-Leibnitz Zentrum (MLZ) and Physics Department, Technische Universität München, Lichtenbergstr. 1, 85748 Garching, Germany

<sup>i</sup> Universidade Estadual Paulista, Departamento de Física, Faculdade de Ciências, Caixa Postal 473, 17033-360 Bauru, São Paulo, Brazil

### HIGHLIGHTS

- Ni–Mn oxide partially-inverted spinel made by modified polymeric precursor method.
- Magnetic measurements showed a ferrimagnetic and a parasitic magnetic transition.
- NPD revealed a magnetic structure consistent with a star-like moment arrangement.
- INS measurements indicated four distinct temperature-dependent magnetic regimes.

### ARTICLE INFO

#### Article history:

Received 31 October 2013

Received in revised form

4 February 2014

Accepted 27 February 2014

#### Keywords:

Magnetic materials

Chemical synthesis

X-ray scattering

Neutron scattering and diffraction

Rietveld analysis

Magnetic structures

### ABSTRACT

We demonstrate that a Ni–Mn oxide partially inverted spinel  $(\text{Ni}_{1-\nu}\text{Mn}_\nu)[\text{Ni}_\nu\text{Mn}_{2-\nu}]\text{O}_4$  having inversion degree  $\nu \approx 0.8$  and produced by a modified polymeric precursor method exhibits behaviour previously reported only in monophased samples. The structure of the specimen was determined using Rietveld analysis of X-ray and neutron powder diffraction data, showing that at room temperature the material crystallizes in the  $Fd\bar{3}m$  space group with a lattice constant  $a = 8.392 \text{ \AA}$ . Combining magnetization measurements with neutron powder diffraction, we show that the magnetic structure of this spinel is associated with the interplay between the ferromagnetic and antiferromagnetic lattices which coexist due to the cations' presence on both tetrahedral and octahedral sites. Our analysis of the neutron diffraction data confirms the postulated magnetic structure involving a star-like moment arrangement, arising from competition for the  $B$  (octahedral) spinel sites by the Ni and Mn cations. Finally, we show that strong magnetic fluctuations are observed in the inelastic neutron scattering data.

© 2014 Elsevier B.V. All rights reserved.

### 1. Introduction

Oxide spinels can exhibit a variety of magnetic moment configurations in the ground state, including collinear, canted and

spiral ferromagnetic (FM), and antiferromagnetic (AFM) structures [1]. They are also known to be very attractive candidates for applications in spintronics [2], due to a large tunnelling magnetoresistance (TMR) response and high Curie temperatures ( $T_C$ ) combining to produce either conductive or insulating behaviour. Indeed, the renewed interest in spinels with non-collinear magnetic structures is related to the multiferroic properties produced by the modulation of spiral spin configurations.

\* Corresponding author.

E-mail addresses: [wkalceff@uts.edu.au](mailto:wkalceff@uts.edu.au), [wkalceff@gmail.com](mailto:wkalceff@gmail.com) (W. Kalceff).

The relation between the crystallographic and magnetic properties in advanced oxide spinel materials such as manganites is still not fully understood. It is interesting, therefore, to study such compounds in order to establish any eventual correlation which may lead to potential applications, as was the case, for instance, with the giant-magnetoresistance ferromagnetic perovskites [3] and in the application of mesoporous  $\text{NiMn}_2\text{O}_x$  to electrochemical energy storage and catalytic decomposition [4].

Spinel-type structures occur in three common forms. The first has formula  $(A)[B_2]O_4$ , where the notation (A) denotes a tetrahedral site occupied by cation A and having four oxygens as nearest neighbours, while  $[B_2]$  denotes an octahedral site occupied by two B cations with six oxygen atoms as nearest neighbours [5–8]. Using the same notation, the second structure—known as a *perfectly inverted spinel*—has formula  $(B)[AB]O_4$ . There is also an intermediate structural possibility, represented by  $(A_{1-\nu}B_\nu)[A_\nu B_{1-\nu}]O_4$ ; here  $\nu$  is the inversion degree, which can be affected by the atmosphere and heat treatment used in its preparation [9,10]. Generally, spinel systems crystallize as face-centred cubic (FCC) or body-centred tetragonal (BCT) structures in which the oxide anions ( $O^{2-}$ ) occupy preferential positions, while the metallic cations ( $A^{2+}$  and  $B^{3+}$ ) are distributed in tetrahedral and octahedral sites, respectively.

$\text{NiMn}_2\text{O}_4$  possesses a spinel-type structure with a certain degree of inversion and showing a rich magnetic response, including AFM, FM or ferrimagnetism, depending on the cation occupancy and oxygen content [10,11]. The complexity of the magnetic behaviour is related to the fact that  $\text{Ni}^{2+}$  and  $\text{Mn}^{3+}$  ( $3d^4$ ) occupy octahedral sites, while  $\text{Mn}^{2+}$  ( $3d^5$ ) and  $\text{Mn}^{4+}$  ( $3d^3$ ) have a preference for tetrahedral sites. However, the ferri-paramagnetic transition temperature in this material is extremely dependent on the synthesis process. For instance, ferrimagnetic behaviour has been observed, with strong antiferromagnetic interactions producing large negative Curie–Weiss temperatures [5,7,12] and Curie temperatures varying from 100 K to 145 K [7,12–14]. Therefore, a controlled synthesis process opens the possibility for materials to be developed with desirable structural and micro-structural properties, and therefore may generate a better understanding of the magnetic behaviour of these systems.

Chemical methods for metallic oxide preparation have been used for several years as an excellent alternative to traditional solid-state reaction routes, the latter invariably producing unreactive, inhomogeneous samples with undesirable secondary phases and large grains. On the other hand, the modified polymeric precursor (MPP) method has been used reliably to produce high quality samples without these shortcomings [15]. The MPP method involves the polyesterification of a metal chelate complex using a hydroxycarboxylic acid and a polyhydroxy alcohol in an aqueous solution of metal ions to produce a polymeric gel. Subsequent heat treatment produces an amorphous powder which is then calcined to achieve a product of the desired unsegregated phase. This material is an extremely homogeneous, very fine, agglomerate-free ceramic powder which is reactive at temperatures significantly lower than those required for powders obtained by traditional routes [15].

Another point of interest in the study of  $\text{NiMn}_2\text{O}_4$  is that it can present different physical behaviours depending on the size and shape of the final material. Bulk systems usually exhibit a ferri-magnetic to paramagnetic transition at about 100 K followed by a parasitic ferrimagnetic transition at lower temperatures, around 70 K [7], while nanoscale materials exhibit only one ferrimagnetic to paramagnetic transition around 105 K [8]. Interestingly, thin films seem to exhibit both behaviours, depending on the heat treatment [16].

In this paper we present results obtained from X-ray (XPD) and neutron powder diffraction (NPD) measurements on a ceramic

oxide of nominal composition  $\text{NiMn}_2\text{O}_4$ , prepared using the MPP method. We show that the use of this method can improve the purity of the resulting material. Its magnetic behaviour was determined from magnetization measurements as functions of temperature ( $M-T$ ) and applied magnetic field ( $M-H$ ). By correlating the nuclear and magnetic structures obtained using Rietveld analysis to the bulk magnetic data, we were able to confirm a star-like magnetic configuration formed by the Mn and Ni moments in this compound. Furthermore, inelastic neutron scattering showed the presence of collective magnetic excitations below 40 K.

## 2. Experimental

The synthesis procedure used to obtain nickel manganate was the modified polymeric precursor (MPP) method [15], wherein stoichiometric amounts of the reagents  $\text{MnCO}_3$ ,  $\text{Co}(\text{NO}_3)_2 \cdot \text{H}_2\text{O}$  and  $\text{Ni}_2\text{O}_3$  (all  $\geq 99.9\%$  purity) were weighed and mixed with nitric acid while stirring at a temperature of 70 °C. After visually checking for the formation of a metallic cation solution, a citric acid solution was added to the reagents to enhance the metallic cation chelation, and ethylene glycol was used to enhance the polyesterification of metallic citrate. The pH of the resulting solution was adjusted to a value of 3 by adding ethylenediamine. Stirring was maintained at a temperature of 70 °C until the elimination of volatiles and water was complete. The homogeneous polymer gel produced was then air-dried in a furnace at 350 °C for 4 h. The resulting powder was macerated in an agate mortar, heated at 800 °C for 4 h and finally heated at 1000 °C for 16 h.

The homogeneity of the sample was confirmed with energy dispersive X-ray (EDX) mapping in a Leo Stereoscan 440 scanning electron microscope (SEM). X-ray diffraction (XRD) analysis was performed with a Rigaku DMAX-2100/PC diffractometer using  $\text{CuK}_\alpha$  ( $K_\beta$ -filtered) radiation ( $\lambda = 1.5406 \text{ \AA}$ ). Room temperature  $2\theta$  scans from 10° to 100° in steps of 0.02° and at fixed counting times of 1.6 s were recorded. More detailed crystallographic studies were later performed at the Brazilian Synchrotron Light Laboratory (LNLS) on the X-ray powder diffraction beamline [17], with energies in the Fe-absorption K-edge ( $\lambda = 1.6650 \text{ \AA}$ ) and Mn K-edge ( $\lambda = 1.5406 \text{ \AA}$ ), using a six-circle Huber diffractometer and a step size of 0.02°. A germanium (111) crystal analyzer was used to achieve high resolution, the X-ray scans being measured in the  $2\theta$  range 15°–120°. Structural refinements were carried out by the Rietveld method [18,19] using GSAS [20], based on JCPDS phase identification data (2003) and the ICSD (2003) structural database. The sample diffraction profiles were modelled using the pseudo-Voigt Thompson–Cox–Hastings (TCH) function [21].

The magnetic structure was inferred from data taken on the high resolution neutron powder diffractometer E9 at the Berlin Neutron Scattering Center (BENSCH) at the Helmholtz-Zentrum Berlin (HZB). The data were measured in zero magnetic field as a function of temperature between 2 K and 280 K at a wavelength of 1.797 Å giving a resolution (full width at half maximum, FWHM) of  $\Delta d/d \sim 0.2\%$ . Neutron data were analysed by the Rietveld method using the FULLPROF suite of programs [22].

Bulk magnetization measurements were performed using a Quantum Design 6000 magnetometer with both zero field cooling (ZFC) and field cooling (FC) between 10 K and 300 K using applied fields of 100 Oe, 500 Oe and 1 kOe. Magnetic hysteresis curves were measured between 10 K and 300 K in a field range of –9 kOe to +9 kOe. These measurements allowed the evolution of the magnetic properties of the material to be followed.

Finally, inelastic neutron scattering (INS) measurements were performed using the TOFTOF spectrometer [23] at the Garching research reactor (FRM-II), Munich. A wavelength of 5 Å and a chopper velocity of 16,000 rpm were selected as a compromise

between a good elastic resolution of 100  $\mu\text{eV}$  (FWHM), large enough  $q$ -range ( $2.2 \text{ \AA}^{-1}$ ) and sufficient intensity. The sample was placed in a cylindrical aluminium can and data were recorded at a range of temperatures from 4 K to 110 K. The raw data were processed by subtracting the scattering from an empty can and normalizing to a vanadium scan. Standard data treatments were performed using MATLAB procedures.

### 3. Results and discussion

SEM-EDX analysis of the  $\text{NiMn}_2\text{O}_4$  sample prepared using the MPP method showed the expected stoichiometric ratios of the constituent elements. Fig. 1 is an SEM image of the specimen, with a distribution of particle diameters ranging from sub-micron to several microns. Mapping of the elements Ni, Mn and O using EDX showed a uniform distribution throughout the material, with no agglomeration. Moreover, Rietveld refinement of the  $\text{NiMn}_2\text{O}_4$  XPD data at room temperature for a sample treated at 1000 °C for 16 h gave a lattice constant  $a = 8.392 \text{ \AA}$ , in agreement with values obtained from specimens prepared by other methods [7,8,24].

In crystalline spinel-type structures such as the system here, the metallic cations occupying the tetrahedral sites are often divalent (in our case,  $\text{Ni}^{2+}$  and  $\text{Mn}^{2+}$ ), while the trivalent cations occupy both sites ( $\text{Mn}^{3+}$  in our sample). In  $\text{NiMn}_2\text{O}_4$  it is expected that the  $\text{Ni}^{2+}$  ( $3d^8$ ),  $\text{Mn}^{3+}$  ( $3d^4$ ) and  $\text{Mn}^{4+}$  ( $3d^3$ ) cations will preferentially occupy the octahedral sites, while the  $\text{Mn}^{2+}$  ( $3d^5$ ) cations will occupy the tetrahedral ones [25]. A common approach to accurately resolving such site occupancy questions is to use X-ray anomalous diffraction to analyse the charge balance. Such analyses also provide a means of verifying the oxidation states of the manganese, which in  $\text{NiMn}_2\text{O}_4$  are expected to be (III) and (IV). To resolve this question, we used program FPRIME [26] to estimate the scattering factors in the absorption K edge of Fe (1.6500  $\text{Å}$ ) and Mn (1.8962  $\text{Å}$ ). As seen in Table 1, we obtained different anomalous scattering for Ni, Mn and O in the whole  $2\theta$  range, thus confirming the occupancy factors for the tetragonal and octahedral sites in these spinel structures.

As a second step in the characterization of our bulk samples using the XPD data, we were able to determine the oxygen positions, the atomic displacements (UISO) and the occupancy factors of Mn and Ni. The final refined values are given in Table 1. Interestingly, we note that while in normal spinels the divalent cations (e.g.  $\text{Ni}^{2+}$ ) preferentially occupy the tetrahedral (A) sites and the trivalent cations (e.g.  $\text{Mn}^{3+}$ ) occupy the octahedral (B) sites, the refined data of Table 1 shows them to be distributed on both crystallographic sites. It can therefore be concluded that the spinel

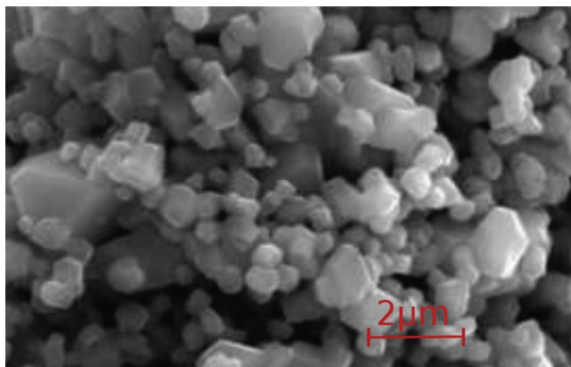


Fig. 1. Scanning electron micrograph of a representative sample of nickel manganite powder obtained by the modified polymeric precursor method, followed by heat treatment in air at 1000 °C for 16 h.

Table 1

Summary of results from the Rietveld analysis of XPD data for MPP-prepared nickel manganite sample at room temperature and at two wavelengths. The space group used was  $Fd\bar{3}m$ , and the Ni and Mn atoms were considered to occupy both tetrahedral (0.125,0.125,0.125) and octahedral (0.5,0.5,0.5) sites.

	$f$	$f'$			
$\lambda = 1.6500 \text{ \AA}$					
Ni	-1.964	0.586			
Mn	-1.084	3.17			
O	0.056	0.038			
$\lambda = 1.8962 \text{ \AA}$					
Ni	-1.354	0.739			
Mn	-9.009	0.462			
O	0.069	0.050			
Atoms	$x$	$y$	$z$	Occupancy	UISO
O	0.2624	0.2624	0.2624	1	0.028296
Mn(tet.)	0.125	0.125	0.125	0.80	0.011351
Ni(tet.)	0.125	0.125	0.125	0.20	0.011351
Mn(oct.)	0.5	0.5	0.5	0.58	0.004206
Ni(oct.)	0.5	0.5	0.5	0.42	0.004206

undergoes an inversion transformation, thus confirming the expected results of crystal field stabilization energy (CFSE) calculations [27]. Therefore, the composition of this particular synthesized spinel can be written as  $(\text{Ni}_{0.20}\text{Mn}_{0.80})_{\text{tet}}[\text{Ni}_{0.84}\text{Mn}_{1.16}]_{\text{oct}}\text{O}_4$ .

We now turn to the magnetic properties of our specimen, elucidated via volumetric magnetization measurements. Fig. 2 shows the magnetization as a function of temperature measured in ZFC and FC cycles in an applied magnetic field  $H = 100 \text{ Oe}$ . The observed irreversibility at  $T_{\text{irr}} = 91 \text{ K}$  between the ZFC and FC curves is a well-known characteristic of ferrimagnetic materials [28,29]. This thermal hysteresis is usually observed in spinel-type systems in which different crystallographic sites are occupied by the same cation, consistent with our Rietveld refinements. The inset of Fig. 2 shows the derivative of the FC curve, indicating the ferrimagnetic transition  $T_c$  at 96 K together with changes in the magnetic configuration of the system at  $T_m = 105 \text{ K}$ ,  $T_1 = 77 \text{ K}$  and at  $T_2 = 63 \text{ K}$ .  $T_m$  is the setting point of the ferri-paramagnetic transition, while  $T_1$  and  $T_2$  are related to parasitic magnetic transitions [5] occurring before the ferrimagnetic–paramagnetic transition at  $T_c$ , attributed to a transition from a Yafet–Kittel (triangular) configuration to a collinear Néel state. Later in our paper this behaviour

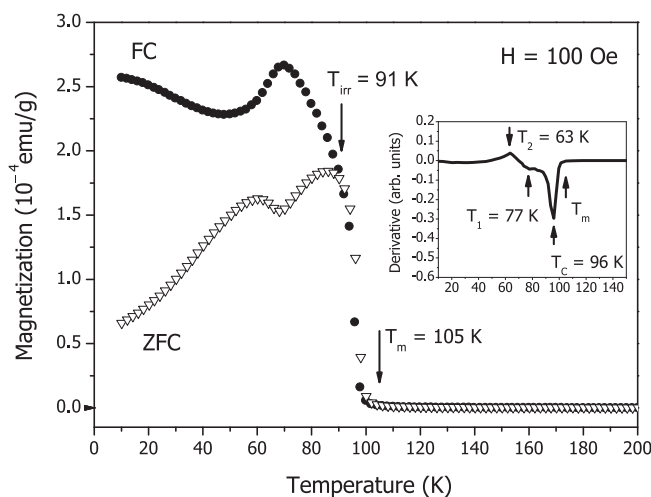


Fig. 2. Magnetization versus temperature plots for  $(\text{Ni}_{0.20}\text{Mn}_{0.80})_{\text{tet}}[\text{Ni}_{0.84}\text{Mn}_{1.16}]_{\text{oct}}\text{O}_4$  at a constant applied field of 100 Oe. The closed circles denote the FC curve and the open triangles the ZFC curve. The inset figure shows the derivate of the FC data, with the magnetic transition temperatures indicated.

will be related to the configuration of the magnetic structure. The observed  $T_m$  and  $T_c$  are similar to those previously reported in the literature [5,7–9,12].

As shown in Fig. 3(a) and (b), increasing the applied magnetic field causes an enhancement in the measured magnetization and a clear reduction of  $T_{irr}$ , while  $T_c$  remains constant. The shape of the magnetisation curves indicates a ferrimagnetic ordering caused by the interplay between the sublattices, with both cooperative (FM) and competitive (AFM) mechanisms being present. Considering the Curie–Weiss model, the predominant magnetic interaction can be determined by extrapolating the inverse magnetic susceptibility–temperature curve ( $1/\chi$  vs  $T$ ) in the paramagnetic state, as shown in the inset of Fig. 3(b). A negative Curie–Weiss temperature  $\theta = -78$  K and an effective magnetic moment of  $\mu_{eff} = 5.89$   $\mu_B$  are obtained and are similar to previously reported values [12]; thus, we can conclude that the AFM interactions are predominant in this system.

To further verify our assumptions about the magnetic structure of the sample, NPD studies were carried out. In the NPD data refinement the same cubic spinel structure as determined from the X-ray data was used at all temperatures, with Mn (80%) and Ni (20%) at tetrahedral Wyckoff positions 8a (0.125,0.125,0.125) and Mn (58%) and Ni (42%) at octahedral Wyckoff positions 16d (0.5,0.5,0.5). The O atoms are located on Wyckoff positions 32e ( $x,x,x$ ) with  $x = 0.2624(8)$ . The atom positions were taken from Boucher et al. [12]. Magnetic scattering was observed below 100 K and was simultaneously refined with the nuclear scattering contribution, as shown in Fig. 4. It should be noted that until now Ni–Mn spinels had been obtained by different routes to ours [7,8]. For instance, a study by Almeida et al. [8] showed that the NiMn<sub>2</sub>O<sub>4</sub>

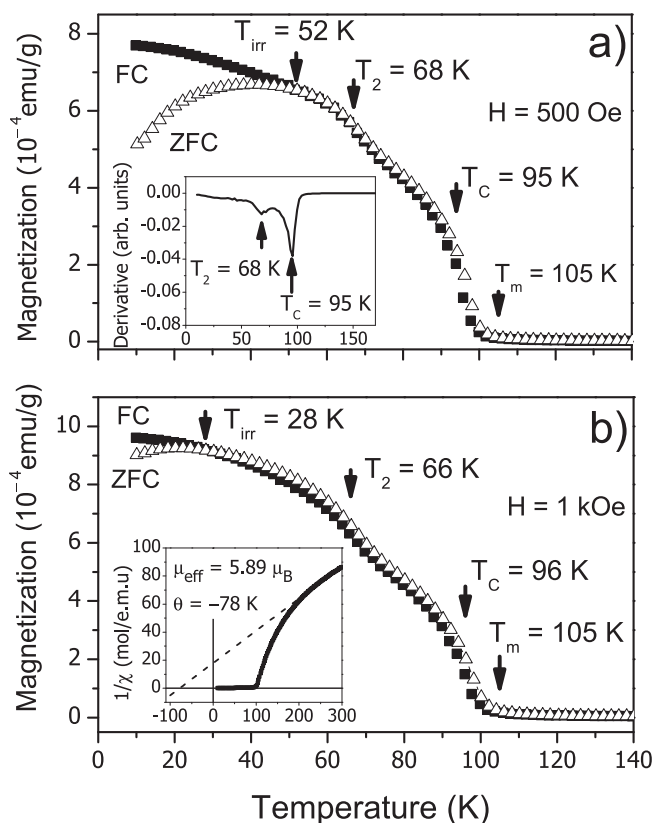


Fig. 3. (a) and (b) (main plots) Magnetization Vs temperature at constant applied fields of 500 Oe and 1 kOe, respectively; inset (a) derivative of magnetisation versus temperature; inset (b) inverse susceptibility versus temperature.

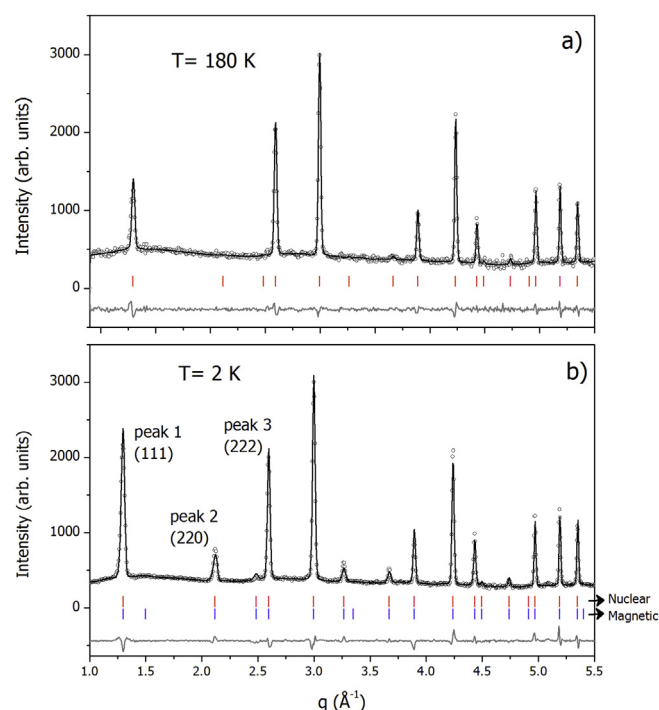
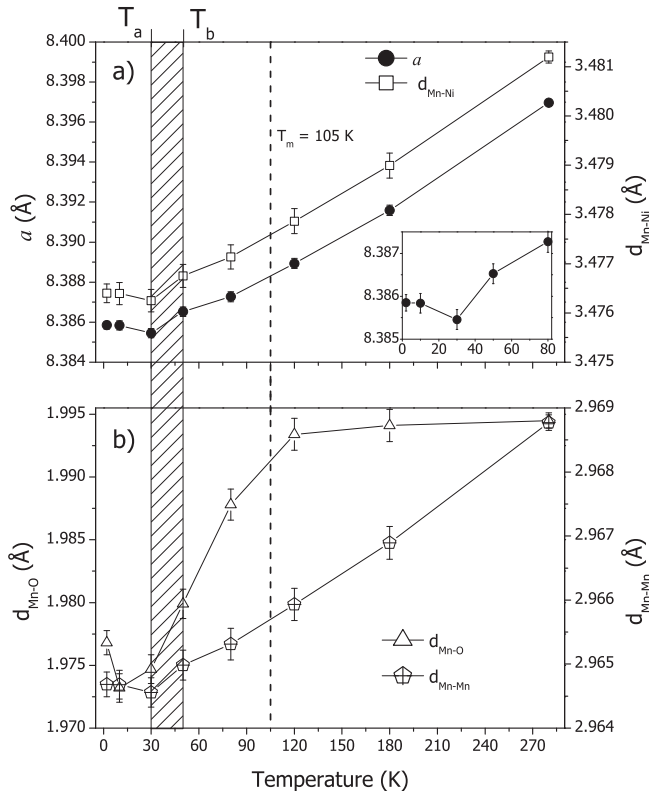


Fig. 4. Rietveld refinement of NPD data for sample  $(\text{Ni}_{0.20}\text{Mn}_{0.80})_{\text{tet}}[\text{Ni}_{0.84}\text{Mn}_{1.16}]_{\text{oct}}\text{O}_4$  measured on E9–BERII–HZB at (a) 180 K and (b) 2 K in zero field using  $\lambda = 1.797$  Å. The circles represent the experimental data, while the black and grey lines correspond (respectively) to the refined intensities and the difference plot between the calculated and observed intensities. The top row of vertical (red) marks on both plots show the calculated positions of the Bragg reflections in NiMn<sub>2</sub>O<sub>4</sub>. The bottom row of (blue) marks in (b) indicates the calculated positions of the magnetic reflections. (For interpretation of the references to colour in this figure legend, the reader is referred to the web version of this article.)

obtained from xerogels in a process similar to the MPP method produced nanoparticles when allowed to crystallise at 600 °C; however, a high content of secondary phases was present. Díez et al. [7] reported the synthesis of the same material through thermal decomposition yielding 3% impurities, while Sagua et al. [24] (using a hydroxide route) obtained a slightly Ni-defective global stoichiometry, attributed to the presence of 1.6(1)% NiO. Within the accuracy of the data, no evidence of impurity phases was observed in our method.

Structural parameters determined by the Rietveld analysis of the NPD data are shown as a function of temperature in Fig. 5. A spherical harmonics approach was used to model the scattering contributions in the Rietveld refinement, considering the Mn atoms in a primitive unit cell at the A sites, and Mn and Ni atoms at the B sites, as reported previously [9,12,14,28,29]. Our analysis confirmed that the magnetic structure consists of a star-like arrangement of moments, as shown schematically in Fig. 6. This model is effectively a three-sublattice model, first described by Boucher et al. [29] in 1970, where the magnetic moments of sublattice A interact differently with the magnetic moments of sublattice B, depending on the magnetic ion that occupies the site B (Mn or Ni). This is also in agreement with the previously mentioned Yafet–Kittel configuration. It is seen from Fig. 5(a) that the cubic lattice constant  $a$ , as well as the Mn–Ni bond lengths (i.e. distances between the A and B sites) vary approximately linearly with temperature between 50 K and 280 K. The Mn–Mn bond lengths (i.e. distances between the B sites) vary as shown in Fig. 5(b), having a similar linear thermal expansion behaviour over this temperature range. On the other hand, the Mn–O bond lengths plotted in Fig. 5(b) remain



**Fig. 5.** (a) Temperature dependence of the lattice constant  $a$  and the Mn–Ni bond length (distance between the A and B sites); (b) Mn–Mn bond lengths (distance between the B sites) and Mn–O bond lengths as a function of temperature. The dashed line is a visual guide for comparison of the two plots.  $T_m$  indicates a ferrimagnetic transition, when the magnetic peaks start to appear. Also, a magnetostriction is observed at a temperature within a range indicated by the hatched region  $T_a < T < T_b$  (with  $T_a = 30$  K and  $T_b = 50$  K) and is related to a second magnetic rearrangement of the lattice.

temperature-invariant on cooling from 280 K (not shown) to 120 K and then decrease. The re-arrangement of the magnetic structure causes a small magnetostriction to be observed at lower temperatures, but the precise temperature of the onset of this behaviour cannot be specified due to the small number of available experimental points; hence it is shown in Fig. 5 as a hatched region between 30 K and 50 K.

Fig. 7(a) shows the integrated intensity around  $\omega = 0$  extracted from the TOFTOF data at 4 K, together with the identification of the diffraction peaks. Peaks 1 and 2 are the (111) and (220) reflections already observed in the NPD data as shown in Fig. 4, while the broad hump identified as peak A is related to the magnetic fluctuations also seen in Fig. 4 and reported by Boucher et al. [12]. To better understand these features, the integrated intensities of peaks 1, 2 and 3 (the latter related to the (222) nuclear reflection) obtained from the analysis of the NPD data, are shown in Fig. 7(b). As the integrated intensities of peaks 1, 2 and 3 closely follow the evolution of the magnetization Vs temperature curve (see Fig. 3), they can be directly related to the magnetic ordering of the system. Of more interest, however, is the change in the behaviour of peak 3 occurring over the same (hatched) temperature range defined in Fig. 5. In Fig. 7(b), a very slight increase of the integrated intensity is observed, being more evident close to 50 K ( $T_b$ ); a decrease in intensity occurs below 30 K ( $T_a$ ). This behaviour closely follows the evolution of the lattice parameters and bond lengths shown in Fig. 5. Our observations appear to indicate a further rearrangement

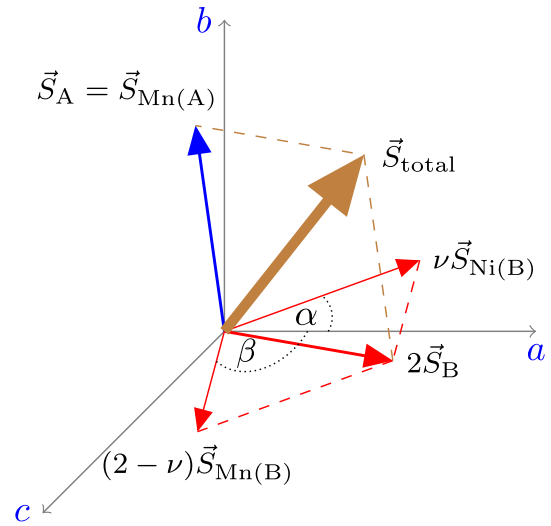


**Fig. 6.** Schematic representation of the star-like magnetic structure of  $(\text{Ni}_{0.20}\text{Mn}_{0.80})\text{-tet}[\text{Ni}_{0.84}\text{Mn}_{1.16}]_{\text{oct}}\text{O}_4$ . The blue arrow shows  $\vec{S}_{\text{Mn}(A)}$ , the magnetic moment of sublattice A, and the red arrows show  $\nu \vec{S}_{\text{Ni}(B)}$ , the magnetic moment for the Ni atom in the B sublattice,  $(2-\nu)\vec{S}_{\text{Mn}(B)}$ , the magnetic moment for the Mn atom in the B sublattice, and  $2\vec{S}_B$ , the resultant magnetic moment for the B sublattice. In the present case,  $\nu \approx 0.8$ ,  $\alpha \approx 60^\circ$  and  $\beta \approx 70^\circ$ . (For interpretation of the references to colour in this figure legend, the reader is referred to the web version of this article.)

of the magnetic moments, and this idea is also supported by the inelastic neutron scattering results discussed below.

We now turn to the analysis of the INS data. Fig. 7(c) shows the scattering intensity with an energy transfer up to 8 meV as a function of temperature. In this region no phonon contribution is expected, therefore the observed fluctuations are attributed to magnetic scattering. Four temperature regimes can be identified:

- i.  $T > T_m$  (purple line (in the web version)) where the magnetic correlations have collapsed.
- ii.  $T_b < T < T_m$  (blue line) where due to the collinear arrangement of the moments the magnetic response becomes a broad inelastic contribution at 2 meV with a full width at half maximum of about 1 meV.
- iii.  $T_a < T < T_b$  (red line) where a significant broadening of the inelastic magnetic scattering intensities occurs, while the quasi-elastic signal,  $\omega = 0$ , seems to be unchanged. This behaviour is characteristic of a canted spin system, where due to the distribution of the magnetic moments among the different sites some type of a dynamical spin-frustration effect can be observed [30].
- iv.  $T < T_a$  (black line) where the inelastic intensity of  $(\text{Ni}_{0.20}\text{Mn}_{0.80})\text{-tet}[\text{Ni}_{0.84}\text{Mn}_{1.16}]_{\text{oct}}\text{O}_4$  again reveals features of collective magnetic excitations around 3 meV. This response is similar to the excitation observed in (ii). This observation, together with the increase in intensity at energy equal to zero, seems to corroborate the idea that a new rearrangement of the spins occurs below  $T_a$ .

#### 4. Conclusion

The Ni–Mn specimen obtained by a modified polymeric precursor method brings new insights into its magnetic properties, observed via magnetization, XPD, NPD and INS measurements. It is interesting to note that the data in Table 1 and other results obtained in this paper, when compared with the literature [7,8] support the conclusion that the MPP method yields monophased

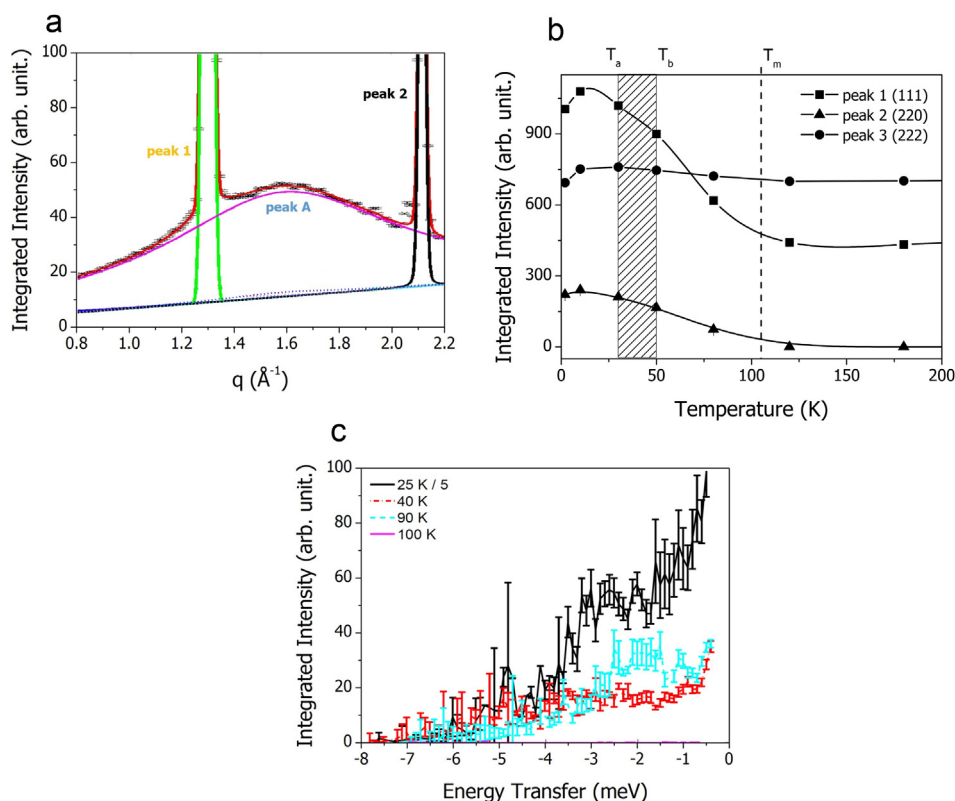


**Fig. 7.** (a) Peak intensities around  $\omega = 0$ , extracted from the TOFTOF data at 4 K, together with the identification of the diffraction peaks. (b) Temperature dependence of the integrated intensity of selected diffraction peaks observed in the E9 and TOFTOF data. (c) Dynamic structure factor of  $(\text{Ni}_{0.20}\text{Mn}_{0.80})_{\text{tet}}[\text{Ni}_{0.84}\text{Mn}_{1.16}]_{\text{oct}}\text{O}_4$  at various temperatures.

samples. The high-temperature treatment causes an increase in crystallite size [8], as well as the formation of monophased material, which are essential to avoid contamination of the magnetic data.

Structural refinement using the Rietveld method showed that the specimen obtained is a bulk-like monophased material with a partially inverted spinel-type structure. The XPD data collected at two distinct wavelengths allowed the site occupancies of the structure to be refined, showing that it had an inversion parameter  $\nu = 0.80$  and hence a nominal formula  $(\text{Ni}_{0.20}\text{Mn}_{0.80})_{\text{tet}}[\text{Ni}_{0.84}\text{Mn}_{1.16}]_{\text{oct}}\text{O}_4$ . ZFC and FC measurements showed typical behaviour for a ferrimagnetic material. The ensemble of ZFC–FC curves obtained at lower fields indicates a clear competition between two sublattices, AFM and FM, with a  $T_c$  and  $T_m$  close to 100 K. NPD data showed magnetic peaks appearing below 100 K, and the Rietveld refinement was consistent with the star-like magnetic structure reported by Boucher et al. [12], arising from the coexistence of Ni and Mn atoms in the B sites of the spinel structure. Of most interest was the observation of a collective magnetic excitation at very low temperatures which seems to be related to the observation of a small magnetostriction of the lattice.

### Acknowledgements

The research of JCGT was supported by the *Brazilian Science Without Borders* program (funds from CNPq). RAF was financed by the bilateral exchange program France–Brazil CAPES–COFECUB, project number 706/11 through the Joint PhD International Program, UNESP–Université de Rennes 1. The work performed by JOB, NR and HNB was financed by Danscatt. WK acknowledges a travel grant from UTS allowing him to visit NBI while on sabbatical leave.

All authors gratefully acknowledge BER2 and FRM2 for the provision of beam time.

### References

- [1] T. Rudolf, C. Kant, F. Mayr, J. Hemberger, V. Tsurkan, A. Loidl, Spin-phonon coupling in antiferromagnetic chromium spinels, *New J. Phys.* 9 (3) (2007) 76.
- [2] U. Lüders, A. Barthélémy, M. Bibes, K. Bouzehouane, S. Fusil, E. Jacquet, J.-P. Contour, J.-F. Bobo, J. Fontcuberta, A. Fert,  $\text{NiFe}_2\text{O}_4$ : a versatile spinel material brings new opportunities for spintronics, *Adv. Mater.* 18 (13) (2006) 1733–1736.
- [3] P.R. Savage, *Giant Magnetoresistance: Technology and Markets for Sensors, Disk Storage, Mram, and Spintronics*, John Wiley & Sons, Inc., 2000.
- [4] Y. Ren, Z. Ma, P.G. Bruce, Ordered mesoporous  $\text{NiMn}_2\text{O}_x$  with hematite or spinel structure: synthesis and application in electrochemical energy storage and catalytic conversion of  $\text{N}_2\text{O}$ , *CrystEngComm* 13 (23) (2011) 6955–6959.
- [5] S. Asbrink, A. Waśkowska, M. Drozd, E. Talik, Physical properties and X-ray diffraction of a  $\text{NiMn}_2\text{O}_4$  single crystal below and above the ferrimagnetic transition at  $T_c = 145$  K, *J. Phys. Chem. Solids* 58 (5) (1997) 725–729.
- [6] H.T. Zhang, X.H. Chen, Size-dependent X-ray photoelectron spectroscopy and complex magnetic properties of  $\text{CoMn}_2\text{O}_4$  spinel nanocrystals, *Nanotechnology* 17 (5) (2006) 1384.
- [7] A. Díez, R. Schmidt, A.E. Sagua, M.A. Frechero, E. Matesanz, C. Leon, E. Morán, Structure and physical properties of nickel manganite  $\text{NiMn}_2\text{O}_4$  obtained from nickel permanganate precursor, *J. Eur. Ceram. Soc.* 30 (12) (2010) 2617–2624.
- [8] J. Almeida, C. Menezes, A. de Menezes, R. Jardim, J. Sakaki, Synthesis and characterization of  $\text{NiMn}_2\text{O}_4$  nanoparticles using gelatin as organic precursor, *J. Magn. Magn. Mater.* 320 (14) (2008) e304–e307.
- [9] P. Lisboa-Filho, M. Bahout, P. Barahona, C. Moure, O. Peña, Oxygen stoichiometry effects in spinel-type  $\text{NiMn}_2\text{O}_{4-\delta}$  samples, *J. Phys. Chem. Solids* 66 (7) (2005) 1206–1212.
- [10] K.P. Chae, J.-G. Lee, H.S. Kweon, Y.B. Lee, The crystallographic, magnetic properties of al, ti doped  $\text{CoFe}_2\text{O}_4$  powders grown by sol–gel method, *J. Magn. Magn. Mater.* 283 (1) (2004) 103–108.
- [11] Y. Shen, T. Nakayama, M. Arai, O. Yanagisawa, M. Izumi, Magnetic phase transition and physical properties of spinel-type nickel manganese oxide, *J. Phys. Chem. Solids* 63 (6–8) (2002) 947–950.
- [12] B. Boucher, R. Buhl, M. Perrin, Etude cristallographique du manganite spinelle cubique  $\text{NiMn}_2\text{O}_4$  par diffraction de neutrons, *Acta Crystallogr. Sect. B Struct. Crystallogr. Cryst. Chem.* 25 (11) (1969) 2326–2333.

- [13] C. Boudaya, L. Laroussp, E. Dhahrp, J.C. Joubert, A. Cheikh-Rouhou, Preparation and characterization of the spinel series  $\text{Co}_{6-x}\text{Ni}_{4-x}\text{Mn}_8\text{O}_{24}$  ( $0 \leq x \leq 4$ ), *Phase Trans.* 68 (4) (1999) 631–642.
- [14] O. Peña, X. Cailleaux, B. Piriou, M. del Canto, S. Abarca, E. Ríos, J. Ortiz, J. Gautier, P. Lisboa-Filho, C. Moure, Magnetic properties of  $\text{Cu}_{1+x}\text{Mn}_{2-x}\text{O}_4$  and  $\text{Ni}_{1+x}\text{Mn}_{2-x}\text{O}_4$  solid solutions, *J. Eur. Ceram. Soc.* 27 (13) (2007) 3911–3914.
- [15] P. Lisboa-Filho, A. Momburu, H. Pardo, W. Ortiz, E. Leite, Influence of processing conditions on the crystal structure and magnetic behavior of  $\text{La}_{0.7}\text{Ca}_{0.3}\text{MnO}_{3\pm\delta}$  samples, *J. Phys. Chem. Solids* 64 (4) (2003) 583–591.
- [16] B. Nelson-Cheeseman, R. Chopdekar, J. Iwata, M. Toney, E. Arenholz, Y. Suzuki, Modified magnetic ground state in  $\text{NiMn}_2\text{O}_4$  thin films, *Phys. Rev. B* 82 (14) (2010) 144419.
- [17] F.F. Ferreira, E. Granado, W. Carvalho Jr., S.W. Kycia, D. Bruno, R. Droppa Jr., X-ray powder diffraction beamline at D10B of LNLS: application to the  $\text{Ba}_2\text{FeReO}_6$  double perovskite, *J. Synchrotron Radiat.* 13 (1) (2005) 46–53.
- [18] H. Rietveld, A profile refinement method for nuclear and magnetic structures, *J. Appl. Crystallogr.* 2 (2) (1969) 65–71.
- [19] H. Rietveld, Line profiles of neutron powder-diffraction peaks for structure refinement, *Acta Crystallogr.* 22 (1) (1967) 151–152.
- [20] A. Larson, R. Von Dreele, General Structure Analysis System (GSAS), Report LAUR 86-748, Los Alamos National Laboratory.
- [21] P. Thompson, D. Cox, J. Hastings, Rietveld refinement of Debye–Scherrer synchrotron X-ray data from  $\text{Al}_2\text{O}_3$ , *J. Appl. Crystallogr.* 20 (2) (1987) 79–83.
- [22] J. Rodríguez-Carvajal, Recent advances in magnetic structure determination by neutron powder diffraction, *Phys. B Condens. Matter* 192 (1) (1993) 55–69.
- [23] T. Unruh, J. Neuhaus, W. Petry, The high-resolution time-of-flight spectrometer TOFTOF, *Nucl. Instrum. Methods Phys. Res. Sect. A Accel. Spectrom. Detect. Assoc. Equip.* 580 (3) (2007) 1414–1422.
- [24] A. Sagua, G.M. Lescano, J. Alonso, R. Martínez-Coronado, M. Fernández-Díaz, E. Morán, Neutron structural characterization, inversion degree and transport properties of  $\text{NiMn}_2\text{O}_4$  spinel prepared by the hydroxide route, *Mater. Res. Bull.* 47 (6) (2012) 1335–1338.
- [25] D.F. Shriver, P.W. Atkins, *Inorganic Chemistry*, third ed., Oxford University Press, Oxford, 1999.
- [26] R.B. von Dreele, *FPrime for Windows*, 1994 (cited October 2013), URL: <http://www.ccp14.ac.uk/ccp/ccp14/ftp-mirror/gsas/public/gsas/windows/fprime.zip>.
- [27] K. Yatsimirskii, N. Kostromina, Crystal field stabilization energy in halides of the rare earth elements taking account of spin-orbital interaction, *Theor. Exp. Chem.* 2 (5) (1966) 436–439.
- [28] B. Boucher, R. Buhl, M. Perrin, Structure magnetique a trois sous-reseaux dans l'approximation du champ moleculaire, *J. Phys. Chem. Solids* 30 (10) (1969) 2467–2477.
- [29] B. Boucher, R. Buhl, M. Perrin, Structures magnetiques anisotropes dans les spinelles, *J. Phys. Chem. Solids* 31 (10) (1970) 2251–2266.
- [30] K. Tomiyasu, H. Hiraka, K. Ohoyama, K. Yamada, Resonance-like magnetic excitations in spinel ferrimagnets  $\text{FeCr}_2\text{O}_4$  and  $\text{NiCr}_2\text{O}_4$  observed by neutron scattering, *J. Phys. Soc. Jpn.* 77 (12) (2008) 124703.

## Magnetic properties of ultra-small goethite nanoparticles

This content has been downloaded from IOPscience. Please scroll down to see the full text.

2014 J. Phys. D: Appl. Phys. 47 365003

(<http://iopscience.iop.org/0022-3727/47/36/365003>)

View [the table of contents for this issue](#), or go to the [journal homepage](#) for more

Download details:

IP Address: 130.225.102.1

This content was downloaded on 28/10/2014 at 15:48

Please note that [terms and conditions apply](#).

# Magnetic properties of ultra-small goethite nanoparticles

E Brok<sup>1,2</sup>, C Frandsen<sup>1,8</sup>, D E Madsen<sup>1</sup>, H Jacobsen<sup>3</sup>, J O Birk<sup>3</sup>,  
K Lefmann<sup>3</sup>, J Bendix<sup>4</sup>, K S Pedersen<sup>4</sup>, C B Boothroyd<sup>5</sup>, A A Berhe<sup>6</sup>,  
G G Simeoni<sup>7</sup> and S Mørup<sup>1</sup>

<sup>1</sup> Department of Physics, Technical University of Denmark, DK-2800 Kgs. Lyngby, Denmark

<sup>2</sup> Center for Electron Nanoscopy, Technical University of Denmark, DK-2800 Kgs. Lyngby, Denmark

<sup>3</sup> Nano-Science Center, Niels Bohr Institute, University of Copenhagen, DK-2100 Copenhagen Ø, Denmark

<sup>4</sup> Department of Chemistry, University of Copenhagen, DK-2100 Copenhagen Ø, Denmark

<sup>5</sup> Ernst Ruska-Centrum und Peter Grünberg Institut, Forschungszentrum Jülich, D-52425 Jülich, Germany

<sup>6</sup> Life and Environmental Sciences Group, University of California, Merced, CA 95343, USA

<sup>7</sup> Heinz Maier-Leibnitz Zentrum (MLZ) and Physics Department, Technische Universität München, D-85748 Garching, Germany

E-mail: [fracaf@fysik.dtu.dk](mailto:fracaf@fysik.dtu.dk)

Received 11 April 2014, revised 20 June 2014

Accepted for publication 1 July 2014

Published 21 August 2014

## Abstract

Goethite ( $\alpha$ -FeOOH) is a common nanocrystalline antiferromagnetic mineral. However, it is typically difficult to study the properties of isolated single-crystalline goethite nanoparticles, because goethite has a strong tendency to form particles of aggregated nanograins often with low-angle grain boundaries. This nanocrystallinity leads to complex magnetic properties that are dominated by magnetic fluctuations in interacting grains. Here we present a study of the magnetic properties of 5.7 nm particles of goethite by use of magnetization measurements, inelastic neutron scattering and Mössbauer spectroscopy. The ‘ultra-small’ size of these particles (i.e. that the particles consist of one or only a few grains) allows for more direct elucidation of the particles’ intrinsic magnetic properties. We find from ac and dc magnetization measurements a significant upturn of the magnetization at very low temperatures most likely due to freezing of spins in canted spin structures. From hysteresis curves we estimate the saturation magnetization from uncompensated magnetic moments to be  $\sigma_s = 0.044 \text{ A m}^2 \text{ kg}^{-1}$  at room temperature. Inelastic neutron scattering measurements show a strong signal from excitations of the uniform mode ( $q = 0$  spin waves) at temperatures of 100–250 K and Mössbauer spectroscopy studies show that the magnetic fluctuations are dominated by ‘classical’ superparamagnetic relaxation at temperatures above  $\sim 170$  K. From the temperature dependence of the hyperfine fields and the excitation energy of the uniform mode we estimate a magnetic anisotropy constant of around  $1.0 \times 10^5 \text{ J m}^{-3}$ .

Keywords: magnetic dynamics, nanoparticles of antiferromagnetic materials, nano-crystallinity

(Some figures may appear in colour only in the online journal)

## 1. Introduction

Goethite ( $\alpha$ -FeOOH) is a common mineral on Earth [1] and it has also recently been found on Mars [2]. The crystal structure of goethite is orthorhombic with space group  $Pnma$ . It is

antiferromagnetic with antiferromagnetic modulation along the orthorhombic  $a$ -axis and a Néel temperature around 400 K [3, 4]. Goethite usually forms rod-shaped nanoparticles, which often lack long-range crystalline order, because the particles consist of many grains, typically around 3–7 nm in size, with low-angle grain boundaries [5–7], both when found in nature and when laboratory synthesized. The complex influence of

<sup>8</sup> Author to whom any correspondence should be addressed.

the nanocrystallinity on the magnetic properties of goethite is apparent in Mössbauer spectroscopy studies [5] and the magnetic properties have been the subject of many such studies [4, 5, 8–13].

The magnetic properties of nanoparticles have been studied extensively by use of several experimental techniques, and the understanding of the magnetic properties of nanoparticles is of great importance for their many applications in, for example, magnetic data storage, ferrofluids, bioseparation and medicine [14, 15]. In many studies, collective magnetic properties of interacting grains and interacting particles seem to play an important role [16–18]. In case of antiferromagnetic goethite, dipolar interactions may be negligible, and inter-grain and inter-particle interactions may be predominantly due to exchange interactions.

Usually, Mössbauer spectra of non-interacting magnetic nanoparticles show a superposition of a doublet due to particles with fast superparamagnetic relaxation and a sextet due to particles with slow relaxation. The relative areas of the two components depend on temperature because of the temperature dependence of the superparamagnetic relaxation time. However, inter-particle interactions can have a significant influence on the magnetic dynamics and result in magnetically split Mössbauer spectra with asymmetrically broadened lines at temperatures where non-interacting particles show a quadrupole doublet because of fast superparamagnetic relaxation [14, 15].

Using a mean field model for exchange interacting particles, the magnetic energy,  $E_p$ , of a nanoparticle  $p$  may be written as a sum of a uniaxial anisotropy term  $E_p^a$  and an exchange interaction term,  $E_p^{\text{int}}$  [14–17]

$$E_p = E_p^a + E_p^{\text{int}} = K V_p \sin^2 \theta_p - J_{\text{eff}}^p \vec{M}_p \cdot \langle \vec{M}_p \rangle \quad (1)$$

where  $V_p$  is the particle volume,  $K$  is the magnetic anisotropy constant,  $\theta_p$  is the angle between the sublattice magnetization vector and the easy magnetization direction,  $\vec{M}_p$  is the sublattice magnetization,  $\langle \vec{M}_p \rangle$  is the average value of the sublattice magnetizations of neighbouring particles and  $J_{\text{eff}}^p$  is the effective inter-particle exchange coupling constant (with dimensions  $\text{J m}^2 \text{A}^{-2}$ ).  $J_{\text{eff}}^p \langle \vec{M}_p \rangle$  can be considered as an effective interaction field acting on  $\vec{M}_p$ .

Almost all Mössbauer studies of goethite particles have shown spectra, which consist of sextets with asymmetrically broadened lines, typical for interacting nanoparticles that are influenced by relaxation effects. This is the case even for quite large goethite particles (e.g., rods which are around 100 nm wide and 1000 nm long) [10]. The magnetic anisotropy constant is relatively large ( $K \approx 5 \times 10^4 \text{ J m}^{-3}$ ) [5] and therefore one might expect that relaxation effects should be negligible at room temperature for particles of this size. However, within the rod-shaped nanoparticles there are usually many defects such as low-angle grain boundaries, dislocations and interstitial water and/or  $\text{OH}^-$  [5–8, 19, 20] that may lead to a reduced magnetic coupling between the grains [5]. Because of the many defects, the magnetic dynamics is dominated by fluctuations of the sublattice magnetization directions in small interacting grains within the particles. In a mean field model,

the magnetic energy,  $E_g$  of such a grain  $g$  may be written as a sum of a uniaxial anisotropy term,  $E_g^a$ , and an exchange interaction term,  $E_g^{\text{int}}$ ,

$$E_g = E_g^a + E_g^{\text{int}} = K V_g \sin^2 \theta_g - J_{\text{eff}}^g \vec{M}_g \cdot \langle \vec{M}_g \rangle, \quad (2)$$

where  $V_g$  is the grain volume,  $\theta_g$  is the angle between the sublattice magnetization vector and the easy magnetization direction,  $\vec{M}_g$  represents the sublattice magnetization vector of the grain,  $\langle \vec{M}_g \rangle$  is the average sublattice magnetization of neighbouring grains and  $J_{\text{eff}}^g$  is an effective exchange coupling constant representing the exchange interactions with neighbouring grains such that  $J_{\text{eff}}^g \langle \vec{M}_g \rangle$  can be considered as an effective interaction field acting on  $\vec{M}_g$ . This grain model can explain the asymmetric line broadening in the Mössbauer spectra of larger goethite particles [5].

There is usually a large tendency for oriented attachment or nearly oriented attachment of particles and grains in goethite samples [5–7, 19, 20]. Therefore, the interaction field can be considered approximately parallel to the easy direction of magnetization. Equations (1) and (2) may therefore be written in the form [5]

$$E(\theta) \approx K V \sin^2 \theta - J_{\text{eff}} M_0^2(T) b(T) \cos \theta, \quad (3)$$

where  $M_0(T)$  is the sublattice magnetization and

$$b(T) = \frac{|\langle \vec{M}(T) \rangle|}{M_0(T)} \quad (4)$$

is the order parameter at temperature  $T$ . In thermal equilibrium, the order parameter can be calculated by the use of Boltzmann statistics:

$$b(T) = \frac{\int_0^\pi \exp\left(-\frac{E(\theta)}{k_B T}\right) \sin \theta \cos \theta d\theta}{\int_0^\pi \exp\left(-\frac{E(\theta)}{k_B T}\right) \sin \theta d\theta}. \quad (5)$$

Equations (3) and (5) are a set of coupled equations, which can be numerically solved self-consistently to find the order parameter  $b(T)$  [5, 17].

For interacting nanoparticles or grains the relative size of the two terms in equations (1) or (2) is important. If the interaction energy is predominant, there will only be one energy minimum, and the relaxation will then take place between states in this energy well and is expected to be fast [5]. The magnetic hyperfine splitting can therefore be considered to be proportional to  $|\langle \vec{M}(T) \rangle| = M_0(T) b(T)$ . If the anisotropy energy is predominant or comparable to the interaction energy, there will be two (non-equivalent) energy minima, which are separated by an energy barrier. In the absence of interactions, there are two equivalent minima and the magnetic dynamics is dominated by ‘classical’ superparamagnetic relaxation with a relaxation time given by [21, 22]

$$\tau = \tau_0 \exp\left(\frac{K V}{k_B T}\right), \quad (6)$$

where  $\tau_0$  is on the order of  $10^{-9} - 10^{-13}$  s.

Classical superparamagnetic behaviour, i.e. reversals of the sublattice magnetization directions of a particle as a whole, is rarely observed in studies of goethite, because magnetic fluctuations within the exchange-coupled grains are predominant [5]. However, if the particles are sufficiently small and separated such that inter-particle interactions are negligible ( $E_p^{\text{int}} \ll E_p^{\text{a}}$ ), the magnetic dynamics may be dominated by superparamagnetic relaxation of individual particles, and it may then be possible to estimate, for example, the magnetic anisotropy energy by use of Mössbauer spectroscopy and neutron scattering as it has been done in earlier studies of hematite ( $\alpha\text{-Fe}_2\text{O}_3$ ) nanoparticles [16, 23–25]. No previously published studies of goethite particles have included inelastic neutron scattering but recently, Pankhurst *et al* suggested investigations by this technique to help understand the magnetic properties of goethite [26].

In this paper we present studies of a commercial sample of ultra-small goethite particles before and after low-energy ball-milling together with rock salt (NaCl) nanoparticles. The goethite nanoparticles have an average diameter of around 5.7 nm, but each particle is made of up to a few smaller interacting grains (or clusters). We therefore have two types of magnetic interactions in the samples, namely interactions between particles and interactions between grains. The interactions between most of the particles are weak, especially in the ball-milled sample, and because the particles are very small the Mössbauer spectra are dominated by classical superparamagnetic relaxation at temperatures above  $\sim 170$  K in contrast to larger goethite particles in which the magnetic dynamics was dominated by fluctuations in interacting grains. Due to the small particle size and weak inter-particle interaction, we have been able to study more directly the intrinsic magnetic properties of goethite particles by use of Mössbauer spectroscopy, magnetization measurements and inelastic neutron scattering.

## 2. Experimental details

A goethite powder sample was obtained from the company NanoChemionics Inc. The sample was sold as F-2506 (Blend 07PSL-204). In the following this sample is named G1. Part of G1 was ball-milled with NaCl nanoparticles (weight ratio 1:3) at low intensity (40 rpm) for 48 h in an agate mill in order to reduce inter-particle interactions. NaCl nanoparticles, here termed ‘nano’-salt, were prepared by high-intensity (200 rpm) ball-milling in a tungsten carbide (WC) ball-mill for 24 h. This sample of goethite ball-milled with ‘nano’-salt is named GBM and used as prepared for the neutron scattering, Mössbauer spectroscopy and magnetization measurements, but with the salt washed out for the x-ray diffraction (XRD) and transmission electron microscopy (TEM) measurements.

XRD over an angular range of  $15^\circ$ – $90^\circ$  was performed at room temperature, using a Bruker D8 Advance powder diffractometer with a Co anode ( $\lambda = 1.79 \text{ \AA}$ ). Rietveld refinement of the orthorhombic *Pnma* structure of goethite was performed using the WINPOW program, a modified version of the LHMP1 program [27]. The G1 sample was

measured for 8 h on a plexiglas sample holder whereas the washed GBM sample was dried on a single crystal Si disc and measured for 18 h. The least squares refinements were performed with Voigtian peak profiles and the background was modelled with Chebyshev polynomials. Initial structural and atomic parameters were taken from [28].

TEM bright and dark-field images of the samples were taken using an FEI Technai T20 G2 microscope with a thermionic LaB<sub>6</sub> filament and an accelerating voltage of 200 kV.

$^{57}\text{Fe}$  Mössbauer spectroscopy was carried out using conventional constant acceleration spectrometers with sources of  $^{57}\text{Co}$  in rhodium and calibration was carried out using a  $12.5 \mu\text{m}$  foil of  $\alpha\text{-Fe}$  at room temperature. Spectra obtained at temperatures down to 20 K were recorded in a closed cycle helium refrigerator from APD Cryogenics. A spectrum obtained with an applied magnetic field of 6 T was recorded in a liquid helium cryostat with a superconducting coil.

Inelastic neutron scattering measurements were performed at the time-of-flight spectrometer TOFTOF at FRMII, Munich [29]. A neutron wavelength of  $7.0 \text{ \AA}$  was used, with a chopper speed of 12 000 rpm, giving an energy resolution of the elastic line of  $10 \mu\text{eV}$ . Data were taken in a temperature range of 10–300 K using the two samples G1 and GBM. Both samples had a mass of about 2 g and were filled in hollow cylinder Al cans. The typical exposure time was 5 h (8 h) for the G1 (GBM) sample.

AC and DC magnetization measurements were performed with a quantum design MPMS-XL magnetometer using a SQUID detector. The sample for the dc magnetization measurements was comprised of 33.06 mg of GBM mixed with 28.65 mg of eicosane. The mixture was heated to approximately  $40^\circ\text{C}$  where eicosane is a liquid. When the sample is cooled the eicosane becomes a solid wax, ensuring that the particles in the sample maintain the original (random) orientation. The sample was loaded in a capsule of gelatine. A sample with a larger amount of goethite (139.4 mg GBM) was prepared in a similar way for the ac measurements. Zero field cooled (ZFC) magnetization measurements were performed in a temperature range from 4.2 to 300 K in applied fields  $\mu_0 H = 2.0 \text{ mT}$  and 4.8 T. After each ZFC measurement the sample was cooled to 4.2 K and a field cooled (FC) magnetization measurement was performed in the same way as the ZFC. To isolate the contribution to the magnetization coming from the goethite particles we have subtracted the diamagnetic contributions from NaCl, eicosane (wax) and gelatine (capsule) in the ZFC/FC and hysteresis measurements, using the corresponding mass susceptibilities (in  $10^{-9} \text{ m}^3 \text{ kg}^{-1}$ ) of  $-6.4$ ,  $-10.8$  and  $-6.3$ , respectively. AC magnetization measurements were performed over the same temperature range with a driving field amplitude of 0.38 mT, at frequencies ranging from 1.0 to 1000 Hz. The magnetization as a function of applied field (hysteresis loops) was measured in fields over the range between  $-5$  and  $+5$  T at temperatures of 4.2 and 300 K.

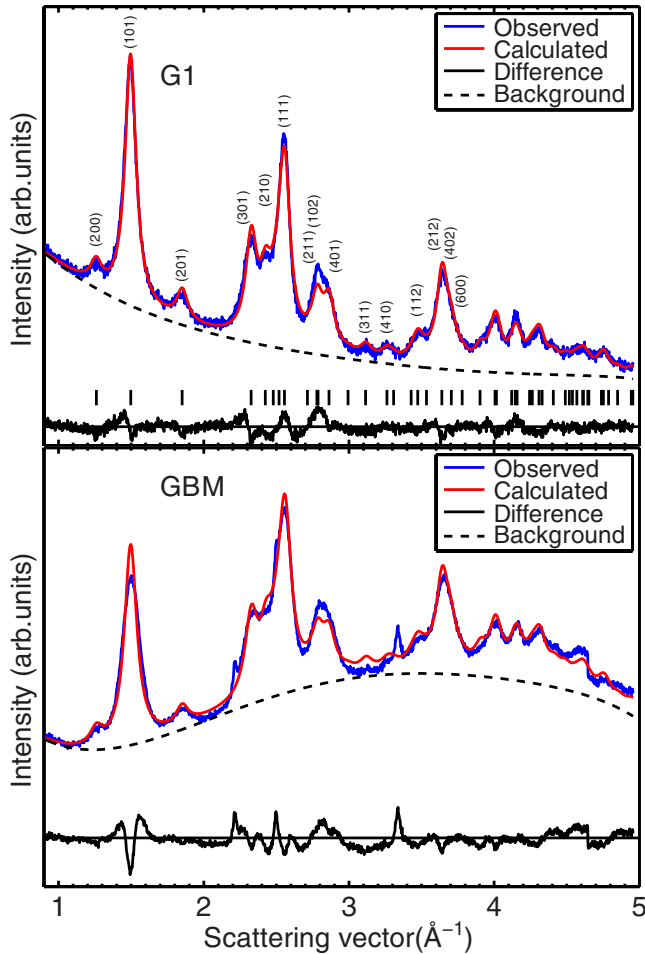


**Figure 1.** XRD patterns of samples G1 and GBM. The refined model, the background and the difference between model and experiment are displayed. The most prominent reflections up to the scattering vector length  $q = 4 \text{ \AA}^{-1}$  have been indexed.

### 3. Results

#### 3.1. Structural characterization

The XRD patterns of sample G1 and sample GBM (after the ‘nano’-salt has been washed away) are shown in figure 1, together with the refined models. For the G1 sample there are no signs of other phases in the sample than the  $Pnma$  goethite represented by the model. For GBM, there is, in addition to  $Pnma$  goethite, minor impurity peaks at the scattering vector length  $q = 2.2$  and  $3.3 \text{ \AA}^{-1}$ . The peak at  $2.2 \text{ \AA}^{-1}$  can be ascribed to the (200) reflection of NaCl ( $Fm3m$ ) (from residual salt after washing). The peak at  $3.3 \text{ \AA}^{-1}$  is from an unidentified impurity. The unit cell parameters, a Lorentzian profile broadening parameter, an overall temperature factor, and background parameters were refined. The instrumental broadening was assumed to be Gaussian and was known from measurement of a corundum ( $\text{Al}_2\text{O}_3$ ) standard, while the sample broadening was assumed to be Lorentzian. The refined lattice parameters are  $a = 9.986(3) \text{ \AA}$ ,  $b = 3.0273(8) \text{ \AA}$ , and  $c = 4.630(2) \text{ \AA}$ , and the weighted-profile-residual ( $R_{WP}$ ) and Bragg- $R$ -value ( $R_B$ ) are 0.95 and 0.30 respectively for sample G1. The refined lattice parameters for GBM are similar

( $a = 9.987(6) \text{ \AA}$ ,  $b = 3.022(2) \text{ \AA}$ , and  $c = 4.627(4) \text{ \AA}$ ), and the  $R$ -values are  $R_{WP} = 1.61$  and  $R_B = 0.31$ . Assuming the line broadening is only due to the finite particle size the refinements result in average particle diameters of  $6.7 \pm 1 \text{ nm}$  for sample G1 and  $4.9 \pm 1 \text{ nm}$  for GBM. While the positions of the diffraction peaks confirm that both samples consist of goethite with limited impurities the agreement between the data and the refined model is not ideal. This is likely due to an anisotropic peak broadening from non-spherical particles, and for the GBM data a large non-uniform background. The particle sizes determined from the diffraction patterns are therefore only estimates of the true average particle size.

TEM bright field images show that the G1 sample consists of micrometer-sized aggregates of pseudo-spherical goethite nanograins with dimensions around 3–5 nm as determined from the morphology of particles at the rim of the aggregates (figure 2(a)). From the lattice fringes (figure 2(a)) we infer that neighbouring grains have some crystalline alignment, but this is not extending over more than a few grains. This crystalline alignment is confirmed by dark-field images (figure 2(b)). From dark-field images of the G1 sample, we have measured the size of 57 particles (figure 2(c)), and calculated a volume-weighted average particle size to  $5.4 \pm 1.7 \text{ nm}$ . This particle size is in agreement (within uncertainty) with that determined from the XRD data. TEM dark-field images of the ball-milled sample, GBM, after the ‘nano’-salt has been washed away, show that the low-energy ball-milling has not significantly altered size and morphology of the goethite nanoparticles (figure 2(d)). Thus XRD and TEM data show that the volume weighted particle size is around 5.7 nm. Assuming spherical particle shape, this corresponds to a particle volume close to  $100 \text{ nm}^3$ .

#### 3.2. Magnetization measurements

Nanoparticles of antiferromagnetic materials usually have small uncompensated magnetic moments due to, for example, uncompensated spins at the surface or defects in the interior of the particles. Magnetization data can have predominant contributions from the uncompensated magnetic moments. The magnetic dynamics of the uncompensated spins may be different from the relaxation of the sublattice magnetization vectors of the particles as a whole. Therefore, magnetization data may not be directly comparable to Mössbauer and inelastic neutron scattering data, which are sensitive to all parts of the particles.

**3.2.1. ZFC/FC measurements** Figure 3 shows the ZFC/FC measurements for GBM. In the low applied field of  $\mu_0 H = 2.0 \text{ mT}$  the magnetization curves in the temperature range from about 30 to 300 K look as expected for nanoparticles undergoing superparamagnetic relaxation. The peak temperature in the ZFC curve is  $T_p = 130 \text{ K}$ . This value depends on the distribution of superparamagnetic blocking temperatures in the sample, and in turn on the particle size distribution as well as the degree of inter-particle interactions [15]. Above a temperature of around 250 K the ZFC and FC curves coincide, indicating that all particles have

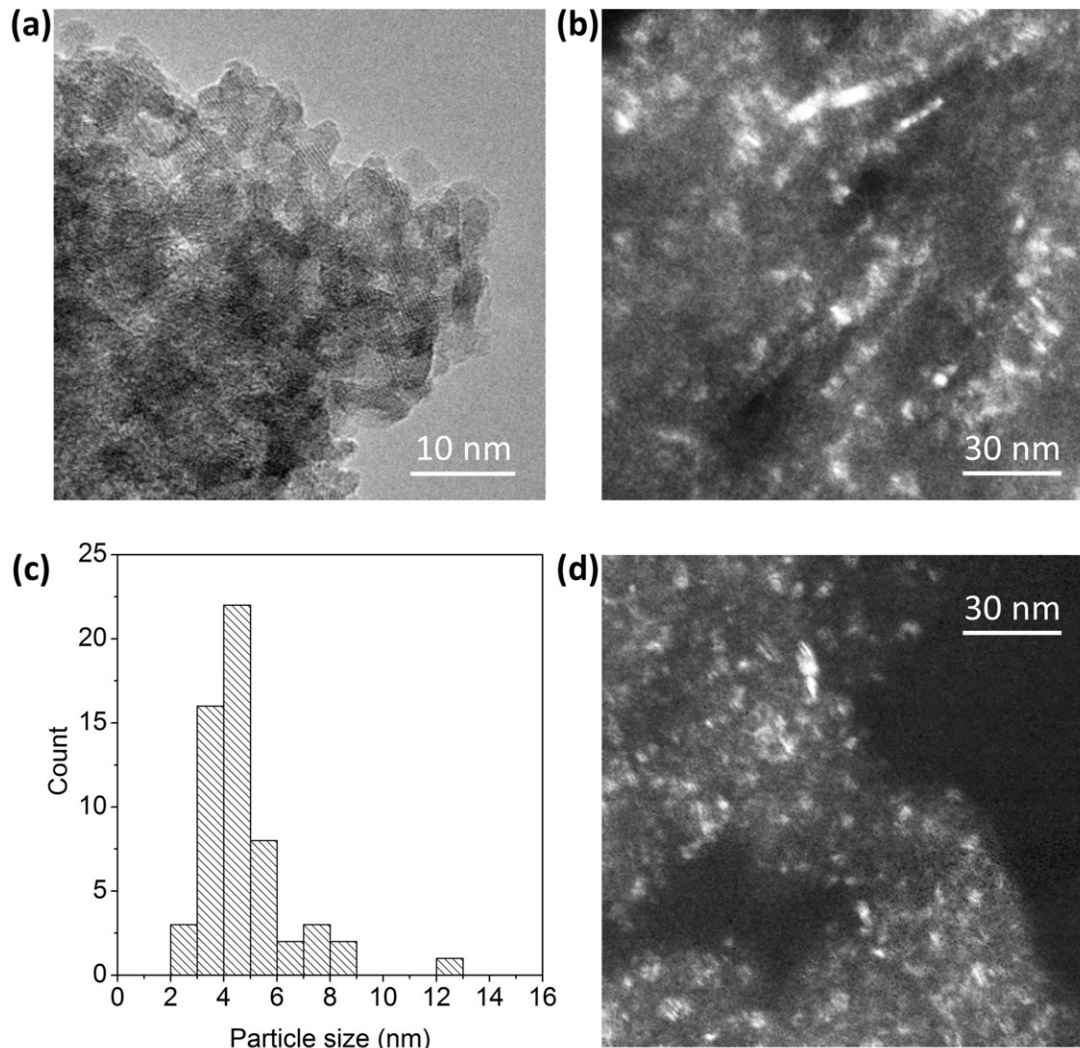


**Figure 2.** TEM images. (a) High-resolution image from the rim of a G1 aggregate. (b) Dark-field image from a G1 aggregate. (c) Particle sizes measured from a dark-field image of the G1 sample. (d) Dark-field image of sample GBM, after the 'nano'-salt has been washed away.

reached their blocking temperature. An interesting feature in the measurements is the sharp increase of the magnetization below 30 K in both the ZFC and the FC measurements. The magnetization in the FC measurement increases by  $3.3 \times 10^{-3} \text{ A m}^2$  per kg goethite from 30 to 4.2 K. The increase in the ZFC magnetization has nearly the same magnitude ( $3.0 \times 10^{-3} \text{ A m}^2 \text{ kg}^{-1}$ ). A similar anomalous temperature dependence of the low-temperature magnetization has been observed in several studies of ferrite nanoparticles [30] and may be explained by freezing of spins in canted spin structures with very low energy barriers [30]. For the measurements in a strong applied field of  $\mu_0 H = 4.8 \text{ T}$  there is no peak in the ZFC curve and the ZFC and FC curves nearly coincide in the whole temperature range. There is an increase in the magnetization below 30 K qualitatively similar to the observations in the 2.0 mT measurements of around  $5.4 \text{ A m}^2 \text{ kg}^{-1}$  both in the ZFC and FC curves. Similar results were obtained for sample G1.

**3.2.2. AC magnetization measurements.** The in-phase ac susceptibility ( $\chi'$ ) data for GBM are shown in figure 4.

From the frequency dependence of the peak positions it was attempted to determine  $\tau_0$  and  $KV$  by plotting  $\ln(\omega)$  versus the reciprocal peak temperature ( $\omega$  is the angular frequency) and fitting a straight line. This method has been demonstrated, for example, in [31]. However, the fit resulted in an unreasonable value of  $\tau_0$  (on the order of  $10^{-24} \text{ s}$ ), indicating that the temperature dependence of the relaxation time is not in accordance with equation (6), presumably because of inter-particle and/or inter-grain interactions. Similar observations have been made in several other ac magnetization studies of interacting nanoparticles, e.g. [32–34]. The increase in magnetization at low temperatures seen in the ZFC/FC measurements is also seen in the in-phase ac susceptibility and is largely independent on the frequency of the driving field. A similar increase in the ac magnetization of goethite nanoparticles at low temperatures has recently been observed by Pankhurst *et al* [26]. This anomaly can be explained by freezing of spin structures, which at higher temperatures are influenced by magnetic fluctuations across very low energy barriers [26, 30]. We also measured the out-of-phase signal ( $\chi''$ ), but the signal was very weak. There was no increase in

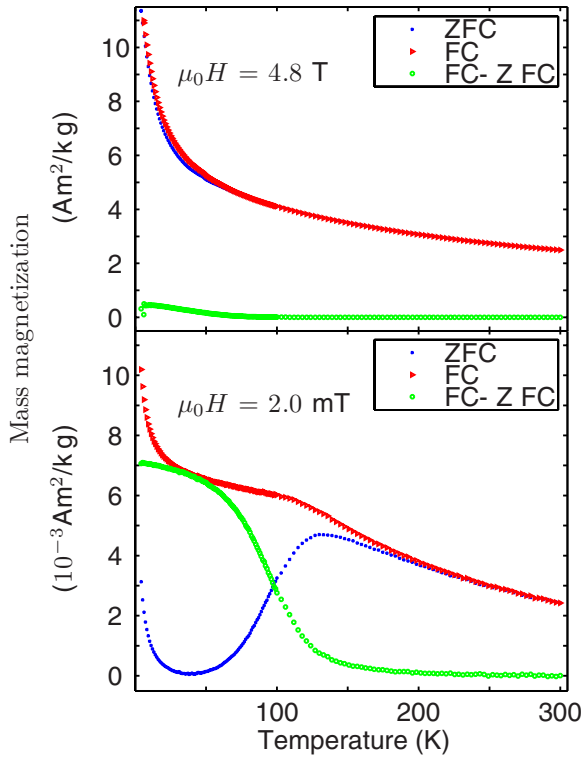


**Figure 3.** ZFC/FC magnetization curves for the sample GBM obtained in an applied field of (top) 4.8 T and (bottom) 2.0 mT. The magnetization is given per kg of goethite in the sample.

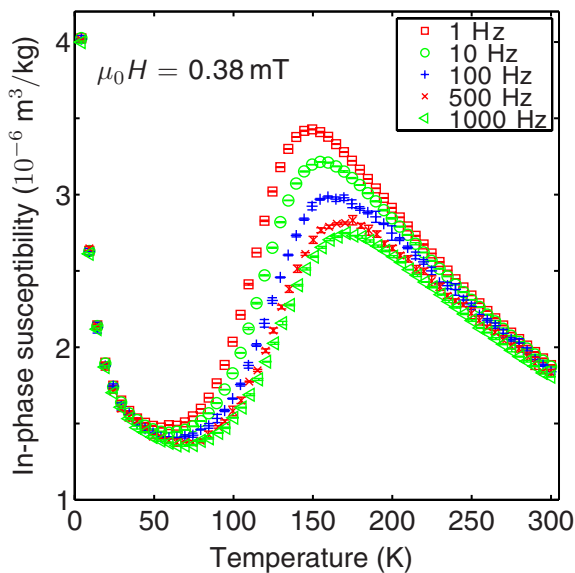


**Figure 4.** In-phase ac susceptibility ( $\chi'$ ) as a function of temperature for the GBM sample. The amplitude of the driving field was  $\mu_0 H = 0.38$  mT.

$\chi''$  at low temperatures. AC magnetization measurements on sample G1 gave results similar to those for GBM. Thus the reduction of inter-particle interactions after ball-milling has only little influence on the ac and dc magnetization data. This may be explained by a large contribution to the magnetization from the uncompensated magnetic moment, which is only slightly influenced by inter-particle interactions.

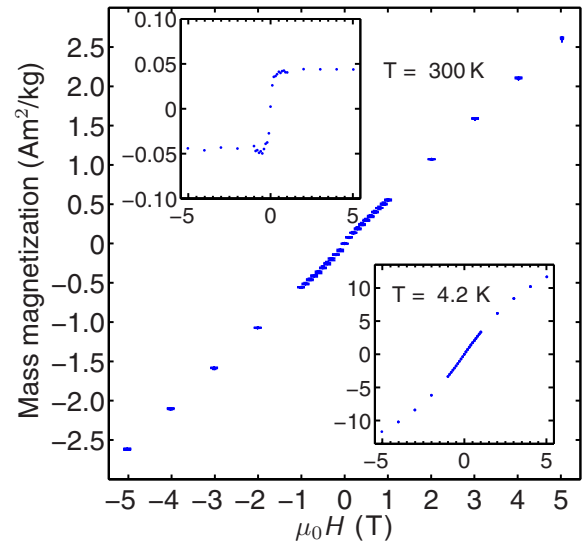


**Figure 5.** Hysteresis loop of the GBM sample at 300 K. The magnetization is given per kg of goethite in the sample. The upper inset shows the average of the positive and negative magnetization curves after subtraction of a linear function resulting from a fit to the high-field parts of the curves. The step in the curve corresponds to a moment of  $0.044 \text{ A m}^2 \text{ kg}^{-1}$ . The lower inset shows the hysteresis loop of the GBM sample at 4.2 K. The units on the insets are the same as on the main figure.

**3.2.3. Hysteresis measurements.** Hysteresis loops in fields up to  $\mu_0 H = 5$  T were measured for the GBM sample at 4.2 and 300 K. The 300 K hysteresis loop is shown in figure 5. At 300 K there is no hysteresis within the experimental uncertainty (i.e. the remanence is less than about  $0.003 \text{ A m}^2 \text{ kg}^{-1}$  and the coercive field is less than a few mT). The hysteresis loop at 4.2 K is shown in the lower inset in figure 5. There is only a very weak hysteresis, with a remanence of approximately  $0.015 \text{ A m}^2 \text{ kg}^{-1}$  and a coercive field of about 5 mT. For the 300 K data the branches of the hysteresis loop were well approximated by a straight line at fields higher than about 2 T. A straight line was fitted to the points at higher fields and subtracted from the hysteresis curve in order to see the response of the uncompensated magnetic moment as demonstrated in [26] and [35]. This is shown in the upper inset in figure 5, where the step in the magnetization corresponds to a saturation specific magnetization of  $\sigma_s = 0.044 \text{ A m}^2 \text{ kg}^{-1}$  of goethite in the sample. The magnetization saturates in an applied field of approximately 0.2 T. For the 4.2 K hysteresis measurement (lower inset in figure 5) the points at higher fields could not be fitted well with a straight line, indicating that there is some unsaturated moment. This is presumably related to the rise in magnetization at low temperatures seen in the ZFC/FC curves.

### 3.3. Neutron scattering

Inelastic neutron scattering data for G1 and GBM at 10–300 K are shown in figure 6 as intensity maps of the neutron momentum transfer,  $q$ , versus the neutron energy transfer,  $\varepsilon$ . The colour scale is chosen to enhance the inelastic features. At the lowest temperature, 10 K, both samples show only elastic scattering (the broad red line at  $\varepsilon = 0$  in all data), while

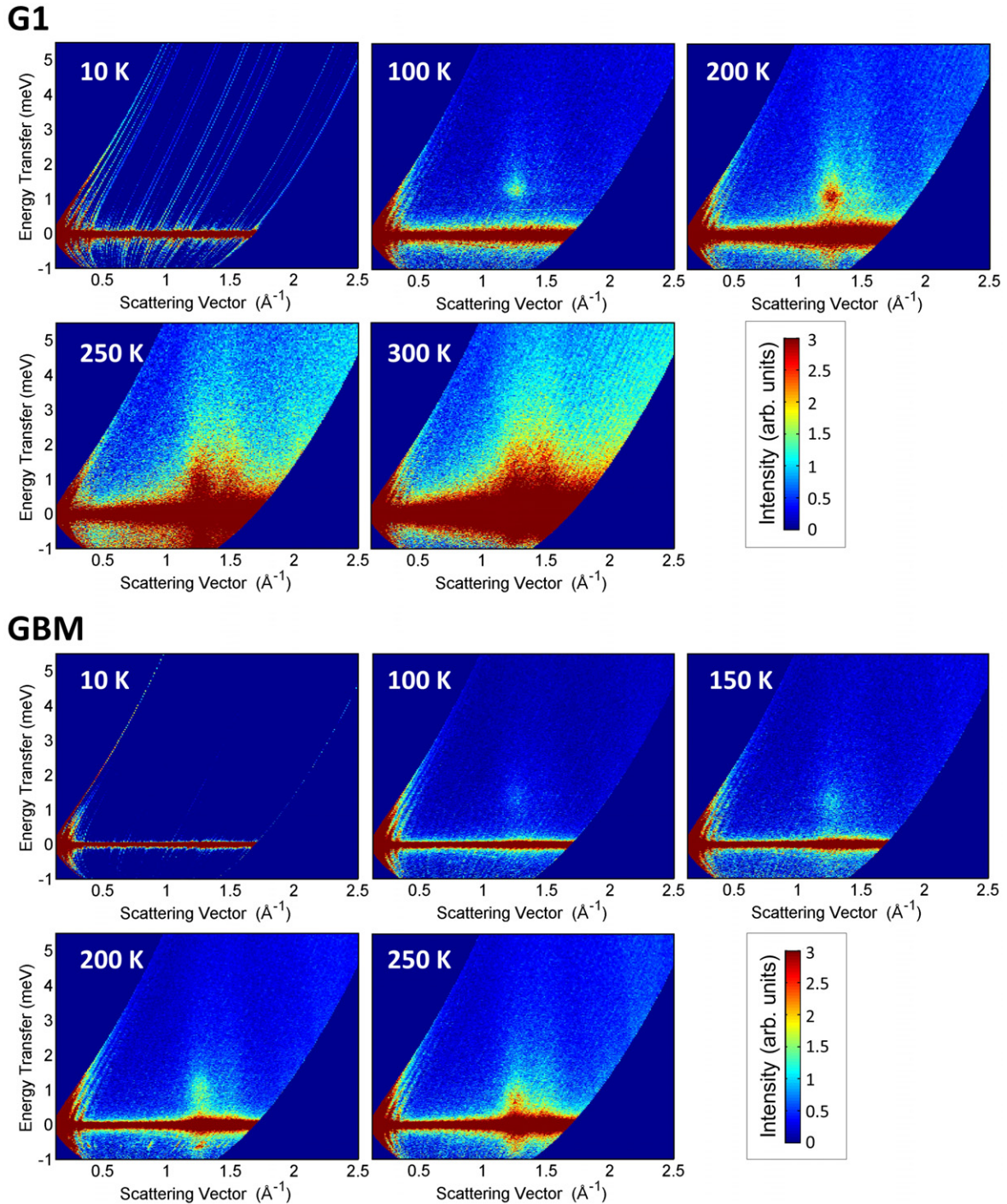


**Figure 6.** Inelastic neutron scattering data for samples G1 and GBM shown as intensity maps of neutron momentum transfer  $q$  and neutron energy transfer  $\varepsilon$  at the indicated temperatures.

inelastic features show up at elevated temperatures of 100–300 K. In the G1 sample at 100 K, a singular inelastic signal appears at  $q = 1.258 \text{ \AA}^{-1}$  and  $\varepsilon \sim 1.5 \text{ meV}$ , with a weaker counterpart at  $q = 1.502 \text{ \AA}^{-1}$ . These two inelastic signals gradually broaden and decrease in energy with increasing temperature, to almost merge with the (quasi-)elastic scattering at 300 K. The GBM sample shows many of the same features as G1, only with a much weaker signal due to the lower amount of goethite in the GBM sample. Again, the most prominent feature is the singular peak at  $q = 1.258 \text{ \AA}^{-1}$  and  $\varepsilon \sim 1-$

$1.5 \text{ meV}$ , showing most clearly at 150 K, but hints of a similar signal at  $q = 1.502 \text{ \AA}^{-1}$  is also visible in this sample. The high-energy background seen at 250 and 300 K in the G1 sample is also present in the GBM sample, but is more difficult to see in the latter due to the generally smaller signal.

$q$ -values of  $1.258$  and  $1.502 \text{ \AA}^{-1}$  correspond to the (2 0 0) and (1 0 1) diffraction peaks. There are both structural and magnetic contributions to the (2 0 0) and (1 0 1) diffraction peaks [3]. The inelastic signal is, however, most likely of magnetic origin because there is an energy gap between the

elastic line and the excitation at temperatures up to about 200 K where after it collapses into the elastic line at a temperature of about 300 K. If the signal was originating from lattice dynamics, i.e. phonons, it might also be gapped because of the finite particle size, but the gap would then be expected to remain at temperatures up to the melting point of the sample. The broadening around  $\varepsilon = 0$  is expected to be due to superparamagnetic relaxation and the strong satellite peak around an energy transfer of 1.0–1.5 meV a signature of excitations of the uniform mode ( $q = 0$  spin waves) as seen in previous studies of antiferromagnetic (e.g., hematite) nanoparticles [16,24]. Although the signals from the two magnetic reflections partially overlap, we performed a separate treatment of the intense  $q = 1.258 \text{ \AA}^{-1}$  signal assuming that all inelastic signal has a magnetic origin.

Figure 7 shows the energy transfer at  $q = 1.258 \text{ \AA}^{-1}$  at 100–300 K for samples G1 and GBM. The data for GBM have a low signal to noise ratio because the sample was diluted with NaCl. If all particles were identical, non-interacting, and without a grain structure, the energy dependence of the magnetic signal would consist of one quasi-elastic peak centered at  $\varepsilon = 0$  and two side peaks at energy  $\pm\varepsilon_0$ . The quasi-elastic peak would have a width and shape determined by the instrumental resolution and the superparamagnetic relaxation time, while the side peaks have an intrinsic broadening due to its damped harmonic oscillator (dho) nature [24]. However, in practice there will be additional broadening due to a distribution of uncompensated spins [36] and inter-particle and inter-grain interactions [16] leading to a distribution of excitation energies. In the data for samples G1 and GBM the side peaks are asymmetrically broadened and can be described as relatively sharp peaks at  $\pm\varepsilon_0$  and broader peaks extending to higher energies. We suggest that a large fraction of the particles have limited interactions, giving rise to the satellite peak at  $\varepsilon_0$ . The broader peaks at higher energies can be attributed to more strongly interacting grains and/or interacting particles, because magnetic interactions result in an increase of the excitation energies [16]. The data are therefore fitted with one Voigtian profile to take account of the (quasi-)elastic line at  $\varepsilon = 0$  plus two dho modes to fit the main peak at  $\varepsilon_0$  and the scattering at higher energies, respectively. The fits are shown together with the data in figure 7. Even though the assumption of only two dho modes to fit the inelastic signal is quite simple, the fit reproduces the observed features reasonably well, including the clear asymmetry with tails extending towards higher energy values. We have used this method consistently in our data analysis for all data from the G1 and GBM samples taken at temperatures between 100 and 300 K. The inelastic signal is too small in the 10 K data to extract any reliable information. Figure 8 shows the temperature dependence of  $\varepsilon_0$ , i.e. the energy positions of the sharp peaks, which we attribute to uniform magnetic excitations of non-interacting particles. We found that for sample G1  $\varepsilon_0$  decreases from around 1.38 meV at 100 K to 1.06 meV at 250 K. Correspondingly, for the GBM sample  $\varepsilon_0$  decreases from about 1.48 meV at 100 K to 1.03 (3) meV at 250 K. The solid lines in figure 8 are fits of the data at temperatures below 300 K to the theoretical model developed by Würger [37] in which the temperature dependence of the

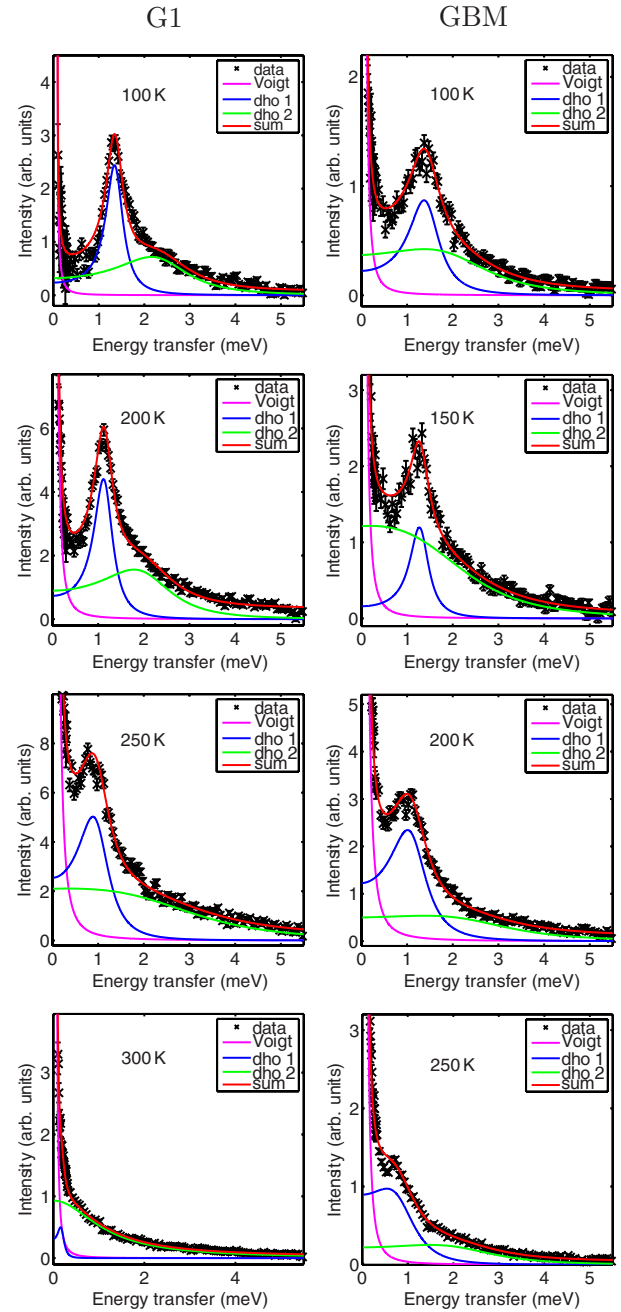


**Figure 7.** Neutron energy transfer data integrated over a narrow  $q$ -range at  $q = 1.258 \text{ \AA}^{-1}$  of samples G1 and GBM at the indicated temperatures. Each data set is fitted with one Voigtian profile (Voigt) and two damped harmonic oscillator modes (dho1 and dho2) as described in the text.

excitation energy is given by

$$\varepsilon_0 = \varepsilon_0(T = 0) \sqrt{1 - \frac{k_B T}{KV}} \quad (k_B T < KV). \quad (7)$$

The model represents the data well and yields the parameters  $\varepsilon_0(T = 0) \approx 1.55 \text{ meV}$  and  $KV/k_B \approx 467 \text{ K}$  for G1, and  $\varepsilon_0(T = 0) \approx 1.68 \text{ meV}$  and  $KV/k_B \approx 417 \text{ K}$  for GBM. With a particle volume of  $100 \text{ nm}^3$  this corresponds to a magnetic anisotropy constant of  $K \approx 0.6 \times 10^5 \text{ J m}^{-3}$  for both samples. (In the calculations we have neglected

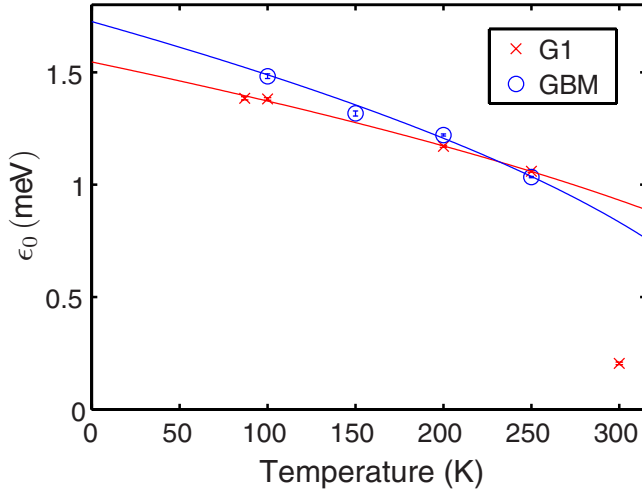


**Figure 8.** The  $\varepsilon_0$ -values as a function of temperature obtained from fitting neutron data of samples G1 and GBM.

the possible temperature dependence of  $K$ ). The distinct  $\varepsilon_0$ -peak has almost disappeared at 300 K (sample G1, figure 7), indicating that there is a transition from coherent precession of the sublattice magnetization around an easy axis to incoherent motion, as expected when the thermal energy becomes comparable to the energy barrier [37].

For an isolated nanoparticle of a simple uniaxial antiferromagnetic material, the position of the satellite peak is given by [16, 38]

$$\varepsilon_0 = g\mu_B \left[ \sqrt{B_A^2 + B_A B_E (2 + \delta) + \frac{B_E^2 \delta^2}{4}} - \frac{B_E \delta}{2} \right] \approx g\mu_B \left[ \sqrt{2B_A B_E} - \frac{B_E \delta}{2} \right], \quad (8)$$

where  $B_A = K/M_0$  is the anisotropy field,  $K$  is the magnetic anisotropy constant,  $M_0$  is the sublattice magnetization and  $B_E$  is the exchange field. In goethite  $B_E \approx 390$  T and  $M_0 = 5.25 \times 10^5 \text{ JT}^{-1} \text{ m}^{-3}$  [39].  $\delta$  is a measure of the uncompensated magnetic moment and is defined as  $\Delta M/M_0$  where  $\Delta M$  is the difference between the magnetic moments of the two sublattices. For an antiferromagnetic nanoparticle with  $N$  magnetic ions the uncompensated magnetic moment is expected to be on the order of  $N^{1/3}$  if the interior of the particle is free of defects, but surface sites are randomly occupied [15, 40, 41]. Using the saturation magnetization estimated from the magnetization measurements shown in figure 5 we find that  $\delta$  is about  $3.6 \times 10^{-4}$ . The neutron data show that  $\varepsilon_0 \approx 1.6$  meV at very low temperatures. Inserting  $\varepsilon_0 = 1.6$  meV and  $\delta = 3.6 \times 10^{-4}$  in equation (7) we find  $K \approx 1.3 \times 10^5 \text{ J m}^{-3}$ . This is same order of magnitude as the values estimated in earlier studies ( $K = 6 \times 10^4 \text{ J m}^{-3}$  [26],  $K \approx 3 \times 10^5 \text{ J m}^{-3}$  [42, 43] and  $K > 6 \times 10^4 \text{ J m}^{-3}$ ) [44]. The particles in GBM are much smaller than those used for earlier estimates of the magnetic anisotropy constant, and therefore the surface contribution to the magnetic anisotropy is expected to be larger [15, 45].

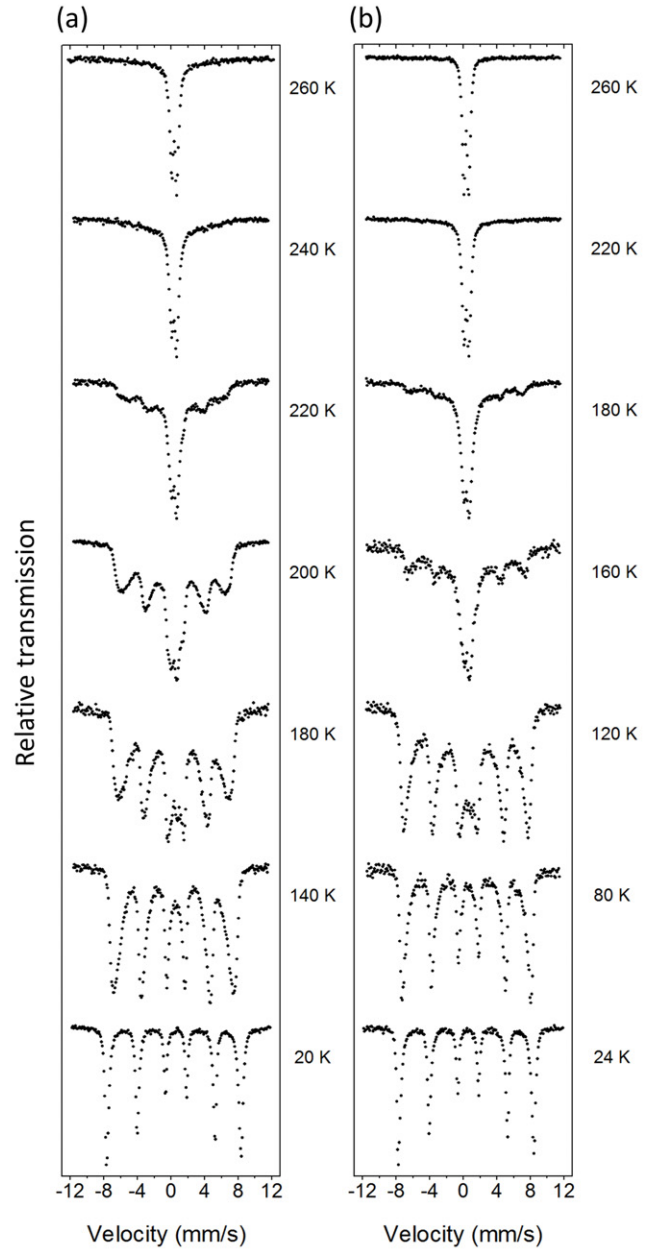


**Figure 9.** Mössbauer spectra of G1 (a) and GBM (b) obtained at the indicated temperatures in zero applied field.

### 3.4. Mössbauer spectroscopy

Mössbauer spectra of the samples G1 and GBM, obtained at the indicated temperatures, are shown in figures 9(a) and (b), respectively. At the lowest temperatures the spectra are magnetically split with a magnetic hyperfine field of 49.5 T, an isomer shift of  $0.49 \text{ mms}^{-1}$  and a quadrupole shift of  $-0.13 \text{ mms}^{-1}$ , which is in accordance with previous Mössbauer studies of goethite particles [4, 42]. There is no indication of impurity phases. Thus the ball-milling of GBM has not affected the chemical state of iron. At higher temperatures, the spectra of G1 and GBM show an asymmetric line broadening, indicating that the magnetic properties are influenced by magnetic fluctuations in interacting grains, as typically seen in goethite. However,

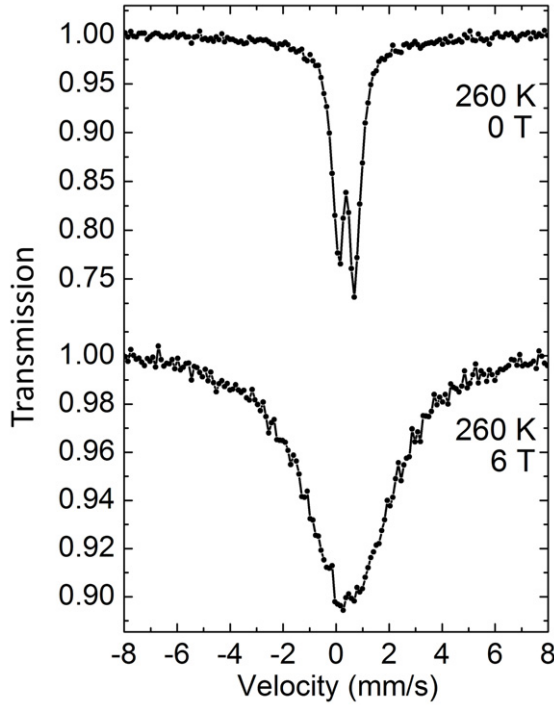


**Figure 10.** Mössbauer spectra of G1 obtained at 260 K with and without an applied field of 6 T.

already at temperatures of  $\sim 220$  and  $\sim 170$  K the spectra of G1 and GBM collapse to doublets suggesting that the particles exhibit fast superparamagnetic relaxation. It has previously been suggested [12] that such a collapse of the magnetic splitting in Mössbauer spectra of goethite is not due to the onset of fast superparamagnetic relaxation, but a low Néel temperature. We have investigated this possibility by applying a magnetic field to G1 of 6 T at 260 K, i.e. above the temperature where the magnetic splitting has collapsed to a doublet. If the goethite was paramagnetic at this temperature, the spectrum should only show a slight line broadening compared to the zero-field spectrum. However, the spectrum in figure 10 shows a substantial line broadening, corresponding to magnetic hyperfine fields up to around 40 T. This clearly shows that the collapse of the magnetic splitting is not due to a low Néel temperature, but due to fast superparamagnetic relaxation.

The distribution of anisotropy energies and interaction energies in a sample will result in a distribution of magnetic hyperfine fields at finite temperatures. In the superferromagnetism model [4, 17, 46], the values of the anisotropy energy,  $KV$  and the interaction energy parameter  $T_p^0$  are free parameters for each quantile, where the quantile,  $f$ , is defined as

$$f = \int_0^{B_f(T)} p(B_{hf}(T)) dB_{hf}. \quad (9)$$

$T_p^0$  is defined as the ordering temperature for a sample with zero anisotropy ( $KV = 0$ ) and is given by the expression [4, 5, 17]

$$T_p^0 = \frac{J_{\text{eff}} M_0 (T_p^0)^2}{3k_B}. \quad (10)$$

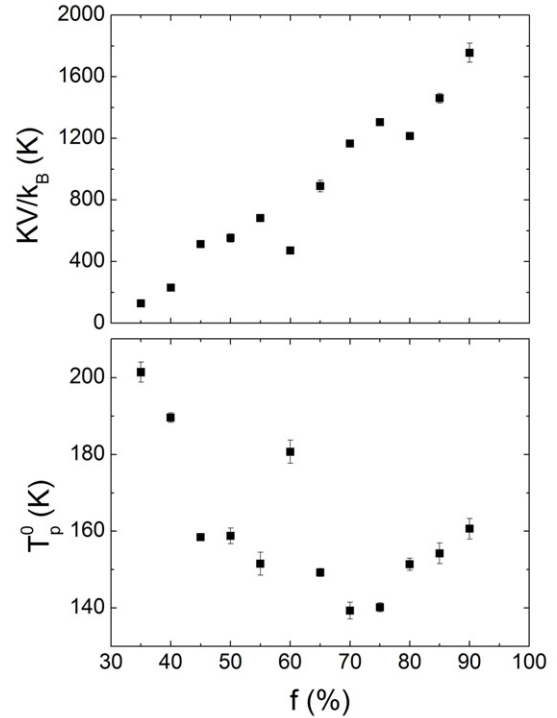


**Figure 11.** Magnetic anisotropy energy (top) and interaction energy (bottom) for sample G1 in units of Kelvin as a function of the quantile.

It has been found that the temperature dependence of quantiles in the hyperfine field distribution  $p(B_{hf}(T))$  in hematite nanoparticles gave values of the magnetic anisotropy energies, which were in accordance with those found for the non-interacting particles [17]. This strongly supports the validity of the model. The interaction energy,  $E_i(T) = J_{\text{eff}} M_0(T)^2 b(T)$  depends on temperature, because both  $b(T)$  and  $M_0^2(T)$  are temperature dependent. As an approximate measure of the interaction energy well below  $T_p$  we use the value  $E_{\text{int}} = 3k_B T_p^0$ .

In an earlier Mössbauer study of goethite with particle size on the order of  $1800 \text{ nm}^3$  the anisotropy energy  $KV/k_B$  was found to increase from around 400 K for the 40% quantile to around 1400 K for the 80% quantile [5]. The interaction energy  $E_{\text{int}}/k_B$  was on the order of 800 K for all quantiles in the same range. Thus, the interaction energy and the anisotropy energy were on the same order of magnitude in this sample. For a particle with volume of  $1800 \text{ nm}^3$  and a magnetic anisotropy constant  $K \geq 5 \times 10^4 \text{ J m}^{-3}$  and  $\tau_0 \approx 10^{-11} \text{ s}$  the relaxation time at 300 K should be on the order of 0.03 s or longer, i.e. much longer than the time scale of Mössbauer spectroscopy. Therefore, the line shape in the Mössbauer spectra could not be explained by fluctuations of the sublattice magnetization in the particle as a whole, but by magnetic fluctuations in small grains within the particles.

For our sample G1, the analysis of hyperfine field distributions was only performed at temperatures below 200 K, because the doublet becomes predominant at higher temperatures. The estimated values of  $KV$  and  $T_p^0$  for sample G1, obtained from the superferromagnetism model, are shown in figure 11. Presumably, the magnetic hyperfine

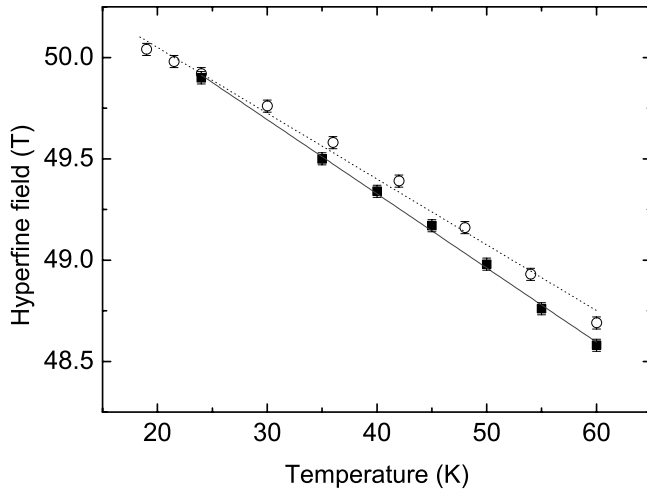


**Figure 12.** Magnetic hyperfine field of samples G1 (open circles) and GBM (solid squares) as a function of temperature. The lines represent linear fits (equation (11)).

field distribution is influenced by both inter-grain interactions and inter-particle interactions. The total interaction  $3T_p^0$  varies between  $\sim 400$  and  $600$  K for all quantiles shown in figure 11, but a quantification of the two interaction energy contributions is not feasible by the superferromagnetism model. The anisotropy energy,  $KV$ , varies from around  $200$  K to around  $1600$  K with a value around  $500$  K for the  $50\%$  quantile, and the interaction energy was on the order of  $450$  K. If we assume that the volume  $V$  is the average volume of the particles ( $\sim 100$  nm<sup>3</sup>) we find an anisotropy constant  $K \approx 0.7 \times 10^5$  J m<sup>-3</sup> which is close to that estimated by other methods.

In our sample GBM the magnetic hyperfine splitting has almost completely collapsed at a much lower temperature (around  $170$  K) than in sample G1, indicating that inter-particle interactions have been reduced by the milling. An analysis based on the superferromagnetism model was not made for sample GBM because the doublet is predominant at quite low temperatures. Instead we plotted the average hyperfine field as a function of temperature, see figure 12. In non-interacting magnetic nanoparticles at low temperatures this temperature dependence is given by [14, 15]

$$B_{hf}(T) \approx B_{hf}(0) \left[ 1 - \frac{k_B T}{2KV} \right]. \quad (11)$$

A fit of the data to a straight line gave the value  $K = 0.9 \times 10^5$  J m<sup>-3</sup> for  $V = 100$  nm<sup>3</sup>. However, if inter-particle interactions and magnetic fluctuations in grains are not negligible, this value may be overestimated [16]. For comparison (see figure 12), sample G1 shows a smaller decrease of  $B_{hf}$  with temperature presumably due to interparticle interactions.

#### 4. Discussion

Magnetic relaxation in non-interacting nanoparticles of most magnetic materials, such as, for example,  $\alpha$ -Fe<sub>2</sub>O<sub>3</sub>,  $\gamma$ -Fe<sub>2</sub>O<sub>3</sub>, NiO and  $\alpha$ -Fe, is usually dominated by ‘classical’

superparamagnetic relaxation with a relaxation time given by equation (6) [15]. Mössbauer spectra then show a superposition of a sextet due to particles with relatively slow relaxation and a doublet due to particles with fast relaxation. The area ratio of the two components depends on temperature because of the temperature dependence of the relaxation time. However, Mössbauer spectra of goethite nanoparticles commonly show an unusual behaviour because the magnetic relaxation is dominated by fluctuations of the sublattice magnetization directions in strongly interacting grains within the particles, and this results in Mössbauer spectra consisting of sextets with asymmetrically broadened lines in a broad range of temperatures without the presence of a doublet [5].

Mössbauer spectra of magnetic nanoparticles showing asymmetrically broadened lines have in several papers been analysed by using the multi-level model originally proposed by Jones and Srivastava [47]. In this model one considers not only jumps of the magnetization direction between the two minima of the magnetic energy of non-interacting particles, but also transitions between states within the two energy wells. Using this model it is in fact possible to reproduce the asymmetric line broadening in the Mössbauer spectra. However, in order to simulate the spectra one has to assume a relatively slow relaxation. For example, van Lierop and Ryan [48] found a pre-exponential factor  $\tau_0$  on the order of  $10$  ns in fits of spectra of  $\gamma$ -Fe<sub>2</sub>O<sub>3</sub> nanoparticles. In other papers on simulations and fits of Mössbauer spectra of magnetic nanoparticles [49, 50] it was found that the spectra were magnetically split with asymmetrically broadened lines for  $KV/k_B T \leq 1$ , indicating that  $\tau_0$  is considerably larger than  $1$  ns. This is in contradiction to numerous published Mössbauer and magnetization studies. Therefore, another model is needed to explain the spectra. In several papers we have demonstrated that magnetic nanoparticles, which show superpositions of doublets and sextets when non-interacting, show sextets with asymmetrically broadened lines, when the particles are in close proximity. Even well above the temperature where non-interacting particles show doublet spectra, interacting particles from the same batch can show magnetically split spectra with asymmetrically broadened lines [16–18, 51–53]. In accordance with this we believe that our model for the magnetic dynamics of interacting nanoparticles is the most realistic approach to interpret our data for goethite nanoparticles.

The reason for the unusual behaviour of goethite nanoparticles is that goethite usually is poorly crystalline and contains defects like dislocations and low-angle grain boundaries. The particles can therefore be described as consisting of grains that interact due to exchange coupling [5]. The present studies of ultra-small goethite particles have clearly shown that particles with dimensions below a critical size and weak inter-particle interactions show a magnetic relaxation that is dominated by ‘classical’ superparamagnetic relaxation. Our studies also show that inter-particle interactions can be reduced by ball-milling together with nanosized NaCl particles. This reduction of the inter-particle interactions can be clearly seen from the temperature dependence of the Mössbauer spectra.

Inelastic neutron scattering has earlier revealed that uniform excitations are the predominant spin-wave excitations in  $\alpha$ -Fe<sub>2</sub>O<sub>3</sub> [16, 24] and NiO [54] below the superparamagnetic blocking temperature. The present neutron study shows that this is also the case for goethite. In the inelastic neutron data for both G1 and GBM, a relatively sharp peak at around 1.0–1.5 meV was attributed to particles with negligible inter-particle interactions, whereas a broader component with higher energy was attributed to magnetic fluctuations in interacting particles and interacting grains. This can explain why the position of the sharp peak is not much affected by the ball milling. This interpretation is in accordance with earlier studies of  $\alpha$ -Fe<sub>2</sub>O<sub>3</sub> [16] and NiO [54] with varying inter-particle interactions. We have previously performed inelastic neutron scattering studies of larger goethite particles in which the magnetic fluctuations are dominated by fluctuations of the sublattice magnetization of interacting grains (unpublished). In these studies no sharp satellite peaks were observed. Instead the data showed very broad features, similar to the broad satellite peaks in figure 7. In inelastic neutron studies of 8 nm hematite particles [16] and disc shaped NiO nanoparticles [54] it was also found that inter-particle interactions result in broadening of the satellite peaks and a shift towards higher energies. This supports the interpretation of the broad components in the inelastic neutron scattering data for G1 and GBM.

The magnetic anisotropy of goethite has been the subject of much controversy. In early Mössbauer studies it was noticed that the magnetically split spectra had strongly asymmetric lines and the magnetic hyperfine splitting in relatively large goethite particles collapsed well below the Néel temperature [55, 56]. It was therefore concluded that the magnetic anisotropy constant was much smaller than that of  $\alpha$ -Fe<sub>2</sub>O<sub>3</sub> and was on the order of only  $10^3$  J m<sup>-3</sup> [56]. Later, Mössbauer studies of a single crystal of goethite in large applied magnetic fields indicated a much larger value,  $K > 6 \times 10^4$  J m<sup>-3</sup> [44], whereas Mössbauer studies of the line shape of a polycrystalline sample in large applied fields indicated a value of  $3 \times 10^5$  J m<sup>-3</sup> [42]. Magnetization measurements at 4.2 K revealed a spin flop transition at an applied field of 20 T, corresponding to a magnetic anisotropy constant of around  $6 \times 10^4$  J m<sup>-3</sup> [39]. The present estimates of the magnetic anisotropy constant from inelastic neutron scattering data and Mössbauer data are on the order of  $10^5$  J m<sup>-3</sup>. In a recent study of hysteresis loops of natural goethite samples a much smaller value of only 210 J m<sup>-3</sup> at 5 K was estimated from the values of the coercivity [35]. The samples are substituted by Al and Mn, and it is likely that this results in uncompensated magnetic moments. Indeed, the saturation magnetization is relatively large ( $\sim 0.3$  A m<sup>2</sup> kg<sup>-1</sup>). Irrespective of the origin of the uncompensated moment, the field dependence of the magnetization of the uncompensated spins may not be directly related to the reversal of the sublattice magnetization vectors of the particles as a whole. Therefore, the analysis of magnetization data may give incorrect values for the anisotropy constant.

In antiferromagnetic nanoparticles, it has been predicted that the initial susceptibility at low temperature and the

magnetization should increase with temperature because of thermally induced magnetization [57]. This has been observed in a study of akaganeite ( $\beta$ -FeOOH) nanoparticles [58]. In goethite nanoparticles, the magnetization at low temperatures is dominated by a large upturn of both the ac and dc magnetization with decreasing temperature, as one can see in figures 3 and 4. This was also observed in an earlier ac magnetization study of goethite particles [26]. We interpret this as a result of freezing of the magnetization of uncompensated spins and canted spin structures around defects and at the surface of the particles [30].

The ZFC magnetization curve of GBM (figure 3) shows a maximum at around 130 K. Such a peak may be explained as a result of blocking of superparamagnetic particles. However, the blocking temperature estimated from Mössbauer spectroscopy with a time scale on the order of  $5 \times 10^{-9}$  s is around 160 K, and for the ZFC measurement with a time scale of around 100 s one should therefore expect a much lower blocking temperature (around 30 K). Therefore, the peak at 130 K cannot be explained by superparamagnetic blocking. Pankhurst *et al* [26] found a similar peak in ZFC magnetization studies of goethite particles. They suggested that it is related to ‘cluster ordering’ of magnetically interacting clusters or particles. Our estimates of the interaction energy from the Mössbauer data indicate values on the order of 150 K, i.e. close to the peak temperature in the ZFC measurement of GBM. This supports the interpretation in terms of ‘cluster ordering’.

## 5. Conclusions

The present Mössbauer studies have shown that in ultra-small goethite particles the magnetic relaxation is dominated by ‘classical’ superparamagnetic relaxation at temperatures above  $\sim 170$  K, in contrast to larger goethite particles in which the relaxation commonly is dominated by magnetic fluctuations in interacting grains. We have estimated the value of the uncompensated magnetic moment from magnetization measurements. The temperature dependence of the magnetization shows a large anomalous upturn at very low temperatures. This can be explained by freezing of canted spin structures at the surface and around defects. Inelastic neutron scattering and Mössbauer spectroscopy both show that the value of the magnetic anisotropy constant is close to  $10^5$  J m<sup>-3</sup>. Previously, the value of the magnetic anisotropy constant for goethite has been much debated. The difficulty in determining  $K$  relies partly on difficulties in separating the magnetic anisotropy energy from the interaction energy in samples of interacting grains. In the present study of small particles with limited inter-grain and inter-particle interactions this problem has been reduced. The inelastic neutron scattering data show that for small particles not dominated by interaction effects, this technique can be very useful in determining  $K$  as the measurements single out (with a sharp inelastic signal) the excitation energy of the  $q = 0$  modes at low temperatures.

## Acknowledgments

We acknowledge funding from the Danish Councils for Independent Research (DanScatt, and CF Steno grant). AAB

acknowledges financial support from the National Research Initiative of the US Department of Agriculture Cooperative State Research, Education, and Extension Service through Competitive Grant No. 2007-35107-17893.

## References

- [1] Cornell R M and Schwertmann U 2003 *The Iron Oxides: Structure, Properties, Reactions, Occurrences and Uses* 2nd edn (Weinheim: Wiley-VCH)
- [2] Morris R V et al 2006 *J. Geophys. Res.* **111** E02S13
- [3] Forsyth J B, Hadley I G and Johnson C E 1968 *J. Phys. C* **1** 179
- [4] Mørup S, Madsen M B, Franck J, Villadsen J and Koch C J W 1983 *J. Magn. Magn. Mater* **40** 163
- [5] Madsen D E, Cervera-Gontard L, Kasama T, Dunin-Borkowski R E, Koch C B, Hansen M F, Frandsen C and Mørup S 2009 *J. Phys.: Condens. Matter* **21** 016007
- [6] Burleson D J and Penn R L 2006 *Langmuir* **22** 402
- [7] Penn R L, Erbs J J and Gulliver D M 2006 *J. Cryst. Growth* **293** 1
- [8] Barrero C A, Betancur J D, Greneche J M, Goya G F and Berquó T S 2006 *Geophys. J. Int* **164** 331
- [9] Madsen D E, Hansen M F, Bender Koch C and Mørup S 2008 *J. Phys.: Condens. Matter* **20** 135215
- [10] Koch C J W, Madsen M B and Mørup S 1985 *Surf. Sci.* **156** 249
- [11] Murad E 1982 *Am. Miner.* **67** 1007
- [12] Bocquet S, Pollard R J and Cashion J D 1992 *Phys. Rev. B* **46** 11657
- [13] Berquó T S, Imbernon R L, Blot A, Franco D R, Toledo M C M and Partiti C S M 2007 *Phys. Chem. Miner.* **34** 287
- [14] Mørup S, Madsen D E, Frandsen C, Bahl C R H and Hansen M F 2007 *J. Phys.: Condens. Matter* **19** 213202
- [15] Mørup S, Hansen M F and Frandsen C 2011 *Comprehensive Nanoscience and Technology* vol 1, ed D Andrews et al (Amsterdam: Elsevier) pp 437–91
- [16] Theil Kuhn L, Lefmann K, Bahl C R H, Klausen S N, Lindgård P-A, Frandsen C, Madsen D E and Mørup S 2006 *Phys. Rev. B* **74** 184406
- [17] Hansen M F, Bender Koch C and Mørup S 2000 *Phys. Rev. B* **62** 1124
- [18] Lartigue L, Hugouenq P, Alloyeau D, Clarke S P, Lévy M, Bacri J-C, Bazzi R, Brougham D F, Wilhelm C and Gazeau F 2012 *ACS Nano* **6** 10935
- [19] Banfield J F, Welch S A, Zhang H, Ebert T T and Penn R L 2000 *Science* **289** 751
- [20] Nesterova M, Moreau J and Banfield J F 2003 *Geochim. Cosmochim. Acta* **67** 1177
- [21] Néel L 1949 *Ann. Geophys.* **5** 99
- [22] Brown W F 1963 *Phys. Rev.* **130** 1677
- [23] Bødker F, Hansen M F, Bender Koch C, Lefmann K and Mørup S 2000 *Phys. Rev. B* **61** 6826
- [24] Hansen M F, Bødker F, Mørup S, Lefmann K, Clausen K N and Lindgård P-A 1997 *Phys. Rev. Lett.* **79** 4910
- [25] Klausen S N, Lefmann K, Lindgård P-A, Kuhn L T, Frandsen C, Mørup S, Roessli B and Cavadini N 2004 *Phys. Rev. B* **70** 214411
- [26] Pankhurst Q A, Barquín L F, Lord J S, Amato A and Zimmermann U 2012 *Phys. Rev. B* **85** 174437
- [27] Howard C J and Hill R J 1986 AAEC (now ANSTO) Report M112 (Lucas Heights Research Laboratory)
- [28] Szytula A, Burewickz A, Dimitrij Z, Krasnick S, Rzany H, Todorovi J, Wanic A and Wolski W 1968 *Phys. Status Solidi* **26** 429
- [29] Unruh T, Neuhaus J and Petry W 2007 *Nucl. Instrum. Methods A* **580** 1414
- [30] Jacobsen H, Lefmann K, Brok E, Frandsen C and Mørup S 2012 *J. Magn. Magn. Mater.* **324** 3218
- [31] Madsen D E, Hansen M F, Bendix J and Mørup S 2008 *Nanotechnology* **19** 315712
- [32] Majetich S A and Sachan M 2006 *J. Phys. D: Appl. Phys.* **39** R407
- [33] Parker D, Dupuis V, Ladieu L, Bouchaud J-P, Dubois E, Perzynski R and Vincent E 2008 *Phys. Rev. B* **77** 104428
- [34] Sharma S K, Kumar R, Kumar S, Knobel M, Meneses C T, Kumar V V S, Reddy V R, Singh M and Lee C G 2008 *J. Phys.: Condens. Matter* **20** 235214
- [35] Martin-Hernandez F and Garcia-Hernández M M 2010 *Geophys. J. Int.* **181** 756
- [36] Bahl C R H, Garde J, Lefmann K, Jensen T B S, Lindgård P-A, Madsen D E and Mørup S 2008 *Eur. Phys. J. B* **62** 53
- [37] Würger A 1998 *Europhys. Lett.* **44** 103
- [38] Kittel C 1951 *Phys. Rev.* **82** 565
- [39] Coey J M D, Barry A, Brotto J-M, Rakoto H, Brennan S, Mussel W N, Collomb A and Fruchard D 1995 *J. Phys.: Condens. Matter* **7** 759
- [40] Néel L 1961 *Comptes Rendus Hebdomadaires des Seances de L'academie des Sciences* **252** 4075
- [41] Richardson J T, Yiagas D I, Turk B, Forster K and Twigg M W 1991 *J. Appl. Phys.* **70** 6977
- [42] Pankhurst Q A and Pollard R J 1990 *J. Phys.: Condens. Matter* **2** 7329
- [43] Pankhurst Q A 1994 *Hyperfine Interact.* **90** 201
- [44] Meagher A, Pankhurst Q A and Dickson D P E 1986 *Hyperfine Interact.* **28** 533
- [45] Bødker F and Mørup S 2000 *Europhys. Lett.* **52** 217
- [46] Mørup S, Frandsen C and Hansen M F 2010 *Beilstein J. Nanotechnol.* **1** 48
- [47] Jones D H and Srivastava K K P 1986 *Phys. Rev. B* **34** 7542
- [48] van Lierop J and Ryan D H 2001 *Phys. Rev. B* **63** 064406
- [49] Chuev M A, Cherepanov V M and Polikarpov M A 2010 *JETP Lett.* **92** 21
- [50] Chuev M A 2011 *J. Phys.: Condens. Matter* **23** 426003
- [51] Xu M, Bahl C R H, Frandsen C and Mørup S 2004 *J. Colloid Interface Sci.* **279** 132
- [52] Frandsen C et al 2005 *Phys. Rev. B* **72** 214406
- [53] Frandsen C and Mørup S 2003 *J. Magn. Magn. Mater.* **266** 36
- [54] Bahl C R H, Lefmann K, Kuhn L T, Christensen N B, Várquez H and Mørup S 2006 *J. Phys.: Condens. Matter* **18** 11203
- [55] van der Kraan A M and van Loef J J 1966 *Phys. Lett.* **20** 614
- [56] Shinjo T 1966 *J. Phys. Soc. Japan* **21** 917
- [57] Mørup S and Frandsen C 2004 *Phys. Rev. Lett.* **92** 217201
- [58] Urtiberea A, Luis F, Millán A, Natividad E, Palacio F, Kampart E and Zeitler U 2011 *Phys. Rev. B* **83** 214426

# CAMEA ESS - The Continuous Angle Multi-Energy Analysis Indirect Geometry Spectrometer for the European Spallation Source.

P. G. Freeman<sup>1,a</sup>, J. O. Birk<sup>2</sup>, M. Markó<sup>3</sup>, M. Bertelsen<sup>2</sup>, J. Larsen<sup>4</sup>, N. B. Christensen<sup>4</sup>, K. Lefmann<sup>2</sup>, J. Jacobsen<sup>2</sup>, Ch. Niedermayer<sup>3</sup>, F. Juranyi<sup>3</sup>, and H. M. Ronnow<sup>1,b</sup>

<sup>1</sup>Laboratory for Quantum Magnetism, ICMP, École Polytechnique Fédérale de Lausanne (EPFL), CH-1015 Lausanne, Switzerland

<sup>2</sup>Niels Bohr Institute, University of Copenhagen, Universitetsparken 5, 2100 Copenhagen, Denmark.

<sup>3</sup>Laboratory of Neutron Scattering, Paul Scherrer Institute, 5232 Villigen-PSI, Switzerland.

<sup>4</sup>Department of Physics, Technical University of Denmark, Kongens Lyngby 2800, Denmark.

**Abstract.** The CAMEA ESS neutron spectrometer is designed to achieve a high detection efficiency in the horizontal scattering plane, and to maximize the use of the long pulse European Spallation Source. It is an indirect geometry time-of-flight spectrometer that uses crystal analysers to determine the final energy of neutrons scattered from the sample. Unlike other indirect geometry spectrometers CAMEA will use ten concentric arcs of analysers to analyse scattered neutrons at ten different final energies, which can be increased to 30 final energies by use of prismatic analysis. In this report we will outline the CAMEA instrument concept, the large performance gain, and the potential scientific advancements that can be made with this instrument.

## 1 Introduction

For measuring excitations such as phonons and magnons in materials there are two dominant types of inelastic neutron spectrometers presently in use, i) direct geometry time-of-flight (ToF) spectrometers and ii) triple-axis spectrometers (TAS). Direct ToF instruments compensate a low incident neutron flux from using monochromatic pulses, by detecting the scattered neutrons of all energies over a large solid angle in position sensitive detectors. In contrast TAS focus a continuous high flux monochromatic beam of neutrons on a sample but have a low detection coverage of counting neutrons at one final neutron energy at one position, or tens of angles in the case of multiplexed TAS[1–3].

The European Spallation Source (ESS) will be a 5 MW long pulse spallation neutron source, and will have the world's highest peak brightness for cold neutrons[4]. The time averaged cold neutron flux of the ESS will also be greater than that of world leading continuous sources such as the Institut Laue-Langevin high flux reactor. The instrument design phase for the ESS is an ideal opportunity to consider new possibilities for instrument concepts.

Researchers of magnetism are the largest user community of single crystal spectrometers. This community often use applied magnetic fields to tune the magnetic properties of materials across phase transitions in to new phases of matter, where inelastic neutron scattering uniquely determines the nature of the magnetic phase. Cryomagnets used

in these experiments however restrict the access for neutrons. For example, currently the highest vertical field cryomagnetic for neutron spectroscopy is the 16 T 'Fat Sam' produced by Bruker, for the Spallation Neutron Source (SNS) as a collaborative project between the Swiss Neutron Scattering Society (SGN/SSDN) and the Oak Ridge National Laboratory[5]. This magnet has a vertical opening angle of  $\pm 4^\circ$ . When used on the direct geometry ToF Cold Chopper Neutron Spectrometer (CNCS) at SNS, 75% of CNCS's detectors out of the horizontal plane are blocked, reducing the instruments efficiency. TAS spectrometers operate in the horizontal plane and are therefore less restricted by the neutron access of split-pair cryomagnets. A similar situation holds for using anvil cells for extreme pressure to tune magnetic properties of materials[6]. TAS spectrometers are the instrument of choice for these types of experiments, however a TAS would not take advantage of the pulsed nature of the ESS. This provides an initial motivation to examine optimizing a spallation source instrument that maximizes the neutron count rate within the horizontal plane.

## 2 Concept

We directed our attention to indirect geometry ToF spectrometry where the final energy of the neutron is determined by a crystal analyser. Present indirect spectrometers analyse neutrons scattered from a sample at one final fixed energy, from knowing the final energy and the time-of-flight the scattering process is determined. Present indirect ToF spectrometers are inefficient as the scattered neutron energy is only analysed once, any neutron that

<sup>a</sup>e-mail: paul.freeman@epfl.ch

<sup>b</sup>e-mail: henrik.ronnow@epfl.ch

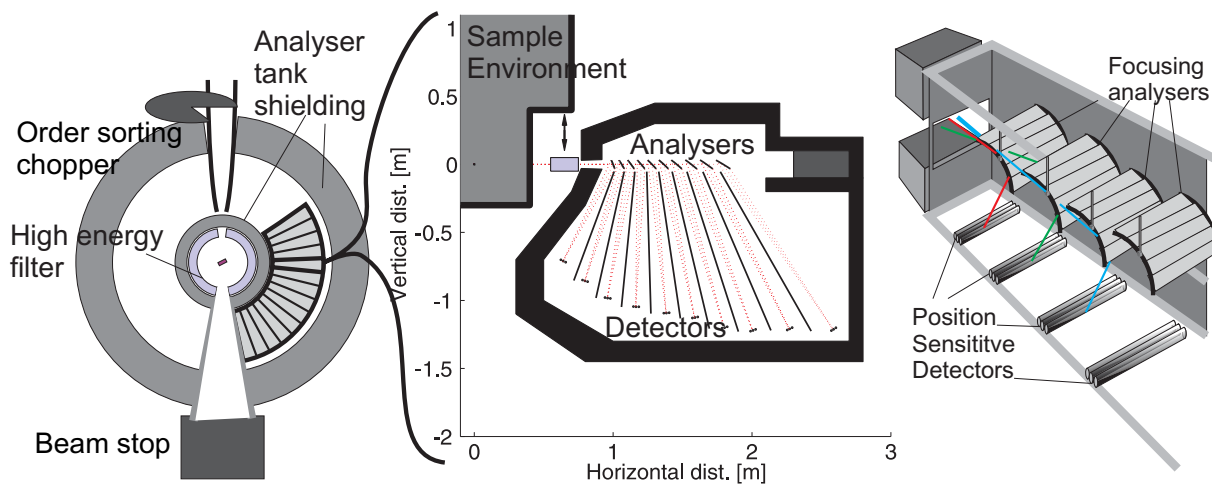


**Figure 1.** Left: A simplified overview of the CAMEA spectrometer from the end of the neutron guide, not to scale. The sample is surrounded on one side by the analyser-detector chamber that covers a large angle within the horizontal plane. Centre: A cross section to scale of one  $9^\circ$  multi-analyser-detector module is shown on the right. There is large 90 cm diameter space for sample environment, and a removable cooled Be high energy filter placed in front of the entry to the secondary spectrometer. We show how 10 analysers sat behind each other working at different final neutron energies can geometrically be spaced with neutron shielding between the analyser to detector channels. After the last analyser the neutrons are directed into a get lost tube into a beamstop. Right: A simplified three-dimensional sketch of the analyser and detector setup in a module of the secondary spectrometer for the first four of ten analysers, omitting all flight-path definition elements for the purpose of clarity.

does not have the correct final energy only increases the background signal. We note that the indirect spectrometers such as PRISMA (ISIS)[8] and CQS (Los Alamos)[9] did work with variable final neutron energies, but only analysed a scattered neutron's energy a single time. The majority of spallation source indirect ToF spectrometers are ultra high resolution backscattering spectrometers, or vibrational spectrometers that measure phonon density of states. Neither of these two instrument classes are ideally suited for mapping phonon or magnon dispersion curves in single crystals, however the back scattering spectrometer Osiris at the ISIS facility is successfully used to study magnetic excitations in single crystals[7].

The essential evolution in neutron instrumentation of CAMEA is the secondary spectrometer:

- 1) Vertically scattering analysers that allows for increased coverage of in plane scattering.
- 2) Multiple concentric arcs of analysers sat behind each other to perform multiple final energy analysis.
- 3) Use of Position Sensitive Detectors (PSDs) for quasi-continuous angular coverage.
- 4) Prismatic analysis from a distance collimated analyser allowing multi-energy analysis from a single analyser.
- 5) An order sorting chopper that enables use of first and second order reflections off the analysers.

Neutrons have large penetration depths, for analyser crystals of pyrolytic graphite (PG) of 1 mm thickness mounted on 1 mm Si wafers, the transmission rate we have experimentally determined as  $> 98\%$ . Typically 2 mm PG analyser crystals are used, but reducing to 1 mm halves the cost, increases transmission, for only a small cost in reflectivity. We propose an instrument with 10 concentric arcs

of analysers that direct analysed neutrons vertically into detectors, if a neutron scattered from the sample is not at the energy of the first analyser the neutron is transmitted to be analysed by up to nine further analysers working at different final energies. Scattering vertically has been shown not to reduce energy resolution when studying samples of small vertical height ( $< 1$  cm)[3]. The increased efficiency of this Multi-Energy Analysis for 10 energies gives a gain factor  $> 9.1$ , considering transmission rates. In figure 1(a) we sketch an overview of the secondary spectrometer, and in Fig.1(b) we outline how ten analysers placed behind each other can be positioned.

Continuous Angular coverage is obtained by using PSDs that are arranged tangentially, as shown in the right panel of figure 1. The position along the PSD that the neutron is detected determines the angle at which the neutron was scattered from the sample, and knowing the sample orientation the wavevector of the scattered neutrons is determined. To map out excitations in  $(h, k, \omega)$  of a single crystal a sample rotation scan is performed, in the same way as a scan of a reciprocal plane is produced on a multiplexed spectrometer such as MACS or Flatcone [2, 3]. In figure 2 we show how the magnetic dispersion from a one dimensional spin system can be measured without the need for a sample rotation scan. For Continuous Angular coverage we need to resolve the issue of dead angles between segment wedges of the secondary spectrometer. Continuous Angular coverage can be achieved in two ways, 1) re-position the secondary spectrometer so that the dead angles and active angles swap positions, 2) in a sample rotation scan we can use the detected neutrons observed by different analysers to create a continuous map of the excitations measured with different final neutron energies.

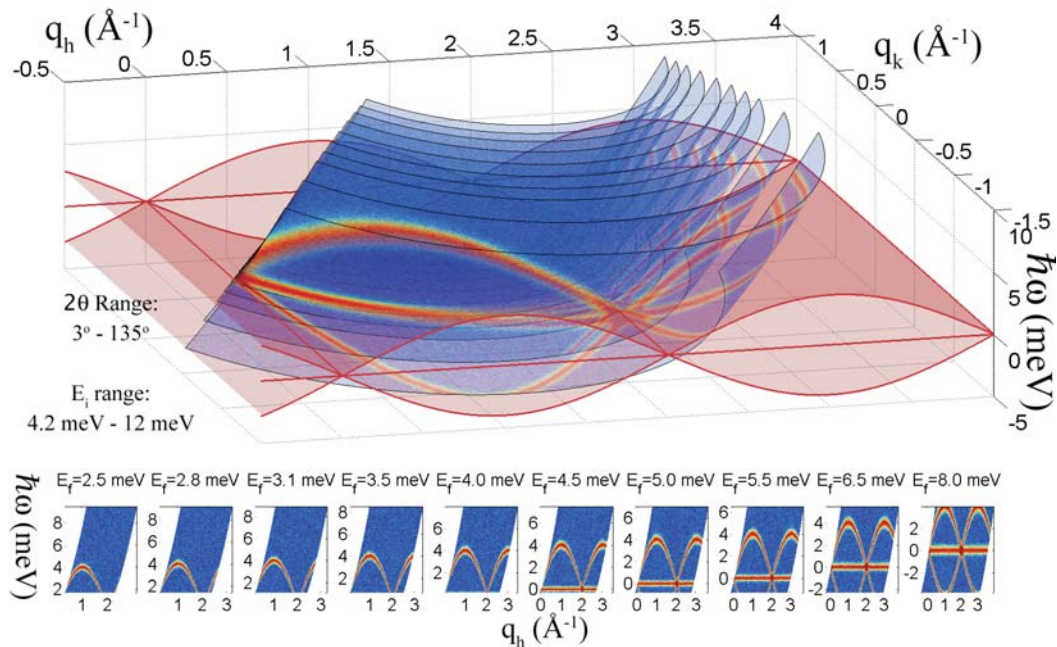


**Figure 2.** A diagram to represent the measuring capabilities of CAMEA measuring the magnon spin excitation spectrum of a one dimensional spin system, in a single point scan. The main figure shows the surfaces in reciprocal space mapped by CAMEA, and the red surface represents the magnon dispersion. Below the main figure shows the projected excitation spectrums measured by the ten different analysers of CAMEA. No spinon continuum excitation is included, and dead angles between the analyser sections have been omitted (equivalent to measuring two points, the second being where the dead angles and active analyser angles of the secondary spectrometer swap position).

### 3 Design

The specifics of the secondary spectrometer of CAMEA-ESS are shown in figure 1(a) Each segment of the secondary spectrometer consists of fifteen wedges of  $9^\circ$  width covering a horizontal scattering angle of  $3\text{-}135^\circ$ . Each wedge consists of 10 PG analysers sat behind each other, with each analyser working at a different final neutron energy, and three linear PSDs for each analyser. In this way we have ten concentric arcs of analysers working at ten final neutron energies.

Analysers will be constructed of PG crystals mounted on Si wafers, five or more blades will be used in a vertical focusing Rowland geometry covering  $\sim \pm 1.4^\circ$  vertically, to focus the analysed neutrons into three PSD tubes arranged to be parallel to the analysers. An analyser wedge of  $9^\circ$  width will consist of  $6^\circ$  active analyser, and  $3^\circ$  of dead angle for support structures, etc.. As the energy resolution of the secondary spectrometer is limited by distance collimation, the three PSD tubes are at a different scattering angle from a single analyser arc, so each PSD detects a different final neutron energy. This prismatic analysis allows for 30 final energies to be examined by CAMEA at a higher energy resolution[10].

For the primary spectrometer, CAMEA will be placed on cold neutron moderator. The neutron guide was optimised by simulations using the McStas package and the optimizer package GuideBot[11, 12]. A wide range of guide shapes were examined, and the best guide shape identified[13]. From the neutron moderator there is a guide feeder to a virtual source at 6.5 m[14], where a pulse

shaping chopper is placed at the closest possible distance to the moderator. To be able to use the full length of the 2.86 ms neutron pulse of the 14 Hz ESS, filling the counting window, a pulse shaping chopper at 6.3 m gives a natural length of 165 m[15]. The neutron guide is then two ellipses separated by a small angular kink in the guide to remove line-of-sight from the neutron source. Elliptical guides reduce neutron losses by reducing the number of reflections required along the guide's length, and the pinch point between the ellipses provide background reduction. A bandwidth chopper will be placed in the kink section of the guide, and the instrument requires three frame overlap choppers, that can be positioned in the first ellipse.

A prototype of the secondary spectrometer of CAMEA has been built, and tested on the MARS spectrometer at the SINQ neutron source, Paul Scherrer Institut, Switzerland. The results of this testing validates the CAMEA design and will be reported in detail elsewhere[18]. In addition to this, analytical calculations of CAMEA have been performed[19].

For any spectrometer background reduction is critical, and requires a clear strategy to achieve. A set of beam definition jaws at the end of the guide section will define the beam divergence that reaches the sample position, as has been implemented on WISH at the ISIS facility[20]. The divergence jaws are followed by diaphragm to define the beam size at the sample position. Any neutrons that pass straight through the sample will be directed along a get lost tube to the beam stop. The secondary spectrometer will either be in an Ar atmosphere or under vacuum to

**Table 1.** Specifications for the CAMEA instrument at the ESS.

<b>Primary Spectrometer</b>	
Moderator	Cold
Wavelength Range (Energy Range)	1 Å to 8 Å (81.8 meV to 1.3 meV)
Bandwidth	1.7 Å
Neutron Guide	165 m - Parabolic feeder to double elliptical guide
Line-of-Sight Removal	Kink between elliptical guide sections
Number of Choppers	7, operating from 840 rpm to 12600 rpm
Beam Divergence	2.0° vertical, 1.5° horizontal
Divergence Control	5 divergence jaws intergrated into the end of the guide
Incoming Energy Resolution	Adjustable from 0.1 % to 3 % at 5 meV
Polarizer	Removeable polarizing supermirror s-bender
<b>Sample</b>	
Maximum Flux on Sample Position	$1.8 \times 10^{10}$ n/s/cm <sup>2</sup> /1.7 Å
Wavector Range at Elastic Position (Including PG(004) reflections)	PG(002) reflections: $0.058 \text{ \AA}^{-1}$ to $3.6 \text{ \AA}^{-1}$ PG(004) reflections: $0.12 \text{ \AA}^{-1}$ to $7.26 \text{ \AA}^{-1}$
Background Count Rate	$< 5 \times 10^{-5}$ comparted to the elastic signal of vanadium (result obtained from prototype testing)
Beam Size at Sample position	1.5 cm × 1.5 cm
Beam Size Resolution Optimization	0.1 cm × 0.1 cm – 1.0 cm × 1.0 cm
Sample Environment Space	90 cm diameter with possible side access
<b>Secondary Spectrometer</b>	
Collimation	Radial collimation after Sample Cross-talk collimation in secondary spectrometer
Filter	Removable cooled Be-filter before analyzers
Analyser crystals	2 m <sup>2</sup> cooled Pyrolytic Graphite (PG) 60" mosaic using (002) and (004) reflections
Detectors	2.5 m <sup>2</sup> position sensitive <sup>3</sup> He at 7 bar
Number of Analyzer Arcs	10
Number of Analyzer-Detector Segments	15 (9.0° per segment, 6.0° active)
Sample to Analyzer Distances	1.00 m to 1.79 m
Analyzer to detector Distances	0.8 m to 1.45 m
Horizontal Angular Coverage	3° to 135°
Horizontal Angular Resolution	0.79° to 0.46°
Vertical Angular Coverage	± 1.4°
Final Neutron Energy PG(002)	2.5, 2.8, 3.1, 3.5, 4.0, 4.5, 5.0, 5.5, 6.5, 8.0 meV
Final Neutron Energy Range PG(002) and PG(004)	2.5 meV to 32 meV
Secondary Energy Resolution	0.77 % to 1.3 %
Polycrystal Elastic Wavevector Resolution	1.1 % for $E_f = 5.0$ meV
Time Resolution	20 μs
Neutron Polarization	Polarizing supermirrors

remove background from air scattering of neutrons. Line-of-sight between the PSDs and the sample position will be shielded by neutron absorbing materials. Radial collimation between the sample and analysers, and cross talk collimation inside the secondary spectrometer are foreseen. A removable Be-filter can be placed in the scattered neutron beam to remove high energy neutrons, although this restricts CAMEA to working with the first seven analysers. The effectiveness of our background reduction strategy has been confirmed in our prototype testing of CAMEA, where a the background count rate is  $5 \times 10^{-5}$  times that from the incoherent scattering from a vanadium sample.

The energy range can be expanded to measure excitations of thermal energies on CAMEA using the order sorting chopper. If thermal neutrons are scattered

off the sample, the scattered neutrons can be analysed by the PG(002) or PG(004) analyser reflections with  $E_f(PG(004)) = 4 \times E_f(PG(002))$ , and we cannot directly differentiate between them. In figure 3 we show a time-distance plot for the order sorting chopper. The order sorting chopper for CAMEA consists of two counter rotating disc choppers that run at 180 Hz with two symmetric openings, effectively 360 Hz a non-integer multiple of the the source's repetition rate. The time distance plot of Fig. 3 for the  $E_f(PG(002)) = 5$  meV shows that neutrons that arrive at the detector at a given time are uniquely determined from the PG(002) or PG(004) analyser reflection. Using the order sorting chopper CAMEA has analysers working from  $E_f = 2.5$  meV to 32 meV. The order sorting chopper however reduces the incident neutron inten-

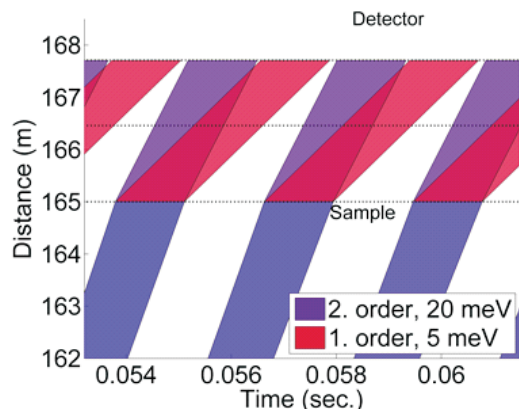


**Figure 3.** Time-of-flight diagram of the order sorting chopper and the 7th PG(002)  $E_f = 5$  meV analyser. At 162 m the chopper divides the pulse into  $\sim 26$  pulses per source pulse, at 3 m from the detector the neutrons hit the sample and scatter. The time distance diagram clearly shows how the neutrons that scatter of the analyser at 166.5 m by the first and second order reflections are detected over unique time windows at the detector. The time gaps between the signals at the detector are necessary due to a small time broadening of the signals that is mainly due to the choppers open and closing time.

sity by 59 % when placed 3 m from the sample position. The greater the distance for the order sorting chopper to the sample position, the greater the reduction in incident neutrons, 3 m represents a safe distance from stray fields from future  $>20$  T cryomagnet possibilities.

## 4 Performance

In table one we outline specifications of the CAMEA spectrometer. Ten analysers represents a compromise on coverage, the cost increase of the analyser for increasing sample to analyser distance, and the reduced performance due to transmission losses. The CAMEA analyser resolution is limited by distance collimation, not mosaic quality, so  $60^\circ$  mosaic PG crystals can be used to improve count rates without reducing the energy resolution. When the primary and secondary resolutions are matched, CAMEA will achieve a higher energy resolution than than triple-axis spectrometers, whose energy resolution is limited by mosaic quality.

If the full ESS pulse width is used the primary spectrometer energy resolution is 4 %, with  $1.8 \times 10^{10}$  neutrons  $s^{-1} cm^{-2}$  for a  $1.7 \text{ \AA}$  bandwidth centred at  $3 \text{ \AA}$ [13]. We consider the simulated performance of ThALES the upgraded IN14 at the ILL, which to the best of our knowledge will be the highest flux cold TAS in the world with a monochromatic flux maximum of  $3.5 \times 10^8$ [16], a factor of 50 lower than the maximum polychromatic flux of CAMEA. The energy resolution of the primary spectrometer of CAMEA can be improved to 0.8% to match the secondary spectrometer, with the primary resolution being directly proportional to the pulse width from the pulse shaping chopper. For example the flux for 2% total energy

resolution on CAMEA is  $0.9 \times 10^{10}$ . Due to the high flux of CAMEA special care must be taken with regards to activation. A simple mechanical interlock device has been designed for removing active samples from the instrument to an active sample store on the instrument zone, removing the need to directly handle samples[21]. Indirect handling of active samples can be avoided by use of a robotic arm for sample removal. Design of instrument components and sample environment also requires attention to the choice of materials placed in the neutron beam.

Within  $\pm 1.4^\circ$  vertical range of CAMEA, and taking into account transmission rates, we estimate the solid angle gain of CAMEA over Flatcone to be 36[3], or 23 over MACS at NIST[2]. Comparing CAMEA's flux gain for 2% energy resolution, and the increased solid angle coverage gives a gain factor of  $\sim 900$  compared to ThALES using Flatcone, provided all detected signal is of use in both cases. With this gain factor CAMEA will enable inelastic neutron scattering on samples of  $1 \text{ mm}^3$  and smaller as a routine measurement. Neutron simulations were also used to compare CAMEA to a 150 m long cold direct ToF spectrometer that uses Repetition Rate Multiplication, with a large vertical coverage of  $\pm 30^\circ$ , at the ESS. These simulations indicated within the horizontal plane CAMEA has a 22 times higher count rate than the direct ToF[17]. If we consider the total counts of the direct ToF ESS spectrometer including a large vertical angular coverage, CAMEA has a slightly higher count rate.

Polarized inelastic neutron scattering will be available for CAMEA from the beginning. The incident neutron beam will be polarized by a polarizing supermirror S-bender, inserted near the end of the guide by a guide changer, a setup successfully used on instruments such as FLEXX[22]. Polarization analysis of the scattered beam will be performed by a wide angle polarized supermirror analyser replacing the Be filter, which is equivalent to the setup used on the D7 instrument[23]. We chose a polarized supermirror analyser over a wide angle He-3 polarization cell, to enable the use of cryomagnets which produce stray fields, and to keep a large sample environment space available with the polarized option.

## 5 Scientific Demand for Extreme Conditions

The CAMEA geometry is especially suitable for inelastic neutron scattering in applied magnetic fields, and under extreme pressure. In table two we outline the results of a survey into the use of extreme environments on cold inelastic neutron spectrometers in Europe. Typically there are overload factors of 2.5 for these instruments, with  $\sim 33\%$  requesting the use of a cryomagnet. The lack of demand for use of high pressure for neutron spectroscopy is likely due to the highly restrictive sample volume of pressures cells, and the present need for large single crystals for inelastic studies. In September 2012 attendees of an ESS Science Symposium on Strongly Correlated Electron Systems were asked to name three instruments you would like to have at the ESS, and a spectrometer for extreme

**Table 2.** Demand for several European based cold TAS and indirect geometry spectrometers that measure magnetic excitations in single crystals, and the demand for extreme environments conditions on these instruments. The overload of an instrument is defined as the number of days applied for experiments divided by the total number of days available to perform experiments.

Instrument (Instute/Neutron Source)	Overload	Magnetic Fields (% of proposals )	Pressure (%)	$\leq 1, K$ (%)	Polarized neutrons (%)
RITA-II, TASP (PSI)	2.5	34	4	19	N/a
PANDA (FRM-II)	2.7	30	5	20	N/a
IN14 (ILL)	2.5	30-40	$< 5$	60	20-25
IN12 (JCNS@ILL)	2.6	24	0	28	10
Osiris (ISIS)	2	40	0	40	Planned
FLEX (HZB)	1.5	56	0	20	Commissioning

conditions was one of the three instruments[24]. There is a significant scientific demand for spectroscopy under extreme conditions in Europe, which the ESS can accommodate through CAMEA.

## 6 Scientific Capabilities of CAMEA

The massive gain factor of CAMEA ESS has the potential to enable scientific discoveries in several fields of research, a few of which are discussed below.

The present user community for using extreme environments in inelastic neutron scattering is based in the magnetic scattering community, which includes magnetic materials, strongly correlated electron systems, superconductors, quantum magnets, etc. CAMEA offers this community high counting rates to study weak excitations to a level of accuracy that present instrumentation cannot reach, bridging the gap between the accuracy theoretical calculations can reach and present inelastic neutron scattering. Alternatively rapid mapping of excitations will be enabled for parametric studies of dynamics across critical transitions, providing a unique tool to study wavevector and energy evolution across transitions. The large gain factor of the instrument and the low background count rate will unlock the ability to study magnet materials under extreme pressure.

At present the sample size required for inelastic neutron scattering is prohibitive, limiting the technique to crystals grown by techniques such as floating zone mirror light furnaces. The ability to study samples of less than  $1 \text{ mm}^3$  opens up the possibility for sample growth for neutron scattering in both material discovery and soft matter. For example it will be possible to study materials grown by high-pressure synthesis (which is how the highest Tc iron-based superconductors were first crystalized) and hydrothermal synthesis (which is how the best known realization of a kagome quantum magnet is synthesized) CAMEA will enable neutron scattering to be part of the iterative process to discover new materials classes. This will lead to input from inelastic neutron scattering immediately after materials are discovered, or directly lead to discovery of materials. At present a large amount of experimental and theoretical work is wasted due to incorrect assumptions made about the spin and lattice interactions in materials, inelastic neutron scattering unambiguously resolves these issues.

CAMEA has the potential to open up the application of neutron spectroscopy in new fields of reasearch including biophysical studies of collective dynamics in membranes. In membranes collective dynamics are believed to drive transport of molecules, pore opening, membrane fusions and protein-protein interactions[29], which can be determined by inelastic neutron scattering. At present studies of collective dynamics in membranes by neutrons is restricted to model systems which can be prepared in large multi-layer stacks, the small sample capability of CAMEA will enable studies of the actual membranes of interest.

There exist a great hitherto unaccommodated interest to study lattice dynamics in simple materials under extreme pressure, and for geo- and planetary science related studies such as hydrogen diffusion in materials of the Earth's upper mantle. CAMEA is ideally suited for both of these purposes. Despite the fact that water is vital for life on Earth we have little knowledge on the extent of the water cycle in the Earth's mantle. Estimates on the water in the mantle wildly vary from ten percent to two and a half times the water on the Earth's surface [25]. The uptake of water into the material of the Earth's mantle greatly influences the properties of the materials, which has consequences for flow of material and sound velocities in the mantle, studying these materials has the potential to provide great insight into plate-tectonics and seismic activity[25, 26]. To study the effects of hydrogen on the different phases of the material of the Earth's mantle requires performing neutron scattering at pressure up to 30 GPa for temperatures of the order of 2000 K. The experimental conditions imply a pressure cell with a sample volume  $< 5 \text{ mm}^3$ [27], and an instrument resolution of a cold TAS is required, well within CAMEA's capability[28].

In table 3 we outline some of the desirable sample environment for CAMEA to perform these experiments.

For time dependent studies the time resolution of CAMEA is only from the secondary spectrometer, and of the order of  $20 \mu\text{s}$ . An analyser arc of CAMEA measures one excitation energy for a time of the order of the 2.86ms source pulse width with  $20 \mu\text{s}$  resolution, that is the time dependence of excitations at ten different energies are simultaneously measured. This capability of CAMEA opens up experimental possibilities in inelastic neutron scattering for example in soft matter stimulated

**Table 3.** Desirable sample environments for CAMEA, within predicted technical developments.

Sample Environment	Performance
Low Temperature	Dilution to <100 mK
Magnetic fields	Vertical >20 T
Pressure	30 GPa with 5 mm <sup>3</sup> sample, T = 3 – 2000 K 10 GPa with 50 mm <sup>3</sup> sample, T = 0.1 – 1800 K
Magnetic Field and Pressure	>10 T with upto 10 GPa T = 0.1 – 350 K

out of equilibrium by pump-probe techniques, or studying excitations in pulsed high magnetic fields beyond 30 T.

## 7 Conclusion

CAMEA provides an evolution in cold neutron indirect spectroscopy by performing analysis of the energy of the scattered neutrons at 10 final energies, that can be increased to 30 energies by prismatic analysis. This instrument has been designed through simulations, with validation of the simulations of the secondary spectrometer achieved by prototype testing on the MARS spectrometer at the SINQ neutron source of the Paul Scherrer Institut. Compared to present cold multiplexed TAS CAMEA has three orders of magnitude gain. At the ESS the in plane count rate of CAMEA is over an order of magnitude higher than cold direct geometry ToF spectrometers, and is equivalent to the total count rate of a cold direct ToF spectrometer. CAMEA therefore enables inelastic neutron scattering on samples of less than 1 mm<sup>3</sup> as a routine measurement, enabling experiments in fields of research such material discovery, soft matter, and extreme pressure studies in magnetism, and geoscience. Finally we note that the secondary spectrometer of CAMEA can be implemented as a multiplexing option for a TAS instrument, that could perform within a factor of 100 of CAMEA at the ESS. A CAMEA TAS is being built for the the RITA-II spectrometer at SINQ neutron source, P.S.I., Switzerland.

The work presented here is part of the European Spallation Source Design Update Programs of Switzerland and Denmark.

## References

[1] M. Jimnez-Ruiz, and A. Hiess, *Physica B: Condensed Matter*, **385-386**, 1086–1088 (2006); K. Lefmann, D. McMorro, H. M. Rønnow, K. Nielsen, K. Clausen, B. Lake, and G. Aeppli, *Physica B: Condensed Matter*, **283**, 343–354 (2000); C.R.H. Bahl, K. Lefmann, A.B. Abrahamsen, H.M. Rønnow, F. Saxild, T.B.S. Jensen, L. Udby, N.H. Andersen, N.B. Christensen, H.S. Jacobsen, T. Larsen, P.S. Häfliger, S. Streule, Ch. Niedermayer, *Nucl. Instr. Meth. A*, **246**, 452-462 (2006); K. Lefmann, Ch. Niedermayer, A.B. Abrahamsen, C. R. H. Bahla, N. B. Christensena, H.S. Jacobsen, T.L.

Larsen, P. Häfliger, U. Filges, and H.M. Rønnow, *Physica B: Condensed Matter*, **385-386**, 1083-1085 (2006). K. Lefmann, U. Filges, F. Treue, J. Kirkenngaard, B. Plesner, K. Hansen, and K. Klenø, *Nucl. Instr. Meth. A*, **634**, S1 – S6, (2011).

[2] J. A. Rodriguez, D. M. Adler, P. C. Brand, C. Broholm, J. C. Cook, C. Brocker, R. Hammond, Z. Huang, P. Hundertmark, J. W. Lynn, N. C. Maliszewskyj, J. Moyer, J. Orndorff, D. Pierce, T. D. Pike, G. Scharfstein, S. A. Smee and R. Vilaseca, *Meas. Sci. Technol.* **19**, 034023 (2008).

[3] M. Kempa, B. Janousova, J. Saroun, P. Flores, M. Boehm, F. Demmel, and J. Kulda, *Physica B: Condensed Matter*, *Proceedings of the Eighth International Conference on Neutron Scattering*, **385-386(0)**, 1080 – 1082 (2006).

[4] S. Peggs, R. Kreier, C. Carlile, R. Miyamoto, A. Paahlsson, M. Trojer, and J. G. Weisend II, *ESS Technical Design Report*. Tech. rep. ESS. (2013).

[5] P. Allenspach, M. Zolliker, and U. Filges, *Swiss Neutron News* **36** 14 (2009).

[6] S. Klotz, J. M. Besson, G. Hamel, R. J. Nelmes, J. S. Loveday, W. G. Marshall and R. M. Wilson, *Appl. Phys. Lett.* **66**, 1735 (1995).

[7] M. T. F. Telling and K. H. Andersen, *Phys. Chem. Chem. Phys.* **7**, 1255 (2004); R. Coldea, D. A. Tennant, E. M. Wheeler, E. Wawrzynska, D. Prabhakaran, M. T. F. Telling, K. Habicht, P. Smedibidl, and K. Kiefer, *Science* **327**, 177 (2010).

[8] U. Steigenberger, M. Hagen, R. Caciuffo, C. Petrillo, F. Cilloco and F. Sachetti *F Nucl. Instrum. Methods B* **53** 87 (1991); M.J. Bull, M.J. Harris, U. Steigenberger, M. Hagen, C. Petrillo, and F. Sacchetti, *Physica B* **234-236**, 1061 (1997).

[9] R. A. Robinson, R. Pynn and J. Eckert, *Nuclear Instruments and Methods in Physics Research A* **241**, 312 (1985).

[10] J. O. Birk, *et. al.*, article in preparation.

[11] K. Lefmann and K. Nielsen, *Neutron News* **10**, 20, (1999); P. Willendrup, E. Farhi and K. Lefmann, *Physica B* **350**, 735 (2004).

[12] M. Bertelsen, *GuideBot software*, University of Copenhagen, 2014.

[13] J. O. Birk and M. Bertelsen, *CAMEA Guide Report*, <http://infoscience.epfl.ch/record/190503?ln=en>

[14] M. Bertelsen, H. Jacobsen, U.B. Hansen, H.H. Carlsen, and K. Lefmann, *Nucl. Instr. Meth. A* **729**, 387-398 (2013)

[15] K. Lefmann, K. H. Klenø, J. O. Birk, B. R. Hansen, S. L. Holm, E. Knudsen, K. Lieutenant, L. von Moos, M. Sales, P. K. Willendrup, and K. H. Andersen, *Rev. Sci. Instrum.* **84**, 055106 (2013).

[16] M. Boehm, A. Hiess, J. Kulda, S. Roux and J. Saroun, *Meas. Sci. Technol.* **19**, 034024 (2008); M. Boehm (Institut Laue-Langevin) personal communication.

[17] J. O. Birk, CAMEA: Comparison to the Colder Chopper Spectrometer,

- <https://infoscience.epfl.ch/record/190496?ln=en>
- [18] M. Marton article in preparation; M. Marton, Building and Testing a Prototype for CAMEA, <http://infoscience.epfl.ch/record/197952?ln=en>
- [19] M. Marton, Analytical Calculations for CAMEA, <https://infoscience.epfl.ch/record/190497?ln=en>
- [20] L. C. Chapon, P. Manuel, P.G. Radaelli, C. Benson, L. Perrott, S. Ansell, N.J. Rhodes, D. Raspino, D. Duxbury, E. Spill, J. Norris, *Neutron News* **22:2**, 22 (2011).
- [21] J. O. Birk, CAMEA: Technical Solutions, <http://infoscience.epfl.ch/record/190506?ln=en>
- [22] M. Skoulatos, and K. Habicht, *Nucl. Instrum. Methods B* **647**, 100 (2011).
- [23] J. R. Stewart, P. P. Deen, K. H. Andersen, H. Schober, J.-F. Barthélémy, J. M. Hillier, A. P. Murani, T. Hayes and B. Lindenau, *J. Appl. Cryst.* **42**, 69-84 (2009).
- [24] A. Boothroyd, T. Perring, S. Hayden, , D. McMorrow, P. Deen, A. Hiess, Report on the ESS Symposium on Spin Dynamics (Abingdon, 2012).
- [25] M. Hirschmann and D. Kohlstedt, *Physics Today* **65** (3), 40 (2012);
- [26] D. G. Pearson, F. E. Brenker, F. Nestola, J. McNeill, L. Nasdala, M. T. Hutchison, S. Matveev, K. Mather, G. Silversmit, S. Schmitz, B. Vekemans, and L. Vincze, *Nature* **507**, 221 (2014).
- [27] S. Klotz ( University Pierre and Marie Curie) personal communication.
- [28] L. E. Bove, S. , *Phys. Rev. Lett.* **111**, 185901 (2013)
- [29] Neutron Applications, Neutron Scattering Applications and Techniques, V. García Sakai, C. Alba-Simionesco, S.-H. Chen. (Springer Science and Business Media, 2012) M.C. Rheinstädter, Chapter 10 Lipid Membrane Dynamics, *Dynamics of Soft Matter*.